Mechanical modeling of crawling cells

Pierre Recho

To cite this version:

Pierre Recho. Mechanical modeling of crawling cells. Biomechanics [physics.med-ph]. Ecole Polytechnique X, 2012. English. NNT : . pastel-00801360

HAL Id: pastel-00801360
https://pastel.hal.science/pastel-00801360

Submitted on 28 Mar 2013

Mechanical modeling of crawling cells

Pierre Recho
Laboratoire de Mecanique des Solides
Ecole Polytechnique

Thèse de doctorat de l'Ecole Polytechnique, Spécialité: Mécanique

Soutenue le 20 Décembre 2012 devant le jury composé de :

Abdul Barakat	Examinateur
Emmanuel de Langre	Examinateur
Jean-François Joanny	Raporteur
Cécile Sykes	Rapporteur
Lev Truskinovsky	Directeur de thèse

Abstract

The ability of most eukaryotic cells to crawl is essential for embryogenesis, immune response and wound healing while functional abnormalities of crawling can provoke different diseases including cancer. Artificial biomimetic machines mimicking eukaryotic cells are of interests as prototypes of versatile engineering devices operating autonomously at a nano-scale. A prototypical scheme of cell motility includes polymerization of actin network coupled with dynamic assembly of focal adhesions, myosin-driven contraction and, finally, the detachment of adhesive contacts followed by de-polymerization which closes the treadmilling cycle. The motor part of an eukaryotic cell is a layer of an active gel whose functions are controlled by complex chemical and mechanical processes. In particular, the coordinated movements of this gel resulting in crawling involve spatial and temporal self-organization at the cytoskeletal level and require a continuous supply of energy. While the molecular and biochemical basis of cell motility is basically known, the qualitative understanding of the mechanical interplay between different active components is still limited despite many recent attempts to construct comprehensive mathematical models. This manuscript aims at presenting an analysis of a simple and one dimensional model accounting for cell crawling.

The first chapter is dedicated to optimization of speed and mechanical efficiency of crawling. Our analysis shows that the obtained optimal distribution of contractile stresses and the optimal friction distribution are in good agreement with the observed distributions.

In the second chapter, we propose a mechanism of cell motility which places emphasis on contraction while ignoring actin treadmilling. At the basis of the model is contraction driven uphill diffusion destabilizing symmetric configuration and causing polarization. The morphological instability is

due to spontaneous internal motion of the cytoskeleton which is generated by active cross-linkers and simultaneously transports them. By studying the simplest one dimensional problem we show that such internal flow can generate steady propulsion of a finite cell body. The model exhibits motility initiation patterns similar to the ones observed in experiments.

In the last chapter we focus on actin treadmilling-based motility which allows the cell not only to self-propel but also exert forces on obstacles (to push) and carry cargoes (to pull). We use a minimal one dimensional model of the crawling cell to show that the pushing dominated force-velocity relation is controlled by the protrusion mechanism. Instead, the pulling dominated force-velocity relation is controlled by the protrusion mechanism only at small values of the force which is replaced by the contraction mechanism at sufficiently large forces.

The chapters are written in such a way they can be read independently.

Several appendixes contain discussions of some auxilliary models and some other results of technical nature.

Remerciements

La nature m'ayant pourvu d'une mémoire bien défaillante, je dois commencer ce difficile exercice par m'excuser des oublis involontaires que je vais forcément perpétrer. Cette frivolité n'en n'est pas pour autant excusable et je vous suis redevable bien au delà des simples références.

La conjonction de deux éléments m'a conduit à vouloir réaliser cette thèse. La rencontre de Lev Truskinovsky et ses explications déjà perçantes de simplicité d'une part et le cours de Biologie cellulaire de René Marc Mège et Cécile Sykes d'autre part. Je dois particulièrement remercier cette dernière d'avoir accepté de relire ce manuscrit malgré le peu de temps qui lui était imparti. Il m'est impossible de mesurer ce que je dois à Lev tant j'ai appris à son contact, et ce bien au delà de mon strict travail.

J'ai eu la chance de commencer cette thèse au Laboratoire de mécanique des solides sous les auspices de Bernard Halphen et de la terminer sous ceux de Patrick Le Tallec, tous deux, ainsi bien sur que tout le personnel du laboratoire et en particulier Alexandra et Christiane me furent d'une très grande aide.

Je dois également beaucoup à Alex Mogilner et son groupe de l'Université de Davis ou j'ai passé quelques mois. Non seulement Alex m'a pointé du doigt certains problèmes centraux en matière de régulation de la motilité cellulaire mais ma reconnaissance se perd aussi sur les sentiers de Point Reyes et du massif central.

C'est à l'Institut Curie que Jean-Francois Joanny m'a donné l'opportunité de venir présenter mes premiers résultats. A lui et tout son groupe, je suis profondément reconnaissant pour leurs questions et leurs suggestions toujours très précises et très étayées. Je remercie également Jean-Francois Joanny de sa disponibilité pour relire ce manuscrit.

De la présentation de mon travail au groupe de mécanique du vivant, j'ai également beaucoup appris. Merci donc à Abdul Barakat, Emmanuel De Langre, Jean Marc Allain et Xavier Boutillon et tous leurs étudiants pour toutes leurs suggestions et leurs remarques qui m'ont permis d'avancer. Je remercie particulièrement les premiers nommés pour avoir accepté de faire parti de mon Jury de thèse.

Merci à Andrei et Kostas pour les heures passées à compter les carreaux entre 7h et 8h30, la passion du froid polaire et des montagnes lointaines. Je n'oublie évidemment pas Umut, de ses dislocations aux surprenantes lois d'échelle jusqu'à ses chaussures de foot qui hantent toujours notre bureau. A tous mes collègues et amis, Matthieu, Raman, Cédric, Paul, Anders, Guido, Peppe, Anup, Christian, Thibault et Joachim je veux également dire un grand merci pour ces trois dernières années. De vous tous, j'ai beaucoup appris.

Cette thèse n'aurait à coup sur ou très probablement (selon les cas) jamais eu lieu sans les interventions attentionnées, appropriées et concertées de Joelle, Naman, Jan, Micheline et Dominique.

Enfin et surtout je dédie ce travail à Charline. Ubi tu Gaia, ego Gaius.

Acknowledgements

I deeply acknowledge Lev Truskinovsky who has been the driving force of my phd work and a constant source of inspiration and support. I am very grateful to Alex Mogilner and Jean-François Joanny for helpfull discussions and comments on both Physics and Biology. I would like to thank Karsten Kruse and two anonymous reviewers for their suggestions regarding this work. François Alouges and Tony Lelievre gave me some precious advice on some mathematical topics. Last but not least, i have greatly benefited from Thibault Putelat's experience on bifuraction theory.

Contents

1 Introduction 1

1.1 Crawling cells 1
  1.1.1 A brief overview of biochemical basis of crawling 1
  1.1.2 Physical models of the cytoskeleton 2
    1.1.2.1 Passive rheology of the cytoskeleton 3
    1.1.2.2 Polymerization/depolymerization in the lamellipodium . 4
    1.1.2.3 Contraction 8
    1.1.2.4 Adhesion 10
1.2 Models of crawling cells 12
  1.2.1 Self induced polarization 14
  1.2.2 Treadmilling driven cell motility 14
  1.2.3 Contraction driven cell motility 16
  1.2.4 Comprehensive models 17
    1.2.4.1 Theory of active gels 17
    1.2.4.2 Discrete approaches 17
    1.2.4.3 Multiphase flow models 18
    1.2.4.4 Other models 18

2 Chapter I: Optimal crawling 21

2.1 Building the model 21
  2.1.1 Main constitutive assumptions 21
  2.1.2 Adhesion and motion 24
2.2 The model of motile cell 24
  2.2.1 Setting the problem 24
  2.2.2 Importance of elasticity 26

2.3 Travelling wave assumption 27
2.4 The optimization criteria 28
2.5 Neglecting treadmilling 29
2.6 Optimization of velocity 30
  2.6.1 Homogeneous adhesion 30
    2.6.1.1 Existence of traveling wave solutions 30
    2.6.1.2 Optimal velocity of traveling wave solutions 33
  2.6.2 The role of adhesion 35
    2.6.2.1 Existence of the traveling wave solutions 37
    2.6.2.2 Optimal velocity of the traveling wave solutions 37
2.7 Optimization of efficiency 40
  2.7.1 Formulation of the variational problem 41
  2.7.2 A priori bounds on efficiency 42
  2.7.3 The subproblem at fixed L and V 43
  2.7.4 Euler-Lagrange equation for problem (2.21-2.22) 44
  2.7.5 Solution of the problem with no sign constraint 47
  2.7.6 Solution of the problem with a sign constraint 48
    2.7.6.1 Case $\epsilon = 0$ 48
    2.7.6.2 Case $\epsilon > 0$ 50
2.8 Conclusions 52

3 Chapter II: Contraction at work 55
3.1 Introduction 55
3.2 The model 57
3.3 Traveling wave solutions 66
3.4 Non motile solutions 67
  3.4.1 Regular solutions 67
  3.4.2 Singular solutions. 75
3.5 Motile bifurcation from trivial non motile states 76
3.6 Numerical study of the non-steady problem with initial data, stability . 84
3.7 Two limiting regimes 89
  3.7.1 The hyperbolic limit 89
  3.7.2 The inviscid limit 95

3.8 The flow of actin 98
3.9 Efficiency of the autotaxis mechanism 103
3.10 Further directions, breaking the symmetry 107
3.11 Conclusion 111

4 Chapter III: Protrusion at work 113

4.1 Introduction 113
4.2 The model 115
4.3 Traveling wave solutions 116
  4.3.1 Force velocity relations 117
  4.3.2 Spatial inhomogeneity of the friction coefficient 120
4.4 Density distribution 122
  4.4.1 Localized depolymerization 123
  4.4.2 Delocalized depolymerization 124
  4.4.3 Density dependent contraction 128
4.5 Energetics 132
4.6 Elasticity regularization 134
4.7 Length regularization 140
  4.7.1 Purely viscous case 140
  4.7.2 Linearized Kelvin case 140
  4.7.3 Non linear Maxwell case 141
4.8 Alternative driving mode 142
4.9 Conclusion 144

5 Conclusion and perspectives 145

6 Appendixes 149

6.1 Model for front oscillations 149
  6.1.1 Minimal setting, necessity of mass regulation 149
  6.1.2 Mass regulated system 151
  6.1.3 Attempts to get net motion of the front 154
  6.1.4 $L_0(M)$ 154
  6.1.5 More realistic passive elements 155
  6.1.6 More precise mass balance 158

6.2 A remark on the distributions of integrins and myosins 159
    6.2.1 Dynamics of c_1 (integrins) 159
    6.2.2 Dynamics of c_2 (myosins) 161
6.3 Imposing the sign constraint $g \geq 0$ in the minimization problem (2.21) . 162
6.4 Justification of the 1D model from the perspective of a 2D model 164
6.5 Numerical methods 169
    6.5.1 Numerical method for the Cauchy problem 169
    6.5.2 Efficiency Optimization 173

References **175**

1

Introduction

1.1 Crawling cells

1.1.1 A brief overview of biochemical basis of crawling

One of the most striking property that distinguishes a living cell is its capacity to reproduce and thus transmit its genetic material to its offsprings. Directional motion is another feature of cells associated with living and requiring constant energy intake. While most of the cells constituting a multicellular organism are static, some are motile because of their function. In their early life, stem cells of the embryo have to move with respect to each other to form tissues and organs. During the immune response, leukocytes can migrate through capillaries to attack infections. Wound healing requires the motion of fibroblasts and cancer produces abnormaly moving cells that create metastasis. More fundamentaly, most cells when released from the entanglement by their neighbors [27] can polarize and undergo directed motion. While we often associate cell motion with swimming meaning that a solid body undergoes directed motion by performing strokes, in this thesis, we focus on crawling which we associate with the directed motion of a viscoelastic body on a solid substrate. Several prototypical types of cells such as fibroblasts, keratocytes, nematodes spermatozoa or neutrophils are known to perform crawling and have been the subject of intense experimental and modeling activities. The characteristic size of these cells ranges from 10 μm to 100 μm and they can crawl at speeds ranging from $1 \mu m/min$ to 50 $\mu m/min.$ The ability of cells to polarize and crawl in a given direction depending on the substrate rigidity relies on the highly dynamic and self organized properties of cytoskeleton. Motion of the cell requires constant energy supply in the form of ATP which drives three main active networks of biopolymers constituting the cytoskeleton: microtubules, intermediate filaments and actin filaments. We shall concentrate on the cross linked actin filaments as a prototype of an active network.

Actin forms filaments of a characteristic diameter of 7 nm which are polarized and undergo polymerization with a net growth at their barbed end and depolymerization at the pointed end. In some metabolic conditions, the filaments can keep a constant length while undergoing constant polymerization and depolymerization in a cyclic way (treadmilling) fueled by the energy uptake through ATP hydrolysis. The actin filaments are cross-linked to form a network by passive and active cross-linkers (motors). In this thesis, we concentrate on one prototypical active cross-linker, myosin II (or conventional myosin) which generate relative contraction between two active filaments. There are other motor proteins such as Kinesins whose role is to enable reorganization of the microtubules network and intracellular transport. Yet another motor protein, Dynein enables cilia beating and is rather related to swimming.

The active acto-myosin network transmits mechanical and chemical stimuli from and to the substrate through the plasmic membrane for adhesion and signalling purposes. This function is performed by complexes of proteins such as integrins that link the active network and the substrate and use energy from ATP hydrolysis to actively engage or disengage with a subsrate.

The whole cycle of cell motility is usually presented as a combination of the following mechanisms [1, 18, 19, 169]: protrusion through growth (polymerization of actin) in the frontal area of the cell called lamellipodium with the formation of localized adhesions at the leading edge, detachment at the rear accompanied by contraction and lessening (through depolymerization), and then another protrusion. All these phenomena happen simultaneously and lead to a nearly steady motion of the cell.

1.1.2 Physical models of the cytoskeleton

The cytoskeleton contains several networks and around 100 actin binding proteins types and many different types of substrate binding proteins that can tune in different ways its dynamic response. Full comprehensive models [93, 106, 107] lead to dramatic complexity which is not necessarily relevant for all individual cell processes [122]. We shall concentrate on crawling only and consider the physical models involving only the main players.

1.1.2.1 Passive rheology of the cytoskeleton

The rheological behavior of the cytoskelleton is complex and depends significantly on the testing conditions [24, 46, 122]. Under sufficiently "small sollicitations" (say, in stress) the cytoskeleton is widely regarded as a viscoelastic material with both loss and storage moduli frequency dependent. Focusing on motility of keratocytes, we consider the effect brought by simple rheological models: Maxwell viscoelasticity advocated in [34, 83, 89, 151, 156] and a Kelvin viscoelasticity which was p in [13, 14, 24, 37, 53, 58, 102, 122, 138].

The differential Maxwell model [87] reduces in one dimension to the equation,

$$\lambda \frac{d\sigma_e}{dt} + \sigma_e = \eta \partial_x v$$

where x is the space coordinate, t the time coordiate, σ and v respectively denote the elastic part of the internal stress and the velocity of matter inside the cytoskeleton, λ is a relaxation time that was estimated to range from $1s$ to $10s$ [95, 137, 189] and η is a bulk viscosity that was estimated $5 \times 10^4 Pa \cdot s$ [97]. The time derivative is most often interpreted as a corotational derivative [21]. Within such model, the cytoskeleton can be viewed as a solid at short time scales and like a fluid at long time scales [87]. It is a basic model often used for polymers which neglects the storage modulus at a large enough time (linked with the observation time via the Deborah number) when full relaxation of the elastic stress takes place [156].

On the contrary, Kelvin model does not neglect the long time storage modulus E. In one dimensional case, we can write

$$\sigma_e = \eta \partial_x v - E f(\frac{\rho}{\rho_0}),$$

where ρ denotes the cytoskeleton density while ρ_0 is some reference density. The function f is a dimensionless function and since the cytoskeleton is very soft, E ranges from $0.1kPa$ to $10kPa$. This estimate of E is very rough since the stiffness of the cytoskeleton is known to be actively varying over at least one order of magnitude by active cross-linkers [94, 113, 165]. We observe that in one dimension, $\frac{\rho_0}{\rho}$ is a dimensionless measure of local strain. The function f penalizes deviations of density away from ρ_0 by creating larger stresses. Some classical expressions are:

$$f = \frac{\rho}{\rho_0} - 1,$$

which penalizes infinite stretch while,

$$f = 1 - \frac{\rho_0}{\rho},$$

penalizes infinite compression. An other expression used for the description of cell population in [10] is:

$$f = \log(\frac{\rho}{\rho_0})$$

On can see that it penalizes both infinite stretch and compression.

The origin of the elastic properties may not be related to actin only as microtubules (much stiffer) and cross linkers also play a fundamental role [176]. The role of the plasmic membrane is also important. This has motivated the appearance of coarse models aiming at capturing the elastic behavior qualitatively by connecting the front and rear by a spring. The stiffness of the spring was estimated in [14, 58, 110] to range from $1kPa$ to $10kPa$. In [14] it was associated with mean field cytoskeletal elasticity while in [58] it was rather linked to the membrane.

1.1.2.2 Polymerization/depolymerization in the lamellipodium

The chemical basis of polymerization/depolymerization of an actin filament at the leading edge of the cytoskeleton is basically known [3, 27, 134, 145]. In the absence of ATP, after the formation of a precursor nucleus, the (F-actin) filament elongates proportionally to the monomer (G-actin) concentration with a rate k_{on} and disassembles with a rate k_{off}. There is then an equilibrium monomer concentration $C_c = k_{off}/k_{on}$. At this concentration, the filament stabilizes (See Fig.1.1). The difference between the pointed and barbed end of the filament only shows in the kinetics of the chemical reaction but the equilibrium concentration is the same. In the presence of ATP, the situation changes and the equilibrium concentration is not the same any more for the two ends and it can be as much as 10 times smaller at the barbed (C_c^b) end then at the pointed (C_c^p) end [27]. Then, for concentrations between C_c^b and C_c^p, there is net polymerization at the barbed end and net depolymerization at the pointed end with each monomer undergoing

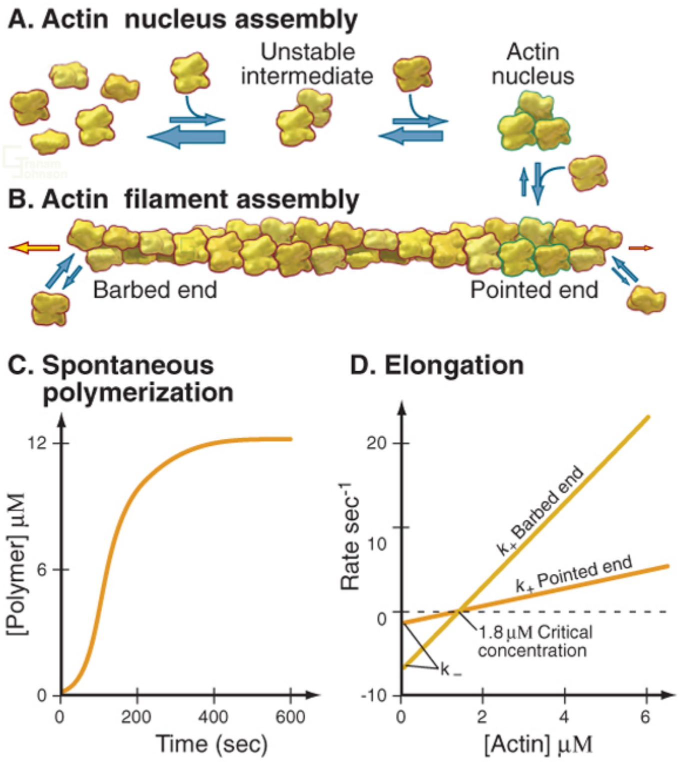

Figure 1.1: Actin filament assembly. A, Formation of a trimeric nucleus from monomers. B, Elongation of the two ends of a filament by association and dissociation of monomers. C, Time course of spontaneous polymerization of purified ADP-actin under physiological conditions. D, Dependence of the rates of elongation at the two ends of actin filaments on the concentration of ADP-actin monomers. Taken from [145]

treadmilling from the barbed to the pointed end. In the meantime, the system remains of constant length outside thermodynamical equilibrium. For the whole actin network, the situation is more complex due to the interactions of the actin network with other proteins (See Fig.1.2). In particular, actin filaments may be capped and stop growing. One filament may also branch to give birth to a secondary filament. The presence of the neighboring membrane creates mechanical forces that interfere with the polymerization process.

These effects have been physically modeled and molecular dynamic simulations of the whole network have been performed. Of particular interest is the role of the membrane exerting a force on the network that has been studied in the framework of the

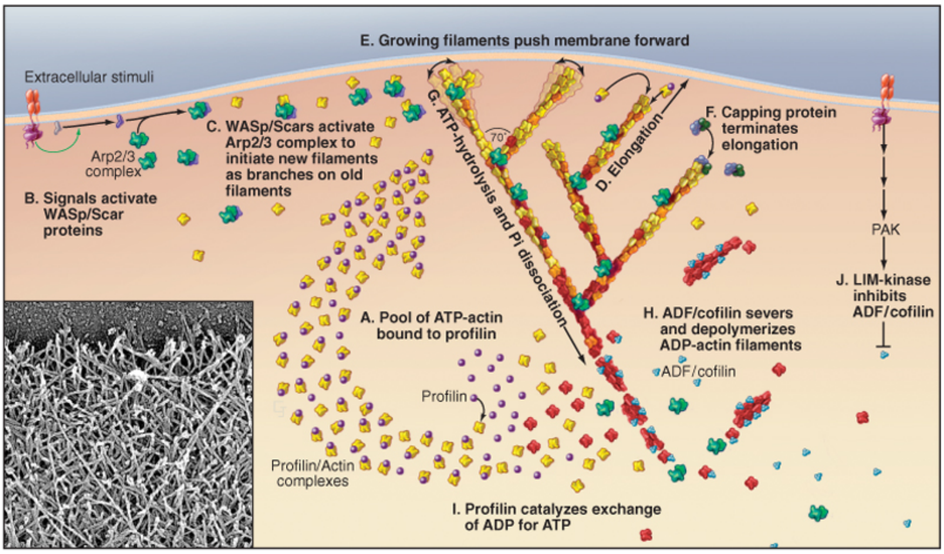

Figure 1.2: A model For actin filament assembly and disassembly at the leading edge. The reactions are separated in space for clarity but actually occur together along the leading edge. A, Cells contain a large pool of unpolymerized actin bound to profilin. B, Stimulation of cell surface receptors produces activated Rho-family guanosine triphosphatases (GTPases) and other signals that activate WASp/Scar proteins. C, These proteins, in turn, activate nucleation of new actin filaments by Arp2/3 complex on the side of existing filaments. D, The new filaments grow at their barbed ends until they are capped (see F). E, Growing filaments push the plasma membrane forward. F, Capping protein terminates elongation. G, Polymerized ATP-actin (yellow) hydrolyzes the bound ATP to ADP and inorganic phosphate (Pi) (orange), followed by slow dissociation of phosphate yielding ADP-actin (red). H, ADF/cofilins bind and sever ADP-actin filaments and promote disassembly of ADP-actin. I, Profilin promotes the exchange of ADP for ATP, restoring the pool of unpolymerized ATP-actin bound to profilin. J, Some of the same stimuli that initiate polymerization can also stabilize filaments when LIM-kinase phosphorylates ADF/cofilins, inhibiting their depolymerizing activity. Inset, Electron micrograph of the branched network of actin filaments at the leading edge. PAK, p21-activated kinase. Taken from [145]

brownian ratchet theory. In their pioneering paper [143], the authors considered one actin filament polymerizing against a given force when the whole system is connected to a thermal bath. The rate at which monomers can attach to the actin filament depends on whether there is enough room for them to attach the main filament under the condition that the membrane undergoes equilibrium thermal fluctuations. This model leads to a steady filament growth against an applied force. The theory was then considerably refined taking into account the angle between the membrane and the branching and capping properties as well as the presence of some actin binding molecules [41, 79, 123, 125]. Viscoelastic rheology of the actin filaments and the membrane were also taken into account [11, 12, 37, 92] which allowed the authors to explain different morphologies of the cell leading edge. In a comprehensive model [38] the experimentally observed oscillatory behavior of the edge was investigated and related to fracture of filaments. The fluctuations were shown to have non-gaussian statistics. In appendix (6.1), we show how a much simpler one dimensional model can be used to link fluctuations of the leading edge and fracture.

Seeking to capture the main effects only we model in this work the acto myosin filemantal network as a continuous one dimensional layer. It describes an active gel (filaments polarized in the same direction) composed of two species: actin polymers (F-actin) which receive mechanical stimuli from the exterior and actin monomers (G-actin) which are free to diffuse inside the lamellipodium. As the pool of G-actin is very large [145], it is a valid assumption to consider its concentration is constant. Proteins promoting polymerization such as ARP2/3 [145] are assumed to be present only close to the leading edge. In this setting, polymerization is modeled by a mass flux of monomers $\dot{m} < 0$. The complete polymerization/depolymerization cycle of the gel are governed by the conservation equation for F-actin:

$$\left\{ \begin{array}{c} \partial_x \rho(x,t) + \partial_x(\rho v(x,t)) = -\gamma(x,t)\rho(x,t) \\ \rho(l_+(t),t)(v(l_+(t),t) - \dot{l}_+(t)) = \dot{m} \end{array} \right.$$

Here t is time and $x \in [l_-(t), l_+(t)]$ is the space coordinate in the finite moving layer with rear boundary $l_-(t)$ and front boundary $l_+(t)$. The F-actin density is denoted ρ and v is the velocity field of actin, γ is a depolymerization rate. In most of the thesis, we make additional simplifying assumption [89, 97] that depolymerization is also localized at the trailing edge of the lamellipodium. Then we can write,

$$\left\{ \begin{array}{c} \partial_x \rho(x,t) + \partial_x(\rho v(x,t)) = 0 \\ \rho(l_+(t),t)(v(l_+(t),t) - \dot{l}_+(t)) = \dot{m} \\ \rho(l_-(t),t)(v(l_-(t),t) - \dot{l}_-(t)) = \dot{m} \end{array} \right.$$

where we assumed that the total mass of F-actin is conserved in time because the depolymerized actin at the trailing edge is instantaneously polymerized at the leading edge. By prescribing the mass flux, we fix an amount of incoming and outcoming material brought each second. However, we say nothing about the way the new material is assembled (see Fig.1.3). As the branching structure of actin at the leading edge is basically known, it can be considered (e.g.[89, 97, 102]) that instead of the mass mass flux, it is the polymerization ($v_+ > 0$) (depolymerization ($v_- > 0$)) velocity that is prescribed. The implicit assumption here is that depolymerization is more important at the rear than in the rest of the cell. This leads to the following system :

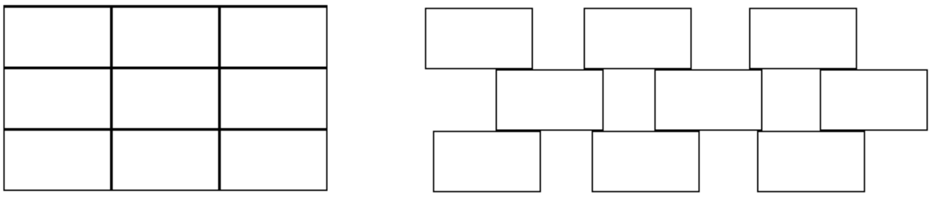

Figure 1.3: Two different ways to build a "wall" given the same mass flux.

$$\left\{ \begin{array}{c} \partial_x \rho(x,t) + \partial_x(\rho v(x,t)) = 0 \\ \dot{l}_+(t) = v_+ + v(l_+(t),t) \\ \dot{l}_-(t) = v_- + v(l_-(t),t). \end{array} \right.$$

1.1.2.3 Contraction

Myosin II was initially discovered as the main player responsible for contraction of striated muscles[80, 81] however it also induces contraction inside the cytoskeleton of almost all eukaryote cells [27]. Myosin molecule is composed of two helix shaped heavy chains which possess heads and tails and two light chains stabilizing and regulating heavy chains (see Fig.1.4). The tails of two myosin molecules can bundle to form a dimer bipolar filament with heads pointing in different directions and this structure can be linked in parallel with others of the same type to form larger bipolar filaments. Each set of heads can then interact with two parallel actin filaments by pulling in opposed directions thus inducing relative movement (contraction) of the the two actin filaments (See Fig.1.4). Actin network with myosin II crosslinkers can be studied in molecular dynamic simulations. In particular, the influence of contractility on network elasticity has been studied in [94, 176]. In this work, we focus on very coarse models

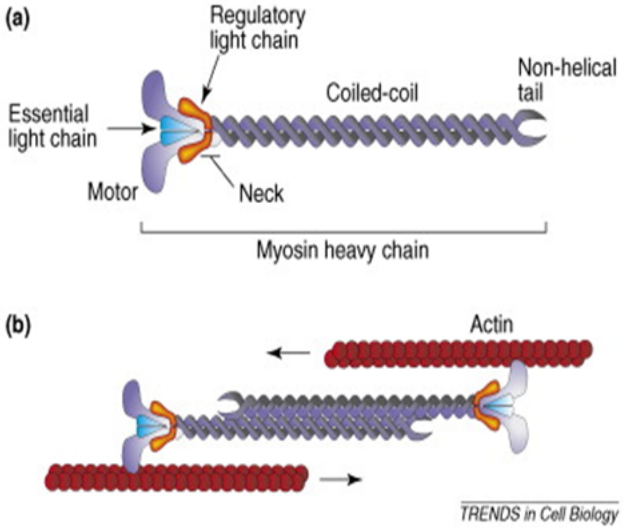

Figure 1.4: The actomyosin cytoskeleton. (a) Schematic diagram of a myosin II monomer, depicting the light and heavy chains. The different parts of the heavy chain, including the motor, neck, coiled-coil and nonhelical domains, are indicated. (b) Myosin II self-assembles into bipolar filaments through interactions of the C-terminus; the N-terminus binds to actin filaments. Activation of the myosin II motor domain leads to the pulling of actin filaments (in the direction of the arrows) to induce cortical tension. Taken from [48].

accounting for contractility at the level of continuous media as it is done in the theory of active gels by including a new active term in the expression of the entropy production [34, 83, 84, 98].More precisely, we suppose that in the presence of ATP, the actin network is submitted to a negative (contraction) constant prestress:

$$\sigma_c = \chi h(\frac{c(x,t)}{c_0}) < 0,$$

where χ is the contraction modulus that is of order $1kPa$ [89], c is the concentration of myosin II molecules crosslinking actin fibers and c_0 is some reference density. Yhe function h is potentially non linear. It increases linearly for small ($c << c_0$) concentrations and then saturates when concentration becomes large ($c >> c_0$). For example the expression,

$$h(u) = \frac{u}{1+u}$$

was considered in [25]. For simplicity, it has often been assumed that $h \equiv 1$ in [89, 98]. Due to its resemblance with elasticity, we shall label this contribution to internal stress as 'anti-elastic'. Macro models dynamic must contain an equation for the myosin motors concentration c. It can be derived from the fact myosin forms bipolar filaments between actin fibers and hence is driven by the motion of actin [15, 25, 156, 172, 187]. We may then write,

$$\partial_t c(x,t) + \partial_x (cv(x,t)) - D\partial_{xx} c(x,t) = 0,$$

where D is diffusion coefficient accounting for the mobility of bipolar filaments with respect to actin. The origin of such diffusion is the non negligible [126] stochastic dynamics due to the thermal fluctuations.

1.1.2.4 Adhesion

A mechanical link between the cell membrane and the adjacent membrane or extra cellular matrix is ensured by various surface proteins generically called CAM (cell adhesion molecules). The CAMs are connecting the intracellular domain (C-terminal region) to the extracellular domain (N cellular region). While cadherins, immoglobulines and selectins are involved in the anchorage of a cell to its neighbors, integrins are the main receptors to the extracellular matrix (represented, for example, by collagen or fibronectin). Integrins are composed of two proteic subunits, which are extended across the cell membrane and connect the inside of the cell with the outside. These subunits are called alpha chain and beta chain and both of them contribute to the bindings of the cell with the environment (see Fig.1.5) They can be quite versatile in nature and can adapt to different kinds of substrates (17 alpha subunits and 8 beta subunits have been identified [3]).

The alpha and beta subunits are intracellularly connected via proteins such as talin and vinculin to the actin filaments of the cytoskeleton and can transmit stress (and more generally signals) throughout the whole network. The integrins can only bind to their binding partners on the substrate when there is a minimum number of integrins present at specific places known as focal contacts. The affinity of integrins for their ligands is not very strong. Therefore, to form sufficiently strong contacts, several integrins must be grouped into a highly localized focal contact. Instead, when the integrins are diffusely distributed over the cell surface, strong adhesion is not possible. Low affinity of integrins to their ligands is necessary however to prevent irreversible binding, which would inhibit motility. As mentionned above, by actively creating and

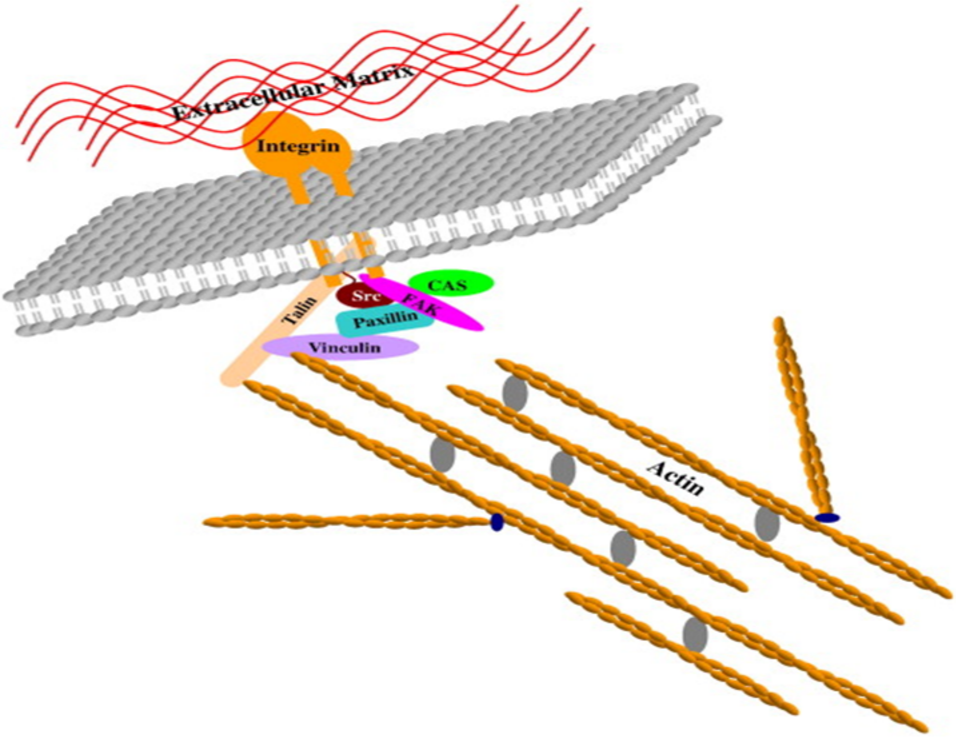

Figure 1.5: Focal adhesions as ideal checkpoints controlling inside-out and inwards transduction of mechanical signals. Focal adhesion components including transmembrane integrins and intracellular Src, FAK, Paxillin, Talin, Vinculin and CAS all assemble at the cell surface to create a physical anchorage point linking the extracellular matrix to the intracellular meshwork of actin filaments. Taken from [193].

breaking focal contacts, cells can self propell along the substrate. Additionally, cells are able to "sense" their substrate stiffness and choose their direction of motion accordingly; preferentially moving from soft to hard surfaces and migrating faster on stiffer substrates [69] (haptotaxis). This reveals the central role of the extracellular matrix in cell migration and development. Developing the pioneering work of Bell [17], Erdmann et al. [59, 60] studied a cluster of parallel bonds submitted to a given loading equally shared between the bounds. They allowed for rebinding to show that the cluster lifetime is increasing with its size. More advanced studies [43, 62, 139, 194, 195] including mean field elasticity for both the cell and the matrix which couples the adhesion clusters where carried out to understand the characteristic size of adhesion clusters, the effect of the matrix stiffness and the role of the load orientation. These studies are however oversimplified and they cannot desribe (except in large scale Monte Carlo simulations) the observed stress-strain (and stress-strain rate) relations ruling interaction of a cell with the substrate. In this field macro models of adhesion [13] have been developped to relate substrate stiffness with polarization of the cell however they still do not account for motile states of the cell. As the dynamics of adhesion complexes is very complex [23], the stress generated by adhesion clusters is often considered as a passive factor depending only on the internal flow of actin. A usual assumption made in the context of cell motility [56, 74, 89, 102, 156, 163] is to model adhesion as viscous friction. In this approach, the time averaged tension generated by constantly engaging and disengaging focal adhesions is proportional to the velocity of the retrograde flow (see [173] for a microscopic justification).

$$\sigma_{adh} = -\xi v$$

where ξ is a friction coefficient that was estimated to be around $1000 pN.s/\mu m^3$ in [89, 156]. There is evidence (both experimental [25, 63, 64, 126, 161] and theoretical [53, 118]) that this assumption describes the behavior of focal adhesions accurately only if the retrograde flow is sufficiently slow and that the behavior of adhesion strength in the broader range of velocities is bi-phasic. We neglect the bi-phasic effect and potentially misrepresent sufficiently fast dynamics. However, we shall also consider the inhomogeneity of ξ which has been evaluated experimentally in [26, 191] for nematode spermatozoa and in [156] for keratocytes directly or by assuming that ξ is proportional to local integrin concentration that is ruled by a diffusion equation with a drift proportional to the actin flow [15].

1.2 Models of crawling cells

While many of the biochemical details of the processes involved in the crawling process remain unclear, three main steps (See Fig.1.6), occurring simultaneously, have been clearly identified [1, 18, 19, 169]

1. The cell forms a lamellipodium at the leading edge. This is a thin active gel type structure of about $200nm$ which elongates under the influence of polymerizing actin and pushes the plasmic membrane. The newly polymerized actin filaments then treadmill to the rear where they are depolymerized.

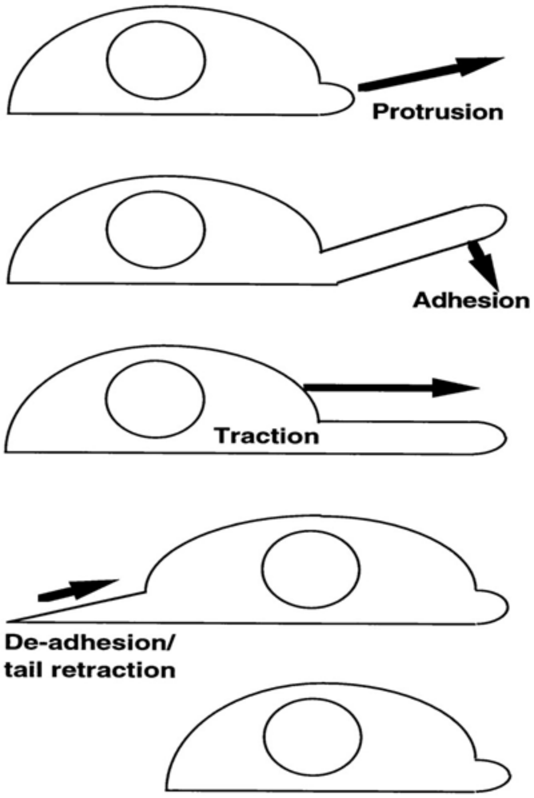

Figure 1.6: A single cell moving across a two-dimensional substrate is shown in cartoon form (time increases down the page). Detailed morphology varies between cell types, but the same basic types of motility can be distinguished. In cells where the processes occur simultaneously, the morphology is constant during locomotion. Taken from [121].

2. While the nascent lamellipodium is being created, focal adhesions are built in and serve as anchorage points to transfer momentum from the cytoskeleton to the extra cellular substrate through the creation of stress fibers.

3. The trailing edge of the cell contracts under the influence of myosin motors creating active stress in the cytoskeleton. As a consequence, the nucleus can be pulled and a prograde flow is created transporting actin monomers to the leading edge where they can be polymerized again. This contraction also induces debonding of focal contacts at the rear.

There is a wide range of mathematical models describing the above processes and accounting for cell motility. Before making a review of the synthetic models, we give a brief overview of 'submodels' that account for cell crawling by neglecting contraction and emphasizing actin treadmilling. To initiate motion, however, the cell has to chose a direction (i.e. to polarize). Such polarization can be induced by chemoatractants (Chemotoaxis) but can also be self induced and it is natural to start with the description of this phenomenon.

1.2.1 Self induced polarization

How exactly the cytoskeleton induces self-asymmetry [129] is still not fully understood. Several mechanisms have been proposed. Spontaneous polarization of the cell initiated by polymerization in confined geometries has been proposed in [72, 73]. Symmetry breaking in polymerizing actin gels due to mechanical [86] and chemical [178] effect has also been considered. A different perspective was proposed in [13] where spontaneous polarization of cells was linked to the interplay between substrate stiffness and contractile activity. It has also been interpreted in terms of Turing mechanism and linked to reaction-diffusion dynamics of signalling substances inside an elastic membrane [128, 179]. In the same spirit, a membrane releasing markers that modify the cytoskeleton state was also linked to polarization in [71]. A minimal description of this type reminiscent of Keller Segel [142] model was proposed in [35].

In important experiments [180, 190], cell polarization of fish keratocytes was observed in vivo and directly linked to the asymmetry of myosin distribution inside the cell (see Fig.1.7). This asymmetry was achieved either by transient mechanical stimulus [180] or by transient chemical stimulus [190]. While most of the models account rather indirectly for myosin II, some recent approaches of [74, 78, 144] present a perspective where cell polarization is explained by active contractile stress only.

1.2.2 Treadmilling driven cell motility

Motors of the myosin II family are not necessary for the crawling motion of cells. Polymerization and depolymerization of actin may be sufficient. A prototypical example is the bacterium Listeria monocytogenes which moves by developping an actin comet tail pushing the bacterium forward [66, 148, 175] (see Fig.1.8). It continuously adds new polymerized actin filaments to its surface and squeezes them between the tail made of previously polymerized actin filaments and the main body of the cell. This creates propulsive stress which advances the cell.

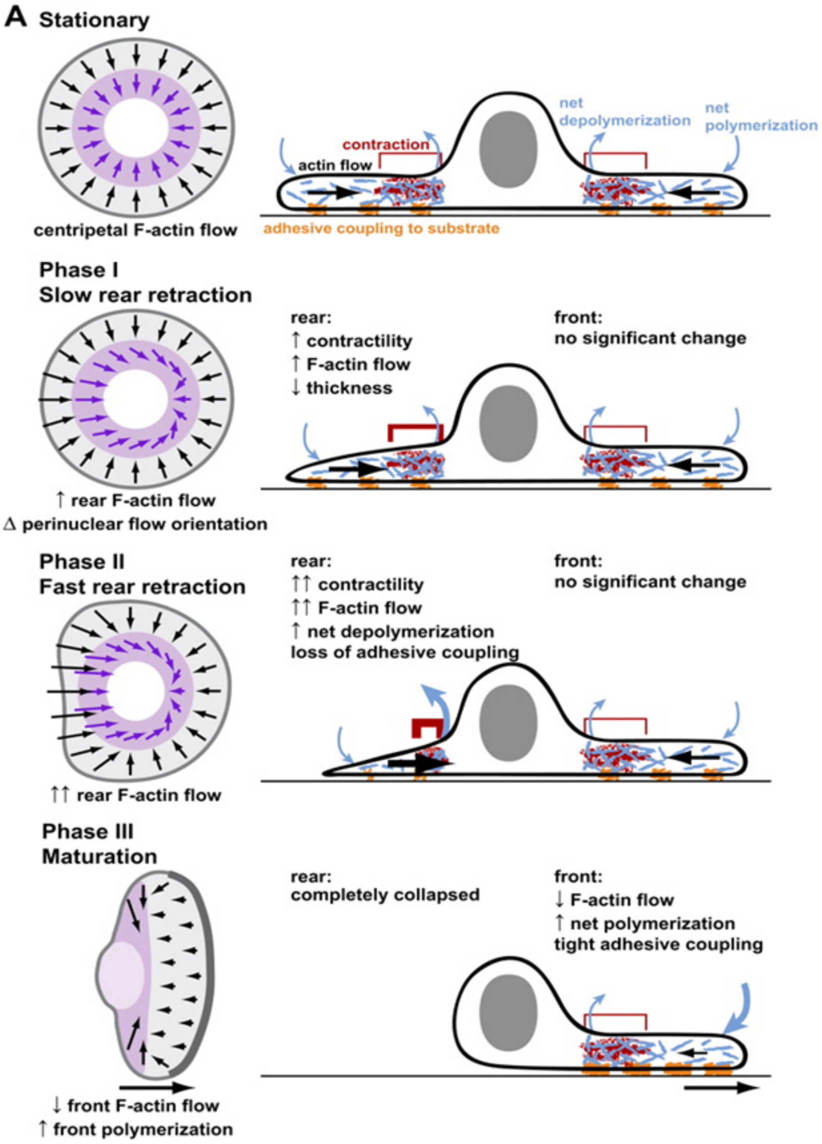

Figure 1.7: Model for symmetry breaking and motility initiation in keratocytes. Taken from [190].

This situation can be reproduced in vitro with polystyrene beads [115] and in this particular case the mechanism leading to spontaneous motion is well understood [86, 131]. Directional motion can be initiated spontaneously due to mechanical instability breaking symmetry of the initially isotropic growth and converting it into a directional one. It was found that the symmetry breaking time increases with the radius of the

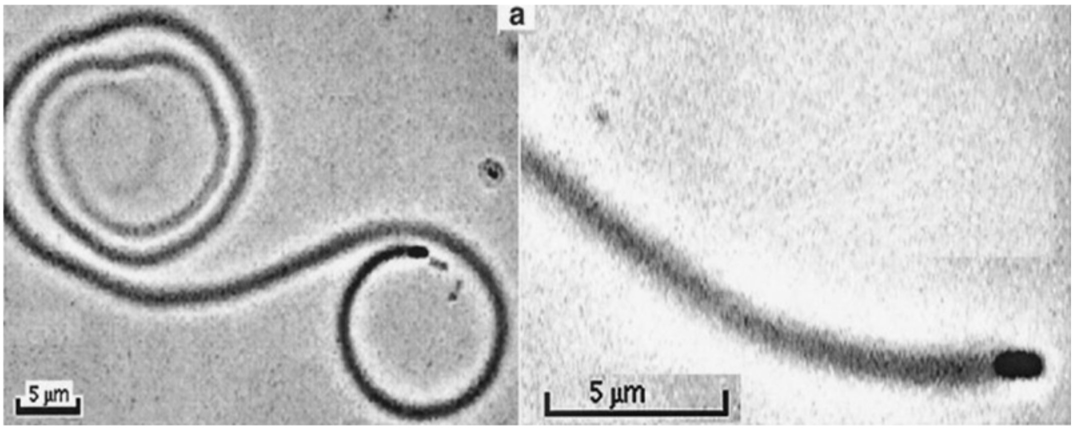

Figure 1.8: Observation of Listeria moving in platelet extract, observed by phase-contrast microscopy. The bacteria move at $\sim 8\mu m/min$. The tail can be more than $100\mu m$ long when the depolymerization is slow enough. Bars $= 5\mu m$. Taken from [66].

bead. The ensuing force velocity relation can be well explained by the brownian ratchet theory based modeling of the polymerization forces [117, 125].

This theory has been broadly generalized to account for cell motility based on polymerization based growth [22, 37, 52, 72, 124, 160] with micro models describing self organization of actin filaments and macro models reprensenting the process in continuum mechanical framework. We mention the approach based on the theory of active gels (see Section 1.2.4.1) accounting for asters and vortices structures that can explain sub cellular structures [54, 55].

1.2.3 Contraction driven cell motility

An other important factor in cell crawling that can, in principle, explain cell motion independently of actin treadmilling [39, 187] is the activity of molecular motors such as myosin II [94, 182] which convert chemical energy into mechanical work. A number of different motors can be related to different motility mechanisms [61] which are not necessarily related to crawling. Most of the models of cell crawling accounting for contraction consider the essential role of myosin engines [172]. However they do not consider the effect of myosin contraction independently of treadmilling. The role of contraction role has been more thorougly investigated in the studies of cytokinesis which is the central cell process for cell division.

1.2.4 Comprehensive models

Treadmilling, contraction and adhesion mechanisms have been put together in many whole cell models to account for realistic motile properties. Some extensive reviews of the subject are [40, 126, 150, 184]. It is in fact difficult to categorize models as the level of details and the captured phenomena can be very different. We give a brief overview of the main models but the subject is too large and active for this list to be exhaustive.

1.2.4.1 Theory of active gels

Even though the cytoskeleton itself can be analytically described at a microscopic level, relying on the fact that motility takes place at large time and space scales which are independent of the molecular details, the hydrodynamic theory of active gels has been proposed in [34, 83, 84, 89, 98]. It provides a generic theoretical tool to derive coarse grained phenomenological theories widely used to incorporate active terms in the usual physical balances for passive materials. Conservation of densities of the filaments, solvent and monomers is assumed as well as momentum conservation. The dynamics of the system is then known as long as the fluxes of different components are related to densities. Taking into account the polar nature of the gel by introducing a polarization vector representing the average polarity of the gel (as it is done for liquid crystals) is an other feature of this model. The rate of change of the free energy can be then written down as a product of force-flux pairs where an essential pair driving the system out of equilibrium is introduced: the chemical force multiplied by the ATP production rate. The rate of change in the free energy is decomposed into a reactive and dissipative part that are characterized by odd and even structures with respect to time reversal. Within a rheological model with quadratic dissipation (say, a Maxwell model) this implies a decomposition of reactive and dissipative fluxes that are linearly linked with respective generalized forces and satisfy Onsager relations. Even if, this last step requires that the system is near equilibrium, which is not truly the case, the theory provides a simple phenomenological description of the behavior of the gel.

1.2.4.2 Discrete approaches

In search of simple rheological models, some authors describe the cell as a set of points connected by springs, dashpots and active elements such as contractile elements. In

[53], such a model is used to find the speed of the cell in different cell-substrate configurations. For instance, this allows one to derive the biphasic relation between speed and adhesiveness, experimentally confirmed in [25, 63, 64, 126, 161]. Similar conclusions can be obtained in a continuum model in [68]. In [16], the cell is divided in three parts with elastic or poroelastic connections and the authors are able to simulate many general features of cell migration. A simple discrete perspective is also considered in [14] where elastic coupling between trailing and leading front explains oscillatory advance of the cell. Some discrete models [124] show that the regulation of actin dynamics plays a very important role. Thus, too few F-actins are not sufficient to push the membrane but too many completely deplete the G-actin pool and lead to a lack of monomers near the leading edge which also decrease the velocity. Making the bridge with continuous models, we also mention the paper [26] which describes nematode sperm motility and where an interplay between protrusion and contraction as well as a simple dissipative adhesive mechanism are implemented into a finite element code allowing the authors to make quantifiable predictions.

1.2.4.3 Multiphase flow models

A successful approach to whole cell modeling has been to apply reactive multiphase flow theory to the permeation of the solvent through the cytoskeleton [7, 75, 133] . In this two fluids approach the actin polymer network is modeled as a very viscous fluid generating internal contractile stress and moves through a fluid cytoplasm. Mass and momentum balance are formulated for each phase with transfer terms. Adhesion is modelled by a slip coefficient and polymerization/depolymerization properties of actin are taken into account through polymerization messengers generated at activated portions of the plasma membrane and diffusing into the cytoplasm. This type of modelling adequately predicts rapid cell translocation and questions the role of contractile forces. Models including more components and computationally relying on phase field methods are presented in [184].

1.2.4.4 Other models

Other models of cell motility rely on some additional physical mechanisms which may in fact all be operative at the same time for a robust motion. In [188] a one dimensional model with non linear friction was shown to display stick-slip oscillations independently of substrate rigidity. The cell is powered by protrusion and retraction rates and an active contractile stress described in terms of a chemical balance between bipolar filaments and free motors. The one dimensional model of [102] investigates different directions and reproduces steady motion of an elastic layer accounting for maximal phenomenology between actin polymerization and depolymerization, contraction, adhesion and membrane tension. In [156] an extensive 2D model of the viscoelastic lamellipodium of a keratocyte involving linear friction, motors balance and treadmilling enables quantitative comparison with experiments. Along the same line, a very complete model using phenomenological relations between different internal variables was investigated in [15]. It involves myosin-powered retrograde actin flow with drift-diffusion non linear adhesion strength model and drift-diffusion model for motors concentration to understand the correlation between keratocytes shape and quantitative changes in either adhesion strength or myosin contraction. In [187], several comprehensive models based on different powering machinery (myosin contraction-driven motility, G-actin transport-limited motility, Rac/Rho-regulated motility) were investigated and shown to explain shape and speed of keratocytes. The coupling of different models was shown to stabilize the shape of the motile cell and induce robustness of the translocation process. Two dimensional phase field models [163, 196] were used to investigate some peculiar shapes of the moving cells. The models involve polymerizing and depolymerizing polar filaments driven by molecular motors confined inside an inextensible membrane and explain steady motion and cell shapes with various aspect ratios depending on system parameters as well as shape oscillations. We also mention the paper of [170] which numerically investigates the coupling between actin turnover, actomyosin contractility and adhesion dynamics. Motion is induced by protrusion at the leading edge with contractility responsible for the nucleation and maturation of adhesion spots necessary to transmit momentum to the substrate. This model predicts a biphasic relation between cell speed and adhesion strength which is observed in experiments. In [74] the proposed model places emphasis on actomyosin contraction of the cell cortex though it also describes actin polymerization/depolymerization with the goal of understanding spontaneous polarization of tumor cells migrating in three-dimensional environments. This motility initiation problem was also considered in [56] with a much finer description for polymerization/depolymerization process. It shows waves of actin confined in a membrane and responsible for the initiation of spontaneous motion. A different perspective is taken in [179] where the authors consider a deformable elastic membrane from where signalling substances obeying reaction diffusion equation are issued. Relying on Turing mechanism [142], the model also predicts spontaneous motion. Finally, in [166, 192] cell motility powered by polymerization and traction forces on a three-dimensional substrate is investigated and a biphasic relation of speed versus ligand density was also found.

2

Chapter I: Optimal crawling

The motor part of an eukaryotic cell is a layer of an active gel with three main active functions: growth (retraction), contraction and attachment (detachment). These functions are controlled by complex chemical and mechanical processes inside the cell. In this chapter we take a reverse engineering approach and pose a problem of finding the optimal spatial and temporal organization of these functions ensuring either maximum velocity of crawling or maximum efficiency of energy transduction. We circumvent the problem of self consistent transportation for the biological elements ensuring the required performance (actin filaments, myosin crosslinkers, integrins, etc.) and assume that the required spatial distributions can be created if necessary. We formulate the variational problem of finding the optimal configuration of active elements in a limited setting when polymerization/depolymerization processes are suppressed and solve it in an even more limited setting when the spatial distribution of contractile stresses is the only minimized function. Our analysis shows that the obtained optimal distribution and the real, observed distribution are in good agreement.

2.1 Building the model

2.1.1 Main constitutive assumptions

Following [97], we consider a one dimensional layer of viscous fluid representing the cell lamellipodium. We assume that the layer has free boundaries at its rear ($l_-(t)$) and front ($l_+(t)$):

$$l_-, l_+ : \left| \begin{array}{rcl} \mathbb{R}^+ & \longrightarrow & \mathbb{R} \\ t & \longmapsto & l_-(t), l_+(t) \end{array} \right.$$

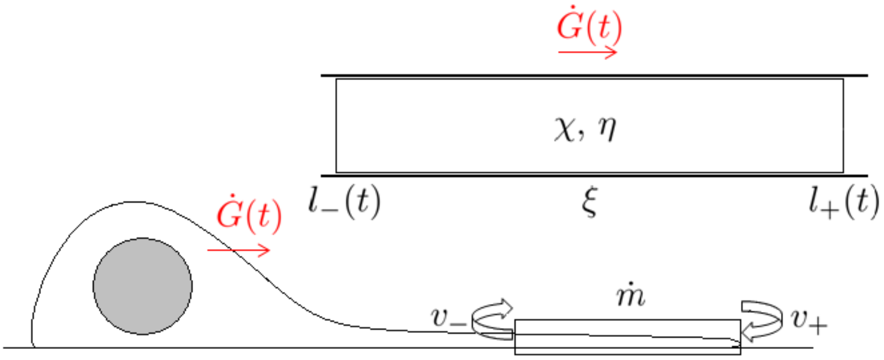

Figure 2.1: Schematic representation of the model for the cell lamellipodium

We suppose that $l_- < l_+$ for all times and denote Ω the set between the two curves l_- and l_+. $\Omega = \text{epi}\ l_- \cap \text{epi}\ l_+$ where 'epi' stands for epigraph. We define on Ω the functions $\rho(x,t)$,$\sigma(x,t)$ and $v(x,t)$ which denote respectively density, stress and velocity field inside the cell in the referential coordinate system of the lab. All functions v, σ, ρ depend on of space and time:

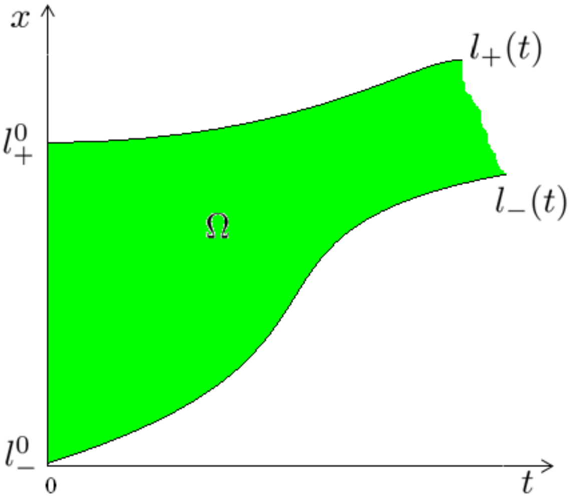

Figure 2.2: The set Ω

$$v, \sigma, \rho : \left| \begin{array}{ccc} \Omega & \longrightarrow & \mathbb{R}_+ \\ (x,t) & \longmapsto & v(x,t), \sigma(x,t), \rho(x,t) \end{array} \right.$$

We first consider a fully passive viscous layer (no active contraction, adhesion or protrusion). Mass and force balance equations along with constitutive law imply that:

$$\begin{cases} \partial_t \rho + \partial_x(\rho v) = 0 \\ \rho(\partial_t v + v\partial_x v) = \partial_x \sigma \\ \sigma = \eta \partial_x v. \end{cases}$$

where η is the dynamic viscosity. The absence of a pressure term implies infinite compressibility (dust) of intracellular filaments with a justification given in [156]. This set of equation must be equipped with initial and boundary conditions that will be specified latter on.

Combining the last two equations gives a pressureless Navier-Stokes equation on an a priori moving domain. Following [103], we can build the Reynolds number and frequency Reynolds number which are both small ensuring that we can neglect the inertial term and write,

$$\begin{cases} \partial_t \rho + \partial_x(\rho v) = 0 \\ \partial_x \sigma = 0 \\ \sigma = \eta \partial_x v. \end{cases}$$

The boundary conditions corresponding to the absence of loads at the rear and the front and mass flux going through the system (no treadmilling of actin filaments, see 1.1.2.2) take the form:

$$\begin{cases} \sigma(l_-(t), t) = \sigma(l_+(t), t) = 0 \\ \frac{dl_-(t)}{dt} = v(l_-(t), t) \\ \frac{dl_+(t)}{dt} = v(l_+(t), t). \end{cases}$$

Finally, the initial conditions can be written as,

$$\begin{cases} l_-(0) = l_-^0 \text{ and } l_+(0) = l_+^0 \\ \rho(x, 0) = \rho^0(x). \end{cases}$$

It is clear that in view of these equations, stress vanishes in the whole body of the cell while internal velocity is an arbitrary constant V. Also,

$$\dot{l}_- = \dot{l}_+ = V,$$

which means that the cell moves as a rigid body with constant velocity. Mass balance is then reduced to a simple transport equation on a moving domain and we can write,

$$\rho(x, t) = \rho^0(x - Vt).$$

The velocity V being arbitrary, the problem has an infinite number of solutions that only depend on the initial conditions and an untermined scalar V.

2.1.2 Adhesion and motion

If the layer is placed on a substrate, we must include friction applied on the boundaries. We consider a simple homogeneous (The conclusion would be the same with non homogeneous friction coefficient by use of weak maximum principle for elliptic equations [20]) viscous friction (See section 1.1.2.4) which gives:

$$\left\{\begin{array}{c} \partial_t\rho + \partial_x(\rho v) = 0 \\ \partial_x\sigma = \xi v \\ \sigma = \eta\partial_x v. \end{array}\right.$$

In this case, the solution is unique with,

$$\sigma \equiv 0\ ,\ v \equiv 0\ ,\ \rho \equiv \rho^0,$$

and ,

$$l_- \equiv l_-^0\ ,\ l_+ \equiv l_+^0.$$

As could have been physically foreseen: the layer is not moving: In the presence of dissipative mechanisms, we have to give the cell a "motor" to self-propell. Two main choices are treadmilling (filament-driven motility) or/and contraction (motor driven motility) [154].

2.2 The model of motile cell

2.2.1 Setting the problem

In this chapter, we consider the following general problem,

$$\left\{\begin{array}{c} \partial_x\sigma = \xi\phi_1\left(\frac{c_1}{c_1^0}\right)v \\ \sigma = \eta\partial_x v + \chi\phi_2\left(\frac{c_2}{c_2^0}\right), \end{array}\right. \tag{2.1}$$

where $c_1(x,t)$ denotes the concentration of proteins binding the cytoskeleton to the substrate (integrins) and $c_2(x,t)$ is the concentration of proteins responsible for contraction (myosin II). Here, ξ and χ give characteristic levels scales describing contraction and friction while c_1^0 and c_2^0 are characteristic concentrations. The functions ϕ_1 and ϕ_2 are potentially non linear giving an explicit dependence between the concentrations and the corresponding stress. The models ruling the distribution c_1 and c_2 and the functions ϕ_1

and ϕ_2 are discussed in Appendix 6.2 while here we assume that the resulting space-time dependancies are the external controls to be determined in the process of optimization.

The problem will be equipped with stress boundary conditions,

$$\sigma(l_-(t),t) = -k\frac{L(t)-L_0}{L_0} = \sigma(l_+(t),t), \tag{2.2}$$

describing the internal stiffness [24] of the cytoskeleton and the elasticity of the plasmic membrane that resists reshaping of the body of the cell [14]. The importance of this modification of the previously announced zero stress conditions will be further justified in the next section.

To describe filament treadmilling (see section 1.1.2.2), we assume that the cell is also driven by the prescribed kinematic fluxes producing the following Stefan-type boundary conditions,

$$v(l_\pm(t),t) - \dot{l}_\pm = v_\pm, \tag{2.3}$$

where $v_+ > 0$ and $v_- > 0$ are the polymerization and the depolymerization velocities.

Now, the full system of equations includes the subsystem,

$$\begin{cases} -\eta\partial_x\big(\frac{1}{\xi\phi_1\left(\frac{c_1}{c_1^0}\right)}\partial_x\sigma\big) + \sigma = \chi\phi_2\left(\frac{c_2}{c_2^0}\right) \\ \sigma(l_\pm(t),t) = -k\frac{L(t)-L_0}{L_0} \\ \partial_x(l_\pm(t),t) - \dot{l}_\pm = v_\pm, \end{cases}$$

which expresses momentum balance in the layer with moving boundaries, and another subsystem

$$\begin{cases} \partial_t\rho + \partial_x\left(\frac{\rho}{\xi\phi_1\left(\frac{c_1}{c_1^0}\right)}\partial_x\sigma\right) = 0 \\ \rho(l_-(t),t)v_- = \rho(l_+(t),t)v_+ \end{cases}$$

which expresses mass balance for actin filaments with the assumption that the total mass of actin is conserved. The initial conditions remain the same,

$$\begin{cases} l_-(0) = l_-^0 \text{ and } l_+(0) = l_+^0 \\ \rho(x,0) = \rho^0(x). \end{cases}$$

Due to, the inifinite compressibility hypothesis, the mass balance subproblem uncouples from the momentum balance subproblem which can be solved separately. To this end, we denote $\alpha_1 = \frac{c_1}{c_1^0}$ and $\alpha_2 = \frac{c_2}{c_2^0}$ the dimensionless concentrations and suppose that the function ϕ_1 is positive while the function ϕ_2 is non negative. Using the dimensionless variables,

$$\sigma := \frac{\sigma}{\chi}, x := \frac{x}{\alpha}, t := \frac{t}{\tau} \text{ with } \alpha = \sqrt{\frac{\eta}{\xi}}, \tau = \frac{\eta}{\chi},$$

we can then write the closed set of equations describing the decoupled mechanical problem,

$$\left\{ \begin{array}{c} -\partial_x(\frac{1}{\phi_1(\alpha_1)}\partial_x\sigma) + \sigma = \phi_2(\alpha_2) \\ \sigma(l_-(t),t) = -k\frac{L(t)-L_0}{L_0} = \sigma(l_+(t),t) \\ \dot{l}_- = \frac{\partial_x\sigma}{\phi_1(\alpha_1)}(l_-(t),t) + v_- \text{ and } \dot{l}_+ = \frac{\partial_x\sigma}{\phi_1(\alpha_1)}(l_+(t),t) + v_+. \end{array} \right. \tag{2.4}$$

2.2.2 Importance of elasticity

The importance of elasticity can be formally understood by considering $(2.4)_{1,2}$ without treadmilling rates ($v_- = v_+ = 0$). It is clear by application of weak maximum principle for elliptic PDEs [20] to $(2.4)_1$ that,

$$\underset{(x,t)\in\Omega}{min}\ \sigma \geq max(0, k\frac{L(t)-L_0}{L_0}).$$

When $k = 0$ we then have that,

$$\underset{(x,t)\in\Omega}{min}\ \sigma = 0$$

and this minimum is reached at both boundaries. As a consequence, applying this time strong maximum principle, as σ cannot be constant, (otherwise we have a trivial problem) we have that :

$$\partial_x\sigma(l_-(t),t) > 0 \text{ and } \partial_x\sigma(l_+(t),t) < 0.$$

Using $(2.4)_3$, we conclude that the boundaries of the domain are moving inward as there is no mechanism that can oppose contraction. If we further suppose that $\phi_2 > const > 0$, we can prove that an initial domain shrinks to zero in finite time. Thus, to obtain a non trivial problem in the absence of treadmilling we need to add elasticity. Our simplest assumption

$$\sigma(l_-(t),t) = -k\frac{L(t)-L_0}{L_0} = \sigma(l_+(t),t)$$

introduces the mean field elasticity which may be interpreted in different ways (membrane, cytoskeleton).

2.3 Travelling wave assumption

To simplify the analysis, we suppose that both the unknown functions and the controls can be expressed as travelling waves (TW). We introduce the speed V of the TW and L the length of the moving domain. By using the TW coordinate $y = x - Vt \in [-\frac{L}{2}, \frac{L}{2}]$, we can write (2.4) in the form:

$$\begin{cases} -\partial_y(\frac{1}{\phi_1(\alpha_1)}\partial_y\sigma) + \sigma = \phi_2(\alpha_2) \\ \sigma(-L/2) = -k\frac{L-L_0}{L_0} = \sigma(L/2) \\ V = v_- + \frac{\partial_y\sigma}{\phi_1(\alpha_1)}(-L/2) \\ V = v_+ + \frac{\partial_y\sigma}{\phi_1(\alpha_1)}(L/2). \end{cases} \tag{2.5}$$

In particular our assumption implies that the distributions $\alpha_2(x,t)$ and $\alpha_1(x,t)$ are advected with the cell. The problem of of obtaining such distributions asymptotically ($t \to \infty$) from a system of physical equations is not considered in this chapter. However we can refer to experimental evidence that the overall motion of a cell is closed to a travelling wave type translocation.

We need to impose some constraints on the distributions α_1 and α_2 (see Appendix 6.2). To be specific, we shall choose,

$$\phi_1(x) = \phi_2(x) = x$$

and assume that (Assumption A)

$$\int_{-L/2}^{L/2} \alpha_1 = L \text{ and } \int_{-L/2}^{L/2} \alpha_2 = 1.$$

Which means that the average friction coefficient is one and does not depend on the size of the domain L while as the total number of motors is conserved, the average contraction decreases with the domain size (see Appendix 6.2). Next we introduce the functions,

$$\forall u \in [-1/2, 1/2],\ g_1(u,L) = \alpha_1(Lu) \text{ and } g_2(u,L) = L\alpha_2(Lu)$$

and conclude that they sum to one. We shall additionally suppose (Assumption B) that these functions do not depend on L and therefore only characterize the "shape" of the distributions.

$$g_1(u,L) = g_1(u) \text{ and } g_2(u,L) = g_2(u)$$

This assumption will not be used extensively.

2.4 The optimization criteria

First af all, we would like to study the distributions $\alpha_1(y)$, $\alpha_2(y)$ and the scalars v_-, v_+ that maximizes the speed of the traveling wave V. The second problem is to optimized efficiency transduction (See also a special case in section 3.9). In the absence of cargo, the efficiency Λ has to be understood in the sense of Stokes [108, 171, 183]

$$\Lambda = P/H$$

where $P = \xi V^2 L$ is the power required for translocation with constant velocity in the presence of external friction preventing such motion and $H > 0$ is the internal energy supply rate associated with ATP hydrolysis which drives the motility process. In a weakly non-equilibrium regime H is proportional to the square of the thermodynamical force (affinity) keeping the hydrolysis reaction out of equilibrium [88, 89]. To compute H we notice that it can be decomposed into a sum of a power H_A exerted by active forces on the constraining environment and the dissipation ϵ which takes place even if the active force is generated but no work is produced. The term $H_A > 0$ is an anti-dissipation which operates in the domain where force-velocity relation $f(V)$ is such that $f(V)V < 0$. The term $\epsilon > 0$ can be identified with the maintenance heat introduced by A.V. Hill to describe isometric contractions of skeletal muscles (in stall conditions) [76]. The signs of the terms H_A and ϵ may also be different which requires special interpretation [88]. To compute the anti-dissipation term H_A, we multiply $(2.1)_1$ by v and $(2.1)_2$ by $\partial_x v$ and sum these two contributions. Then, integrating on the moving domain we get,

$$-k\frac{L-L_0}{L_0}(\dot{L}-(v_+-v_-)) = \xi\int_{l_-}^{l_+}\phi_1(\alpha_1)v^2 + \eta\int_{l_-}^{l_+}(\partial_x v)^2 + \chi\int_{l_-}^{l_+}\phi_2(\alpha_1)\partial_x v.$$

In the travelling wave (steady state) regime $\dot{L} = 0$ and $y = x - Vt$, therefore

$$k\frac{L-L_0}{L_0}(v_+-v_-) - \chi\int_{-L/2}^{L/2}\phi_2(\alpha_1)\partial_y v = \xi\int_{-L/2}^{L/2}\phi_1(\alpha_1)v^2 + \eta\int_{-L/2}^{L/2}(\partial_y v)^2.$$

The term in the left hand side describes the power performed by the contractile forces and treadmilling mechanism and therefore it can be identified with anti-dissipation H_A:

$$H_A = \xi\int_{-L/2}^{L/2}v^2 + \eta\int_{-L/2}^{L/2}(\partial_y v)^2 > 0$$

One can see that this power goes into overcoming the viscous resistance in the bulk of the cell and the frictional resistance between the cell body and the substrate. We can then write the efficiency as,

$$\Lambda = \frac{\xi V^2 L}{k\frac{L-L_0}{L_0}(v_+ - v_-) - \chi\int_{-L/2}^{L/2}\phi_2(\alpha_1)\partial_y v + \epsilon}.$$

The 'maintenance' power term ϵ describes microscopic dissipation taking place even in the absence of a macroscopic motion. Therefore it cannot be evaluated based on our equations and requires an access to the microscopic model of active force generation.

In non dimensional form, the efficiency reads,

$$\Lambda = \frac{V^2 L}{k\frac{L-L_0}{L_0}(v_+ - v_-) - \int_{-L/2}^{L/2}\phi_2(\alpha_1)\partial_y v + \epsilon},$$

where we redifined,

$$\epsilon := \frac{\sqrt{\eta\xi}}{\chi^2}\epsilon.$$

2.5 Neglecting treadmilling

The main concern of this chapter will be with contraction-driven motility ($v_- = v_+ = 0$) and in this section we partly justify the neglect the treadmilling with respect to the optimization procedure. Suppose for simplicity that adhesion and contraction mechanisms are homogeneous. Then we can set,

$$\alpha_1 \equiv 1 \text{ and } \alpha_2 = \frac{1}{L}.$$

Then, (2.5) can be easily solved. By setting,

$$\begin{cases} V_m = (v_- + v_+)/2 > 0 \\ \Delta V = v_+ - v_- \end{cases}$$

we have,

$$\begin{cases} V = V_m \\ \Lambda = 2\frac{LV_m^2}{(\Delta V)^2}\tanh\left(\frac{L}{2}\right) \end{cases} \tag{2.6}$$

with,

$$\Delta V = 2\left(\frac{1}{L} + k\frac{L-L_0}{L_0}\right)\tanh\left(\frac{L}{2}\right).$$

It is then clear that both velocity and efficiency can be maximized by setting V_m as large as possible for any fixed ΔV. Still the interplay between non homogeneous adhesion and treadmilling properties is of interest (See section 4.3). In the rest of the chapter we simplify the problem and only consider contraction driven motility. We then set,

$$v_- = v_+ = 0.$$

2.6 Optimization of velocity

Without treadmilling, system (2.5) can be rewritten as,

$$\begin{cases} -\partial_y(\frac{1}{\alpha_1}\partial_y\sigma) + \sigma = \alpha_2 \\ \sigma(-L/2) = -k\frac{L-L_0}{L_0} = \sigma(L/2) \\ V = \frac{\partial_y\sigma}{\alpha_1}(-L/2) = \frac{\partial_y\sigma}{\alpha_1}(L/2) \end{cases} \tag{2.7}$$

and we first consider the problem of optimizing velocity V by choosing appropiate controls $\alpha_1(y)$ and $\alpha_2(y)$.

2.6.1 Homogeneous adhesion

To start with, consider the case where $\alpha_1 \equiv 1$, meaning that adhesion strength is proportional to speed of the retrograde flow with a constant coefficient.

In this case, $(2.7)_{1,2}$ can be integrated in a closed form and using $(2.7)_3$, the unknown parameters V and L can be written in the form:

$$\begin{cases} -2k\frac{L-L_0}{L_0}\sinh(\frac{L}{2}) = \int_{-L/2}^{L/2}\cosh(y)\alpha_2(y)dy \\ V = -\frac{1}{2\sinh(\frac{L}{2})}\int_{-L/2}^{L/2}\sinh(y)\alpha_2(y)dy. \end{cases} \tag{2.8}$$

The problem is now to find the optimal distribution α_2 maximizing the velocity V.

2.6.1.1 Existence of traveling wave solutions

The first question is wether the system (2.8) has solutions. If we use Assumption B, then $(2.8)_1$ can be rewritten as

$$\mathcal{L}(L) = -2k\frac{L-L_0}{L_0}\sinh(\frac{L}{2}) = \int_{-1/2}^{1/2}\cosh(Lu)g_2(u)du = \mathcal{R}(L). \tag{2.9}$$

Here $\mathcal{R}(L)$ is an increasing convex function of L satisfying $\mathcal{R}(0) = 1$, while $\mathcal{L}(L)$ is a concave function which is positive on $[0, L_0]$ and negative on $[L_0, \infty[$. The function $\mathcal{L}(L)$ vanishes at $L = 0$ and $L = L_0$ and increases until the treshold $L^*(L_0) \leq L_0$ defined by the unique solution of (see Fig 2.3):

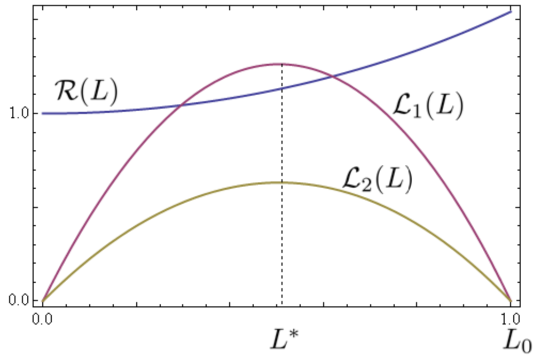

Figure 2.3: Sketch of $\mathcal{L}$ and $\mathcal{R}$ for two values of k associated to zero or two solutions

$$2\tanh\left(\frac{L^*}{2}\right) + L^* = L_0$$

Then using assumption A, and Mean Value theorem we obtain:

$$1 + 2k\frac{L^* - L_0}{L_0}\sinh\left(\frac{L^*}{2}\right) < \mathcal{R}(L^*) - \mathcal{L}(L^*) < \cosh\left(\frac{L^*}{2}\right) + 2k\frac{L^* - L_0}{L_0}\sinh\left(\frac{L^*}{2}\right).$$

So we can claim that,

- If,

  $$\cosh\left(\frac{L^*}{2}\right) + 2k\frac{L^* - L_0}{L_0}\sinh\left(\frac{L^*}{2}\right) < 0$$

  then (2.9) has two solutions.

- If,

  $$1 + 2k\frac{L^* - L_0}{L_0}\sinh\left(\frac{L^*}{2}\right) > 0$$

  then (2.9) has no solutions. For other values of parameters the number of solutions depends on the exact shape of the function $g_2(s)$.

These results are graphically represented on Fig.2.4. We will always consider the case when there are two solutions, eliminating cases with no solution when contraction is too strong (or equivalently when elasticity is too weak). we observe that if $L_0 << 1$, expanding the trigonometric functions near $L = 0$, a necessary and sufficient condition for existence of two solutions to (2.9) can be written in the form:

$$1 < \frac{kL_0}{4} \tag{2.10}$$

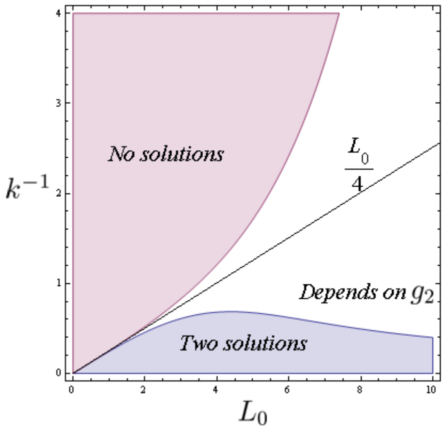

Figure 2.4: Phase diagram of some necessary conditions

which has been also ploted on Fig.2.4.

From the perspective of the unsteady system corresponding to $(2.8)_2$, the two solutions are not equivalent. One is stable (largest length) while the other is unstable (smallest length).

Stability is here understood as the stability of the moving fronts within an unsteady analogue of Assumptions (A) and (B) that include a class of controls outside the class of traveling waves. Denoting,

$$L(t) = l_+(t) - l_-(t) \text{ and } G(t) = \frac{l_-(t) + l_+(t)}{2}$$

and integrating (2.4), we obtain

$$\left\{ \begin{array}{r} \dot{L}(t) = -2k\frac{L(t)-L_0}{L_0}\tanh(\frac{L(t)}{2}) - \frac{1}{\cosh(\frac{L(t)}{2})}\int_{l_-(t)}^{l_+(t)} \cosh(G(t)-x)\alpha_2(x,t)dx \\ \dot{G}(t) = \frac{1}{2\sinh(\frac{L(t)}{2})}\int_{l_-(t)}^{l_+(t)} \sinh(G(t)-x)\alpha_2(x,t)dx. \end{array} \right. \tag{2.11}$$

The "general dynamic" analogues of assumptions (A) and (B) are then:
Assumption (A')

$$\int_{l_-(t)}^{l_+(t)} \alpha_2(x,t)dx = 1,$$

meaning that the total amount of motors is conserved and,
Assumption (B')

$$\alpha_2(x,t) = T(t)S\left(\frac{x - l_-(t)}{L(t)}\right),$$

meaning that the spatio temporal inhomogeneities of myosin distribution can be separated into a contribution depending on space coordinate in the referential coordinate system of the moving cell and a mulptiplicative time modulation. These assumptions, of course contain the more specific travelling wave ansatz. We can then write,

$$\alpha_2(x,t) = \frac{S\left(\frac{x-l_-(t)}{L(t)}\right)}{L(t)\int_0^1 S(u)du},$$

which gives,

$$g_2(u) = \frac{S(u)}{\int_0^1 S(u)du}.$$

Then the system (2.11) can be rewritten as,

$$\begin{cases} \dot{L}(t) = -2k\frac{L(t)-L_0}{L_0}\tanh(\frac{L(t)}{2}) - \frac{1}{\cosh(\frac{L(t)}{2})}\int_0^1 \cosh(L(t)(1/2-u))g_2(u)du \\ \dot{G}(t) = \frac{1}{2\sinh(\frac{L(t)}{2})}\int_0^1 \sinh(L(t)(1/2-u))g_2(u)du, \end{cases} \tag{2.12}$$

and $(2.12)_1$ becomes $\dot{L} = \mathcal{L}(L) - \mathcal{R}(L)$. As it can be seen in Fig.2.5, in the case where

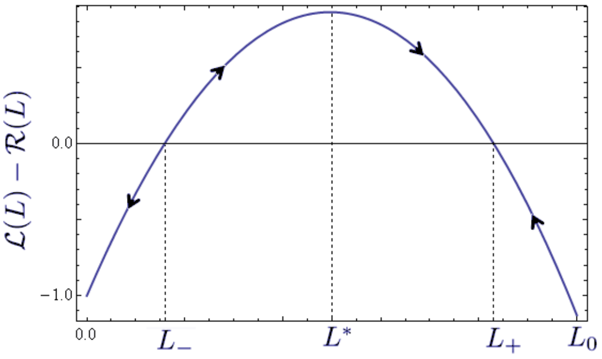

Figure 2.5: $\dot{L} = \mathcal{L}(L) - \mathcal{R}(L)$ as a function of L

there are two solutions L_- and L_+, L_- is unstable and L_+ is stable with a basin of attraction in $[L_-, \infty[$.

2.6.1.2 Optimal velocity of traveling wave solutions

As we have made sure that solutions exist, we may wonder about optimizing the velocity given by $(2.8)_2$. It is clear that if $\alpha_2(y)$ is even, $V = 0$. This is not really surprising as nothing in the formulation of the problem distinguishes left from right in such a configuration. This result can be interpreted as an analogue of Purcell's theorem [103, 149]. More generally, relation $(2.8)_2$ can be interpreted as a barycentric relation with weights given by the function sinh. Given an initially even distribution $\alpha_2(y)$, if we now bias it by putting more motors to the rear, the sign of velocity will become positive and it will be negative in the opposite case. We notice that the velocity dependence on $\alpha_2(y)$ has a central symmetry: flipping $\alpha_2(y)$ with respect to the cell center 0 we only change the sign of the velocity.

The problem of finding the maximal velocity can be formulated as follow:

$$\left\{\begin{array}{c} \underset{g_2\in L^1([-1/2,1/2])}{max} \left(-\frac{1}{2\sinh(\frac{L}{2})}\int_{-1/2}^{1/2}\sinh(Ls)g_2(u)du\right) \\ \text{with the constraints,} \\ \int_{-1/2}^{1/2} g_2(u)du = 1 \\ -2k\frac{L-L_0}{L_0}\sinh(\frac{L}{2}) = \int_{-1/2}^{1/2}\cosh(Lu)g_2(u)du \\ \cosh\left(\frac{L^*}{2}\right) + 2k\frac{L^*-L_0}{L_0}\sinh\left(\frac{L^*}{2}\right) < 0. \end{array}\right.$$

One can see using mean value theorem that the maximal positive velocity is reached when all the motors are localized at the rear for

$$g_2(u) = \delta(u + 1/2)$$

where δ denotes the dirac mass at 0. The maximal velocity is

$$V = \frac{1}{2}$$

which reads in dimensional form:

$$V = \frac{1}{2}\frac{\chi}{\eta}A_T$$

Here $A_T = \frac{K_{on}M_T}{c_2^0(K_{on}+K_{off})}$ (See appendix 6.2) is a length proportional to the total amount of motors. This upper bound is within the constraints for existence of a length as with such a distribution we have:

$$\cosh\left(\frac{L}{2}\right) + 2k\frac{L-L_0}{L_0}\sinh\left(\frac{L}{2}\right) = 0$$

and we are on the border of admissibility.

One can see that only half of the motors is "useful".

2.6.2 The role of adhesion

Having treated the case when adhesion was homogeneous, we now wouldlike to understand the less analytically transparent case when the distribution of integrins is arbitrary. To find the length L and the velocity V in this case, we first observe that $(2.7)_{1,2}$ is a Sturm-Liouville problem. Its solution can be written in term of Green's function :

$$\sigma(y) = -k\frac{L-L_0}{L_0} - \int_{-L/2}^{L/2} G(y,s)\left[\alpha_2(s) + k\frac{L-L_0}{L_0}\right] ds. \tag{2.13}$$

The Green's function itself can be expressed in term of two auxillary solutions of the equation [120].

$$(\frac{1}{\alpha_1}U')' = U.$$

These two solutions U_1 and U_2 are associated with two sets of boundary conditions $U_1(-L/2) = 0, U_1(L/2) = 1$ and $U_2(-L/2) = 1, U_2(L/2) = 0$, respectively. These solutions form a basis in the space of all solutions as their wronskian W is non zero. Indeed, $W(-L/2) = -U_1^{'}(-L/2)$ and if $U_1^{'}(-L/2) = 0$ as $U_1(-L/2) = 0$ then $U_1 \equiv 0$ which is in contradiction with $U_1(L/2) = 1$. Note additionally that using Abel formula one can prove that the quantity,

$$A = \frac{W}{\alpha_1}$$

is a constant, which leads to identity:

$$-\frac{U_1^{'}(-L/2)}{\alpha_1(-L/2)} = \frac{U_2^{'}(L/2)}{\alpha_1(L/2)}.$$

We can then express the Green's function as:

$$G(y,u) = \frac{1}{A}\left(U_1(s)U_2(y)1_{[s<y]} + U_1(x)U_2(s)1_{[s>y]}\right)$$

where,

$$1_{[s<y]} = \begin{cases} 1 \text{ if } s < y \\ 0 \text{ if } s \geq y \end{cases} \quad \text{and } 1_{[s>y]} = \begin{cases} 1 \text{ if } s > y \\ 0 \text{ if } s \leq y \end{cases}$$

By substituting this expression into (2.13), we obtain:

$$\begin{cases} \sigma^{'}(-L/2) = -\frac{1}{A}\int_{-L/2}^{L/2} U_1^{'}(-L/2)U_2(s)\left[\alpha_2(s) + k\frac{L-L_0}{L_0}\right] ds \\ \sigma^{'}(L/2) = -\frac{1}{A}\int_{-L/2}^{L/2} U_2^{'}(L/2)U_1(s)\left[\alpha_2(s) + k\frac{L-L_0}{L_0}\right] ds. \end{cases}$$

and

$$V = \int_{-L/2}^{L/2} U_2(s)\left[\alpha_2(s) + k\frac{L-L_0}{L_0}\right] ds = -\int_{-L/2}^{L/2} U_1(s)\left[\alpha_2(s) + k\frac{L-L_0}{L_0}\right] ds.$$

We can now define $h(s) = U_2(s) + U_1(s)$ and $f(s) = U_2(s) - U_1(s)$ which implies that,

$$\left\{\begin{array}{c} (\frac{1}{\alpha_1}h')' = h \\ h(-L/2) = 1 \text{ and } h(L/2) = 1 \end{array}\right. \quad \text{and} \quad \left\{\begin{array}{c} (\frac{1}{\alpha_1}f')' = f \\ f(-L/2) = 1 \text{ and } f(L/2) = -1 \end{array}\right.$$

Taking into account the fact that $h \geq 0$ (Maximum principle), we introduce a new measure of inhomogeneity of contraction:

$$\hat{\alpha}_2 = \frac{\int_{-L/2}^{L/2} h(s)\alpha_2(s)ds}{\int_{-L/2}^{L/2} h(s)ds}.$$

By using the function $\hat{\alpha}_2$, the equations for V and L can be written as:

$$\left\{\begin{array}{c} \hat{\alpha}_2 = -k\frac{L-L_0}{L_0} \\ V = \frac{1}{2}\int_{-L/2}^{L/2} f(s)(\alpha_2(s) - \hat{\alpha}_2)ds. \end{array}\right. \tag{2.14}$$

Using Assumptions (A) and (B) we may further characterize (2.14). Defining,

$$\forall u \in [-1/2, 1/2],\ \tilde{h}(u) = h(Lu) \text{ and } \tilde{f}(u) = f(Lu),$$

we have

$$\left\{\begin{array}{c} \hat{g}_2 = \frac{\int_{-1/2}^{1/2} g_2(u)\tilde{h}(u)du}{\int_{-1/2}^{1/2}\tilde{h}(u)du} = -kL\frac{L-L_0}{L_0} \\ V = \frac{1}{2}\int_{-1/2}^{1/2}\tilde{f}(u)(g_2(u) - \hat{g}_2)du, \end{array}\right. \tag{2.15}$$

Here we recall that,

$$\left\{\begin{array}{c} (\frac{1}{g_1}\tilde{h}')' = L^2\tilde{h} \\ \tilde{h}(-1/2) = 1 \text{ and } \tilde{h}(1/2) = 1 \end{array}\right., \left\{\begin{array}{c} (\frac{1}{g_1}\tilde{f}')' = L^2\tilde{f} \\ \tilde{f}(-1/2) = 1 \text{ and } \tilde{f}(1/2) = -1 \end{array}\right.$$

and,

$$\int_{-1/2}^{1/2} g_2 = \int_{-1/2}^{1/2} g_1 = 1$$

If we now suppose that $g_1 \equiv 1$ corresponding to homogeneous adhesion, $\hat{f}$ and $\hat{g}$ can be found explicitly as hyperpolic functions and the problem reduces to the one studied in the previous section.

2.6.2.1 Existence of the traveling wave solutions

Based on $(2.15)_1$, we can again obtain some sufficient conditions for existence of TW solutions. We notice that the positiveness of g_2 implies that $L < L_0$ which is expected as contraction shortens the cell. To characterize the situations where independant of the shapes $g_1(y)$ and $g_2(y)$, there exists a solution of $(2.15)_1$ is a difficult task. The problem simplifies if we assume that L_0 is small. A sufficient condition then reads again,

$$kL_0 > 4$$

Indeed, when $L_0 \to 0$, $L \to 0$ and $\hat{g}_2 \to 1$ while $\underset{L<L_0}{max} \left(-kL\frac{L-L_0}{L_0}\right) = \frac{kL_0}{4}$. So locally near $L = 0$, $(2.15)_1$ has two solutions.

2.6.2.2 Optimal velocity of the traveling wave solutions

Symmetry property First of all, we notice, some symmetry properties of our problem. Suppose that g_2 is even and therefore does not favor any direction of motion. Then, if we also suppose that g_1 is even, the functions $\tilde{f}(s)$ and $-\tilde{f}(-s)$ solve the same ODE. Uniqueness then implies that $\tilde{f}$ is odd. Hence, the integral in $(2.15)_2$ is the integral of a product of an odd function by an even function which is an odd function. Consequently the integral vanishes and $V = 0$. This is an expected result as no direction is physically preferred neither by contraction nor by adhesion.

Note the status of adhesion and contraction is quite different though. Indeed, if we consider homogeneous contraction, then $g_2 \equiv \hat{g}_2 \equiv 1$ and $(2.15)_1$ shows the existence of two possible lengths

$$\hat{L}_\pm = \frac{L_0}{2}\left(1 \pm \sqrt{1 - \frac{4}{kL_0}}\right).$$

However $(2.14)_2$ implies that $V = 0$ no matter what the adhesion distribution α_1. We conclude that to ensure motility, contraction must be inhomogeneous while from the previous section we have seen that homogeneous adhesion can still lead to motion. This suggests that the real "mover" is contraction while adhesion offers a "leverage" for contraction making it more efficient.

Maximal speed We now investigate what is the largest possible velocity that can be reached when both contraction and adhesionare inhomogeneous. We obtain the result in two steps. We first show that $V \leq 1$ and then find a configuration, of controls allowing the cell to reach where this upper bound.

Maximum principle dictates that:

$$\forall u \in [-1/2, 1/2],\ 1 \geq \tilde{h}(u) \geq 0 \text{ and } \tilde{h}(u) \geq \tilde{f}(u) \geq -\tilde{h}(u).$$

We cut the domain $[-1/2, 1/2]$ in two distinct (not necessarily connected) pieces S_- and S_+ where,

$$S_- = \{u / g_2(u) \leq \hat{g}_2\}$$

and,

$$S_+ = \{u / g_2(u) > \hat{g}_2\}\,.$$

We then have,

$$V = \frac{1}{2}\left(\int_{S_+} \tilde{f}(u)(g_2(u) - \hat{g}_2)du + \int_{S_-} \tilde{f}(u)(g_2(u) - \hat{g}_2)du\right)$$

and using the bounds on $\tilde{f}$,

$$V \leq \frac{1}{2}\left(\int_{S_+} \tilde{h}(u)(g_2(u) - \hat{g}_2)du - \int_{S_-} \tilde{h}(u)(g_2(u) - \hat{g}_2)du\right).$$

Reorganizing terms we obtain,

$$V \leq \frac{1}{2}\left(\int_{S_+} \tilde{h}(u)g_2(u)du + \hat{g}_2\int_{S_-} \tilde{h}(u)du - \left(\int_{S_-} \tilde{h}(u)g_2(u)du + \hat{g}_2\int_{S_+} \tilde{h}(u)du\right)\right).$$

By elimination of the non positive terms, we can further write,

$$V \leq \frac{1}{2}\left(\int_{S_+} \tilde{h}(u)g_2(u)du + \hat{g}_2\int_{S_-} \tilde{h}(u)du\right).$$

Since all integrated quantities are positive,

$$V \leq \frac{1}{2}\left(\int_{-1/2}^{1/2} \tilde{h}(u)g_2(u)du + \hat{g}_2\int_{-1/2}^{1/2} \tilde{h}(u)du\right).$$

Finally, using $(2.15)_1$ and the fact that $\tilde{h} \leq 1$, we obtain

$$V \leq \int_{-1/2}^{1/2} \tilde{h}(u)g_2(u)du \leq \int_{-1/2}^{1/2} g_2(u)du = 1.$$

In the case of homogeneous adhesion, we obtain only half of this velocity because the function $\tilde{h}$ is explicit.

We can now find a configuration which reaches this maximum. The idea is to take a motor distribution maximizing the speed at homogeneous friction (localized at the trailing edge such that $(2.8)_2$ is maximal) and adjust the integrin distribution. In fact, if we suppose that both g_1 and g_2 are fully localized (Dirac masses) we can reach the maximal speed. To this end, we first suppose that g_1 is a Cauchy distribution:

$$g_1(u) = \frac{1}{\pi} \frac{\theta}{\theta^2 + (u - u_0)^2}$$

where $u_0 \in [-1/2, 1/2]$ and $\theta > 0$. As it is well known, this distribution converges to a Dirac mass when $\theta \to 0$:

$$\lim_{\theta \to 0} g_1(u) = \delta_0(u - u_0).$$

This choice of g_1 is motivated by the fact $\tilde{h}$ and $\tilde{f}$ can be written in term of Legendre polynoms. Then, for this choice of g_1, when $\theta \to 0$ the limiting $\tilde{f}$ and $\tilde{h}$ can be found explicitly:

$$\tilde{h}(u) = 1$$

and

$$\tilde{f}(u) = \begin{cases} 1 \text{ if } u < u_0 \\ -1 \text{ if } u > u_0. \end{cases}$$

From $(2.15)_1$, $\hat{g}_2 = 1$ and two lengths are possible (again $\hat{L}_\pm$) and velocity can be computed from $(2.15)_2$ as follow:

$$V = \frac{1}{2} \left[\int_{-1/2}^{u_0} g_2(u) du - \int_{u_0}^{1/2} g_2(u) du - 2u_0 \right].$$

This expression takes largest value when the support of g_2 is chosen in $[-1/2, u_0]$ so that the second term does not contribute. Then to make the third term contribute in the largest way one should choose $u_0 = -1/2$. Then,

$$g_1(u) = \delta_0(u + 1/2)$$

and,

$$g_2(u) = \delta_0(u + 1/2)$$

producing the velocity,

$$V = 1.$$

One can see that this precial adhesion distribution allows the contraction mechanism to reach a velocity which is twice larger as when adhesion does not favour any direction. This means that in order to reach optimal velocity contraction and adhesion are fully correlated and localized at the trailing edge. Such correlation between the stresses created by contraction and the distribution of focal contacts agrees with experimental observations [62, 167, 182, 185, 186]. The ageement suggests that the velocity is an important parameter to the cell, which it tries to optimize. Still, we show in chapter III (section 4.3), that adhesion complexes also enhance the speed generated by polymerization/depolymerization. This effect is not considered here but to take advantage of this, adhesion has to rather concentrate at the leading edge. This suggests that the optimal distribution of adhesion complexes with respect to speed depends in a non trivial way on the balance between contractile (localization at the trailing edge) and protrusive (localization at the leading edge) effects.

2.7 Optimization of efficiency

As a next step we build a formal optimization procedure of efficiency as it is often done in the context of swimming at low Reynolds number [5, 6, 119, 136]. For simplicity, we consider that adhesion is homogeneous ($\alpha_1 \equiv 1$) and focus on the myosin distribution.

ased on section 2.4, and using Assumptions (A) and (B), we can compute the non dimensional efficiency as follow,

$$\Lambda = \frac{LV^2}{-L^{-2}\int_0^1 g\partial_{uu}\sigma + \epsilon} \tag{2.16}$$

where $g = g_2$ and the function σ solves the system of equations,

$$\begin{cases} -L^{-2}\partial_{uu}\sigma + \sigma = L^{-1}g \\ \sigma(0) = f_L = \sigma(1) \\ \partial_u\sigma(0) = LV = \partial_u\sigma(1). \end{cases} \tag{2.17}$$

Here we denoted,

$$f_L = -k\frac{L - L_0}{L_0}.$$

The efficiency now depends on three non dimensional constants (k, L_0, ϵ) and a function g.

2.7.1 Formulation of the variational problem

By solving (2.17) we obtain,

$$\begin{cases} V = \frac{1}{2\sinh(L/2)} \int_0^1 \sinh\left(L(\frac{1}{2}-u)\right) g(u)du \\ 2f_L \sinh(\frac{L}{2}) = \int_0^1 \cosh\left(L(\frac{1}{2}-u)\right) g(u)du \\ \sigma(u;g) = \frac{f_L \cosh\left(L(\frac{1}{2}-u)\right)}{\cosh(\frac{L}{2})} + \int_0^1 \Psi(v,u)g(v)dv. \end{cases}$$

Here, H is the Heaviside function, and the symmetric ($\Psi(u,v) = \Psi(v,u)$) kernel Ψ has the form (from solution of $(2.17)_1$ with zero Dirichelet boundary conditions),

$$\Psi(u,v) = \frac{1}{\sinh(L)} \left(\sinh(L(1-u))\sinh(Lv) - H(v-u)\sinh(L)\sinh(L(v-u))\right).$$

The efficiency can then be computed as a function of the known constants (k, L_0, ϵ) and the unknown parameters $(g(y), V, L)$,

$$\Lambda(g,L,V) = \frac{LV^2}{L^{-1}\int_0^1 g(u)^2du - 2f_L^2\tanh(L/2) - \int_0^1\int_0^1 \Psi(u,v)g(u)g(v)dudv + \epsilon}.$$

The problem of finding the maximal efficiency can then be formulated as follow:

$$\begin{cases} \underset{g\in L^2([0,1]), L\in\mathbb{R}_+, V\in\mathbb{R}}{max} \Lambda(g,L,V) \\ \text{with the constraints,} \\ 2V\sinh(\frac{L}{2}) = \int_0^1 \sinh\left(L(\frac{1}{2}-u)\right) g(u)du \\ 2f_L\sinh(\frac{L}{2}) = \int_0^1 \cosh\left(L(\frac{1}{2}-u)\right) g(u)du \\ \int_0^1 g(u)du = 1 \\ g \geq 0. \end{cases} \tag{2.18}$$

Note the unusal presence of V and L in the optimized functional. These two constants are implicitely defined by the first two constraints. An equivalent problem can be obtained if the two first constraints are used to find expicitly V and L as functionals of g (and of known parameters) and plug the values in the efficiency,

$$\Lambda(g, \tilde{L}(g), \tilde{V}(g))$$

and the equivalent maximization problem,

$$\begin{cases} \underset{g\in L^2([0,1]), L\in\mathbb{R}_+, V\in\mathbb{R}}{max} \Lambda(g, \tilde{L}(g), \tilde{V}(g)) \\ \text{with the constraints,} \\ \int_0^1 g(u)du = 1 \\ g \geq 0 \end{cases}$$

However, since the constraints are implicit, the first formulation is more convinient.

The ensuing variational problem is not trivial because we know that what maximizes the numerator (the velocity) is a fully localized distribution of g at one of the boundaries (Dirac mass of intensity 1). This distribution sums to 1 and satisfies the length constraint. At last, it is also non negative. On the contrary, what minimizes the denominator by making it equal to zero is taking $g = L\sigma$ which corresponds to $\sigma = f_L$. This is an admissible candidate as g sums to 1 and satisfies the length constraint for $L = \hat{L}_{\pm}$. Also, g is non negative since $L = \hat{L}_{\pm} < L_0$. Yet in this case $V = 0$. So there is a non trivial tradeoff between localizing g at the trailing edge which maximizes the velocity and making g uniform which minimizes the energy consumption.

2.7.2 A priori bounds on efficiency

The fact that efficiency is non negative,

$$\Lambda \geq 0$$

is clear from multiplication of (2.17) by $\partial_{uu}\sigma$ and integration by parts. This result does not depend whether g is non negative or not.

One may wonder if the efficiency is bounded from above (and if the supremum is a maximum). We begin with the following result. There exists a positive function of L, $\mu(L) > 0$ such that, for every L,

$$\Lambda \leq \mu(L).$$

Indeed, for any $f \in H^1(0,1)$ (See [28] for definition of functional spaces) there exists a positive constant C such that:

$$\|f\|_{H^1} \geq C\|f\|_\infty$$

Applying the inequality to $f = \sigma$, we conclude that there exists a constant $\mu(L)$ such that:

$$LV^2 = L^{-1}\left(\partial_y\sigma(0)\right)^2 \leq L^{-1}\mu(L)\left(L^{-2}\int_0^1 \sigma_{yy}^2 + \int_0^1 \sigma_y^2 + \epsilon L\right) = \mu(L)\left(-L^{-2}\int_0^1 g\sigma_{yy} + \epsilon\right).$$

meaning that,

$$0 \leq \Lambda \leq \mu(L)$$

This result is particularly interesting in the case $\epsilon = 0$ where we have seen that we can make the denominator of in the formula for the efficiency go to zero (taking

$g = Lf_L$) at the price of zero numerator, which questions the limiting value of this ratio. This result states that the ratio cannot exceed a finite constant. The bound also implies the existence of a couple (L, g) realizing the maximum of the efficiency. Indeed, as $L \in [L^*, L_0]$ it is clear $\mu(L)$ can be bounded uniformly in L. Then the continuity property of the efficiency and of the constraints for varying L and g ensures the existence of a maximizing couple. Uniqueness does not hold as a central symmetry with respect to 1/2 does leave the problem unchanged (choosing $g(x-1/2)$ or $g(1/2-x)$ is equivalent). It remains to be seen if the solution of the problem is unique up to this symmetry. The optimal constant $\mu(L)$ corresponds to the smallest bound of efficiency in the case $\epsilon = 0$. We shall prove in coming sections that,

$$\mu_{opt}(L) = \frac{L}{2}\coth(\frac{L}{2}) - 1$$

2.7.3 The subproblem at fixed L and V

We observe that the problem (2.18) may be reformulated as follows:

$$\max_{L\in\mathbb{R}_+, V\in\mathbb{R}} \left(\left\{ \begin{array}{c} \max\limits_{g\in L^2([0,1])} \Lambda(g, L, V) \\ \text{with the constraints,} \\ 2V\sinh(\frac{L}{2}) = \int_0^1 \sinh\left(L(\frac{1}{2}-u)\right) g(u)du \\ 2f_L\sinh(\frac{L}{2}) = \int_0^1 \cosh\left(L(\frac{1}{2}-u)\right) g(u)du \\ \int_0^1 g(u)du = 1 \\ g \geq 0 \end{array} \right. \right),$$

This means that we first can maximize at fixed L and V and then maximize with respect to the remaining V and L variables. The first problem at fixed V and L can be formulated as follows,

$$\left\{ \begin{array}{c} \max\limits_{g\in L^2([0,1])} \Lambda(g, L, V) \\ \text{with the constraints,} \\ 2V\sinh(\frac{L}{2}) = \int_0^1 \sinh\left(L(\frac{1}{2}-u)\right) g(u)du \\ 2f_L\sinh(\frac{L}{2}) = \int_0^1 \cosh\left(L(\frac{1}{2}-u)\right) g(u)du \\ \int_0^1 g(u)du = 1 \\ g \geq 0. \end{array} \right. \tag{2.19}$$

The problem (2.19) can be put in the equivalent form,

$$\left\{\begin{array}{c} \underset{g\in L^2([0,1])}{min} \left(L^{-1}\int_0^1 g(u)^2du - \int_0^1\int_0^1 \Psi(u,v)g(u)g(v)dudv\right) \\ \text{with the constraints,} \\ 2V\sinh(\frac{L}{2}) = \int_0^1 \sinh\left(L(\frac{1}{2}-u)\right)g(u)du \\ 2f_L\sinh(\frac{L}{2}) = \int_0^1 \cosh\left(L(\frac{1}{2}-u)\right)g(u)du \\ \int_0^1 g(u)du = 1 \\ g\geq 0. \end{array}\right. \tag{2.20}$$

To simplify the problem in first exposure, we first supress the sign constraint $g \geq 0$ allowing for both contraction and loosening. Then, we obtain a relatively simple classical variational problem,

$$\underset{g\in L^2([0,1])}{min} D(g) \tag{2.21}$$

where,

$$D(g) = L^{-1}\int_0^1 g(u)^2du - \int_0^1\int_0^1 \Psi(u,v)g(u)g(v)dudv$$

with the constraints,

$$\left\{\begin{array}{c} 2V\sinh(\frac{L}{2}) = \int_0^1 \sinh\left(L(\frac{1}{2}-u)\right)g(u)du \\ 2f_L\sinh(\frac{L}{2}) = \int_0^1 \cosh\left(L(\frac{1}{2}-u)\right)g(u)du \\ \int_0^1 g(u)du = 1. \end{array}\right. \tag{2.22}$$

2.7.4 Euler-Lagrange equation for problem (2.21-2.22)

By computing the first varation of D and using the symmetry of Ψ we get:

$$\text{grad}_g D(g) = 2L^{-1}g(u) - 2\int_0^1 \Psi(u,v)g(v)dv.$$

The gradient of the constraints (2.22) reads:

$$\{1, \sinh(L(1/2-u)), \cosh(L(1/2-u))\}$$

which is a free family. If the configuration g is a local minimum, there exists three scalars $(\lambda_0, \lambda_1, \lambda_2)$ such that g satisfies the order two Fredholm integral equation:

$$g(u) - L\int_0^1 \Psi(u,v)g(v)dv = \lambda_0 + \lambda_1\sinh(L(1/2-u)) + \lambda_2\cosh(L(1/2-u)). \tag{2.23}$$

We now need to check three points. 1) We have to show that there exists a unique g satisfying (2.23), 2) that this point is indeed a minimum and not a maximum of functional D and 3) that this minimum is global. Indeed,

1. As Ψ is bounded by $\frac{L\tanh(L/2)}{2}$ and L is smaller than the first eigenvalue of the kernel Ψ (we will elaborate on this point), we know from [120] that there exists a unique solution to this linear problem.

2. To check that this solution is indeed a local minimum, we let r and q be two functions of $L^2(0,1)$ satisfying the constraints (2.22). The Hessian at the solution reads:

$$H(r,q) = 2L^{-1}\int_0^1 r(u)q(u)du - \int_0^1\int_0^1 \Psi(u,v)r(u)q(v)dudv$$

   and since,

$$H(r,r) \geq f_L^2 \tanh(L/2) > 0$$

   any solution of (2.23) is a local minimum.

3. To show that this local minimum is in fact the global minimum, we need to prove that D is always larger than $Const(L)||g||_{L^2}^2$ implying quadratic growth at infinity. Applying twice Cauchy-Schwartz inequality we have,

$$D(g) \geq \left(L^{-1} - \int_0^1\int_0^1 \Psi(u,v)^2 dudv\right)||g||_{L^2}^2 = Const(L)||g||_{L^2}^2$$

   where,

$$\forall L > 0,\ Const(L) = \frac{4L + L\left(-\left(\coth(L) + L\text{csch}^2(L)\right)\right) + 2}{4L^2} > 0.$$

We can nox explicitly compute the solution of (2.23). To this end, we denote by Γ the right hand side of (2.23),

$$\Gamma(u) = \lambda_0 + \lambda_1 \sinh(L(1/2-u)) + \lambda_2\cosh(L(1/2-u)).$$

We have to find the eigencouples of the kernel Ψ to represent g. More specifically, we need to find the non trivial solutions (λ,σ) of the following eigenvalue problem:

$$\begin{cases} -L^{-2}\sigma_{uu} + \sigma = \lambda L^{-1}\sigma \\ \sigma(0) = \sigma(1) = 0. \end{cases}$$

There exists non trivial solutions if and only if, $L < \lambda$ and they can be indexed by $k \geq 1$,

$$\begin{cases} \lambda_k = L + \frac{k^2\pi^2}{L^2} \\ \sigma_k(u) = \sqrt{2}\sin(k\pi u), \end{cases}$$

The eigenfunctions $\{\sigma_k(u)\}$ form an orthonormalized basis of $L^2(0,1)$ vanishing at 0 and 1. Then, by Hilbert-Schmidt theorem, we can write,

$$g(u) = \Gamma(u) + 2L^2 \sum_{k=1}^{\infty} \frac{\int_0^1 \sin(k\pi v)\Gamma(v)dv}{k^2\pi^2} \sin(k\pi u). \tag{2.24}$$

The serie in (2.24) is normally convergent which justifies all reversals of summation and integration in what follows. From the expression of Γ we obtain,

$$g(u) = \lambda_0\psi_0(u) + \lambda_1\psi_1(u) + \lambda_2\psi_2(u) \tag{2.25}$$

where,

$$\left\{\begin{array}{c} \psi_0(u) = 1 + 4L^2 \sum_{k=0}^{\infty} \frac{\sin((2k+1)\pi u)}{((2k+1)\pi)^3} = 1 - \frac{L^2}{2}u(u-1) \\ \psi_1(u) = \sinh(L(1/2-u)) + 4L^2\sinh(L/2)\sum_{k=1}^{\infty} \frac{\sin(2k\pi u)}{2k\pi((2k\pi)^2+L^2)} = 2\left(\frac{1}{2}-u\right)\sinh(\frac{L}{2}) \\ \psi_2(u) = \cosh(L(1/2-u)) + 4L^2\cosh(L/2)\sum_{k=0}^{\infty} \frac{\sin((2k+1)\pi u)}{(2k+1)\pi(((2k+1)\pi)^2+L^2)} = \cosh(L/2). \end{array}\right.$$

We can now compute,

$$\left\{\begin{array}{c} A_0 = \int_0^1 \psi_0(u)du = 1 + \frac{L^2}{12} \\ A_2 = \int_0^1 \psi_2(u)du = \cosh(L/2) \\ S_1 = \int_0^1 \sinh(L(1/2-u))\psi_1(u)du = \frac{2(1-\cosh(L))+L\sinh(L)}{L^2} \\ C_0 = \int_0^1 \cosh(L(1/2-u))\psi_0(u)du = \cosh(L/2) \\ C_2 = \int_0^1 \cosh(L(1/2-u))\psi_2(u)du = \frac{\sinh(L)}{L}. \end{array}\right.$$

The constraints (2.22) can be rewritten as,

$$\left\{\begin{array}{c} 1 = \lambda_0 A_0 + \lambda_2 A_2 \\ 2V\sinh(L/2) = \lambda_1 S_1 \\ 2f_L\sinh(L/2) = \lambda_0 C_0 + \lambda_2 C_2 \end{array}\right.$$

which is a linear system that delivers the Lagrange multipliers as a function of the remaining variables V and L:

$$\left\{\begin{array}{c} \lambda_0 = \frac{12(1-f_L L)\sinh(L)}{(L^2+12)\sinh(L)-6L(\cosh(L)+1)} \\ \lambda_1 = \frac{L^2 V}{L\cosh\left(\frac{L}{2}\right)-2\sinh\left(\frac{L}{2}\right)} \\ \lambda_2 = \frac{2L\left(f_L\left(L^2+12\right)\sinh\left(\frac{L}{2}\right)-6\cosh\left(\frac{L}{2}\right)\right)}{(L^2+12)\sinh(L)-6L(\cosh(L)+1)}. \end{array}\right.$$

We now need to substitute these explicit relations into (2.16) and express efficiency as a function of V and L.

2.7.5 Solution of the problem with no sign constraint

The remaining problem is to maximize Λ with respect to the emaining scalar variables V and L. We have,

$$\Lambda = \frac{L^2V^2}{\int_0^1 g(u)\Gamma(u)du - 2Lf_L^2 \tanh(L/2) + L\epsilon}$$

where,

$$\int_0^1 g(u)\Gamma(u)du = \lambda_0^2 A_0 + \lambda_0\lambda_2(A_2 + C_0) + \lambda_1^2 S_1 + \lambda_2^2 C_2 = \lambda_0 + 2\sinh(L/2)(V\lambda_1 + f_L\lambda_2).$$

After substitutions, we obtain the final formula:

$$\Lambda(V,L) = \frac{L^2V^2}{L\left(\epsilon + \frac{2LV^2}{L\coth\left(\frac{L}{2}\right)-2}\right) + \frac{12\sinh\left(\frac{L}{2}\right)(1-f_L)^2}{(L^2+12)\sinh\left(\frac{L}{2}\right)-6L\cosh\left(\frac{L}{2}\right)}}. \tag{2.26}$$

The function $\Lambda(V, L)$ is illustrated in Fig.2.6 for a generic set of parameters.

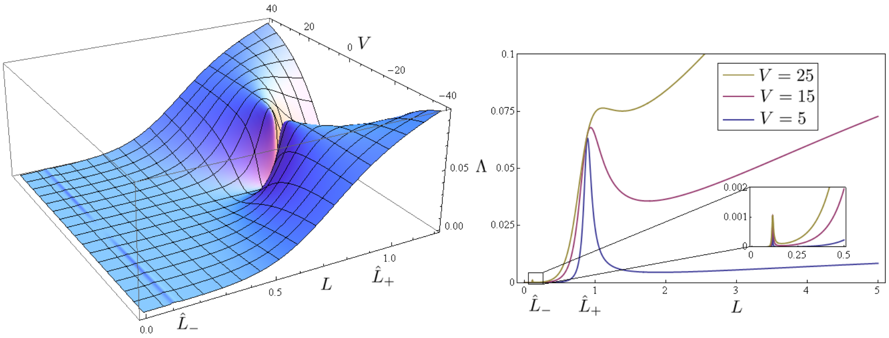

Figure 2.6: Λ as a function of V and L for parameters $L_0 = 1$, $k = 10$ and $\epsilon = 10$, corresponding to $\hat{L}_- \simeq 0.11$ and $\hat{L}_+ \simeq 0.11$.

Observe first that the expression (2.26) is invariant with respect to a change of the velocity sign. This was expected from the original symmetry of the problem where changing $g(x - 1/2)$ in $g(x + 1/2)$ just changes the sign of the velocity. So, if we have a solution moving front left to right, we have a twin solution moving from right to left.

At a fixed speed there are two special lengths corresponding to $\hat{L}_-$ and $\hat{L}_+$ (which we recall are defined by $f_L L = 1$) where efficiency undergoes a localized increase as the second term of the denominator in the efficiency vanishes. Interestingly, $\hat{L}_-$ which is unstable, is also very inefficient comparing to $\hat{L}_+$.

As we see, in the problem with no sign constraint, the efficiency can go to infinity when both speed and length go to infinity. The corresponding configurations g involve infinite contraction at the trailing edge and loosening at the front. Indeed when V and L are large enough, we can approximate the optimal g by:

$$g_\infty(u) = Lf_L + VL(1-2u) - 6(1-Lf_L)u(u-1).$$

Now, when V goes to infinity faster than L (say $V \sim L^2$), we have pointwisely:

$$g_\infty^{opt}(u) = C(L)(1-2u) \text{ with } C(L) = L^3.$$

The integral constraint $(2.22)_3$ is violated in the limit as the leading order term integral vanishes.

$$\int_0^1 VL(1-2u)du = 0$$

The ensuing configuration, has infinite speed, and allows arbitrary large compression (positive part of g) at the trailing edge and as much loosening (negative part of g) at the leading edge. To obtain the optimal configuration with both the speed and the efficiency bounded, we would need to constrain the integrals of positive and negative part of g.

2.7.6 Solution of the problem with a sign constraint

Now, we return to the problem where the constraint $g \geq 0$ is imposed, thus allowing contraction only.

2.7.6.1 Case $\epsilon = 0$

The constraint $g \geq 0$ could be incorporated directly at the level of minimization of D (see Appendix 6.3) but since we have already obtained optimal g given by (2.25), we shall first apply to it three discrete constraints implied by $g \geq 0$ which are sufficient to conclude,

$$\begin{cases} g(0) \geq 0 \\ g(1/2) \geq 0 \\ g(1) \geq 0 \end{cases}$$

These inequalities can be written as:

$$\begin{cases} \frac{L^2(f_L L-1)\sinh\left(\frac{L}{2}\right)}{(L^2+12)\sinh\left(\frac{L}{2}\right)-6L\cosh\left(\frac{L}{2}\right)} + \frac{L^2V}{2-L\coth\left(\frac{L}{2}\right)} + 1 \geq 0 \\ \frac{1}{2}\left(L^2(3-f_L L)+24\right)\sinh(L) - 6L(\cosh(L)+1) \geq 0 \\ \frac{L^2(f_L L-1)\sinh\left(\frac{L}{2}\right)}{(L^2+12)\sinh\left(\frac{L}{2}\right)-6L\cosh\left(\frac{L}{2}\right)} - \frac{L^2V}{2-L\coth\left(\frac{L}{2}\right)} + 1 \geq 0. \end{cases} \tag{2.27}$$

The imposed restrictions on the (L, V) domain of definiton of efficiency supress a major part of the original admissibility domain. On Fig.2.7 we show the efficiency on the new domain addmissible with conditions (2.27). Additionaly, we know that the second term in the denominator in the formula for efficiency (2.26) is positive. Hence, the optimal efficiency Λ^{opt} can be bounded as follow

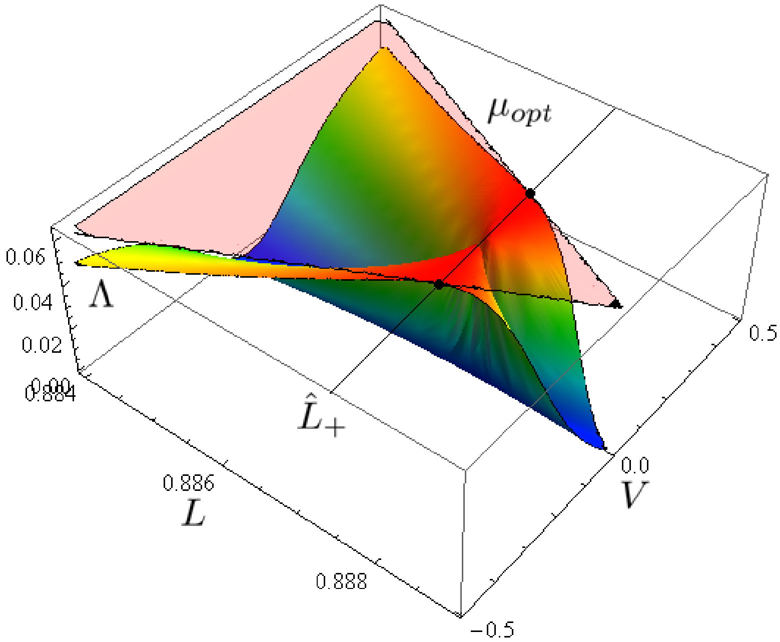

Figure 2.7: Plot of efficiency with constraints on the domain admissible with conditions (2.27) in the $\epsilon = 0$ case with $L_0 = 1$ and $k = 10$. The less opaque surface is $\mu_{opt}(L)$. The black dots are the points where efficiency is the highest and reaches its upper bound.

$$\Lambda^{opt} \leq \frac{L^2V^2}{L\left(\frac{2LV^2}{L\coth(\frac{L}{2})-2}\right)} = \mu_{opt}(L) = \frac{L}{2}\coth(\frac{L}{2}) - 1$$

and one can check that,

$$g^{opt}_{\epsilon=0}(u) = 2(1-u) \geq 0$$

reaches this upper bound (and is positive on $[0, 1]$). The cell lengths associated with $g^{opt}_{\epsilon=0}$ are $\hat{L}_\pm$ and $\hat{L}_+$ clearly correspond to the maximal efficiency (as $\frac{\hat{L}_+}{2}\coth(\frac{\hat{L}_+}{2}) > \frac{\hat{L}_-}{2}\coth(\frac{\hat{L}_-}{2})$). Our sign constraints eliminated larger lengths leading to potentially larger efficiency in the admissible domain and we can now check that the largest efficiency indeed corresponds to $g^{opt}_{\epsilon=0}$. In fact, the maximal efficiency is reached when

$L = \hat{L}_+$ and when the absolute value of the velocity is also maximal (see black dots of Fig.2.7).

To prove these statements, let us consider a positive velocity (the negative case is the same). The constraint $g(1) \geq 0$ is on the limit of activity at the optimal point ($g(1) = 0$) and we have, for velocity

$$V = \frac{\coth(\frac{\hat{L}_+}{2})}{\hat{L}_+} - \frac{2}{\hat{L}_+^2}.$$

Then, the Lagrange multipliers take the values

$$\begin{cases} \lambda_0 = 0 \\ \lambda_1 = \frac{1}{\sinh(\frac{\hat{L}_+}{2})} \\ \lambda_2 = \frac{1}{\cosh(\frac{\hat{L}_+}{2})} \end{cases}$$

and from (2.24), the optimal g is exactly,

$$g^{opt}_{\epsilon=0}(u) = 2(1-u)$$

2.7.6.2 Case $\epsilon > 0$

The problem for arbitrary ϵ is more difficult and we shall stufy it only numerically by using a simple algorithm presented in Appendix (6.5.2).

From Fig.2.8 we can see that the main effect of the sign constraint is to remove the traction component of the active stresses at the front and to impose a finite integral $(2.22)_3$ on the compression part at the rear. This compression component is then neither constant nor fully localized. At small enough L_0, numerical computations shown on Fig.2.8 suggest that the optimal g can be approximated by,

$$g^{opt} = -\frac{2}{a^2_{k,L_0}(\epsilon)}(u - a_{k,L_0}(\epsilon))1_{[0,a_{k,L_0}(\epsilon)]}(u).$$

This function is linear on the set $[0, a_{k,L_0}(\epsilon)]$, like in the unconstrained case and zero outside. The 'first' value where g^{opt} vanishes, $a_{k,L_0}(\epsilon)$ depends on the three non dimensional parameters (k, L_0, ϵ). The larger ϵ the more the optimal distribution tends to a Dirac mass localized at the trailing edge as only numerator counts for infinitely large ϵ. In the other limit, the optimal g is just the linear function $g^{opt}_{\epsilon=0}$ as we have shown above. The value of length remains remarkably near $\hat{L}_+$ in all cases. The effect of an

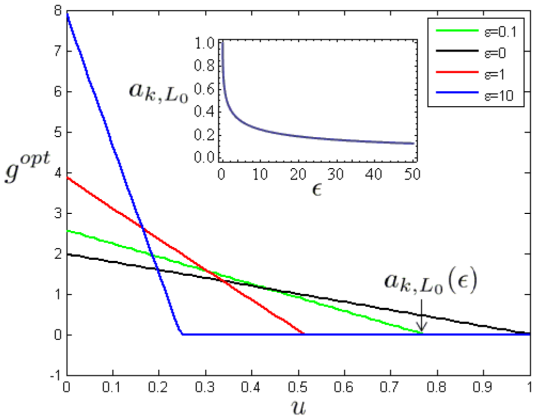

Figure 2.8: Optimal functions g^{opt} for different values of ϵ at $k = 10$ and $L_0 = 1$. In insert the value of a_{k,L_0} as a function of ϵ.

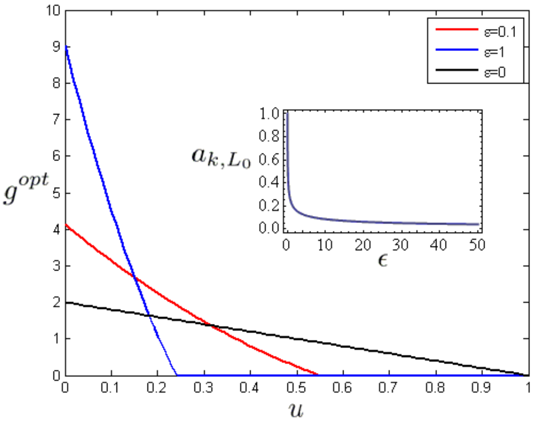

Figure 2.9: Optimal functions g^{opt} for different values of ϵ at $k = 10$ and $L_0 = 5$. In insert the value of a_{k,L_0} as a function of ϵ.

increasing L_0 on the shape of the optimal distribution is to breake the linearity of the non vanishing part of g^{opt} as we show in Fig.2.9. Still, the deviation from linearity is rather small and the piecewise linear approximation can still be used.

The problem of an infinitely stiff active layer can be dealt with the same method. We have to assume $k \longrightarrow \infty$. As we would like σ to remain finite on the boundaries we need to requiere that $L \longrightarrow L_0$ while f_L remains an unknown constant. This transition is similar to the transition from compressible to incompressible fluid with the emergence in the limit of the kinematic pressure (our f_L) In this limit the problem can be reformulated, at fixed parameters (L_0, ϵ) as follows, Find the maximum for $g \in L^2([0,1])$ of the functional,

$$\Lambda(g) = \frac{\left(\int_0^1 \sinh\left(L_0(\frac{1}{2} - y)\right) g(y)dy\right)^2}{\frac{\int_0^1 g(y)^2 dy}{L_0} - \frac{\left(\int_0^1 \cosh\left(L_0(\frac{1}{2}-y)\right)g(y)dy\right)^2}{\sinh(L_0)} - \int_0^1\int_0^1 \Psi(u,v)g(u)g(v)dudv + \epsilon},$$

with constraints,

$$\begin{cases} g \geq 0 \\ \int_0^1 g = 1. \end{cases}$$

The same methods suggest again that the optimum is reached when

$$g(u) = -\frac{2}{a(L_0,\epsilon)^2}(u - a(L_0,\epsilon))1_{[0,a(L_0,\epsilon)](u)}$$

The value of the constant a can be computed analytically (see Fig.2.10) by using the above ansatz and it agrees well with numerics. The function $a(L_0, \epsilon)$ decreases as ϵ increases. Indeed, when ϵ increases, more importance is given to the numerator in the definition of efficiency which favours infinite localization on one of the boundaries.

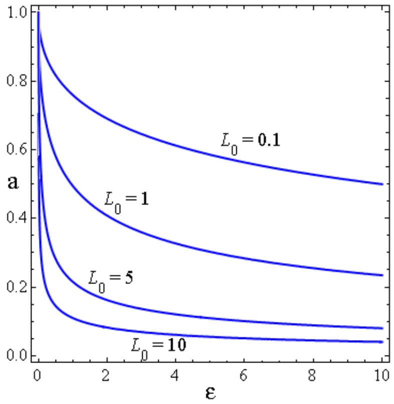

Figure 2.10: Values of a as a function of L_0 and ϵ

2.8 Conclusions

We first investigated the optimal strategy to achieve the largest velocity by tuning myosin and integrins distributions. To do so, we have identified the symmetries of the problem that need to be broken to lead to initiate the motion. In the steady state, the optimal configuration is when myosins and integrins are localized at the trailing edge and fully correlated as suggested by some experimental and theoretical results [43, 44, 62, 194]. The modeling does not take into account the treadmilling side of motility and this effect would lead to a very different optimal distribution of integrins that would favour the leading front of the lamellipodium in order to make the treadmilling more efficient (see Chapter III). In the next step, keeping integrin distribution constant, we investigated the optimal strategy for myosin distribution with the goal to maximize mechanical efficiency. The optimal distribution is a non trivial tradeoff between localization at the trailing edge which maximizes the velocity and a constant distribution that minimizes the energy consumption. As we show in section 6.2.2, it is reasonable to assume that the myosin distribution is governed by a drift diffusion equation. The drift part is rather natural as the bipolar filaments of myosins are crosslinking actin, which implies that they are advected with the actin retrograde flow. The diffusive part is justified from the thermal mobility of bipolar filaments. Here, we see that it can be beneficial in term of mechanical efficiency that myosin is not fully localized. Diffusion introduces a spreading length scale of order $\sqrt{\frac{D\eta}{\chi}}$. Qualitatively, this spreading can be related to ϵ as we can impose the following relation,

$$a_{k,L_0}(\epsilon) \sim \sqrt{\frac{D\xi}{\chi}}.$$

There we assume that the mechanical efficiency of the cell is high. This scaling could in principle lead to an independant estimate of the parameter ϵ which is otherwise difficult to measure.

3

Chapter II: Contraction at work

We propose a mechanism of cell motility which places emphasis on contraction while ignoring treadmilling. At the basis of the model is contraction driven uphill diffusion destabilizing symmetric configuration and causing polarization. The morphological instability is due to spontaneous internal motion of the cytoskeleton which is generated by active cross-linkers and simultaneously transports them. By studying the simplest one dimensional problem we show that such internal flow can generate steady propulsion of a finite cell body. The model exhibits motility initiation pattern similar to the ones observed in experiments.

3.1 Introduction

Coordinated crawling-induced movements of eukaryotic cells involve spatial and temporal self-organization at the cytoskeletal level. If non motile cells are mostly symmetric, in the crawling cells actin polymerization is biased toward the front and myosin contraction is localized at the rear. Cells can polarize and initiate motility submitted to transient asymmetric spatial stimuli. To achieve the motile configuration a cell must first undergo a morphological transition (polarization) [3, 27, 127]. While both contraction and treadmilling usually contribute to cell migration, it is contraction that is crucial for polarization, moreover, cells can be driven by contraction only without polymerization [50, 109, 144, 180, 182, 190]. In terms of [157, 168] the motion will be supported by 'pullers' while 'pushers' will be disabled.

3. CHAPTER II: CONTRACTION AT WORK

In this chapter, we show that the positive feedback mechanism giving rise to symmetry breaking and contraction dominated motility can be interpreted as an uphill diffusion driven at the microscale by advection of molecular motors. Indeed, it is known that myosin motors (active cross-linkers) can mechanically drive actin network by inflicting contraction. In turn, the network drags the motors amplifying contraction and creating an autocatalytic effect (e.g. [116]). The positive feedback leads to build up of motor density which is limited by internal stiffness resisting the runaway and providing negative feedback.

By using the term autotaxis we imply conceptual similarity of the described motility mechanism with chemotaxis. One can say that each motor generates a stress field and the other motors undergo biased random motion in the direction of a higher value of the stress. In this way active cross-linkers use passive actin network as a medium through which they interact and self-organize. After the symmetry of the non motile configuration is spontaneously broken, the resultant active motion inside the cell produces overall steady state translocation of the cell body.

The idea that contraction causes flow which in turn carries regulators of the contraction is incorporated into the hydrodynamic description of active fluids [2, 100, 159, 168]. It has been shown to describe peaks in concentration of stress activator amplified by advective influx due to active stresses under static constraints [25, 78]. In [71, 74] similar idea was used to describe initiation of non-lamellipodial motility associated with angular cortex flows. Heuristic models of the Keller-Segel type [142] describing polarization instability in a non motile cell with fixed length were proposed in [36, 101]. In most of these models, however, the effect of contraction was obscured by the account of other mechanisms, in particular, treadmilling, and the focus was on generation of internal flow rather than on motion of the center of mass. There also exists considerable literature addressing spontaneous motility but emphasizing protrusion [86], Turing patterning [9, 82], or studying the interaction of multiple mechanisms [15, 40, 55, 75, 90, 156, 163, 196].

To make the physics of autotaxis more transparent we study a simple analytically tractable 1D model which captures both the symmetry breaking and the induced macroscopic motion. In addition to motor mediated active contractility the model accounts for long range elastic stiffness coupling the front and the back of the cell [14, 58, 110]. To achieve analytical simplicity we assume infinite compressibility of the cytoskeleton allowing us to uncouple the study of actin distribution and focus exclusively on the dynamics of myosin.

To initiate motility the destabilizing activity of motors must be strong enough to counteract elasticity, frictional resistance and diffusive counterflux. The symmetry loss is therefore controlled by the number of motor proteins and its increase leads to a bifurcation from a symmetric non motile regime to an asymmetric motile traveling wave (TW) regime. We show that the stable motile regimes have motor concentration localized at the trailing edge of the cell as observed in experiments [50, 109, 144, 180, 182, 190].

3.2 The model

We begin by writing the force balance equation for a 1D body in viscous contact with rigid background

$$\partial_x \sigma = \xi v,$$

where we recall $\sigma(x,t)$ is the stress, $v(x,t)$ is the velocity and ξ is the friction coefficient. Following [25, 78, 89, 97] we write

$$\sigma = \eta \partial_x v + \chi c,$$

where η is the bulk viscosity, c is the concentration of motors and $\chi > 0$ is the contractile prestress per motor. The function $c(x,t)$ satisfies advection-diffusion equation

$$\partial_t c + \partial_x (cv) = D \partial_{xx} c,$$

where D is the diffusion coefficient. We assume that $l_-(t)$ and $l_+(t)$ are the unknown boundaries of the cell. Assuming also the existence of a long time global elastic structure [24] due to both the internal stiffness (storage modulus) of the cytoskeleton and the elasticity of the plasmic membrane that resists reshaping of the body of the cell, we write [14],

$$\sigma(l_\pm(t), t) = -k(L - L_0)/L_0,$$

where $L(t) = l_+(t) - l_-(t)$ is the length of the cell, k is the effective elastic stiffness and L_0 is the reference length. Since we neglect treadmilling we can write the kinematic boundary conditions in the form

$$\dot{l}_\pm = v(l_\pm).$$

Finally, we impose zero exterior flux of motors

$$\partial_x c(l_\pm(t),t) = 0$$

which implies that the average concentration $c_0 = L_0^{-1}\int_{l_-}^{l_+} c(x,t)dx$ is conserved. If we now normalize length by L_0, time, by L_0^2/D, stress by k, we obtain a Keller-Segel type system

$$\begin{cases} -\mathcal{Z}\partial_{xx}\sigma + \sigma = \mathcal{P}c/c_0, \\ \partial_t c + \mathcal{K}\partial_x(c\partial_x\sigma) = \partial_{xx}c, \end{cases} \tag{3.1}$$

where the dimensionless constants are $\mathcal{Z} = \eta/(\xi L_0^2)$, $\mathcal{K} = k/(\xi D)$ and $\mathcal{P} = c_0\chi/k$; if σ is expressed through the Green's function of $(3.1)_1$ and substituted into $(3.1)_2$ the resulting nonlocal diffusion-advection problem is structurally similar to the one proposed in [101], however the effective kernel is different. The dimensionless integral constrain on the total amount of motors reads,

$$c_0 = \int_{l_-(t)}^{l_+(t)} c(x,t)dx$$

while free boundary conditions take the form

$$\begin{cases} \sigma(l_\pm(t),t) = -(L(t)-1), \\ \partial_x c(l_\pm(t),t) = 0, \\ \dot{l}_\pm(t) = \mathcal{K}\partial_x\sigma(l_\pm(t),t). \end{cases}$$

The main system of equations (3.1) contains two differential equations. While the second equation is a nonlinear PDE, the first equation is a linear ODE. Therefore the second equation can be replaced by a Green's function based nonlocal representation of the stress σ through the concentration c which takes into account the boundary conditions. Then the second nonlinear equation can be written as a single nonlocal PDE. The ensuing formulation is interesting because similar nonlocal continuum theories of active actin networks have been derived directly from a micro-model in the papers of Kruse and coauthors [99, 101, 177].

Since we are dealing with a moving domain, the Green's functions take unusual form. To make the analysis more transparent, we can first map the problem on a fixed domain $[0,1]$ and move the corresponding time dependence into the coefficients of the linear ODE which then become parametrically dependent on time. More specifically, we introduce a new spatial variable:

$$u(x,t) = \frac{x - l_-(t)}{l_+(t) - l_-(t)}$$

and new unknown functions

$$\hat{\sigma}(u,t) = \sigma(l_- + (l_+(t) - l_-(t))u, t)$$

and

$$\hat{c}(u,t) = Lc(l_- + (l_+(t) - l_-(t))u, t).$$

On the fixed domain the original problem (3.1) can be written as

$$\begin{cases} -\frac{\mathcal{Z}}{L^2}\partial_{uu}\hat{\sigma} + \hat{\sigma} = \frac{\mathcal{P}\hat{c}}{Lc_0} \\ \partial_t\hat{c} + \frac{1}{L}\partial_u(\hat{c}\left(\mathcal{K}\frac{\partial_u\hat{\sigma}}{L} - \dot{G} - (u - \frac{1}{2})\dot{L}\right) - \frac{\partial_u\hat{c}}{L}) = 0 \end{cases} \tag{3.2}$$

where we recall that $L(t) = l_+(t) - l_-(t)$ and $G(t) = (l_-(t) + l_+(t))/2$ and from the Stefan boundary conditions we know that

$$\begin{cases} \dot{G} = \frac{\mathcal{K}}{2L}(\partial_u\hat{\sigma}(1,t) + \partial_u\hat{\sigma}(0,t)) \\ \dot{L} = \frac{\mathcal{K}}{L}(\partial_u\hat{\sigma}(1,t) - \partial_u\hat{\sigma}(0,t)). \end{cases}$$

The remaining boundary conditions can be written as:

$$\begin{cases} \hat{\sigma}(0,t) = \hat{\sigma}(1,t) = -(L-1) \\ \partial_u\hat{c}(0,t) = \partial_u\hat{c}(1,t) = 0 \end{cases} \tag{3.3}$$

And we must also prescribe the initial data,

$$\hat{c}(u,0) = \hat{c}^0(u).$$

From the linear equation $(3.2)_1$ and the boundary condition $(3.3)_1$ we obtain the following representation of $\hat{\sigma}$ in terms of $\hat{c}$:

$$\hat{\sigma}(u,t) = -(L-1)q(u) + \frac{\mathcal{P}}{\sqrt{\mathcal{Z}}c_0}\int_0^1 \Psi(u,v)\hat{c}(v,t)dv.$$

The function q and the kernel Ψ can be written explicitly,

$$\Psi(u,v) = \frac{\sinh(\frac{L}{\sqrt{\mathcal{Z}}}(1-u))\sinh(\frac{L}{\sqrt{\mathcal{Z}}}v) - H(v-u)\sinh(\frac{L}{\sqrt{\mathcal{Z}}})\sinh(\frac{L}{\sqrt{\mathcal{Z}}}(v-u))}{\sinh(\frac{L}{\sqrt{\mathcal{Z}}})},$$

where H is the Heaviside function and is represented on Fig.3.1 and,

$$q(u) = \frac{\cosh(\frac{L}{\sqrt{\mathcal{Z}}}(\frac{1}{2} - u))}{\cosh(\frac{L}{2\sqrt{\mathcal{Z}}})}.$$

The internal stress field has two additive (linear ODE) contributions, one from the spring connecting the rear and front which is the analogue to a viscous fluid between

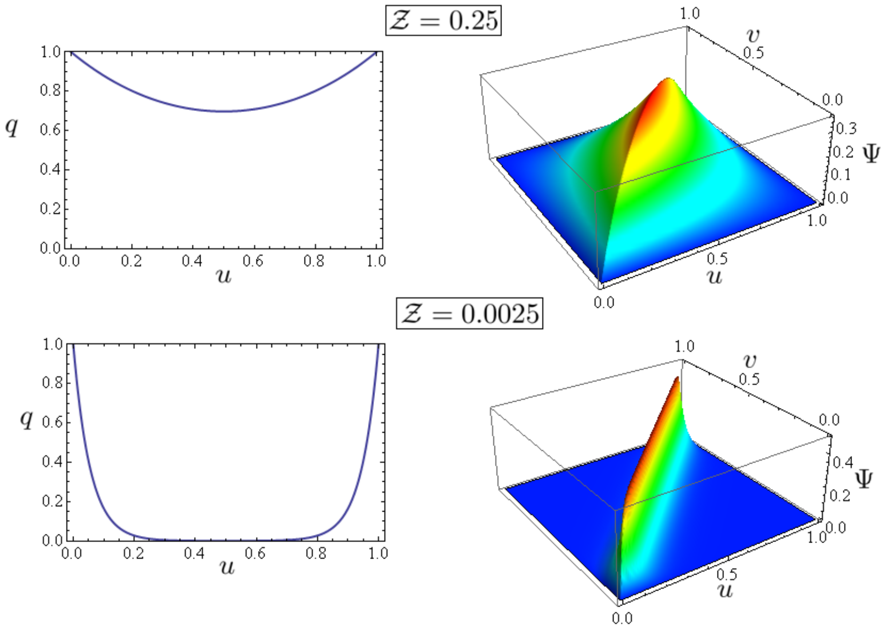

Figure 3.1: Plot of the the stress kernels q and Ψ for $\mathcal{Z} = 0.25$ and $L = 0.9$ (top) and for $\mathcal{Z} = 0.0025$ and $L = 0.9$ (bottom).

two walls connected by a spring and one from the active stress generated by motors (See Fig.3.1). Notice that $\Psi(u, v) = \Psi(v, u)$ because viscosity does not favour any direction. The only way to create an asymmetric (with respect to the center of the layer 1/2) stress is to have an asymmetric distribution of motors.

We can expose the effect of viscosity by taking the limit $\mathcal{Z} \to 0$. Then the 'elastic' part of the internal stress relaxes to zero in the bulk while two infinitely small boundary layers appear to match boundary conditions (See Fig.3.1). The 'contractile' part of the internal stress matches the value,

$$\hat{\sigma} = \frac{\mathcal{P}\hat{c}}{Lc_0}$$

in the bulk while infinitely small boundary layers are created to produce a zero contractile stress on the boundaries (See Fig.3.1). A more rigorous analysis will be carried on in the dedicated section 3.7.

The dynamics of the fronts can be also expressed in terms of $\hat{c}$

$$\left\{\begin{array}{c} \dot{G} = \frac{\mathcal{K}\mathcal{P}}{2c_0\mathcal{Z}} \int_0^1 \frac{\sinh(\frac{L}{\sqrt{\mathcal{Z}}}(\frac{1}{2}-v))}{\sinh(\frac{L}{2\sqrt{\mathcal{Z}}})} \hat{c}(v,t)dv \\ \dot{L} = -2\frac{\mathcal{K}}{\sqrt{\mathcal{Z}}}(L-1)\tanh(\frac{L}{2\sqrt{\mathcal{Z}}}) - \frac{\mathcal{K}\mathcal{P}}{c_0\mathcal{Z}} \int_0^1 \frac{\cosh(\frac{L}{\sqrt{\mathcal{Z}}}(\frac{1}{2}-v))}{\cosh(\frac{L}{2\sqrt{\mathcal{Z}}})} \hat{c}(v,t)dv \end{array}\right. \tag{3.4}$$

where the first of these equations coincided with Eq. (3.9) in the text.

The remaining problem for $\hat{c}$ reduces to a nonlocal PDE with quadratic non linearity:

$$\left\{\begin{array}{c} \partial_t\hat{c}(u,t) - \frac{\mathcal{K}(L-1)}{L\sqrt{\mathcal{Z}}}\partial_u(\theta(u)\hat{c}(u,t)) \\ +\frac{\mathcal{P}\mathcal{K}}{c_0\mathcal{Z}L}\partial_u(\int_0^1 \phi(u,v)\hat{c}(v,t)\hat{c}(u,t)dv) = \frac{\partial_{uu}\hat{c}(u,t)}{L^2} \\ \partial_u\hat{c}(0,t) = \partial_u\hat{c}(1,t) = 0 \\ \hat{c}(u,0) = \hat{c}^0(u). \end{array}\right. \tag{3.5}$$

Here the inhomogeneous velocity field $\theta(u)$ (see Fig.3.2)

$$\theta(u) = \frac{(1-2u)\sinh\left(\frac{L}{2\sqrt{\mathcal{Z}}}\right) - \sinh\left(\frac{L(\frac{1}{2}-u)}{\sqrt{\mathcal{Z}}}\right)}{\cosh\left(\frac{L}{2\sqrt{\mathcal{Z}}}\right)} \tag{3.6}$$

describes the internal flow due to elastic coupling between the rear and the front of the cell which transports the motors but does not experience any feedback from the motion of the motors. The main autotaxis effect is contained in the part of the kernel (see Fig.3.2)

$$\begin{array}{c} \phi(u,v) = \frac{\left(u-\cosh\left(\frac{L(1-u)}{\sqrt{\mathcal{Z}}}\right)\right)\sinh\left(\frac{Lv}{\sqrt{\mathcal{Z}}}\right)-(1-u)\sinh\left(\frac{L(1-v)}{\sqrt{\mathcal{Z}}}\right)}{\sinh\left(\frac{L}{\sqrt{\mathcal{Z}}}\right)} \\ +H(v-u)\cosh\left(\frac{L(v-u)}{\sqrt{\mathcal{Z}}}\right), \end{array} \tag{3.7}$$

which describes the long range mechanical interactions between two motors. The kernel $\phi(u,v)$ has a symmetry

$$\phi(u,v) = -\phi(1-u,1-v) \tag{3.8}$$

which reflects the crucial local momentum balance [99, 101, 177] in that if two filaments are linked by a motor, in the absence of inertia, the force generated by the filaments on each other are opposed.

From the expression of effective drift in (3.2),

$$drift(u,t) = \underbrace{\mathcal{K}\frac{\partial_u\hat{\sigma}}{L}}_{\text{internal}} \underbrace{-\dot{G} - (u-\frac{1}{2})\dot{L}}_{\text{external}},$$

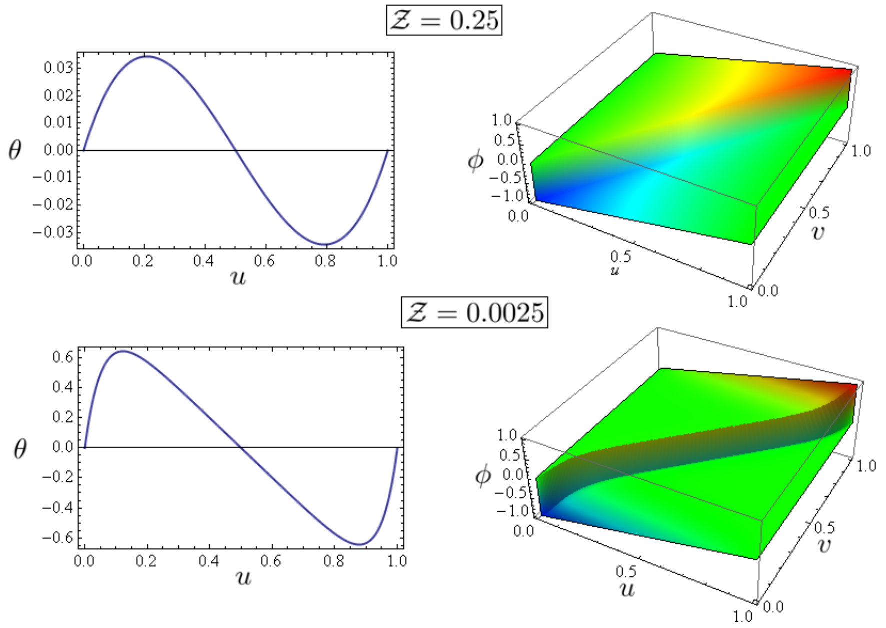
$\boxed{\mathcal{Z} = 0.25}$

$\boxed{\mathcal{Z} = 0.0025}$

Figure 3.2: Plot of the advection field θ and the interaction kernel ϕ for $\mathcal{Z} = 0.25$ (above), $\mathcal{Z} = 0.0025$ (bottom) and $L = 0.9$

both the drift θ and the interaction kernel ϕ can be further represented as sums of two contributions: internal, which is independent of the motion of the boundaries an relies on internal stress and external, which originates from the presence of free boundaries. Thus,

$$\theta(u) = \theta_i(u) + \theta_e(u) = \underbrace{\frac{-\sinh\left(\frac{L(\frac{1}{2}-u)}{\sqrt{\mathcal{Z}}}\right)}{\cosh\left(\frac{L}{2\sqrt{\mathcal{Z}}}\right)}}_{\theta_i} + \underbrace{(1-2u)\tanh\left(\frac{L}{2\sqrt{\mathcal{Z}}}\right)}_{\theta_e}$$

One can see (See Fig.3.3) that the flow contribution θ_i creates a drift of motors away from the center of the cell. Instead, the term θ_e creates a flow convergent to the center of the cell. Indeed, on a fixed domain, the internal stress coming from the spring connecting the rear and the front creates a flux away from the center as the length is smaller than one. One the contrary, the moving fronts tend in reaction to counter this effect and the overall effect is that the flow is towards the center

Similarly, we can write

$$\phi(u, v) = \phi_i(u, v) + \phi_e(u, v),$$

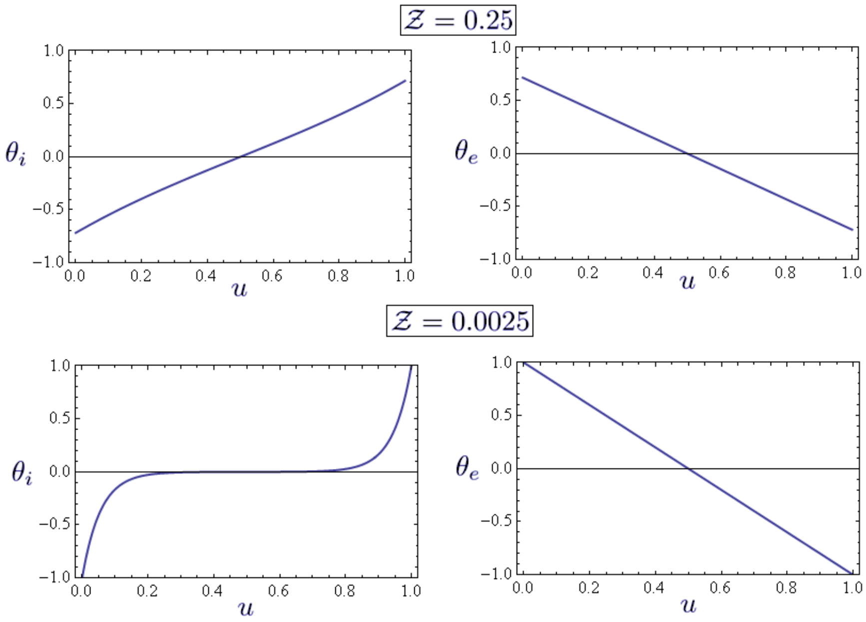

Figure 3.3: Plot of the advection fields θ_i and θ_e for $\mathcal{Z} = 0.25$ (above), $\mathcal{Z} = 0.0025$ (bottom) and $L = 0.9$

where

$$\phi_i(u,v) = \frac{-\cosh(\frac{L}{\sqrt{\mathcal{Z}}}(1-u))\sinh(\frac{L}{\sqrt{\mathcal{Z}}}v) + H(v-u)\sinh(\frac{L}{\sqrt{\mathcal{Z}}})\cosh(\frac{L}{\sqrt{\mathcal{Z}}}(v-u))}{\sinh(\frac{L}{\sqrt{\mathcal{Z}}})}$$

and one can see that the term ϕ_i creates around a given point (over a characteristic length $\sqrt{\mathcal{Z}}$) a flow which is convergent to this point. Instead, the term

$$\phi_e(u,v) = (u - \frac{1}{2})\frac{\cosh(\frac{L}{\sqrt{\mathcal{Z}}}(\frac{1}{2}-v))}{\cosh(\frac{L}{2\sqrt{\mathcal{Z}}})} - \frac{\sinh(\frac{L}{\sqrt{\mathcal{Z}}}(\frac{1}{2}-v))}{2\sinh(\frac{L}{2\sqrt{\mathcal{Z}}})},$$

which is due to the motion of the boundaries, creates in response a divergent flow away from the current point (See Fig.3.4).

To finish with, the whole analysis can be repeated again on a moving domain $x \in [l_-(t), l_+(t)]$, where only the 'internal' part of the stress is explicitly presented in the equation. From (3.1) and boundary conditions we have,

$$\sigma(x,t) = \frac{-(L-1)}{\cosh(\frac{L}{2\sqrt{\mathcal{Z}}})}\cosh(\frac{G-x}{\sqrt{\mathcal{Z}}}) + \frac{\mathcal{P}}{\sqrt{\mathcal{Z}}c_0}\int_{l_-}^{l_+}\tilde{\Psi}(x,y)c(y)dy$$

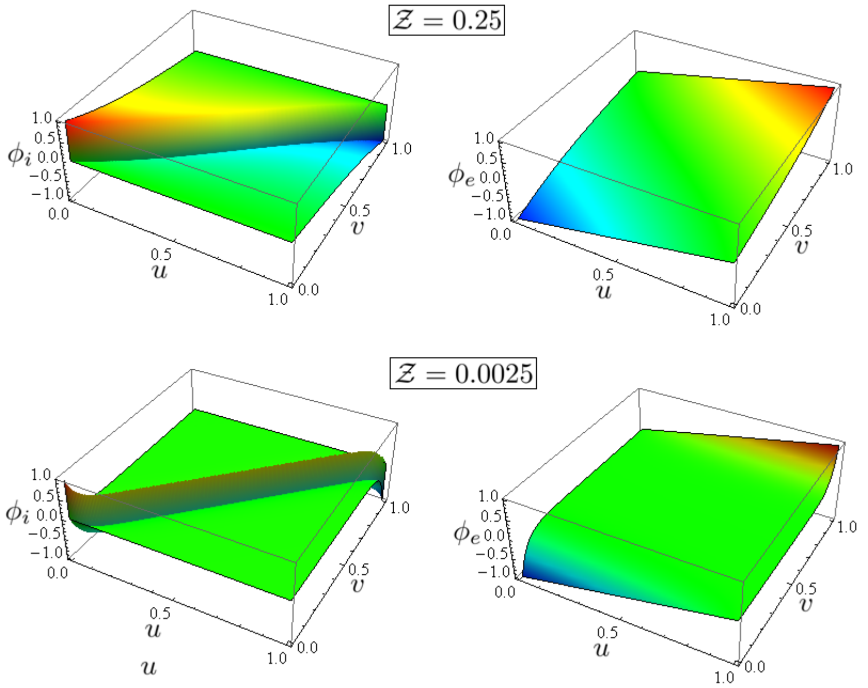

Figure 3.4: Plot of the kernels ϕ_i and ϕ_e for $\mathcal{Z} = 0.25$ (above), $\mathcal{Z} = 0.0025$ (bottom) and $L = 0.9$

where,

$$\tilde{\Psi}(x,y) = \frac{\sinh(\frac{L-x}{\sqrt{\mathcal{Z}}})\sinh(\frac{y}{\sqrt{\mathcal{Z}}}) - H(y-x)\sinh(\frac{L}{\sqrt{\mathcal{Z}}})\sinh(\frac{y-x}{\sqrt{\mathcal{Z}}})}{\sinh(\frac{L}{\sqrt{\mathcal{Z}}})}.$$

And we can write the final problem as,

$$\begin{cases} \partial_t c(x,t) - \mathcal{K}(L-1)\partial_x(\tilde{\theta}(x)c(x,t)) \\ +\frac{\mathcal{PK}}{c_0\sqrt{\mathcal{Z}}}\partial_x(\int_{l_-}^{l_+}\tilde{\phi}(x,y)c(y,t)c(x,t)dx) = \partial_{xx}\hat{c}(x,t) \\ \partial_x c(l_-,t) = \partial_x c(l_+,t) = 0 \\ c(u,0) = c^0(u) \end{cases}$$

where,

$$\tilde{\theta}(x) = -\frac{\sinh(\frac{G-x}{\sqrt{\mathcal{Z}}})}{\cosh(\frac{L}{2\sqrt{\mathcal{Z}}})},$$

and,

$$\tilde{\phi}(x,y) = -\frac{\cosh(\frac{L-x}{\sqrt{\mathcal{Z}}})\sinh(\frac{y}{\sqrt{\mathcal{Z}}}) + H(y-x)\sinh(\frac{L}{\sqrt{\mathcal{Z}}})\cosh(\frac{y-x}{\sqrt{\mathcal{Z}}})}{\sinh(\frac{L}{\sqrt{\mathcal{Z}}})}.$$

As kernel $\tilde{\phi}$ does not include the external effect of boundaries motion, we have the identity,

$$\tilde{\phi}(x,y) = \phi_i(x/L, y/L)$$

The motion of the fronts is given by,

$$\begin{cases} \dot{G} = \frac{\mathcal{KP}}{2c_0\mathcal{Z}} \int_{l_-}^{l_+} \frac{\sinh(\frac{G-x}{\sqrt{\mathcal{Z}}})}{\sinh(\frac{L}{2\sqrt{\mathcal{Z}}})} c(x,t)dx \\ \dot{L} = -2\frac{\mathcal{K}}{\sqrt{\mathcal{Z}}}(L-1)\tanh(\frac{L}{2\sqrt{\mathcal{Z}}}) - \frac{\mathcal{KP}}{c_0\mathcal{Z}} \int_{l_-}^{l_+} \frac{\cosh(\frac{G-x}{\sqrt{\mathcal{Z}}})}{\cosh(\frac{L}{2\sqrt{\mathcal{Z}}})} c(x,t)dx. \end{cases}$$

We may further characterize the kernels by using the asymptotic procedure developed in [152] which enables to distinguish the bulk part from the boundary layers terms. We then define the bulk parts as,

$$\tilde{\Psi}_b(y-x) = \lim_{L\to\infty} \tilde{\Psi}(x+L/2, y+L/2) = \frac{1}{2}\begin{cases} \exp(\frac{x-y}{\sqrt{\mathcal{Z}}}) \text{ if } x-y<0 \\ \exp(\frac{y-x}{\sqrt{\mathcal{Z}}}) \text{ if } x-y>0 \end{cases}$$

and,

$$\tilde{\phi}_b(y-x) = \lim_{L\to\infty} \tilde{\phi}(x+L/2, y+L/2) = \frac{1}{2}\begin{cases} \exp(\frac{x-y}{\sqrt{\mathcal{Z}}}) \text{ if } x-y<0 \\ -\exp(\frac{y-x}{\sqrt{\mathcal{Z}}}) \text{ if } x-y>0. \end{cases}$$

We plot on Fig.3.5 both kernels and their bulk parts.

In [101], authors considered an heuristic analogue of $\tilde{\phi}_b$ which conserves the symmetry of momentum balance in choosing,

$$\tilde{\phi}_h(u) = \frac{1}{2}\text{sign}(u)$$

which is represented along with our mechanical choice on Fig.3.6. The motion of the center of the cell $G(t) = (l_-(t) + l_+(t))/2$ is governed by the equation

$$\dot{G}(t) = \frac{\mathcal{KP}}{2\mathcal{Z}c_0} \int_{l_-(t)}^{l_+(t)} \frac{\text{sh}((G-x)/\sqrt{\mathcal{Z}})}{\text{sh}(L/(2\sqrt{\mathcal{Z}}))} c(x,t)dx. \quad (3.9)$$

It is clear from (3.9) that if the concentration distribution is symmetric then $\dot{G} = 0$ and the cell cannot move, which is a simple analogue of Purcell's theorem [149]. From (3.9) one can also infer that the maximal speed of the cell, equal to $\mathcal{KP}/(2\mathcal{Z})$ which dimensional realistic [82] estimate is $\chi L_0 c_0/(2\eta) \simeq 10\mu m/min$ from data in [25, 89], is achieved when the concentration localizes at the trailing edge as experimentally observed [180].

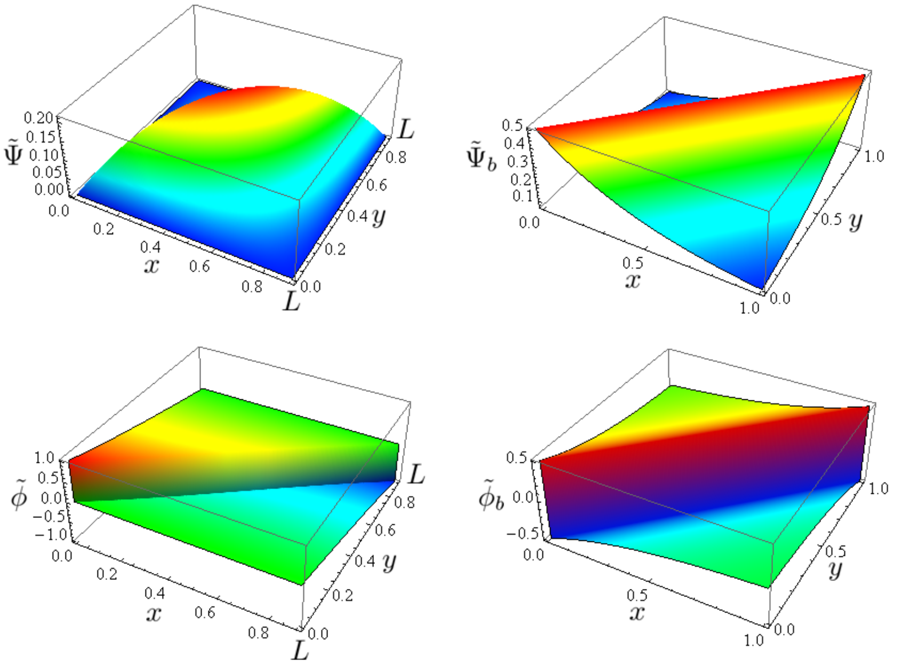

Figure 3.5: Plot of the kernels $\tilde{\Psi}$, $\tilde{\phi}$, $\tilde{\Psi}_b$ and $\tilde{\phi}_b$ for $\mathcal{Z} = 0.25$ and $L = 0.9$ (for the non bulk parts)

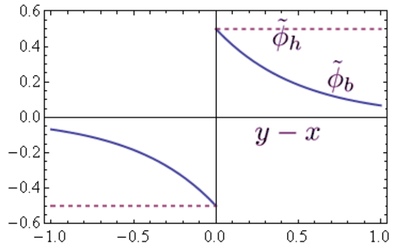

Figure 3.6: Bulk kernels $\tilde{\phi}_b$ (dotted) and $\tilde{\phi}_h$ (dashed) from [101].

3.3 Traveling wave solutions

To study the traveling wave solutions of the system (3.1) we introduce moving coordinate $y = x - Vt$ where V is the cell velocity and assume that $\dot{l}_\pm = V$ and $L(t) = L$. System (3.1) reduces to a single equation

$$-\mathcal{Z}s'' + s - \mathcal{K}(L-1) = \mathcal{K}\mathcal{P}\frac{\exp(s - Vy)}{\int_0^L \exp(s - Vy)dy} \tag{3.10}$$

where $s(y) = \mathcal{K}\left[\sigma(y) + (L-1)\right]$ is the unknown function. The presence of four boundary conditions, $s(0) = s(L) = 0$ and $s'(0) = s'(L) = V$, makes the problem overdetermined and ensures that both parameters V and L can be found along with $s(y)$. After equation (3.10) is solved the motor concentration profile can be recovered from relation

$$c(y) = c_0 \exp(s(y) - Vy)/[\int_0^L \exp(s(y) - Vy)dy]. \tag{3.11}$$

To simplify the description we assume, if not mentioned otherwise, that $\mathcal{Z} = 1$ [89] which means that the elastic and the viscous scales in a cell are correlated. We are then left with two dimensionless parameters $\mathcal{K} \sim 100$ and $\mathcal{P} \sim 0.1$ [71, 89], where $\mathcal{K}$ is the measure of internal stiffness while $\mathcal{P}$ gives the scale of total motor activity. If the cell is rigid , $k \to \infty$ (fixed cell length), we have $\mathcal{K} \to \infty$ and $\mathcal{P} \to 0$ and it is more convenient to restore $\mathcal{Z}$ and use as a dimensionless parameter the surviving product $\mathcal{KP}$ which is proportional to the contraction-based Peclet number $\chi/(D\xi)$ introduced in [25, 71, 78].

3.4 Non motile solutions

Initiation of motility is associated with an instability of a non motile solution of (3.10) with $V = 0$. Although none of these solutions describe the overall motion of the cell (motility), most of them involve active internal flow of both actin and myosin and are therefore not fully static. We also distinguish between regular solutions described by smooth functions and singular solutions, measure-valued corresponding to collapsed cells and requiring for their understanding further regularization of the model. Regular solutions of Eq.3.10 have been previously studied in [25] and we contribute to this analysis with some important details in that we do not consider periodic boundary conditions, expose the bifurcation structure fully and present the singular solutions.

3.4.1 Regular solutions

At $V = 0$ the boundary value problem for Eq.(3.10) with $\mathcal{Z} = 1$ has the form:

$$\begin{cases} -s'' + s - \mathcal{K}(L-1) = \mathcal{KP}\frac{\exp(s)}{\int_0^L \exp(s)} \\ s(0) = s(L) = 0 \\ s'(0) = 0. \end{cases} \tag{3.12}$$

Multiplying $(3.12)_1$ by s' and integrating over the domain, one can show that the remaining boundary condition, $s'(L) = 0$, is satisfied automatically. The ensuing problem

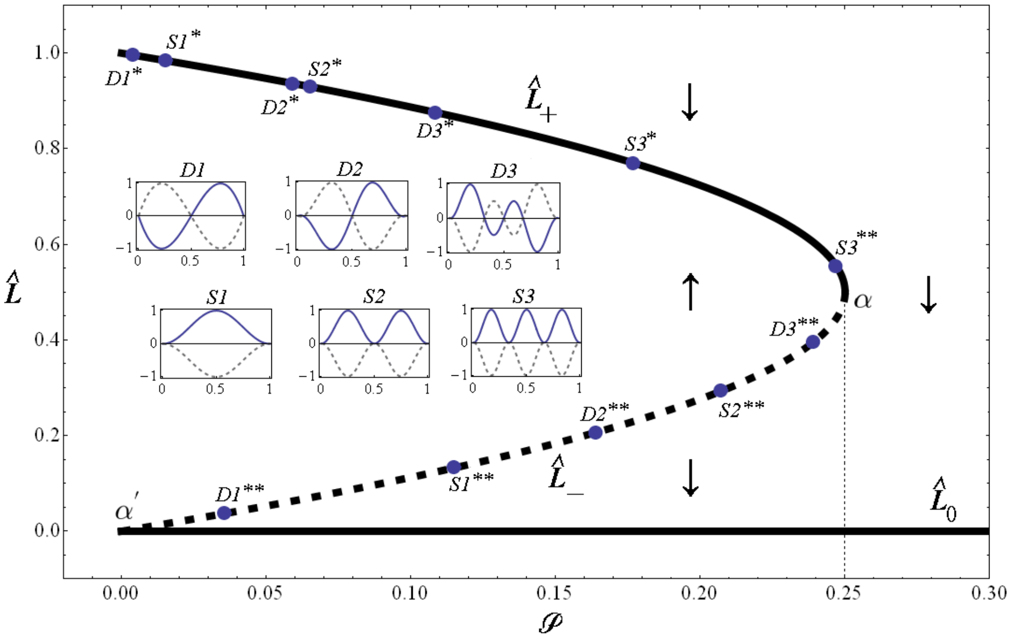

Figure 3.7: Three families of the trivial non motile solutions ($\hat{L}_+, \hat{L}_-$ and $\hat{L}_0$ parametrized by $\mathcal{P}$ at $\mathcal{K} = 2600$. The bifurcation points are labelled as $D1, D2, ...$, when the nontrivial bifurcated solution is motile ($\delta V \neq 0$) and by $S1, S2, ...$ when it is non motile ($\delta V = 0$). Inserts show the eigenfunctions $\delta s(y/L)$. In the inserts solid and dashed lines distinguish eigenfunctions with positive and negative amplitudes (δL or δV).

is not over determined because the parameter L is one of the unknowns. Trivial solutions (See Fig.3.7) of this equation are defined by $s(y) = 0$ and

$$\hat{L}_{\pm} = (1 \pm \sqrt{1 - 4\mathcal{P}})/2, \tag{3.13}$$

Patterns emerging from solving a problem closely related to (3.12) were considered in [25] where parameter L was assumed to be known and boundary conditions were periodic $s(0) = s(L)$ (dropping the condition $s(0) = 0$). This is a special case of our general problem 3.10 which is obtained by considering an infinitely stiff spring with $k \to \infty$ which ensures that $L \to L_0$ and periodic boundary conditions. To obtain this limit we need to consider $\mathcal{Z}$ as the first non-dimensional parameter of the problem and require that $\mathcal{K} \to \infty$ and $\mathcal{P} \to 0$ with the product $\mathcal{K}\mathcal{P}$ remaining finite. The contraction-based Peclet number $\mathcal{K}\mathcal{P}/c_0 = \chi/(D\xi)$ is then a natural second non-dimensional parameter of the problem [25]. Going back to our problem with $\mathcal{Z} = 1$ we observe that it also depends on two non-dimensional parameters, $\mathcal{K}$ and $\mathcal{P}$, which are however different.

Instead of dealing directly with parameters $\mathcal{K}$ and $\mathcal{P}$ it is more convenient to use another set of parameters $A = \mathcal{K}(L-1) < 0$ and $B = \frac{\mathcal{K}\mathcal{P}}{\int_0^L \exp(s(y))dy} > 0$. The problem can then be formulated as,

$$\begin{cases} -s^{''} + s - A = B\exp(s) \\ s(0) = s(L) = 0 \\ s^{'}(0) = 0 \end{cases} \tag{3.14}$$

Then, if s is a trivial solution (constant solution) then $s = 0$ which implies that $A + B = 0$. Length cannot be explicitly computed but we can map all the trivial solutions $(\hat{L}_{-}, \hat{L}_{+}, \hat{L}_0)$ presented on Fig.3.7 in the $(A/\mathcal{K}, B/\mathcal{K})$ space as these solutions clearly not depend on the value of $\mathcal{K}$. (See Fig.3.8)

Otherwise, if s is not uniformly zero, by integrating $(3.14)_1$ and using the boundary conditions we obtain the 'energy integral' $(s^{'})^2 = W(s)$ where the potential has the form $W(s) = s^2 - 2As - 2B(\exp(s) - 1)$. Of course, this potential is not related to the real mechanical energy of the problem which is,

$$E(s) = \int_0^L \left[\frac{(s^{'}(y))^2 + s(y)^2}{2} - \mathcal{K}(L-1)s(y) \right] dy - \mathcal{K}\mathcal{P}\log(\int_0^L \exp(s(y))dy).$$

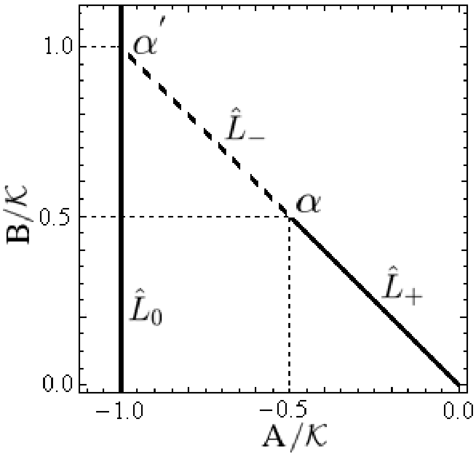

Figure 3.8: Trivial solutions (See Fig.3.7) in the parameter space $(A/\mathcal{K}, B/\mathcal{K})$

As we shall see further on, if we fix parameters $\mathcal{K}$ and $\mathcal{P}$, then we can find uniquely the unknowns, $s(y)$ and L provided we choose an integer m and two spin variables ±

and $'$ corresponding to $Sm^{\pm}$ and $(Sm^{\pm})'$ (See Fig.3.12). ± corresponds to a bifurcation from the $\hat{L}_{\pm}$ branch while m indexes the bifurcation point and is related to the number of identical patterns observed in s. At last the index $'$ differentiates the two segment of each bifurcation branch. In this section, we shall see that at fixed A and B, the problem also has a uniquely defined solution (s,L) provided m is fixed. The difference between branches ± is absent in this parametrization since as mentioned, the static problem cannot be fully resolved in the (A, B) space as length remains arbitrary (See Fig.3.8).

Nontrivial solutions can be written as formal quadratures (see also [25])

$$y = \pm \int^{s(y)} W^{-1/2}(u)du + const.$$

They correspond to closed trajectories on the phase plane (s, s') passing through the point $s = 0, s' = 0$. Different types of these trajectories are shown in Fig.3.9. We first link three different types of static solutions to the number of roots of the equation

$$W(u) = 0. \tag{3.15}$$

Depending on the point in the parametric plane A, B, we can identify five types of behaviors

1. $A + B = 0$, (3.15) has one double root at $u = 0$ and one single root (negative or positive) at $u = s_-$ (Case 3 on Fig.3.9). Then the solution is trivial $s = 0$, see (3.12) and the length cannot be resolved in this parametrization as there is no mapping between values taken by s and space values y.

2. if $A + B < 0$ (3.15) has three roots: $u = 0$, $u = s_- < 0$ and $u = s_+ > 0$. This case corresponds to non motile branches labelled without a $'$ on Fig.3.12 and 3.13 (Case 1 on Fig.3.9). In this domain we find nontrivial static solutions with $0 \leq s(y) \leq s_+$. Different solutions correspond to different numbers (m) of sign changing for the function $s(y)$ and different values of $L = 2m \int_0^{s_+} \text{sign}(\sigma) W(\sigma)^{-\frac{1}{2}} d\sigma$.

3. if
$$\begin{cases} A + B > 0 \\ 1 - \sqrt{A^2 - 2B + 1} < Be^{-\sqrt{A^2-2B+1}+A+1} \\ A < -1. \end{cases} \tag{3.16}$$
(3.15) has three roots: $u = 0$ and $u = s_- < 0$ and $u = s_+ < 0$ with, $s_+ > s_-$. This case corresponds to non motile branches labelled with a $'$ on Fig.3.12 and 3.13

(Case 2 on Fig.3.9). In this domain we find nontrivial static solutions with $s_- \leq s(y) \leq 0$. Again, different solutions correspond to different numbers of sign changing for the function $s(y)$ and different values of $L = 2m\int_0^{s_+} \text{sign}(\sigma)W(\sigma)^{-\frac{1}{2}}d\sigma$.

4. if,

$$\begin{cases} A+B>0 \\ 1-\sqrt{A^2-2B+1} < Be^{-\sqrt{A^2-2B+1}+A+1} \\ A>-1. \end{cases} \tag{3.17}$$

   then (3.15) has three roots: $u = 0$ and $u = s_- > 0$ and $u = s_+ > 0$ with, $s_+ > s_-$ and there is no non motile solution since there is no closed paths in the phase plane passing by point $(0, 0)$.

5. if $1-\sqrt{A^2-2B+1} > Be^{-\sqrt{A^2-2B+1}+A+1}$, (3.15) has only one non degenerate root at $u = 0$. Then there is no non motile solutions again since there is no closed paths in the phase plane at all.

One can see that depending on the number of rotations in the phase plane which we indexed by the integer m, we obtain different families of nontrivial static solutions branching from the family of trivial solutions. In the $(\mathcal{K}, \mathcal{P})$ parametrization, at fixed $\mathcal{P}$, the corresponding bifurcation points on the $\hat{L}_+$ branch of trivial solutions are identified as S_m^+ (e.g. S_1^+, S_2^+...) and on the $\hat{L}_-$ branch correspondingly as S_m^- (e.g. S_1^-, S_2^-...). The parameter L for each of these nontrivial solution can be computed explicitly

$$L = 2m\int_0^{s_+} \text{sign}(\sigma)W(\sigma)^{-\frac{1}{2}}d\sigma,$$

where $s_+(A, B)$ is always the largest root of the equation $W(s) = 0$. This formula does not hold for the trivial case though because there is no mapping between space coordinate and values of s in this case. Along these equilibrium branches one can establish a direct link between parameters A, B and $\mathcal{P}, \mathcal{K}$:

$$\begin{cases} \mathcal{K} = \frac{A}{2m\int_0^{s_+(A,B)} \text{sign}(\sigma)W_{A,B}(\sigma)^{-1/2}d\sigma - 1} \\ \mathcal{K}\mathcal{P} = 2m\int_0^{s_+(A,B)} (\sigma - A\ \text{sign}(\sigma))W_{A,B}(\sigma)^{-1/2}d\sigma \end{cases} \tag{3.18}$$

At fixed $\mathcal{P}$ (See Fig.3.12 and Fig.3.10), the corresponding bifurcation points (see section 3.5) can be found explicitly (see Fig.3.9).

$$\begin{cases} A_m = -1 - \frac{4m^2\pi^2}{\hat{L}(\mathcal{P})^2} < -1 \\ B_m = 1 + \frac{4m^2\pi^2}{\hat{L}(\mathcal{P})^2} > 1 \end{cases} \tag{3.19}$$

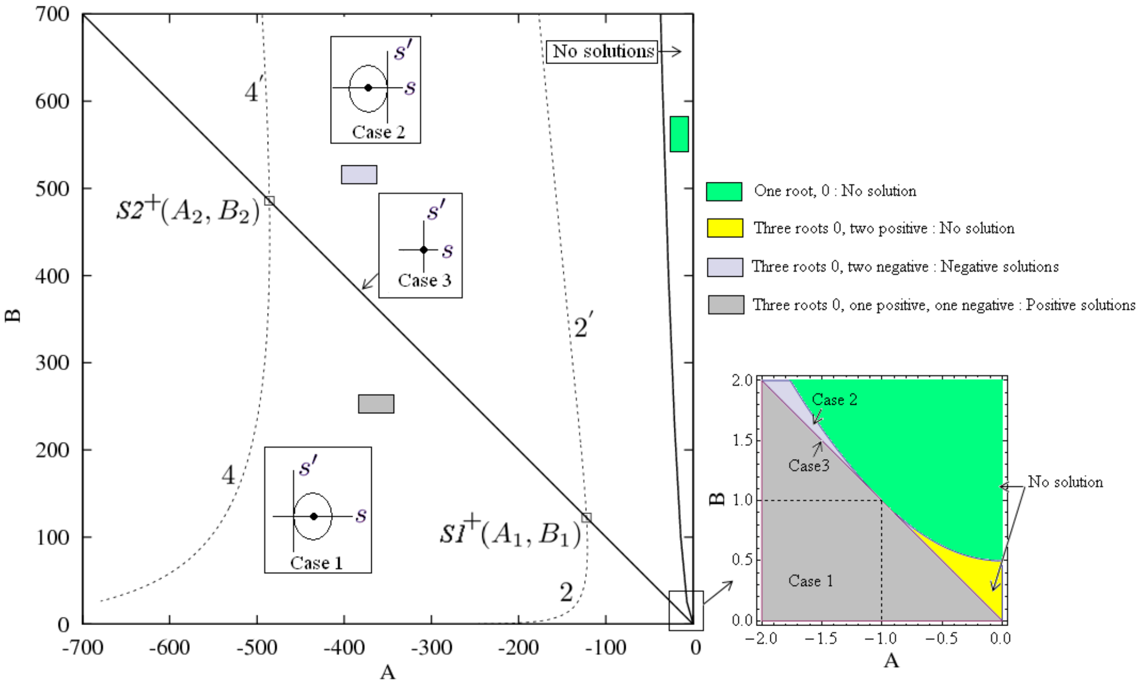

Figure 3.9: Behavior of non motile solutions in the parameter space (A, B). Labels and bifurcation points at fixed $\mathcal{P} = 0.245$ for the $\hat{L}_+$ branch are associated to Fig.3.12, Fig.3.13 and Fig.3.10. In bottom right corner we represent in more details the locus of roots of potential W.

In fact, our access to explicit solutions allows to say much more about the nature of the corresponding bifurcated branches. Thus, near the bifurcation points (near the line $A+B=0$) where $s \simeq 0$ the solutions can be captured by using an approximate potential

$$W_a(s) = s^2 - 2As - 2B(s + \frac{s^2}{2} + \frac{s^3}{6}).$$

Then

$$W_a(s) = \frac{Bs}{3}(s_+ - s)(s - s_-)$$

where,

$$s_- = \frac{3}{2B}\left(1 - B - \sqrt{\Delta}\right), s_+ = \frac{3}{2B}\left(1 - B + \sqrt{\Delta}\right)$$

and,

$$\Delta = (1 - B)^2 - \frac{8Be}{3}.$$

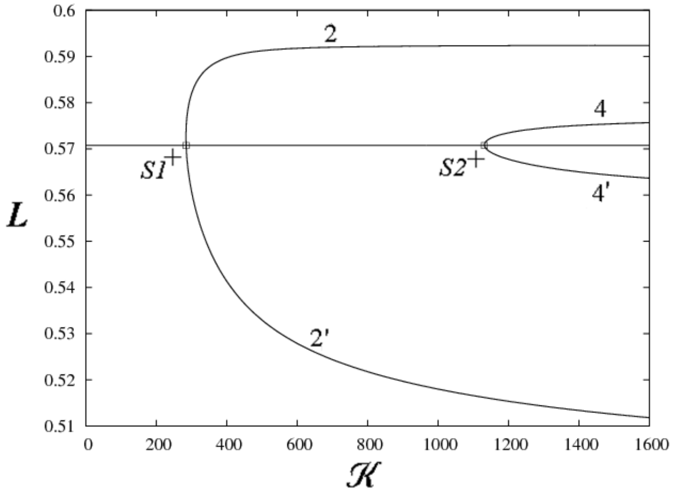

Figure 3.10: Bifurcation diagram from the $\hat{L}_+$ branch of the static problem (3.12) at fixed $\mathcal{P} = 0.245$ (See also Fig.3.12)

Here we have set $e = A + B << 1$. Even in this asymptotic regime all our four regimes are present:

1. if $e = 0$ the potential $W_a(u)$ has a double root 0 and a negative or positive root s_-. (trivial solution)
2. if $e < 0$, the potential $W_a(u)$ has three roots: $u = 0$, $u = s_- < 0$ and $u = s_+ > 0$. (positive solutions)
3. if $e > 0$, $(1 - B)^2 > \frac{8Be}{3}$ and $A < -1$ then $W_a(u)$ has three roots: $u = 0$ and $u = s_- < 0$ and $u = s_+ < 0$ with, $s_+ > s_-$. (negative solutions)
4. if $e > 0$, $(1 - B)^2 > \frac{8Be}{3}$ and $A > -1$ then $W_a(u)$ has three roots: $u = 0$ and $u = s_- > 0$ and $u = s_+ > 0$ with, $s_+ > s_-$. (no solution, the closed trajectory does not passes by point $(0, 0)$)
5. otherwise, the potential has only one root $u = 0$. (no solution, no closed trajectory)

It is easy to see from (3.19) that bifurcations can take place only in the domain where $B > 1$ (and $A < -1$). If we now introduce the complete elliptic integral of the first kind

$$K(x) = \int_0^1 \frac{1}{\sqrt{1 - u^2}\sqrt{1 - x^2 u^2}} du,$$

and the complete elliptic integral of the second kind

$$E(x) = \int_0^1 \frac{\sqrt{1-x^2u^2}}{\sqrt{1-u^2}} du,$$

we can rewrite the first integral term from (3.18) in the form:

$$\int_0^{s_+} \operatorname{sign}(\sigma) W_a(\sigma)^{-1/2} d\sigma = \sqrt{\frac{12}{B(s_+ - s_-)}} K\left(\sqrt{\frac{s_+}{s_+ - s_-}}\right)$$

when $s_+ > 0$ and

$$\int_0^{s_+} \operatorname{sign}(\sigma) W_a(\sigma)^{-1/2} d\sigma = \sqrt{\frac{12}{B|s_-|}} K\left(\sqrt{\frac{s_+}{s_-}}\right).$$

when $s_+ < 0$. We can also write the second integral from (3.18) in the form

$$\int_0^{s_+} \sigma W_a(\sigma)^{-1/2} d\sigma = \sqrt{\frac{12|s_-|}{B}} \left(E\left(\frac{s_+}{s_-}\right) - K\left(\frac{s_+}{s_-}\right)\right).$$

By expanding in e, we obtain

$$\int_0^{s_+} \operatorname{sign}(\sigma) W_a(\sigma)^{-1/2} d\sigma = \frac{\pi}{\sqrt{B-1}} + O(e^2)$$

and,

$$\int_0^{s_+} \sigma W_a(\sigma)^{-1/2} d\sigma = \frac{\pi e}{(B-1)^{3/2}} + O(e^2).$$

Then up to higher order terms we can rewrite equations (3.18) as

$$\begin{cases} \mathcal{K} = \frac{B}{\frac{2m\pi}{\sqrt{B-1}}-1} + \frac{e}{1-\frac{2m\pi}{\sqrt{B-1}}} + O\left(e^2\right) \\ \mathcal{K}\mathcal{P} = -\frac{2m\pi B}{\sqrt{B-1}} + \frac{2m\pi B e}{(B-1)^{3/2}} + O\left(e^2\right). \end{cases}$$

In particular, we can in the limit $e = 0$

$$\begin{cases} -\frac{2m\pi}{\sqrt{B_m-1}}\left(\frac{2m\pi}{\sqrt{B_m-1}} - 1\right) = \mathcal{P} \\ A_m + B_m = 0 \end{cases}$$

From these equations we obtain the location of the bifurcation points on the (A, B) plane (see Section 3.5)

$$\begin{cases} A_m = -1 - \frac{4m^2\pi^2}{\hat{L}(\mathcal{P})^2} < -1 \\ B_m = 1 + \frac{4m^2\pi^2}{\hat{L}(\mathcal{P})^2} > 1. \end{cases} \tag{3.20}$$

which coincide with the expressions for A_m and B_m obtained from the analysis of the linearized problem (3.25) in the static case. This proves consistency of our perturbation approach.

3.4.2 Singular solutions.

From Fig.3.7, it is clear that when $\mathcal{P}$ approaches 0, the function $\hat{L}_{-}(\mathcal{P})$ also approaches 0 (Point $\alpha^{'}$). This suggests that in addition to nonsingular non motile configurations considered above, the system (3.12) allows for singular, measure-valued solutions concentrated on an infinitely small domain. Such solutions (of similar equations) are known in other fields from turbulence to astrophysics, see for instance [32, 45, 67, 132] and the references therein. Such concentration phenomenon is not a mathematical curiosity but a sign that in the properly regularized theory one can expect to see localized solutions describing the cells that are collapsed under the action of contractile forces.

To describe asymptotic solutions of (3.12) with disappearing length, we first map the problem onto a fixed domain $[0,1]$ by using the change of coordinates $y = Lu$. Then we obtain an equivalent formulation which explicitly depends on L

$$\begin{cases} -s^{''}/L^2 + s - \mathcal{K}(L-1) = \mathcal{K}\mathcal{P}\frac{\exp(s)}{L\int_0^1 \exp(s(u))du} \\ s(0) = s(1) = 0 \\ s^{'}(0) = 0. \end{cases} \tag{3.21}$$

Suppose now that $L << 1$ and that the maximum of s is of order L which will be confirmed post factum. Then, by ignoring high order terms, we obtain from (3.21) a simplified boundary value problem

$$\begin{cases} -s^{''} = \frac{\mathcal{K}\mathcal{P}L}{\int_0^1 (1+s(u))du} \\ s(0) = s(1) = 0 \\ s^{'}(0) = 0. \end{cases} \tag{3.22}$$

If we now define $I = \int_0^1 (1 + s(u))du$, we can solve the problem (3.22) with the first two boundary conditions explicitly

$$s(u) = \frac{\mathcal{K}\mathcal{P}}{2I} Lu(1-u).$$

Notice that by definition

$$I^2 - I - \frac{\mathcal{K}\mathcal{P}}{12} L = 0,$$

which implies that, up to first order, $I = 1$ and we can write the above solution in the form

$$s(u) = \frac{\mathcal{K}\mathcal{P}}{2} Lu(1-u).$$

Observe now that the remaining boundary condition $s^{'}(0) = 0$ is automatically satisfied by this function in the limit $L \to 0$. This observation suggests that the measure-valued singular solution $s(y)$ must be necessarily of the form:

$$s(y) = \lim_{r \to 0} r f(y/r)$$

where,

$$f(u) = \frac{\mathcal{K}\mathcal{P}}{2} u(1-u) \text{ and } u \in [0,1].$$

Our numerical simulations of a non-steady problem with initial data (See section3.6), which are naturally regularized because of a finite mesh size, show that these singular solutions are indeed attractors for initial data with $L < \hat{L}_-$ when $\mathcal{P} < 1/4$. Moreover, our numerical experiments suggest that global attractors are the only attractors for $\mathcal{P} > 1/4$ which means that after a critical concentration of motors is reached, the cell necessarily collapses.

3.5 Motile bifurcation from trivial non motile states

We fist show that the nonlinear equation (3.10) has an integral which we used to show that motile solutions of Eq. (3.10) can bifurcate only from the trivial non motile solutions of this equation with $s(y) = 0$ and $L = \hat{L}_\pm$.

Notice first that the integral of s can be computed explicitly by integration of (3.10) over the domain:

$$\int_0^L s(y)dy = \mathcal{K}(L(L-1) + \mathcal{P}).$$

In view of the mechanical analogy it is obvious that Eq.(3.10) has an other (energy) integral. Indeed, let us rewrite Eq.(3.10) in the form:

$$\begin{cases} -\mathcal{Z}s^{''} + s - \mathcal{K}(L-1) = \mathcal{K}\mathcal{P}h^{'} \\ h^{''} - (s^{'} - V)h^{'} = 0 \\ s(0) = s(L) = 0 \\ h(0) = 0 \text{ and } h(L) = 1 \end{cases}$$

If we now multiply the first equation by $s^{'}$ and replace $h^{'}$ in the right hand side by using the second equation we obtain,

$$-\mathcal{Z}s^{''}s^{'} + ss^{'} - \mathcal{K}(L-1)s^{'} = \mathcal{K}\mathcal{P}(h^{''} + Vh^{'})$$

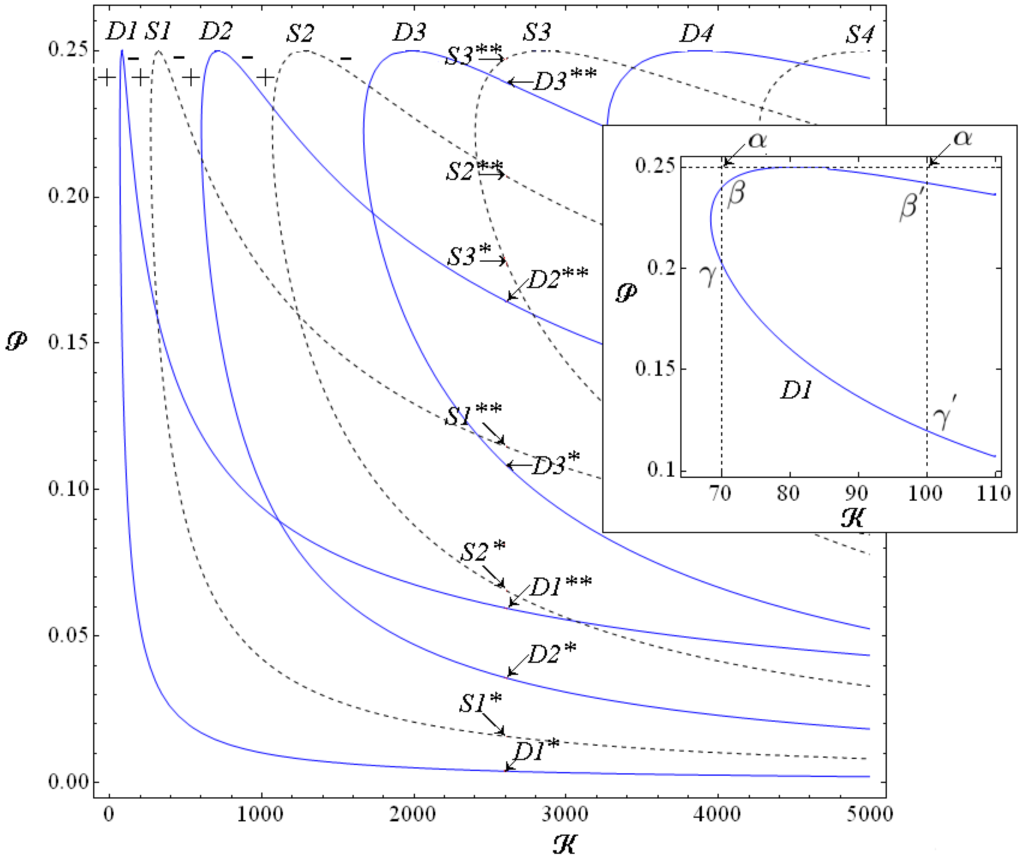

Figure 3.11: Locus of the bifurcation points in the $(\mathcal{K}, \mathcal{P})$ plane. Insert shows a zoom on the $D1$ branch around the turning point at $\mathcal{P} = 1/4$. The detailed bifurcation diagrams for $\mathcal{K} = 2600$ and $\mathcal{P} = 0.245$ are shown in Fig.3.7 and Fig.3.12 from where the meaning of the different labelling becomes clear.

By integrating this equation over the whole domain and using boundary conditions we get,

$$h^{'}(0) - h^{'}(L) = V.$$

As we have,

$$h^{'}(y) = \frac{\exp(s(y) - Vy)}{\int_0^L \exp(s(y) - Vy)dy},$$

we write,

$$1 - \exp(-VL) = V \int_0^L \exp(s(y) - Vy)dy,$$

which in the limit $V \to 0$ gives

$$\int_0^L \exp(s) = L.$$

Since in non-motile solutions $s(y)$ must necessarily have a constant sign (See 3.4.1), this integral implies that $s(y) = 0$ and hence such non motile solutions must be trivial. As we show in Fig.3.7 there are two families of non-singular trivial solutions: with longer ($\hat{L}_+$ family) and shorter ($\hat{L}_-$ family) lengths.

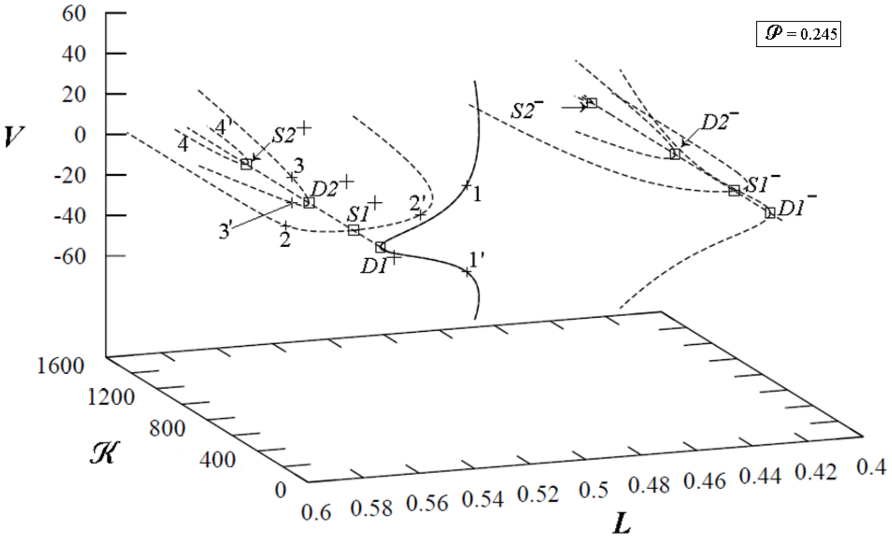

Figure 3.12: Bifurcation diagram with $\mathcal{K}$ as a parameter showing nontrivial solutions branching from the non motile families $\hat{L}_+$ and $\hat{L}_-$. The value $\mathcal{P} = 0.245$ is fixed. Solid lines show stable motile branches while all the dotted lines correspond to unstable solutions. The internal configurations corresponding to branches indicated by numbers $(1, 1', 2, 2', etc)$ are shown in Fig.3.13.

Our starting point is the nonlinear boundary value problem (3.10). We choose a trivial solution with $s(y) = 0$, $V = 0$ and $L = \hat{L}(\mathcal{P})$ and linearise the problem around this solution. More specifically we consider the following expansion

$$\begin{cases} s = 0 + \delta s + ... \\ V = 0 + \delta V + ... \\ L = \hat{L} + \delta L + ... \end{cases}$$

where the perturbations $\delta s(y)$, δV and δL are assumed to be small. By substituting

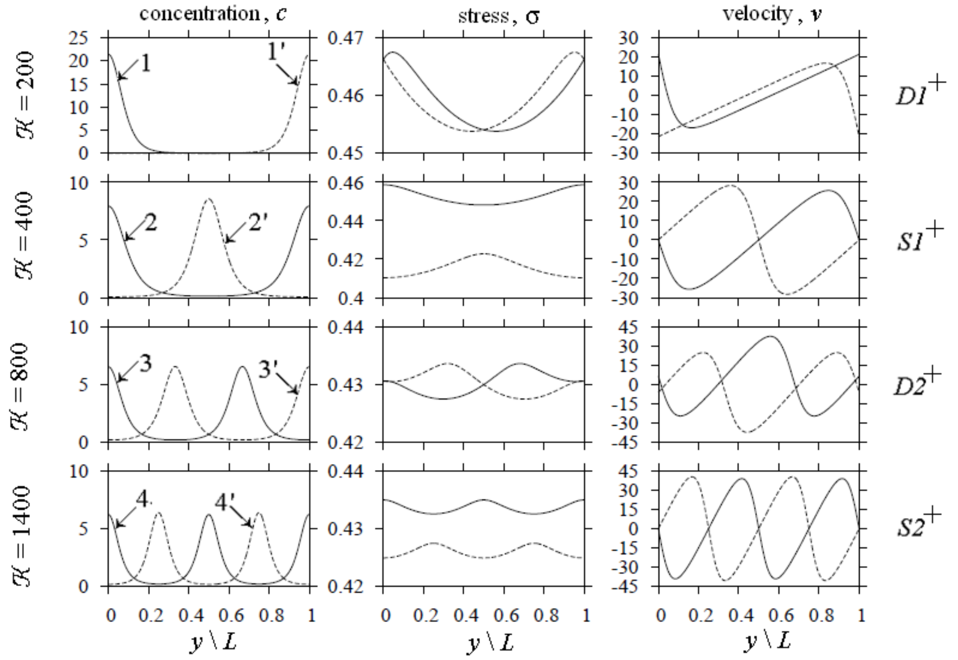

Figure 3.13: Internal profiles associated with successive bifurcated solutions shown in Fig.3.12 for $\mathcal{P} = 0.245$: (1,3) correspond to asymmetric motile branches while (2,4) describe symmetric non motile branches.

these expansions into Eq.3.10 we obtain,

$$\delta s'' - \omega^2 \delta s = \frac{\mathcal{Z}\omega^2 - \hat{L}^2}{\hat{L}^2(\hat{L}-1)} \left(\mathcal{Z}\frac{2\hat{L}-1}{\hat{L}}\omega^2 \delta L + \frac{\hat{L}^3(\hat{L}-1)}{2}(2u-1)\delta V \right), \tag{3.23}$$

where we have introduced a new parameter

$$\omega^2 = \frac{\hat{L}^2 - \mathcal{K}\mathcal{P}\hat{L}}{\mathcal{Z}}.$$

The general solution of the linear equation (3.23) can be written as,

$$s(u) = C_1 \exp(-\omega u) + C_2 \exp(-\omega u) - \frac{\mathcal{Z}\omega^2 - \hat{L}^2}{\omega^2 \hat{L}^2(\hat{L}-1)} \left(\mathcal{Z}\frac{2\hat{L}-1}{\hat{L}}\omega^2 \delta L + \frac{\hat{L}^3(\hat{L}-1)}{2}(2u-1)\delta V \right).$$

To find the four constants $C_1, C_2, \delta L$ and δV, we need to use the four boundary conditions, $\delta s(0) = \delta s(1) = 0$, $\delta s^{'}(0) = \delta s^{'}(1) = \hat{L}\delta V$ which also serve for the determination of δV and δL. As a result we obtain a system of four linear equations with zero right hand side. This algebraic problem has a non trivial solutions when the matrix

$$\begin{pmatrix} 1 & 0 & \frac{(2\hat{L}-1)\left(\hat{L}^2-\omega^2\mathcal{Z}\right)}{(\hat{L}-1)\hat{L}^3} & \frac{1}{2}\hat{L}\left(\frac{\hat{L}^2}{\omega^2\mathcal{Z}}-1\right) \\ \cosh(\omega) & \sinh(\omega) & \frac{(2\hat{L}-1)\left(\hat{L}^2-\omega^2\mathcal{Z}\right)}{(\hat{L}-1)\hat{L}^3} & \frac{1}{2}\hat{L}\left(1-\frac{\hat{L}^2}{\omega^2\mathcal{Z}}\right) \\ 0 & \omega & 0 & -\frac{\hat{L}^3}{\omega^2\mathcal{Z}} \\ \omega\sinh(\omega) & \omega\cosh(\omega) & 0 & -\frac{\hat{L}^3}{\omega^2\mathcal{Z}} \end{pmatrix} \tag{3.24}$$

degenerates. Since $\omega = 0$ corresponds to a trivial solution we can always assume that $\omega \neq 0$. By putting the determinant of (3.24) equal to zero we obtain the characteristic equation

$$2\frac{\hat{L}^2}{\mathcal{Z}}\left(\cosh(\omega)-1\right)-\left(\frac{\hat{L}^2}{\mathcal{Z}}-\omega^2\right)\omega\sinh(\omega)=0.$$

The solutions of this equation can be split into two families depending on whether parameter ω is real or purely imaginary. In the first case we use notation $\omega_c = \mathrm{Re}(\omega)$ and in the second case we denote $\omega_c = \mathrm{Im}(\omega)$. Then we can write

$$\begin{cases} 2\frac{\hat{L}^2}{\mathcal{Z}}(\cosh(\omega_c)-1)+(\omega^2-\frac{\hat{L}^2}{\mathcal{Z}})\omega_c\sinh(\omega_c)=0 \text{ if } \omega^2>0 \\ 2\frac{\hat{L}^2}{\mathcal{Z}}(\cos(\omega_c)-1)+(\frac{\hat{L}^2}{\mathcal{Z}}+\omega_c^2)\omega_c\sin(\omega_c)=0 \text{ if } \omega^2<0. \end{cases} \tag{3.25}$$

It will be convenient to analyse the two equations $(3.25)_1$ and $(3.25)_2$ separately,

1. When $\omega^2 > 0$, the equation $(3.25)_1$ has one unique solution provided

   $$\frac{\hat{L}^2}{\mathcal{Z}} \geq 12.$$

   Otherwise, it has no solution. The corresponding eigenvector can be written as,

   $$\begin{pmatrix} \delta L \\ \delta V \\ \delta s(u) \end{pmatrix} = \begin{pmatrix} 0 \\ 1 \\ \frac{\hat{L}^2}{\mathcal{Z}\omega_c^3\cosh(\omega_c/2)}\left(\sinh\left(\left(u-\frac{1}{2}\right)\omega_c\right)-(2u-1)\sinh\left(\frac{\omega_c}{2}\right)\right) \end{pmatrix}.$$

   Since $\delta V \neq 0$ it is clear that the corresponding bifurcation leads to a motile configuration of the cell that we denote $D1^{\pm}$. (See Fig.3.14 where the eigenfunction related to $D1^{+}$ is shown for $\mathcal{Z} = 0.01$.)

2. When $\omega^2 < 0$, the equation $(3.25)_2$ has the following two families of solutions

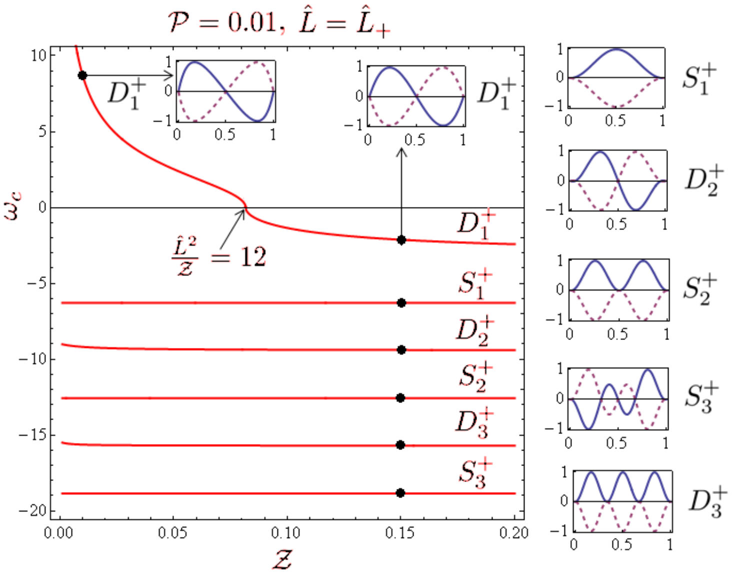

Figure 3.14: locus of critical bifurcation points from the $\hat{L}_+$ branch ω_c as a function of $\mathcal{Z}$ for $\mathcal{P} = 0.01$. We refer to Fig.3.12 for the label of bifurcation points. We represent in inserts the eigenfunctions δs related to $D1^+, S1^+, D2^+, S2^+, D3^+, S3^+$ for $\mathcal{Z} = 0.15$ and the eigenfunction δs related to $D1^+$ for $\mathcal{Z} = 0.01$. The eigenfunctions are normalized at 1 and solid and dashed lines correspond to the two possible directions of the pitchfork.

(a) The first family can be given explicitly $\omega_c = -2m\pi$ with $m \geq 1$. The associated eigenvector-vector has the form

$$\begin{pmatrix} \delta L \\ \delta V \\ \delta s(u) \end{pmatrix} = \begin{pmatrix} 1 \\ 0 \\ \frac{(2\hat{L}-1)(\mathcal{Z}\omega_c^2+\hat{L}^2)}{\hat{L}^3(\hat{L}-1)}\left(\cos(\omega_c u) - 1\right) \end{pmatrix}.$$

Since $\delta V = 0$ the bifurcated solution describes non motile cell. We denote this family $Sm^{\pm}$ (See Fig.3.14 where the eigenfunction related to Sm^+ is shown for $\mathcal{Z} = 0.15$.). The corresponding critical values of parameters $\mathcal{K}, \mathcal{P}$ have been found in section 3.4.1 by a direct method where we could also study the nature of the bifurcation in more details. The fact, the values are the same is easily check from the computation (done at $\mathcal{Z} = 1$),

$$\omega_c^2 = \hat{L}^2 - \mathcal{K}\mathcal{P}\hat{L} = \hat{L}^2 - \frac{A_m \mathcal{P}\hat{L}}{\hat{L} - 1}$$

as $\mathcal{P} = -\hat{L}(\hat{L}-1)$ and $A_m = -1 - \frac{4m^2\pi^2}{\hat{L}^2}$ we find,

$$\omega_c^2 = -4m^2\pi^2$$

and,

$$\omega_c = -2m\pi.$$

(b) The second family consists of a countable set of negative roots of the equation

$$2\frac{\hat{L}^2}{\mathcal{Z}}\tan(\frac{\omega_c}{2}) = (\frac{\hat{L}^2}{\mathcal{Z}} + \omega_c^2)\omega_c \tag{3.26}$$

The largest root exists only if

$$\frac{\hat{L}^2}{\mathcal{Z}} \leq 12$$

and connects smoothly with the $\omega_c^2 > 0$ branch discussed above (See Fig.3.14). The corresponding eigenvector has the form

$$\begin{pmatrix} \delta L \\ \delta V \\ \delta s \end{pmatrix} = \begin{pmatrix} 0 \\ 1 \\ \frac{\hat{L}^2}{\mathcal{Z}\omega_c^3\cos(\omega_c/2)}\left(\sin\left(\left(u-\frac{1}{2}\right)\omega_c\right) - (2u-1)\sin\left(\frac{\omega_c}{2}\right)\right) \end{pmatrix}.$$

These roots of the characteristic equation are associated with motile branches because $\delta V \neq 0$. We denote this family $Dm^{\pm}$ (See Fig.3.14 where the eigenfunction related to Dm^{+} is shown for $\mathcal{Z} = 0.01$.)

The bifurcation points correspond to $\mathcal{Z} = 1$ section of our Fig.3.14.

Our numerical study of the post-bifurcation behavior for the solutions of Eq.3.10 shows that all these bifurcations are supercritical.

The above analysis holds for both trivial branches $\hat{L}_+$ and $\hat{L}_-$ which both leads to the same bifurcations structure (See Fig.3.12) with different values of bifurcation points. For instance, at $\mathcal{P}$ and $\mathcal{Z}$ given, the two families of bifurcation points are characterized by different values of $\mathcal{K}$. In particular , for the branch $\hat{L}_+$ we have $\mathcal{K} = \frac{-\mathcal{Z}\omega_c^2+\hat{L}_+^2}{\mathcal{P}\hat{L}_+}$, giving the points identified in Fig.3.12 as $D1^+, S1^+, D2^+, S2^+$ and for the branch $\hat{L}_-$ we need to take $\mathcal{K} = \frac{-\mathcal{Z}\omega_c^2+\hat{L}_-^2}{\mathcal{P}\hat{L}_-}$ giving the points $D1^-, S1^-, D2^-, S2^-$ also shown in Fig.3.12. Only for illustrations purposes we have used $\hat{L} = \hat{L}_+$ as we shall see in section 3.6 that it corresponds to the stable case.

The locus of the bifurcation points in the parameter plane $(\mathcal{P}, \mathcal{K})$ is shown in Fig.3.11. Each branch (say, $D1$) is represented by two parts ($D1^{+}$ and $D1^{-}$) that meet smoothly at $\mathcal{P} = 1/4$. To follow the bifurcated branches into the nonlinear regime we performed a numerical study of the equation (3.10). A bifurcational diagram at fixed $\mathcal{P}$, showing various motile and nonmotile configurations, is presented in Fig.3.12; the corresponding internal profiles are presented in Fig.3.13.

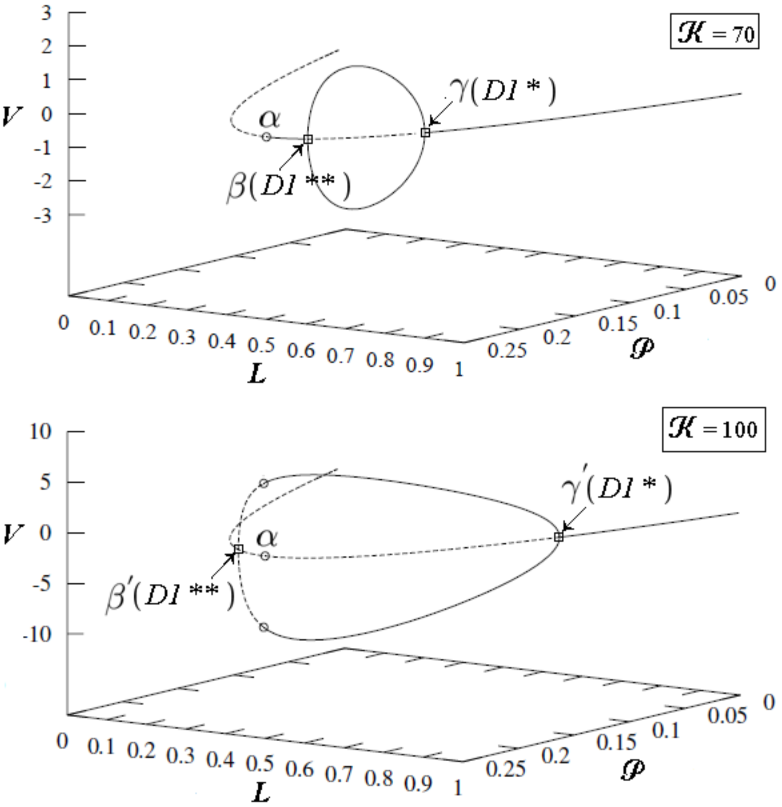

Figure 3.15: Bifurcation diagram with $\mathcal{P}$ as a parameter showing motile branches connecting points $D1^{*}$ and $D1^{**}$. Corresponding bifurcation points are shown in insert in Fig.3.11. Parameter $\mathcal{K}$ is fixed in each graph ($\mathcal{K} = 70$ and $\mathcal{K} = 100$).

We see that each bifurcation point gives rise to two nontrivial solutions. Thus, point $D1^{+}$ is associated with two motile branches, the point $S1^{+}$ - with two non motile branches and then the pattern repeats itself as $D2^{+}, S2^{+}, D3^{+}, S3^{+}$.... Each pair of motile solutions is symmetric with two opposite polarization orientations corresponding to two different signs of the velocity. One can see that along the motile branch originating at $D1^+$, solution with positive velocity has all motors concentrating at the rear, while solution with negative velocity concentrates motors at the front as expected. For the second motile branch originating at $D2^+$ there is an additional peak in the concentration profile which may be interpreted as a precursor of impending splitting of the cell, see (Fig.3.13). The non motile bifurcation point $S1^+$ gives rise to two symmetric configurations with different lengths and with motors concentrated either in the middle of the cell or near the boundaries (Fig.3.13). The subsequent motile and non motile bifurcation points correspond to solutions with more peaks. For the branches bifurcating from the trivial configurations belonging to $\hat{L}_-$ family, the picture is basically similar (see Fig. 3.12).

In Fig. 3.15 we show the nontrivial solutions originating from the motile branch $D1$ at two values of parameter $\mathcal{K}$ corresponding to lines $\alpha\beta$ and $\alpha\beta'$ shown in Fig.3.11(insert). One can see that there is a single solution branch connecting points $D1^*$ and $D1^{**}$ which may belong either to one family $\hat{L}_+$ $(\alpha\beta)$ or to two different families $\hat{L}_+$ and $\hat{L}_-$ $(\alpha\beta')$. In the former case the nontrivial motile branch has a turning point at a finite value of $\mathcal{P} < 1/4$ giving rise to an interesting reentrant behavior. In this regime the increase of the average concentration of myosin can first polarize the cell and initiate motility, but if the concentration is increased further, the cell can get symmetrized again and stabilize in another homogeneous configuration.

3.6 Numerical study of the non-steady problem with initial data, stability

Numerical study of the full non steady problem (3.1) shows that all nontrivial solutions (non motile and motile) are unstable except for the motile branch bifurcating at $D1^+$. Some trivial solutions from the $\hat{L}_+$ family indicated by the solid lines and converging arrows in Fig.3.12 and all the collapsed non motile solutions from the $\hat{L}_0$ family are stable. Numerical simulations also suggest that as in [25, 101], unstable multi-peaked solutions are long living. This behavior is reminiscent of the classical spinodal decomposition modeled by 1D Cahn-Hilliard equation where the coarsening process get critically slowed down near multiple saddle points [42].

The issue of local stability for the nontrivial solutions bifurcating from the two branches of the trivial solutions $\hat{L}_+$ and $\hat{L}_-$ was studied numerically by integrating the full dynamical system (3.2-3.3) with initial data close to the examined steady state solution.

To study numerically the Cauchy problem, we consider system (3.2-3.3) with initial conditions prescribing the function $\hat{c}$, and the location of the boundaries of the cell l_- and l_+. We built two grids on the same interval $[0, 1]$: a grid Z and its dual Z_d (See Fig.3.16).

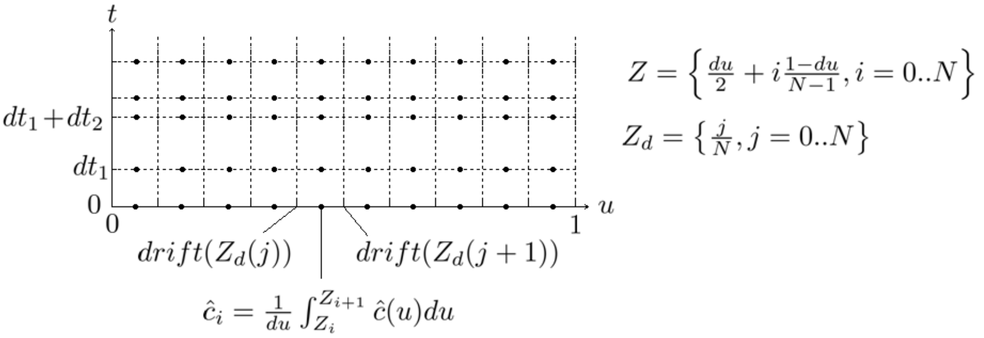

Figure 3.16: Scheme of the finite volume procedure used to integrate numerically (3.2-3.3). The concentration $\hat{c}$ is discretized on the Z grid while the effective drift is discretized on the dual grid Z_d.

Then by using the initial condition on $\hat{c}$, Eq.$(3.2)_1$ is solved and the effective drift

$$drift(u,t) = \mathcal{K}\frac{\partial_u \hat{\sigma}}{L} - \dot{G} - (u - \frac{1}{2})\dot{L}$$

is computed on Z_d. We then apply an upwind finite volume scheme to Eq.$(3.2)_2$ to find the updated concentration profile $\hat{c}$ on Z which now corresponds to the next time step. Then the same procedure is repeated. The time step is chosen in an adaptive way in order to satisfy the Courant-Friedrichs-Lewy condition uniformly on Z_d [105].

Our main numerical finding is that the non motile trivial branch $\hat{L}_-$ is unstable as well as all the branches (motile or non motile) bifurcating from this branch. The $\hat{L}_+$ branch is locally stable until the first (motile) bifurcation $D1^+$ which both segments (1 and $1'$ on Fig 3.12 and 3.13) are stable while the $\hat{L}_+$ branch becomes unstable. All the other regular nontrivial solutions are dynamically unstable. In Fig.3.7, we show the bifurcation diagram with arrows providing schematic depiction of the stable trivial solutions while on Fig.3.12 we show in solid lines the non trivial attractor.

To illustrate instability we show in Fig.3.17 the escape of the phase trajectory from the neighborhood of the trivial non motile solution $\hat{L}_-$, which for $\mathcal{K}$ smaller than the critical value of the first motile bifurcation $D1^+$ reequilibrates to the trivial non motile solution $\hat{L}_+$.

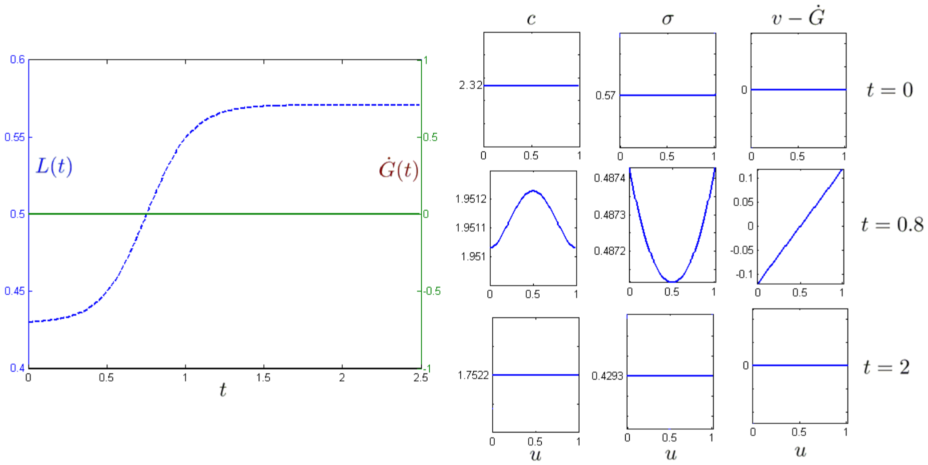

Figure 3.17: $L(t)$, $\dot{G}(t)$ and profiles c, σ and $v-\dot{G}(t)$ for parameters $\mathcal{P}=0.245$, $\mathcal{K}=50$ and $c_0=1$(See Fig.3.12). Starting from the $L_i=\hat{L}_-$ and the homogeneous concentration $c^0(u)=c_0/\hat{L}_-$

In Fig.3.18 we show convergence of two initial nearly homogeneous profiles that differ from a bias to the rear or to the front to the twin stable motile solutions $D1^{\pm}$. As suggested by the restricted analysis of section 3.7, the initial bias is conserved in time and chooses the segment of the $D1$ branch which attracts the solution.

Finally in Fig.3.19 we illustrate the attractive nature of the singular non motile solutions when starting with a length smaller than $\hat{L}_-$. We can numerically observe the result obtained in section 3.4.2 that $s(u)/L \to \frac{\mathcal{KP}}{2}u(u-1)$.

Note the local stability of some TW solutions is more difficult to study both analytically and numerically. In particular, one faces an interesting effect first observed in [25], that some of the unstable solutions (motile or non motile) may be long living. By using the analogy with much better studied Cahn-Hilliard model of spinodal decomposition [33, 111] one can conjecture that these states correspond to saddles and that the dynamical system is first attracted to such saddles along the stable manifold but then eventually finds the unstable manifold and departs. We illustrate this situation in

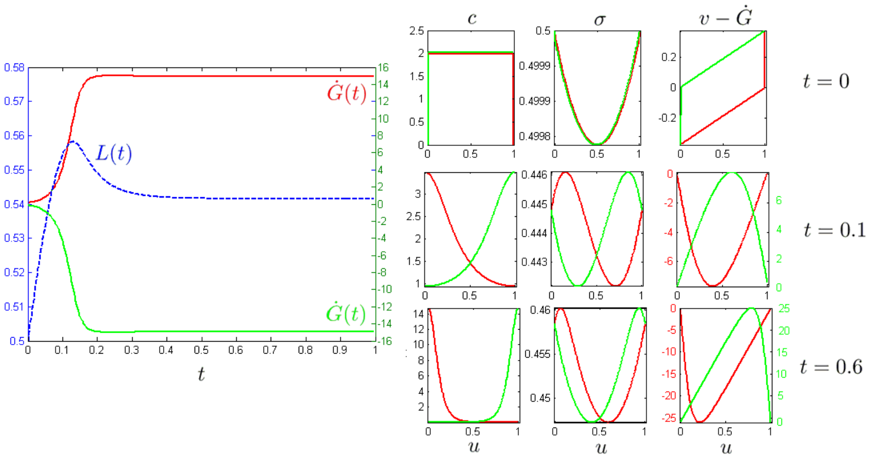

Figure 3.18: $L(t)$, $\dot{G}(t)$ and profiles c, σ and $v-\dot{G}(t)$ for parameters $\mathcal{P}=0.245$, $\mathcal{K}=150$(See Fig.3.12) and $c_0=1$. Starting from the $L_i=0.5$ and nearly homogeneous concentrations with a bias to the rear (in red) and a bias to the front (in green)

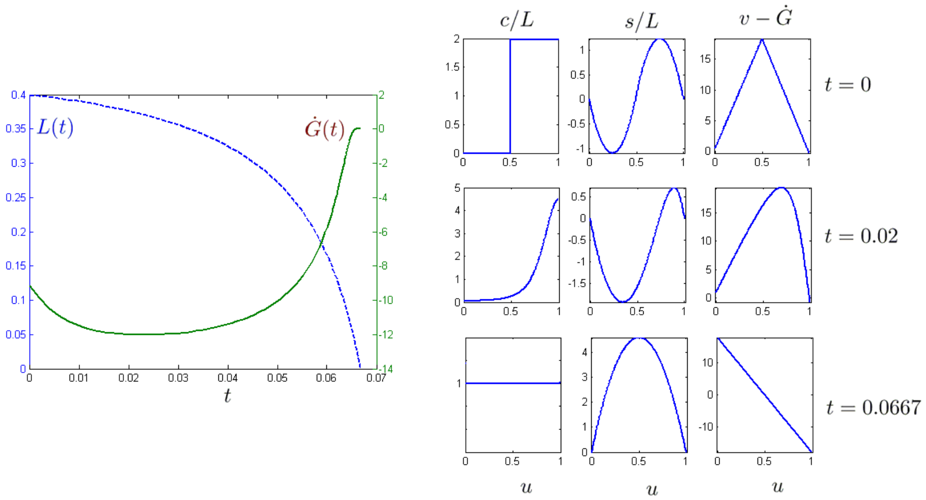

Figure 3.19: $L(t)$, $\dot{G}(t)$ and profiles c/L, $s/L=\mathcal{K}\frac{\sigma+(L-1)}{L}$ and $v-\dot{G}(t)$ for parameters $\mathcal{P}=0.245$, $\mathcal{K}=150$(See Fig.3.12) and $c_0=1$. Starting from the $L_i=0.4$ and a concentration fully biased to the front.

Fig.3.20 by showing that our branch 2 from Fig.3.12 and 3.13 is approached by the phase trajectory before it finds the stable configuration $1'$. Interestingly, the symmetric branch $2'$ is also first approached from a slightly different initial data but is then abandoned much faster than the branch 2 . Based on our numerical experiments we conjecture that the life time of a branch increases with the value of $\int_0^1 \cosh(L(\frac{1}{2}-u))c(u)du$ in the corresponding steady state. In physical terms we find that the lifespan of the branch is linked with the distribution of motors and the states with localized distribution of motors on the periphery of the cell survive longer than the states where motors are concentrated in the center of the cell.

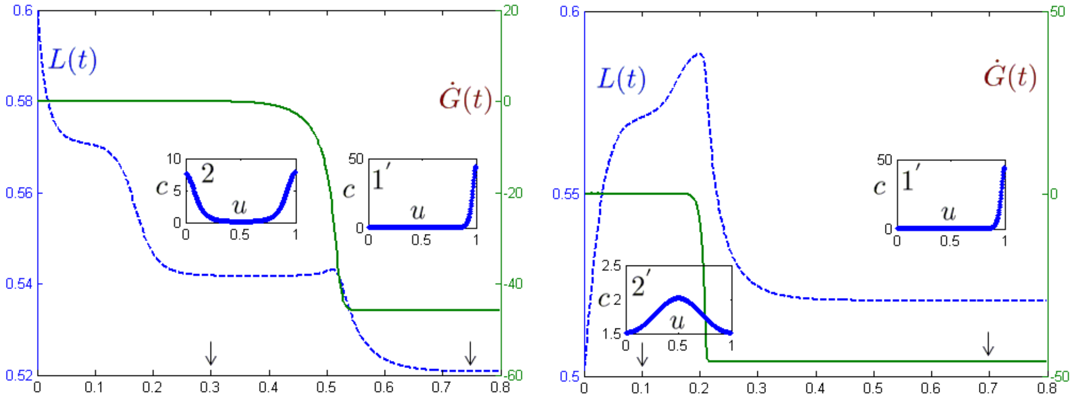

Figure 3.20: $L(t)$ and $\dot{G}(t)$ for parameters $\mathcal{P} = 0.245$ $\mathcal{K} = 400$ starting from homogeneous initial state with different initial lengths $L_i = 0.6$ (left) and $L_i = 0.5$ (right). The labels refer to Fig.3.12 and Fig.3.13.

To study analytically linear stability, one has to linearized system (3.5-3.4) near a steady state (solving the TW problem (3.10)) that we denote with the index $_{eq}$. We set,

$$\left\{ \begin{array}{c} G(t) = \dot{G}_{eq}t + \delta G(t) \\ L = L_{eq} + \delta L \\ \hat{c}(u,t) = \hat{c}_{eq}(u) + \delta\hat{c}(u,t) \end{array} \right.$$

Supposing that the perturbation δ is small enough, we can consider the system up to first order to get a linear system of the type,

$$\partial_t \begin{pmatrix} \delta G \\ \delta L \\ \delta\hat{c} \end{pmatrix} = H \begin{pmatrix} \delta G \\ \delta L \\ \delta\hat{c} \end{pmatrix}$$

where H is an linear operator with variable coefficients. The linear stability properties of the system are then given by the spectrum of H but we stopped short of characterizing it.

3.7 Two limiting regimes

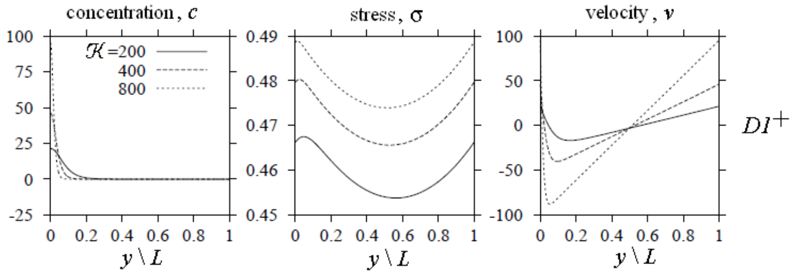

Figure 3.21: Internal configuration of the moving cell on the motile branch $D1^+$ showing the localization with increasing $\mathcal{K}$ at $\mathcal{P} = 0.245$.

In some limiting cases the presented theory can be simplified at the expense of certain degeneracy. Thus, in the hyperbolic limit $\mathcal{K} \to \infty$ (no diffusion), the number of nontrivial solutions grows to infinity and solutions become singular. For instance, as we show in Fig.3.21, the concentration profile for the first motile branch ($D1^+$) localizes at the trailing edge. In the inviscid limit $\mathcal{Z} \to 0$ the system (3.1) reduces to

$$\partial_t u = \partial_x (u \partial_x u),$$

where $u = 1 - \mathcal{K}\mathcal{P}c/c_0$, which is a sign-indefinite porous flow equation exhibiting an uphill diffusion when $c/c_0 > (\mathcal{K}\mathcal{P})^{-1}$.

The general mathematical problem for the autotaxis system (3.1) depends on four non-dimensional parameters: $\mathcal{P}$, $\mathcal{Z}$, c_0 and $\mathcal{K}$. While all of these parameters play an important role, it is of interest to study some limiting cases showing particular transparency in depicting one of the effects at the expense of misrepresenting certain other effects. Two of such limits are briefly discussed below. They provide an exaggerated representation of the concentration phenomenon because in each model one of the stabilizing mechanisms, either diffusion and bulk viscosity, is disabled.

3.7.1 The hyperbolic limit

Suppose first that diffusion of motors can be neglected ($D \to 0$) which means that $\mathcal{K} \to 0$. In this case the equation for motors describes pure transport (or drift) and becomes hyperbolic implying a direct dependence of the steady state on initial data. The limiting system depends on the three dimensionless parameters $\mathcal{P}$, $\mathcal{Z}$ and c_0.

Already from our general study we see that with $\mathcal{K} \to 0$ the number of bifurcated branches increases indefinitely (see Fig.3.12) and we observe configurations with increasing number of peaks. On the other side, the main stable motile branch D_1^+ shows progressive localization at the trailing edge (See Fig.3.21). These features, the increased complexity of solutions and the localization, are also characteristic for Navier-Stokes equations where the analogue of our diffusion is the bulk viscosity. By using this analogy we can identify our 'hyperbolic limit' with the 'high Reynolds number limit' in the theory of turbulence. It is not surprising that this limit is very degenerate.

To obtain some quantitative results in the limit $D = 0$ we need to change the scaling of variables which was originally based on the assumption that $D \neq 0$. To this end we re-normalize time by η/χ while letting all other scales the same. Then Eq. 3.1 becomes

$$\begin{cases} -\mathcal{Z}\partial_{xx}\sigma + \sigma = \mathcal{P}c/c_0, \\ \partial_t c + \frac{\mathcal{Z}c_0}{\mathcal{P}}\partial_x(c\partial_x\sigma) = 0, \end{cases}$$

The boundary conditions on the diffusional fluxes should be now dropped and the remaining boundary conditions can be written as

$$\begin{cases} \sigma(l_\pm(t), t) = -(L(t) - 1) \\ \dot{l}_\pm(t) = c_0\frac{\mathcal{Z}}{\mathcal{P}}\partial_x\sigma(l_\pm(t), t) \end{cases}$$

The ensuing hyperbolic Keller-Segel type system is similar to the one studied in [140, 141] on a fixed domain. An additional complexity of our problem is that system (3.1) is prescribed on a moving domain with free boundaries governed by Stefan type conditions.

It will be convenient to map the problem into a fixed domain at the expense of introducing additional explicit time dependence into the operator. More specifically, we consider the change of variables

$$u = \frac{x - l_-(t)}{L(t)},\ \hat{c}(u,t) = L(t)c(l_-(t) + L(t)u, t) \text{ and } \hat{\sigma}(u,t) = \sigma(l_-(t) + L(t)u, t).$$

In these new variables the system (3.2) takes the form,

$$\begin{cases} -\frac{\mathcal{Z}}{L^2}\partial_{uu}\hat{\sigma} + \hat{\sigma} = \frac{\mathcal{P}\hat{c}}{Lc_0} \\ \partial_t\hat{c} + \frac{1}{L}\partial_u(\hat{c}(\frac{\mathcal{Z}c_0}{L\mathcal{P}}\partial_u\hat{\sigma} - \dot{G} - (u - \frac{1}{2})\dot{L})) = 0 \end{cases} \tag{3.27}$$

The boundary conditions can now be written as

$$\begin{cases} \hat{\sigma}(0,t) = \hat{\sigma}(1,t) = -(L(t) - 1) \\ \dot{G} = \frac{\mathcal{Z}c_0}{2\mathcal{P}L}(\partial_u\hat{\sigma}(1,t) + \partial_u\hat{\sigma}(0,t)) \\ \dot{L} = \frac{\mathcal{Z}c_0}{\mathcal{P}L}(\partial_u\hat{\sigma}(1,t) - \partial_u\hat{\sigma}(0,t)) \end{cases} \tag{3.28}$$

System (3.27-3.28) was first studied numerically by using the method detailed in section 3.6 except for the fact there are no additional boundary conditions to $(3.27)_2$ as a zero flux of motor at the boundaries is already ensured by $(3.28)_{2,3}$. Depending on the initial condition $\hat{c}(u,0) = \hat{c}^0(u)$ we observed the following three main types of long time behavior:

1. If the initial concentration profile $\hat{c}^0$ is biased to the left, more precisely, if
$$\int_0^1 \hat{c}^0(u)\sinh(\frac{L}{\sqrt{\mathcal{Z}}}(\frac{1}{2}-u))du > 0,$$
then the numerical solution of (3.27) converges to a TW steady state characterized by positive velocity. The limiting TW profile exhibits localized myosin peaks (approximating Dirac delta).
2. If the initial profile $\hat{c}^0$ is biased to the right, i.e.
$$\int_0^1 \hat{c}^0(u)\sinh(\frac{L}{\sqrt{\mathcal{Z}}}(\frac{1}{2}-u))du < 0,$$
then the numerical solution of (3.27) is converging to a TW steady state with a negative velocity. The limiting profile concentration exhibits localized myosin peaks.
3. If $\hat{c}_0$ is unbiased, say
$$\int_0^1 \hat{c}^0(u)\sinh(\frac{L}{\sqrt{\mathcal{Z}}}(\frac{1}{2}-u))du = 0$$
which means for instance that the initial distribution is even with respect to the center of the cell then the numerical solution of (3.27) converges to a non motile solution characterized by localized myosin peaks distributed evenly.

This purely numerical result can be illustrated by the following extremely rough analysis revealing, nevertheless, the mechanism of polarity amplification and confirming the extreme localization tendency. The idea is to consider a simplified piece wise constant ansatz for the concentration profile and trace its evolution by solving a coupled system of ordinary differential equations.

Suppose that the ansatz is the minimal one which can still capture the localization. This means that the concentration profile has three levels separated by moving internal boundaries. Here we use an implicit assumption that inside each domain with continuous concentration field the convergence to a constant state (which solves our transport equation) is instantaneous. The gradients are then supported only on the jump discontinuities which are also admissible by the diffusion free dynamic model.

To be more specific we assume that the initial concentration profile at $t = 0$ has the form:

$$\hat{c}^0(u) = \begin{cases} 0 \text{ if } u < a_0 \\ \frac{c_0}{b_0 - a_0} \text{ if } a_0 \leq u \leq b_0 \\ 0 \text{ if } b_0 < u \end{cases}$$

where $0 < a_0 < b_0 < 1$. We then assume that the concentration profile maintains the same structure also for $t > 0$

$$\hat{c}(u,t) = \begin{cases} 0 \text{ if } u < a(t) \\ \frac{c_0}{b(t) - a(t)} \text{ if } a(t) \leq u \leq b(t) \\ 0 \text{ if } b(t) < u \end{cases}$$

where now $a(t)$ and $b(t)$ are the unknown functions. One can then use the weak form of (3.27) and the boundary conditions (3.28) to find equations for the four unknown functions: $a(t)$, $b(t)$, $G(t)$ and $L(t)$. From (3.27), we isolate the flux,

$$\frac{\mathcal{Z} c_0}{L\mathcal{P}} \partial_u \hat{\sigma} - \dot{G} - (u - \frac{1}{2})\dot{L}$$

which gives the speed of moving discontinuities and imply the system,

The equation for $G(t)$ can be uncoupled and for the remaining three unknown functions we obtain the following system of equations:

$$\begin{cases} \dot{a} = \frac{c_0 \mathcal{Z}}{\mathcal{P} L} \left[\partial_y \sigma \mid_a - \partial_y \sigma \mid_0 + a(\partial_y \sigma \mid_1 - \partial_y \sigma \mid_0)\right] \\ \dot{b} = \frac{c_0 \mathcal{Z}}{\mathcal{P} L} \left[\partial_y \sigma \mid_b - \partial_y \sigma \mid_0 + b(\partial_y \sigma \mid_1 - \partial_y \sigma \mid_0)\right] \\ \dot{L} = \frac{c_0 \mathcal{Z}}{\mathcal{P} L} (\partial_y \sigma \mid_1 - \partial_y \sigma \mid_0) \end{cases}$$

Where the equation for G can be uncoupled and is computed from,

$$\dot{G} = \frac{c_0 \mathcal{Z}}{2\mathcal{P} L} (\partial_y \sigma \mid_1 + \partial_y \sigma \mid_0)$$

By using the normalized variable $\tilde{L} = \frac{L}{\sqrt{\mathcal{Z}}}$ we can write explicitly

$$\left\{\begin{array}{c} \dot{a} = -\frac{\sqrt{\mathcal{Z}}c_0}{\mathcal{P}}(\sqrt{\mathcal{Z}}\tilde{L}-1)\left(\sinh(a\tilde{L}) + \tanh\left(\frac{\tilde{L}}{2}\right)(-\cosh(a\tilde{L}) - 2a + 1)\right) \\ +\frac{c_0}{\tilde{L}(b-a)}\left((\cosh(a\tilde{L}) + a - 1)(\cosh((1-a)\tilde{L}) - \cosh((1-b)\tilde{L})) + a(\cosh(b\tilde{L}) - \cosh(a\tilde{L}))\right) \\ \dot{b} = -\frac{\sqrt{\mathcal{Z}}c_0}{\mathcal{P}}(\sqrt{\mathcal{Z}}\tilde{L}-1)\left(\sinh(b\tilde{L}) + \tanh\left(\frac{\tilde{L}}{2}\right)(-\cosh(b\tilde{L}) - 2b + 1)\right) \\ +\frac{c_0}{\tilde{L}(b-a)}\left((1-b)(\cosh((1-b)\tilde{L}) - \cosh((1-a)\tilde{L})) + (b - \cosh((1-b)\tilde{L}))(\cosh(b\tilde{L}) - \cosh(a\tilde{L}))\right) \\ \dot{\tilde{L}} = -\frac{2c_0}{\mathcal{P}}(\sqrt{\mathcal{Z}}\tilde{L}-1)\tanh(\frac{\tilde{L}}{2}) \\ -\frac{2c_0}{\sqrt{\mathcal{Z}}\tilde{L}(b-a)\cosh(\frac{\tilde{L}}{2})}\cosh(\frac{\tilde{L}}{2}(1-(a+b)))\sinh(\frac{\tilde{L}}{2}(b-a)) \end{array}\right. \tag{3.29}$$

and the counter part of general formula (3.9) is,

$$\dot{G} = \frac{c_0}{\tilde{L}(b-a)\sinh(\frac{\tilde{L}}{2})}\sinh(\frac{\tilde{L}}{2}(1-(a+b)))\sinh(\frac{\tilde{L}}{2}(b-a)) \tag{3.30}$$

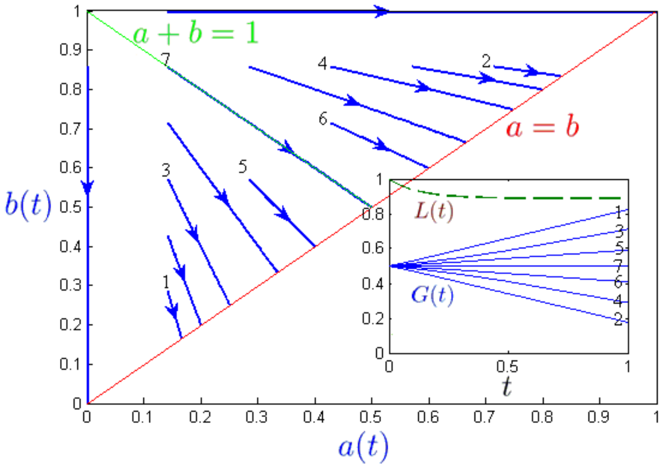

Figure 3.22: Projection on the $[a, b]$ plane of different trajectories of (3.29) starting from different initial conditions (a_0, b_0) for $\mathcal{Z} = 1$, $c_0 = 1$, $\mathcal{P} = 0.1$ and $L_{init} = 1$. Trajectories all converge to the line $a = b$ and stay on the same side the separatrix $a + b = 1$. Insert shows remaining variables L and G as a function of time for some trajectories (indexed)

A numerical solution of this system is illustrated in Fig.3.22 which shows different phase trajectories in the a, b plane. One can see that $\lim_{t\to\infty} a(t) = \lim_{t\to\infty} b(t)$ which means that the profile has a tendency to localize to a delta distribution as the total amount of motors remain equal to c_0. The parametric plane is split in two parts by a $a + b = 1$ which means that for $a_0 + b_0 < 1$ we obtain $\lim_{t\to\infty} a(t) + b(t) < 1$ and for

$a_0+b_0>1$ we see that $\lim_{t\to\infty} a(t)+b(t)>1$. This observation confirms that the initial asymmetry is preserved, moreover our Fig.3.22) shows that it is getting amplified. The computation of velocity $V(t)$ shows that the cell always moves in the direction which is opposite to the direction of the localization which is expected from (3.30) (See Fig.3.22-insert). One can also see that an initially symmetric profile also localizes with time but without a loss of symmetry and without acquiring an overall velocity.

The numerical behavior exhibited by the simplified nonlinear system of ODEs can be at least partially justified by a simple analytical study of the corresponding linearized system. When $\mathcal{Z}$ is large, (3.29) can be simplified since L remains bounded (as for large times $L<1$). Then, making a first order development of trigonometric functions (3.29) reduces to ,

$$\begin{cases} \dot{b}-\dot{a}=\frac{Lc_0}{\sqrt{\mathcal{Z}}}(b-a-1) \\ \dot{b}+\dot{a}=\frac{Lc_0}{\sqrt{\mathcal{Z}}}(b+a-1) \\ \dot{L}=c_0(-\frac{L(L-1)}{\mathcal{P}}-1) \end{cases} \tag{3.31}$$

As a consequence, for this simplified problem, provided $\mathcal{P}<1/4$, length has two stationary points $\hat{L}_\pm$ where only $\hat{L}_+$ is stable (See Fig.3.23). As for $(3.31)_{1,2}$, it is clear that

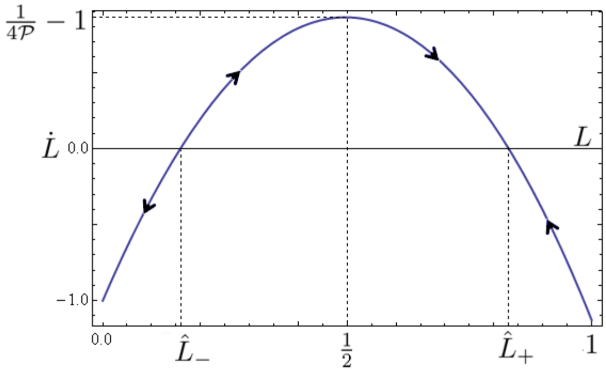

Figure 3.23: Fixed points of ODE $(3.31)_3$

$b_0-a_0<1$ which implies that $\dot{b}-\dot{a}$ remains negative triggering ultimately complete localization of myosin concentration. In the same way if $b_0+a_0<1$ then $\dot{b}+\dot{a}$ remains negative implying that $b+a<1$ and if $b_0+a_0>1$, then $\dot{b}+\dot{a}$ remains positive implying that $b+a>1$. Ultimately for this simplified problem there are only three steady states:

1. $a = b = 1/2$ which occurs only if the system is initially symmetric and is characterized by a zero velocity (from 3.30)
2. $a = b = 0$ which occurs with a initial bias to the rear and is characterized by the maximal velocity $c_0/2$ (from 3.30)
3. $a = b = 1$ which occurs with a initial bias to the front and is characterized by the minimal velocity $-c_0/2$(from 3.30)

The existence of the separatrix in this system shows that the sign of the cell velocity depends only on the initial asymmetry (bias) in the motor concentration. Our numerical simulations of the full system (3.1) shows that similar memory of the asymmetry structure of the initial state is exhibited by the system with diffusion (See section 3.6).

Finally we mention that in the hyperbolic limit the steadily moving cell can have any velocity in the range $[-\frac{c_0}{2}, \frac{c_0}{2}]$ (from 3.30). Different terminal velocities correspond to different localization points in segment $[0, 1]$ which are all reachable starting from the appropriate initial data. Diffusion regularizes the problem and in the limit of disappearing diffusion we obtain only two possible velocities associated with the TW solutions on the $D1_+$ motile branch (other branches being unstable). Interestingly, these two velocities correspond either to the minimum $(-c_0/2)$ or to the maximum $(c_0/2)$ of the admissible range; the associated concentration profiles always localize exactly on the trailing edge of the moving cell.

3.7.2 The inviscid limit

Another interesting limit of the system (3.1) corresponds to the case when the diffusion coefficient D is finite but the bulk viscosity η goes to zero. Then $\mathcal{Z} \to 0$ while the remaining three dimensionless parameters $\mathcal{K}$, $\mathcal{P}$ and c_0 remain finite. From the system (3.1) we see that parameter $\mathcal{Z}$ enters as a coefficient in front of the highest derivative and therefore one can expect in this limit that the solution will exhibit infinitely localized boundary layers. Here, we do not attempt to study the limiting system fully and instead focus on the structure of the bulk equation, while disregarding the structure of the boundary layers. Our goal is to show that the simplifications in the equations brought by this limiting procedure reveal a simple and transparent basic mechanism behind polarization instability and motility initiation.

To obtain the system of governing equations in the limit $\mathcal{Z} \to 0$ one can just drop in $(3.1)_1$ the term with the second derivative of σ and then use the remaining algebraic equation to express in $(3.1)_2$ the stress gradient through the gradient of concentration. However, to reveal the limiting structure of the autotaxis interactions we can instead start directly with the nonlocal equation for the concentration (3.5) and then study the limit of the kernel as $\mathcal{Z} \to 0$.

To this end we recall that in Eq.(3.5) the kernel ϕ can be decomposed in ϕ_i and ϕ_e see (Eq.(3.7)). Inside ϕ_i we can further isolate the 'bulk' part and the surface contribution of ϕ_i by using the asymptotic procedure developed in [152]. More specifically we introduce the new kernel

$$\phi_i^b(x-y) = \lim_{L\to\infty} \phi_s(x/L + L/2, y/L + L/2) = \frac{1}{2}\begin{cases} \exp(\frac{x-y}{\sqrt{\mathcal{Z}}}) \text{ if } x-y<0 \\ -\exp(\frac{y-x}{\sqrt{\mathcal{Z}}}) \text{ if } x-y>0 \end{cases}$$

which is defined for $x, y \in [0, L]$. ϕ_i^b eliminates the boundary layers of ϕ_i and therefore separates the bulk term from the surface term. The structure of the bulk kernel $\phi_i^b(x-y)$ at different values of $\mathcal{Z}$ is shown in Fig.3.24). The characteristic features of this kernel are the jump discontinuity at the diagonal $x-y=0$ and the exponential decay away from the diagonal with the characteristic length scale $\sqrt{\mathcal{Z}}$. As $\mathcal{Z} \to 0$ we obtain the limit

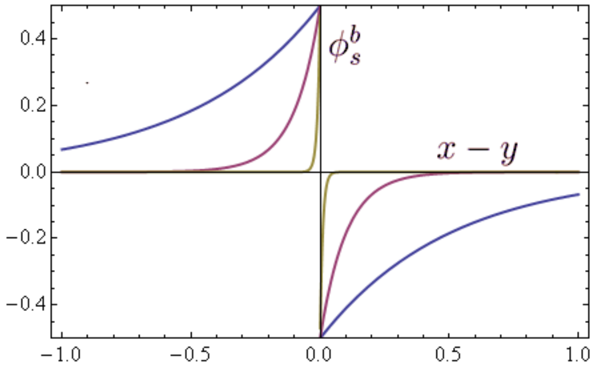

Figure 3.24: Behavior of ϕ_s^b as a function of $x-y$ localizes with decreasing $\sqrt{\mathcal{Z}} = 0.5, 0.1, 0.01$.

$$\lim_{\mathcal{Z}\to 0} \frac{1}{\mathcal{Z}} \phi_i^b(x,y) = \lim_{\mathcal{Z}\to 0} \frac{\delta(x-y+\sqrt{\mathcal{Z}}) - \delta(x-y-\sqrt{\mathcal{Z}})}{2\sqrt{\mathcal{Z}}} = \partial_x \delta(x-y)$$

By using this limiting kernel we obtain,

$$\lim_{\mathcal{Z}\to 0} \frac{1}{\mathcal{Z}} \int_0^1 \phi_i^b(u,v)\hat{c}(v,t)du = \frac{1}{L^2}\partial_u \hat{c}(u,t)$$

The surface part of the kernel also has a nontrivial structure describing two boundary layers on the extremities of the cell. However since the corresponding terms affect only the boundary conditions, we are not presenting them here. Using previous equality, we obtain the following expression for the stress gradient,

$$\frac{1}{L}\partial_u \hat{\sigma} = \frac{\mathcal{P}c_0}{\mathcal{Z}} \int_0^1 \phi_i^b(u,v)\hat{c}(v,t)du = \frac{\mathcal{P}c_0}{L^2}\partial_u \hat{c}(u,t).$$

Then the limit of Eq. $(3.2)_2$ can be presented in the form,

$$\partial_t \hat{c}(u,t) - \frac{1}{L}\partial_u(\hat{c}(u,t)(\dot{G} + (\frac{1}{2} - u)\dot{L})) + \frac{\mathcal{P}\mathcal{K}}{c_0 L}\partial_u(\frac{\hat{c}(u,t)}{L^2}\partial_u \hat{c}(u,t)) = \frac{\partial_{uu}\hat{c}(u,t)}{L^2}$$

Here the functions $L(t)$ and $G(t)$ can be found from the boundary conditions which we leave implicit. If we rewrite this equation in the original coordinates (on a moving domain) we obtain

$$\partial_t c(x,t) + \frac{\mathcal{P}\mathcal{K}}{c_0}\partial_x(c(x,t)\partial_x c(x,t)) = \partial_{xx}c(x,t)$$

Finally by rewriting this equation as

$$\partial_t c(x,t) + \partial_x(\left(\frac{\mathcal{P}\mathcal{K}c(x,t)}{c_0} - 1\right)\partial_x c(x,t)) = 0$$

and introducing a new variable $u = 1 - \mathcal{K}\mathcal{P}c/c_0$ we obtain a sign indefinite porous flow equation,

$$\partial_t u(x,t) + \partial_x(u\partial_x u(x,t)) = 0.$$

The simplicity of this equation is in stark contrast with the complexity of the original system (3.1). One can see that for the regimes with

$$\frac{c}{c_0} > \frac{1}{\mathcal{K}\mathcal{P}}$$

one can expect an uphill diffusion similar to the case of spinodal decomposition which destabilizes homogeneous states and generates complexity. .

3.8 The flow of actin

Our main system of governing equations (see Eq. 3.1) describes two coupled processes: mechanical equilibration of the actin network and the advection of myosin motors which are carried by the network while exerting contractile forces on it. Solving this system allows one to find the density distribution of myosin and the velocity field for actin but not the density distribution for actin. This variable fully decouples because of the assumption of infinite compressibility of actin network which makes stress distribution independent on density distribution. The latter can be recovered after the 'statically determinate' mechanical problem is solved from solving the mass balance equation for actin with a kinematically prescribed velocity field. In this section we show how this program can be implemented for our non motile and motile steady state solutions of the mechanical problem.

Suppose that by solving system (3.1) we obtained the myosin concentration $c(x,t)$, the stress field $\sigma(x,t)$ and the velocity field $v(x,t)$. We also know the associated trajectories of the free surfaces $l_-(t)$ and $l_+(t)$. To find the actin density $\rho(x,t)$ we need to solve separately the following conservation equation with an initial condition:

$$\left\{\begin{array}{c} \partial_t\rho + \partial_x(\rho v) = 0 \\ \rho(x,0) = \rho_0(x) \end{array}\right. \tag{3.32}$$

Here we neglected for simplicity the diffusion of actin, which can be added if necessary. We recall that the boundary conditions in the mechanical problem ensuring that the flux of actin at both rear and front vanish (no active treadmilling) were of the form

$$\left\{\begin{array}{l} \dot{l}_-(t) = v(l_-(t),t)) \\ \dot{l}_+(t) = v(l_+(t),t)) \end{array}\right.$$

These conditions imply that both fronts must coincide with actin particles trajectories and that the total amount of actin is conserved $\int_{l_-(t)}^{l_+(t)} \rho(x,t)dx = M$.

For a given velocity profile $v(x,t)$ (solving (3.1)) one can easily solve (3.32) and find the desired density profile $\rho(x,t)$. A convenient way of solving this equation is by the method of characteristics delivering trajectories of the actin particles $x(\zeta,t)$, where $\zeta \in [l_-(0), l_+(0)]$ is the lagrangian coordinate of actin particle at $t=0$. We then introduce the so called characteristic curves defined by: $\forall s < t$,

$$\left\{\begin{array}{c} \frac{d\phi(\zeta,s)}{dt} = v(\phi(\zeta,s),s) \\ \phi(X,t) = x \end{array}\right.$$

then along these curves, the density distribution is known,

$$\rho(\phi(\zeta,t),t) = \rho_0(\zeta)\exp\Big(-\int_0^t \partial_x v(\phi(\zeta,s),s)ds\Big) \tag{3.33}$$

More specifically, consider a traveling wave solutions with the velocity profile $v = v(x - Vt)$ and the length of the cell L. Introduce a normalized moving variable $\hat{\phi} = (x - Vt)/L$. To find how this variable depends on the lagrangian variable $X = \zeta/(l_+(0) - l_-(0))$ and time t we need to solve for each value of X in $[0,1]$ the following ODE

$$\dot{\hat{\phi}}(X,t) = v(\hat{\phi}(X,t)) - V$$

One can see that the points of the body where $v(\hat{\phi}) = V$ are the singular points of this equation since the flow is stationary at such points. Added to this, it takes infinite time for an actin particle to reach (or leave) such points because the relative velocity field goes is not integrable in their neighborhood. Notice also that if at such points the function v has a negative slope we obtain a sink of particle trajectories (an attractor as $t \to \infty$ which we denote by γ_+) and if v has a positive slope, we obtain a source (an attractor as $t \to -\infty$) which we denote by γ_-). Mass accumulates into sinks in a for large positive times and all comes from sources for large negative times as, (3.33) shows that actin particles initially at X follow the characteristic curves to produce a new density at time t (positive or negative).

For trivial solutions associated to lengths $\hat{L}_\pm$, there is no flow at all ($v = 0$) and the density of actin remains the same throughout time.

To illustrate the global flow of actin particles we can consider the known velocity fields corresponding to nontrivial solutions near the bifurcation points studied in section 3.5. These solutions are characterized by the critical values of parameter ω and we know them up to a multiplier. For the nontrivial static (non-motile) branches, $S_m^\pm$ we obtain the equation

$$\dot{\hat{\phi}}(X,t) = \lambda sin(\omega_c \hat{\phi}(X,t)) \tag{3.34}$$

where $\omega_c = -2m\pi$ and we chose by convention (the value can be absorbed in time scaling) λ such that the maximum of velocity is one.

Similarly, for the motile branches $D_m^\pm$ we need to solve

$$\dot{\hat{\phi}}(X,t) = \lambda\left(-\frac{L^2}{\omega_c^3\cos(\omega_c/2)}\Big(\omega_c\cos(\omega(\hat{\phi}(X,t) - 1/2)) - 2\sin(\omega_c/2)\Big) - 1\right) \tag{3.35}$$

where ω_c solves the equation (3.26). Both equations can be solved analytically by separation of variables. In Fig.3.25 and Fig. 3.26 we show sample solutions of (3.34) and (3.35) corresponding to homogeneous initial conditions $\phi(X,0) = X$ for the first two motile and non motile branches and for positive and negative values of λ corresponding to the two possible direction of each bifurcation.

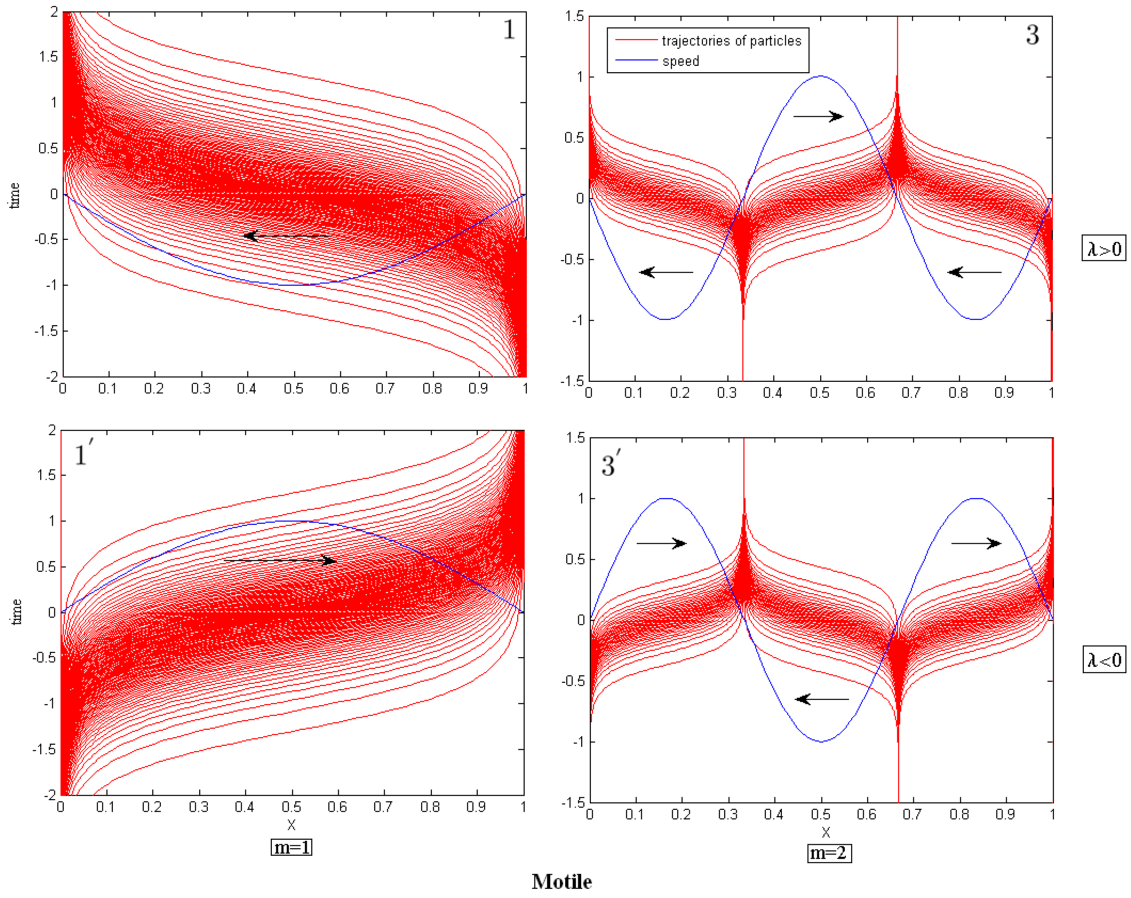

Figure 3.25: Trajectories of particles from sources to sinks for the first two motile bifurcation points for initially homogeneously distributed set of particles . Labels $1, 1^{'}, 3, 3^{'}$ are related to Fig.3.12 and Fig.3.13.

The main feature of the flows presented in Fig.3.25 and Fig. 3.26 is localization of initially homogeneously distributed actin particles in the sinks and spreading of particles initially concentrated in the sources. These singular locations corresponding to points where velocity of the internal flow is equal to the macroscopic velocity of the cell

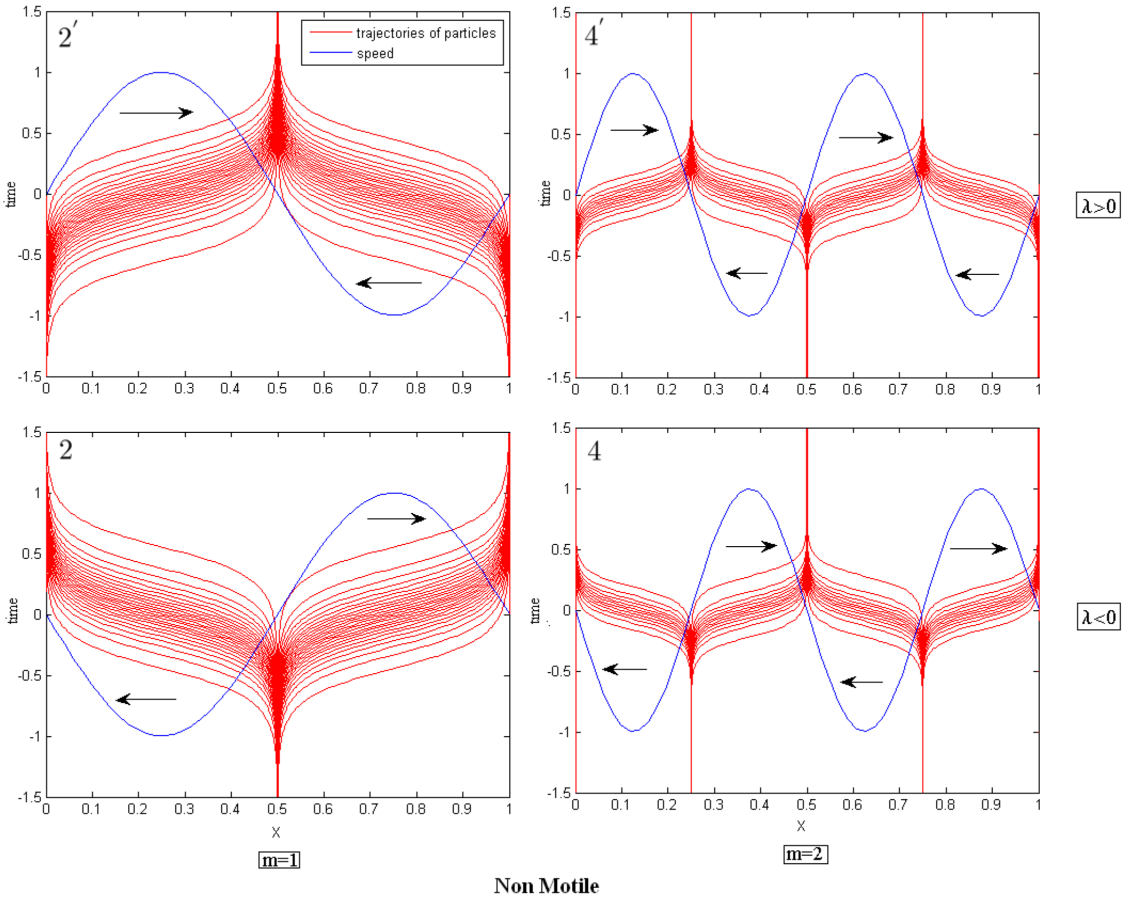

Figure 3.26: Trajectories of particles from sources to sinks for the first two non motile bifurcation points for initially homogeneously distributed set of particles . Labels $2, 2', 4, 4'$ are related to Fig.3.12 and Fig.3.13.

are clearly misrepresented by our simplified model which one dimensional and which neglects both polymerization/depolymerization and diffusion. The one dimensional nature of the model is particularly questionable in view of the expected circulation of actin inside the lamellipodium.

To address the problem of actin circulation in the 1D setting we need to interpret the flow between a source and a sink as a treadmilling cluster. For instance, for the m^{th} static (non motile) branch we would have $2m$ such clusters and for the m^{th} motile branch we obtain $2m-1$ clusters. In the original setting of the problem the time of complete turnover in each cluster is infinite

$$\tau = \int_{\gamma_-}^{\gamma_+} \frac{du}{|v(u) - V|} = \infty$$

and therefore the overall treadmilling flux inside each treadmilling cluster is equal to zero $|\dot{m}| \sim 1/\tau = 0$. To make the picture of actin flow more realistic it is natural to regularize the singular points by cutting out the domains of small size ϵ around both sinks and sources. More specifically, we can define an effective 'polymerization zone' around a source

$$\Gamma_- = \{u \in [0,1]/|u - \gamma_-| < \epsilon\}$$

and an effective 'depolymerization zone' around a sink

$$\Gamma_+ = \{u \in [0,1]/|u - \gamma_+| < \epsilon\}$$

Then a path between a source and a sink will take finite time with particles disappearing in a depolymerization zone (in a regularized sink) and appearing in a polymerization zone (in a regularized source). If we assume that a particle entering the boundary of the sink zone instantaneously reappears on the boundary of the source zone (see Fig.3.27) we obtain an internal circulation in each treadmilling cluster (after an initial transient). Such treadmilling will be passive on the side of actin because it is driven exclusively by the myosin contraction. The effective internal mass flux has the form

$$|\dot{m}| = \frac{M}{\int_{\partial\Gamma_-}^{\partial\Gamma_+} \frac{du}{|v(u)-V|}}$$

We observe that the steady state actin is now nonsingular

$$\rho(u) = \frac{|\dot{m}|}{|v(u) - V|}.$$

In particular, for the non motile regimes we obtain explicitly

$$\rho(u) = \frac{M}{\frac{\log(\cot(\epsilon m\pi))}{|\lambda| m\pi} |\sin(2\pi m u)|}.$$

In the case of motile branches similar computation can be done numerically. The resulting density profiles are shown in Fig.3.28 for the first two motile and first two non motile branches; the passive treadmilling cycles inside each cluster are shown by arrows. As the models of active fluids show such cycles can be spatially resolved already in 2D models [114].

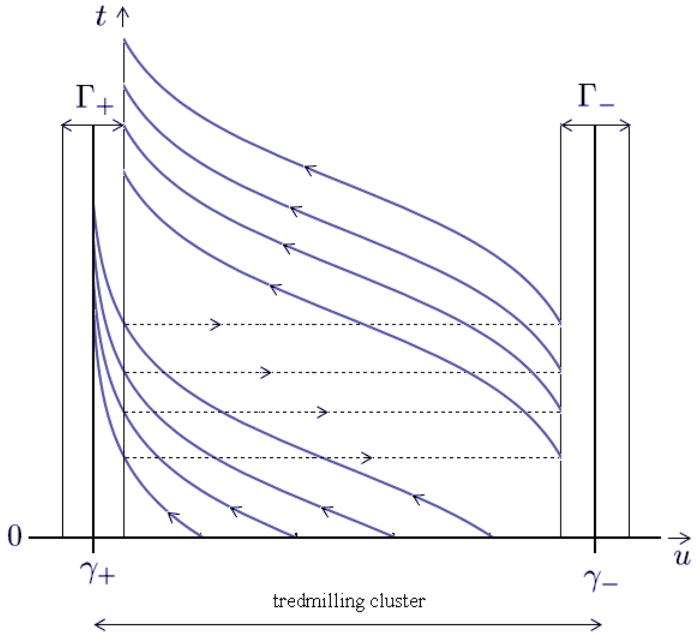

Figure 3.27: Sketch of trajectories of particles in a treadmilling cluster from uniformly distributed actin density.

3.9 Efficiency of the autotaxis mechanism

In this section we study the efficiency of the autotaxis process in a motile steady state regime with velocity V. In the absence of cargo to carry and external sources to perform work, the efficiency Λ has to be understood in the sense of Stokes [108, 171, 183]

$$\Lambda = P/H$$

where $P = \xi V^2 L$ is the power required for translocation with constant velocity in the presence of external friction preventing such motion and $H > 0$ is the internal energy production rate due to ATP hydrolysis which drives the contraction process. In a weakly non-equilibrium regime H is proportional to the square of the thermodynamical force (affinity) keeping the hydrolysis reaction out of equilibrium [88, 89]. To compute H we notice that it can be decomposed into a sum of an power H_A exerted by the active mechanism on the constraining environment and the dissipation ϵ which takes place even if the active force is generated but no work is produced. The term $H_A > 0$ is an anti-dissipation which is known in the domain of molecular motors whose force-velocity

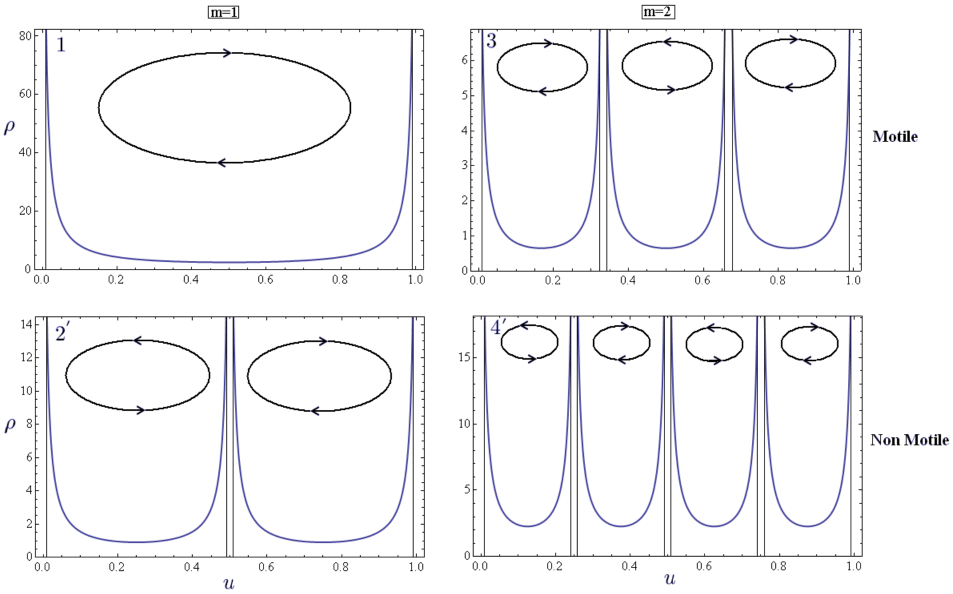

Figure 3.28: Density profiles for the first two motile and non motile branches for $\lambda > 0$, the profiles for $\lambda < 0$ are the same; only the treadmilling cycles (indicated by black circles) are going in the opposite direction. Labels are related to Fig.3.12 and Fig.3.13. Parameters are $M = 1$ and $\epsilon = 0.01$.

relation $f(v)$ has a domain with $f(V)V < 0$ while the term $\epsilon > 0$ can be identified with the maintenance heat introduced by A.V. Hill to describe isometric contractions of skeletal muscles (in stall conditions) [76]. The signs of the terms H_A and ϵ may also be different which requires special interpretation [88].

To compute the anti-dissipation term H_A we first rewrite here the dimensional force balance and the viscous constitutive law

$$\begin{cases} \partial_x \sigma = \xi v \\ \sigma = \eta \partial_x v + \chi c \end{cases}$$

If we multiply the first equation by v, substitute the second equation multiplied by $\partial_x v$ and integrate the result over the moving domain while applying boundary conditions,$\sigma(l_\pm(t), t) = -k(L - L_0)/L_0$ and $\dot{l}_\pm = v(l_\pm)$ we obtain:

$$-k\frac{L - L_0}{L_0}\dot{L} = \xi \int_{l_-}^{l_+} v^2 + \eta \int_{l_-}^{l_+} (\partial_x v)^2 + \chi \int_{l_-}^{l_+} c\partial_x v \tag{3.36}$$

In the travelling wave (steady state) regime $\dot{L} = 0$ and the term in the left hand side in

(3.36) disappears. We obtain

$$-\chi \int_{l_-}^{l_+} c\partial_x v = \xi \int_{l_-}^{l_+} v^2 + \eta \int_{l_-}^{l_+} (\partial_x v)^2$$

The integral in the left hand side describes the (useful) work performed by the contractile forces and therefore it can be identified with anti-dissipation H_A. Therefore one can write

$$H_A = \xi \int_{l_-}^{l_+} v^2 + \eta \int_{l_-}^{l_+} (\partial_x v)^2 > 0$$

and we see that the work goes into overcoming the viscous resistance in the bulk of the cell and the frictional resistance between the cell body and the substrate.

It is interesting that H_A can also be expressed in terms of myosin concentration gradient. Indeed, in the moving coordinate system with $y = x - Vt$ the advection-diffusion equation for myosin takes the form

$$\partial_y v = D\partial_y (\frac{\partial_y c}{c}) \tag{3.37}$$

Therefore we can write

$$H_A = D\chi \int_0^L \frac{(\partial_y c)^2}{c} > 0$$

which means that our anti-dissipation can also be linked to diffusional dissipation. This implies an interesting identity linking viscous and diffusional dissipation in this class of problems which we write co-moving coordinate system as

$$\int_0^L \eta(\partial_{yy}\sigma)^2 + \xi(\partial_y \sigma)^2 = D\chi \int_0^L \frac{(\partial_y c)^2}{c}.$$

Going back to efficiency, we can now write

$$\Lambda = \frac{\xi V^2 L}{D\chi \int_0^L \frac{(\partial_y c)^2}{c} + \epsilon}.$$

The 'maintenance' power term ϵ describes microscopic dissipation taking place even in the absence of a macroscopic motion. Therefore it cannot be estimated based on our equations and requires an access to the microscopic model of active force generation. It is then natural, however, to assume that $\epsilon \sim \mathcal{P}$ where the coefficient can be chosen to ensure that the terms $V^2 L$ and ϵ have the same order of magnitude. Here we make an implicit assumption that the system adds motors when it needs to do more work and in this way the 'maintanance heat' also increased. We may also argue that the creation

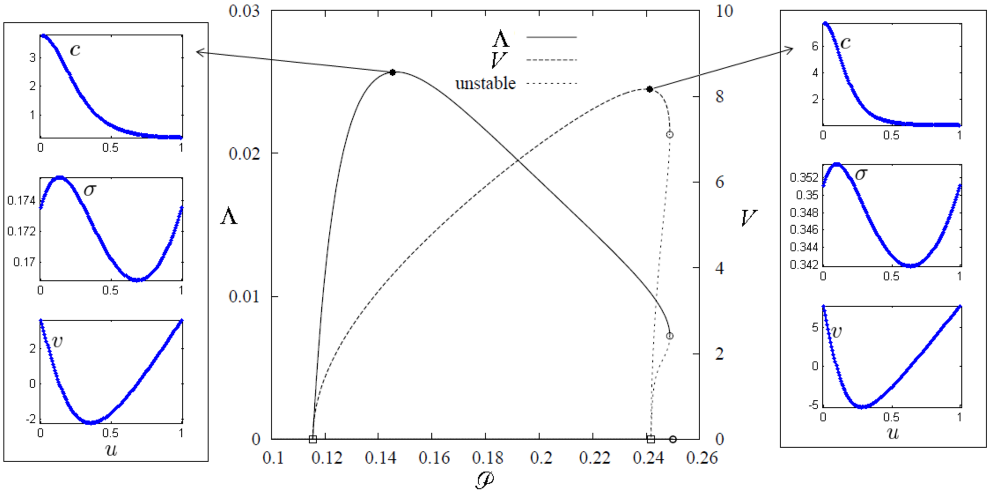

Figure 3.29: Stokes efficiency Λ and cell velocity as functions of the total power of motors along the motile branch $D1^*$ at $\mathcal{K} = 100$ and $\alpha = 10^3$. Unstable motile solutions are shown by the dashed line. In left insert we represent profiles at the maximal efficency while right insert displays the profiles achieving maximal speed.

of an incipient motion takes about the same energy as the generation of a stall force (continuity assumption).

The plot of efficiency computed under these assumptions is shown in Fig.3.29 as a function of the nondimensional parameter $\mathcal{P}$ characterizing the power of contraction. We notice that the efficiency is equal to zero for non motile regimes, has a maximum at a particular concentration of motors and is larger for stable motile solutions than for the unstable ones. On the same graph we show that the velocity of the overall advance for the corresponding cells. One can see that the most efficient cells are not the fastest and that the maximum efficiency and the maximum velocity regimes are drastically different. The concentration, stress and velocity are rather similar though (See Fig.3.29). The main difference is that the concentration profile of motors is more localized at the trailing front when velocity is maximal then when efficency is maximal. This can be justified a priori (without considering the motor balance equation $(3.1)_2$) since speed is maximized when c is fully localized (Dirac mass) at the trailing edge as we deduced from (3.4) while the situation is different for efficency. Indeed the efficency numerator is maximized when speed is maximal, implying a full localization at the trailing edge again but the numerator is minimal when concentration is homogeneous.

$$H_A + \epsilon = \frac{-\chi}{\xi}\int_{l_-}^{l_+} c\partial_{xx}\sigma + \epsilon > \epsilon$$

The lower bound ($H_A = 0$) is reached when $c = \frac{\sigma}{\chi}$ which can be shown positive using maximum principle and sums to L_0c_0 since,

$$\begin{cases} -\frac{\eta}{\xi}\partial_{xx}\sigma + \sigma = \chi c \\ \sigma(l_-(t),t) = \sigma(l_+(t),t) = -k\frac{L-L_0}{L_0} \\ \dot{l_-} = \frac{\partial_x\sigma(l_-(t),t)}{\xi} \text{ and } \dot{l_+} = \frac{\partial_x\sigma(l_+(t),t)}{\xi}. \end{cases}$$

So, $\int_{l_-}^{l_+}\frac{\sigma}{\chi} = \int_{l_-}^{l_+} c$. The minimum of H_A is clearly reached in TW steady state at this point since,

$$\int_{l_-}^{l_+} c\partial_{xx}\sigma = \int_{l_-}^{l_+}\frac{\sigma}{\chi}\partial_{xx}\sigma = 0$$

This configuration corresponds to,

$$\partial_{xx}\sigma = 0.$$

This implies that $\sigma \equiv -k\frac{L-L_0}{L_0}$ and then $c \equiv -\frac{k}{\chi}\frac{L-L_0}{L_0}$ is homogeneous. So efficency is a priori not maximum for full localization at the trailing edge but requires a non trivial tradeoff between localization to maximize the speed and homogeneity to minimize H_A.

3.10 Further directions, breaking the symmetry

The pitchfork bifurcation is known to be a signature of a symmetric system [51] which is indeed the case as no direction is a priori "prefered" as the motile segments constituting the stable branch $D1^+$ are symmetric. Two mechanisms may be added that intrinsicly create asymmetry and thus intrinsic polarization. One passive (not requiring energy intake) is a loading device at rear and/or front and one active is polymerization/depolymerization rates inducing growth and retraction of the gel. In this section we only open the subject which will be dealt with in more depth in further studies.

We take into account these asymmetries by setting:

$$\begin{cases} \sigma(l_\pm(t),t) = -k(\frac{L}{L_0} - 1) + q_\pm \\ \dot{l_\pm} = v(s_\pm(t),t) + v_\pm \end{cases}$$

where $v_{\pm} > 0$ are the rates of polymerization/depolymerization of the actin cytoskeleton while $q_+ < 0$ and $q_- > 0$ are dead loads applied at the boundaries that mimic mechanical actions to which the layer is submitted.

The non dimensional problem can than be formulated:

$$\begin{cases} -\mathcal{Z}\partial_{xx}\sigma + \sigma = \mathcal{P}c/c_0 \\ \partial_t c + \mathcal{K}\partial_x(c\partial_x\sigma) = \partial_{xx}c \end{cases}$$

with boundary conditions,

$$\begin{cases} \sigma(l_{\pm}(t), t) = -(L(t) - 1) + q_{\pm} \\ c(l_{\pm}(t), t)v_{\pm} + \partial_x c(l_{\pm}(t), t) = 0 \end{cases}$$

And the Stefan boundary conditions,

$$\dot{l}_{\pm} = \mathcal{K}\partial_x\sigma(l_{\pm}(t), t) + v_{\pm}$$

we also set,

$$\begin{cases} q_+ = Q\frac{\epsilon-1}{2} \\ q_- = Q\frac{\epsilon+1}{2} \end{cases}$$

and,

$$\begin{cases} v_+ = V_m + \frac{\Delta V}{2} \\ v_- = V_m - \frac{\Delta V}{2} \end{cases}$$

We only consider the effect of loads, the effect of polymerization/depolymerization is quiet similar. For simplicity, we set $\epsilon = 0$ implying that there are two equal loads $Q/2$ pushing at the front and pulling at the rear. The level of pushing and of pulling is thus the same. In Chapter III, we will differentiate pushing and pulling in a simpler framework. We also focus on the first motile branch $D1^+$ bifurcating from $\hat{L}_+$ as we know this is the only stable branch. Then the symmetry of the bifurcation diagram is broken as shown in Fig.3.30.

The two symmetric segments related to positive and negative velocity and associated with a center symmetry of profiles are no longer symmetric. The pitchfork bifurcations are broken and saddle-node bifurcations are created for both the motile and non motile solutions.

As a consequence, if we denote by $\mathcal{K}_c$ the critical $\mathcal{K}$ at which the $D1+$ bifurcation arises, for $\mathcal{K} > \mathcal{K}_c$ the force velocity curve (see section 4.3) displays an hysteresis (see Fig.3.31 and Fig.3.32.) With direct numerical simulations of the Cauchy problem, we can investigate which branch of the hysteresis loop is chosen (Arrows of Fig.3.32)

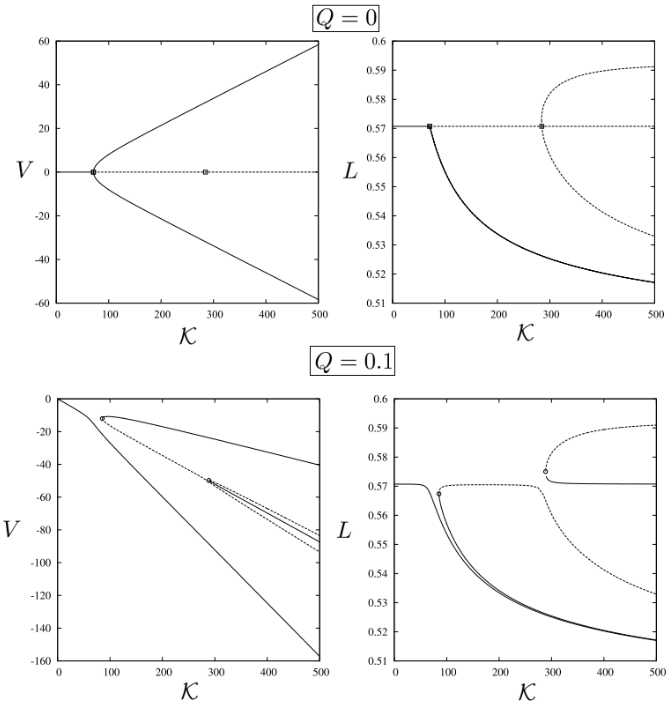

Figure 3.30: Modification of the $D1^+$ under loading, $\epsilon = 0$ and $\mathcal{P} = 0.245$

depending of the loading history. Starting from small enough Q where $V > 0$, the concentration of motors is concentrates at the trailing edge (see c on Fig.3.31, upper line) which is classical. Then while increasing the load, even if velocity becomes negative, the concentration of motors stays concentrated at the same edge until it sudently all switches to the trailing edge again (see c on Fig.3.31, lower line) . After that, reducing the load symetrically leads to the same phenomena in the other direction: when velocity is negative, the motors concentration is at the trailing edge (see c on Fig.3.31, lower line) and remains in the same edge for some loading even though velocity is positive until a critical load at which it switches to the trailing edge again (see c on Fig.3.31, upper line).

As a consequence, the internal sate of the cell (motor distribution) depends on the history of the loading. Arrows of Fig.3.32 indicate which direction is taken on each branch of the hysteresis loop. We finally exhibit a classical cusp catastrophe scheme (See Fig.3.32) which would be very interesting to test experimentally and requires serious investigations since it would imply one speed could be associated to two very different

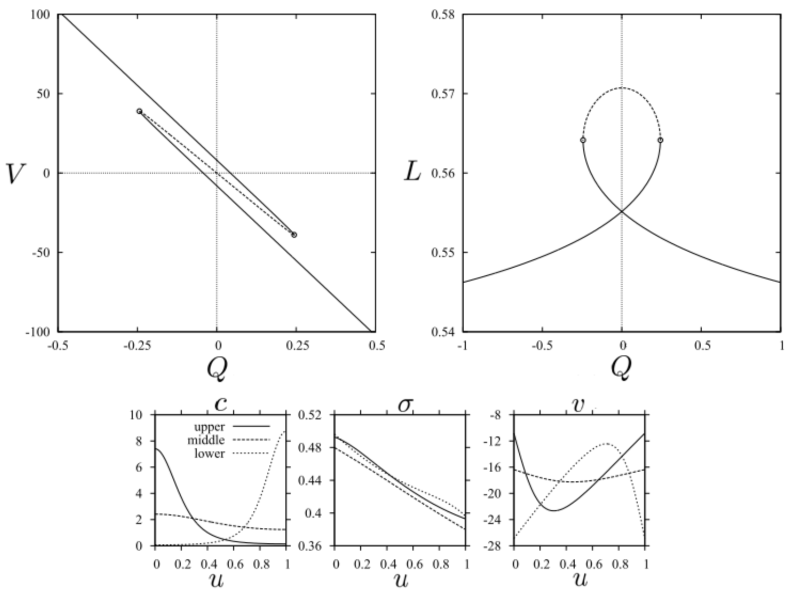

Figure 3.31: Effect of external loading on velocity and length. Parameters: $\mathcal{P} = 0.245$, $\mathcal{K} = 100$, $\epsilon = 0$, Solution profiles are given for $Q = 0.1$

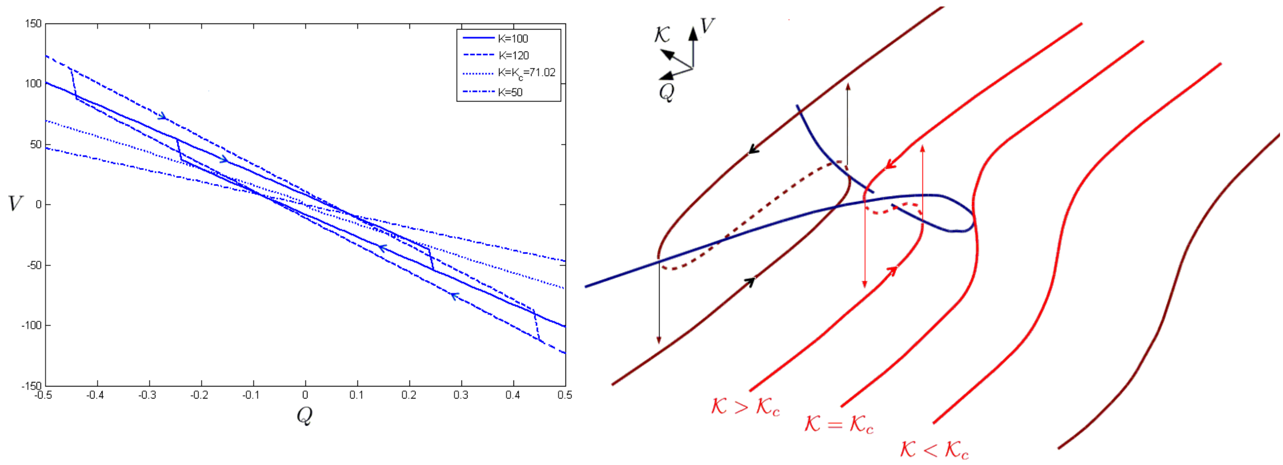

Figure 3.32: Right :Force velocity curves simulated directly from the Cauchy problem for different $\mathcal{K}$. The hysteresis loop appears for $\mathcal{K} > \mathcal{K}_c$ and increases with $\mathcal{K}$. Arrows indicate which direction is taken on each branch of the hysteresis loop depending on the loading history. Parameters are $\mathcal{P} = 0.245$ and $\epsilon = 0$. Left: Scheme of the classical cusp catastrophe in our setting.

concentrations of motors.

3.11 Conclusion

In conclusion, we proposed a prototypical model of a cell showing the possibility of spontaneous polarization leading to steady self propulsion in the conditions when contraction is the only active process while treadmilling is disabled. This model complements the existing theories of polarization which place emphasis on treadmilling and often even ignore contraction. Our model reduces to a Keller-Segel type system with Stefan type boundary conditions however the symmetry breaking is due to mechanical rather than chemical feedback. It generates a variety of motile TW regimes corresponding to finite size self propelling active bodies with free boundaries. Similar to the Navier-Stokes equation where nonlocality is hidden behind the incompressibility assumption the ensuing system has quadratic nonlinearity and shows an infinite sequence of bifurcations as the diffusion coefficient goes to zero.

4

Chapter III: Protrusion at work

Eukaryotic cells possess motility mechanisms allowing them not only to self-propel but also to exert forces on obstacles (to push) and to carry cargoes (to pull). The macroscopic force-velocity relations associated with pushing and pulling are expected to reflect the inherent asymmetry between the two main force generating mechanisms: protrusion and contraction. We use a minimal one dimensional model of the crawling cell to show that the pushing dominated force-velocity relation is controlled by the protrusion mechanism and is described by a concave function. Instead, the pulling dominated force-velocity relation is controlled by the protrusion mechanism only at small values of the force which is replaced by the contraction mechanism at sufficiently large forces. This leads to more complex structure of the force velocity relation, in particular, the interplay between the two mechanisms may produce negative mobility in a biologically relevant range.

4.1 Introduction

A large class of cells including fish keratocytes crawl by protruding the front and retracting the rear. A prototypical scheme of cell motility includes: polymerization of actin network coupled with dynamic assembly of focal adhesions, myosin-driven contraction and, finally, the detachment of adhesive contacts followed by depolymerization which closes the treadmilling cycle. All three main components of the motility mechanism (polymerization, contraction and adhesion) are active and require intricate regulation as well as a continuous supply of energy [1, 53, 77, 126, 153, 169, 181]. While the molecular and biochemical basis of cell motility is basically known, the quantitative understanding of the mechanical interplay between different active components is still limited despite many recent attempts to construct comprehensive mathematical models [56, 75, 163, 184, 187, 188, 196].

In particular, the relative role of contraction and protrusion in exerting forces on obstacles (pushing) and carrying cargoes (pulling) remains hidden behind large scale numerical simulations. Protrusion is known to be the main mechanism of pushing which plays the dominant role in Listeria propulsion [86]. Instead, contraction is crucial for the cell ability to pull organelles. An inherent functional disparity between the protrusion-contraction components of the motility mechanism suggests a fundamental difference in the structure of the force-velocity relations associated with pushing and pulling. Since in experimental studies pushing and pulling are often difficult to distinguish and most of the measured force-velocity data are attributed to pushing [30, 146, 160, 197], it is of great importance to predict the particularities of the cell response to these two loading modalities theoretically.

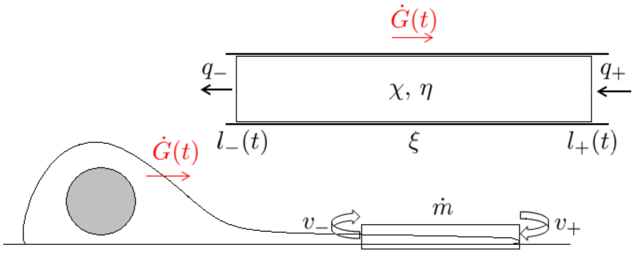

Figure 4.1: Schematic representation of the model.

To capture the basic asymmetry between pushing and pulling we use the simplest model proposed by Kruse et al. [97] which represents the lamellipodium as 1D viscous body with moving boundaries (see Fig.4.1). Actin treadmilling is described as an influx of mass at the front which then disappears at the rear, adhesion is viewed as passive viscous friction and contraction is modeled by a spatially homogeneous prestress. To allow for a nontrivial behavior of the asymmetrically loaded cell we added to this model an overall stiffness which may be ascribed either to a membrane or to elastic components of the cytoskeleton [14, 58, 147, 164]. In the interests of analytical transparency we neglected the stress-mediated nature of active adhesion, the link between contraction and transport of motors and disregarded the distributed character of treadmilling, all of which have been by now successfully integrated into comprehensive computational models [56, 75, 163, 184, 187, 188, 196]. The advantage of our minimal setting is that we can obtain explicit steady state solutions describing asymmetrically loaded self-propelling cells and access stability of these solutions. Such drastic simplification also allows us to compare for the first time the conventional kinematic mode of driving of the cell through the given polymerization/depolymerization velocities with an energetic mode implying direct control by the cell of the ATP driven energy supplies.

4.2 The model

We represent the balance of forces by the equation

$$\partial_x \sigma = \xi v,$$

where $v(x,t)$ is the velocity, $\sigma(x,t)$ is the stress and ξ is the coefficient of viscous friction. The trajectories of the front and the rear boundaries of the cell $l_+(t)$ and $l_-(t)$ are also unknwowns. By using the model of infinitely compressible active fluid we can write

$$\sigma = \chi + \eta \partial_x v,$$

where η is a bulk viscosity and $\chi > 0$ is a spatially homogeneous active pre-stress [97]. The external asymmetric loading is modeled by forces applied at the moving boundaries

$$\sigma(l_\pm(t), t) = q_\pm,$$

where $q_+ < 0$ corresponds to pushing (at the front) and $q_- > 0$ to pulling (at the rear). We first assume that the cell is driven by the prescribed kinematic conditions

$$v(l_\pm(t), t) - \dot{l}_\pm = v_\pm,$$

where $v_+ > 0$ and $v_- > 0$ are the polymerization and the depolymerization velocities, respectively; at the end of the chapter we compare the kinematic driving with an alternative control of the energy intake. If we normalize length by $\sqrt{\eta/\xi}$, time by η/χ and stress by χ, we obtain a free boundary problem containing four dimensionless parameters: two characterize driving ($v_\pm$) and the other two loading ($q_\pm$). It will be convenient to define the total force

$$Q = q_- - q_+ > 0$$

and the asymmetry factor

$$\epsilon = (q_- + q_+)/Q.$$

Then $\epsilon > 0$ corresponds to pulling and $\epsilon < 0$ to pushing. Similarly, we can introduce the maximal cell velocity

$$V_m = (v_- + v_+)/2 > 0$$

characterizing the protrusion power and the velocity asymmetry

$$\Delta V = v_+ - v_- > 0,$$

which, as we show, quantifies the degree of engagement of the contractile mechanism.

4.3 Traveling wave solutions

The force balance equation can be integrated explicitly [97]

$$v(x,t) = \frac{A_- \cosh(l_-(t) - x) + A_+ \cosh(l_+(t) - x)}{\sinh(l_+(t) - l_-(t))}, \tag{4.1}$$

where $A_\pm = \pm(1 - Q(\epsilon \pm 1)/2)$. The elimination of spatial dependence allows one to obtain dynamic equations for the total length $L(t) = l_+(t) - l_-(t)$ and for the position of the geometrical center of the cell $G(t) = (l_+(t) + l_-(t))/2$:

$$\left\{ \begin{array}{l} \dot{L} = \Delta V + (\epsilon Q - 2)\tanh(L/2), \\ \dot{G} = V_m - Q(2\tanh(L/2))^{-1}. \end{array} \right. \tag{4.2}$$

In the $t \to \infty$ limit we obtain a description of a steadily propagating cell with two fronts moving with the same velocity

$$V = V_m - Q/\Delta V + \epsilon Q^2/(2\Delta V); \tag{4.3}$$

the asymptotic cell length is then given by

$$L_\infty = 2\tanh^{-1}(\Delta V/(2 - \epsilon Q)). \tag{4.4}$$

The corresponding asymptotic steady solutions depends only on the reduced coordinate $y = x - Vt$ (traveling waves, TW) and is stable when $2 - \epsilon Q > 0$. We see that pushing $\epsilon < 0$ contributes to stability of a moving cell while pulling $\epsilon > 0$ plays a destabilizing role. Indeed, since the spatial equilibration is assumed to be instantaneous, the non-steady dynamics of the cell is fully described by the two equations Eq.(4.2).

Stable traveling wave solutions with $\dot{L} = 0$ and $\dot{G} = const$ should then be the attractors of this dynamical system. Eq. $(4.2)_1$ above implies that $L(t)$ converges as $t \to \infty$ to a stable equilibrium

$$L_\infty = 2\tanh^{-1}\left(\frac{\Delta V}{2 - \epsilon Q}\right) > 0$$

if and only if $0 < \Delta V < 2 - \epsilon Q$. The cell has a finite size if $0 < \Delta V < 2 - \epsilon Q$: at the lower limit it shrinks to a point while at the upper limit its length diverges. As we show below solutions with $L_\infty = \infty$ (and $V = V_m - Q/2$) are also physically meaningful.

Under these assumptions $\dot{G}$ converges to the constant V given by equations (4.3).

If the initial conditions $L(0)$ and $G(0)$ are known, we obtain the following asymptotic formulas for the fronts $l_\pm(t)$:

$$\begin{cases} l_-(t) \sim Vt - \frac{L_\infty}{2} + G(0) - l_0 \\ l_+(t) \sim Vt + \frac{L_\infty}{2} + G(0) - l_0, \end{cases}$$

where $l_0 = (Q/2\Delta V)\log((\phi^2(1-\phi_0^2))/(\phi_0^2(1-\phi^2)))$, $\phi = (\Delta V/(2-\epsilon Q)$ and $\phi_0 = \tanh(L(0)/2)$.

To find the characteristic time of convergence we can solve $(4.2)_1$ explicitly. At large times, we obtain $|L(t) - L_\infty| \sim e^{-t/\tau}$ where $\tau = (2(2-\epsilon Q))/((2-\epsilon Q)^2 - \Delta V^2)$ is the characteristic time. After this time, which depends on both, the loading (Q, ϵ) and the driving ΔV, the moving cell can be expected to acquire the velocity predicted by the steady force-velocity relation.

4.3.1 Force velocity relations

The structure of the force-velocity relation $V(Q)$, illustrated in Fig.4.2, is expectedly different for $\epsilon > 0$ (pulling) and $\epsilon < 0$ (pushing).

In the case of pushing, where the treadmilling plays major role, the force velocity curve is always concave. It is characterized by the stall force $Q^* = (1 - \sqrt{1 - 2\epsilon\Delta V V_m})/\epsilon$ and the maximum velocity $V^* = V_m$. The concavity of the force velocity relation in the case of pushing agrees with experiments [30, 146, 160, 197].

In the case of pulling, the force-velocity relation is convex for $Q < Q_c = (2 - \Delta V)/\epsilon$, when the length is finite, and is linear for $Q > Q_c$, when the length is infinite (see Fig.4.2). In the convex range the function $V(Q)$ is non-monotone when $\Delta V < 1$ and we can distinguish two regimes: the protrusion dominated branch $Q < Q_n = 1/\epsilon$

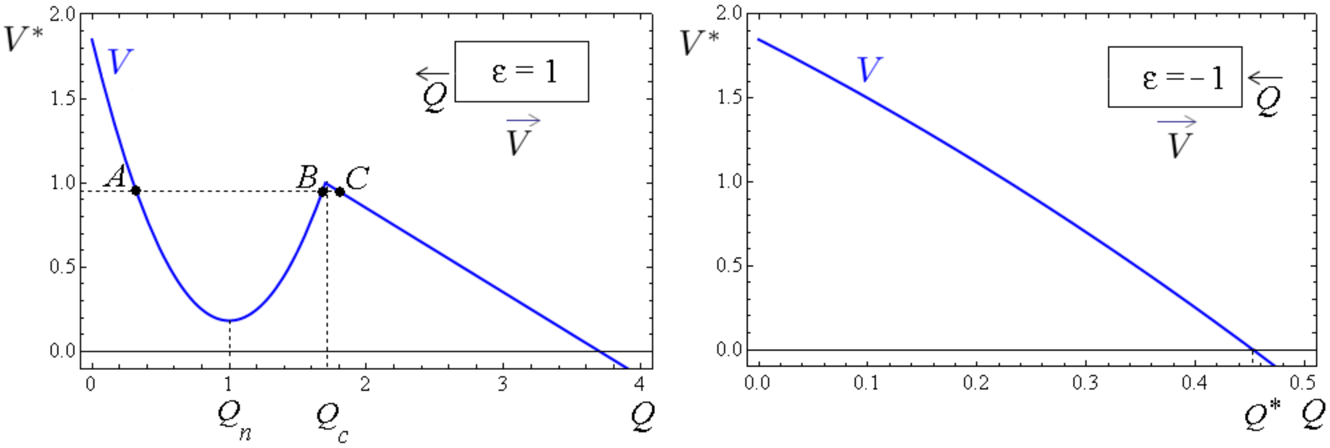

Figure 4.2: Force-velocity relations in the cases of pure pulling and pushing loading modes. Stress and density profiles corresponding to points A,B and C (discussed in the text) are shown in Fig.4.3. Driving parameters are $v_- = 1.7$ and $v_+ = 2$.

where the mobility is positive and $V(Q) \sim V_m - Q/\Delta V$, and the contraction dominated branch $Q_c > Q > Q_n$ where the mobility is negative and $V(Q) \sim \epsilon Q^2/(2\Delta V)$. Along the negative mobility branch the cell elongates to support larger loads till the length diverges at a critical value $Q = Q_c$. Beyond this value, we obtain configurations with infinitely separated boundary layers and mobility becomes again positive.

To illustrate the different roles played by the two active mechanisms (treadmilling and contraction) in the case of asymmetric cargoes, we need to consider the overall balance of moments because the overall force balance does not see active contributions [39, 97]. If we multiply the force balance equation in the steady state regime by the TW coordinate $y = x - Vt$ and integrate over the body of the cell we obtain

$$-\frac{1}{L_\infty}\int_0^{L_\infty/2}(y - L_\infty/2)v(y)dy + Q\frac{\epsilon}{2} = \frac{1}{L_\infty}\int_0^{L_\infty/2}\sigma(y)dy$$

The terms on the left represent the frictional dipole and the moment of applied forces. The integral on the right defines the active dipole

$$(1/L_\infty)\int_0^{L_\infty/2}(1 + \partial_y v)dy,$$

which can be decomposed into the sum of a treadmilling contribution

$$T_t = -\Delta V/L_\infty(Q, \epsilon) < 0$$

and a contraction contribution

$$T_c = 1 > 0.$$

The opposite signs of these terms suggest that the underlying active mechanisms are inherently different and can be viewed as a "pusher" and a "puller" in the terminology of the theory of active suspensions [157, 168]. Due to the presence of a contraction dipole the rear of the cell is pulled forward while the front is pulled backward. The treadmilling/protrusion induced force dipole acts in the opposite way: it pushes the rear of the cell backward while pushing the front of the cell forward. Both active dipoles induce internal flows superimposed on top of the mean flow $\bar{v} = -Q/L_\infty$ which is always retrograde: contraction produces prograde flow at the front and retrograde flow at the rear while treadmilling produces retrograde flow at the front and prograde at the rear. One way to locate the transition from positive to negative mobility is to identify the level of pulling when the relative flow at the rear starts being retrograde, which gives the theoretical threshold value $Q_n = 1/\epsilon = 1$. One can show that in the case of realistic $\Delta V = 0.3$ [97] the corresponding condition of 'contraction domination' is $|T_c| \sim 2|T_t|$ which gives the value of the force $Q^* \sim 2 - \Delta V/\tanh^{-1}(\Delta V) = 0.97$ quite close to the above threshold .

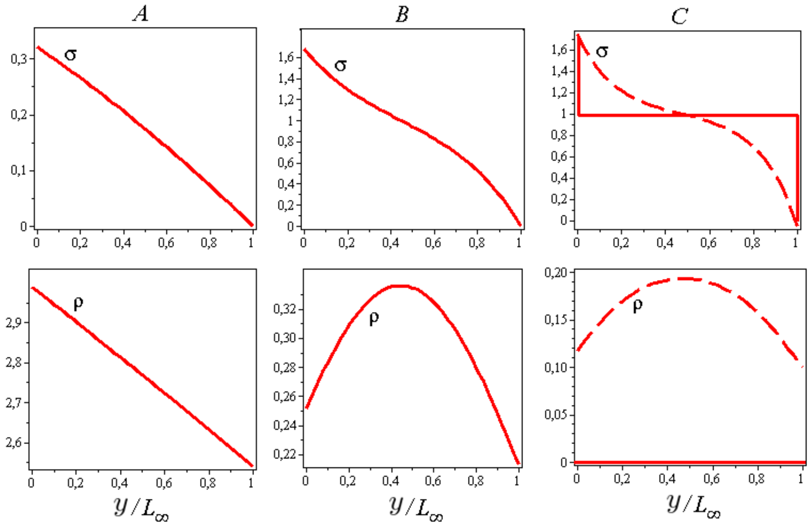

Figure 4.3: Stress and density distribution inside a moving cell in the regimes indicated as A, B and C in Fig.4.2. Dashed line shows elasticity-regularized profiles corresponding to point C' in Fig.4.15.

Negative mobility has been discussed previously in the context of individual [49, 70, 112, 155] and interacting [29, 135] Brownian motors. The regimes where velocity of the crawling cell increases with opposing force have been envisioned in [85] where the overall negative mobility was attributed to the coupling between the velocity of protrusion and the applied force $v_-(Q)$ [143]. In our study such coupling is neglected which shows that negative mobility may be also related to contraction.

To estimate if negative motility is feasible for real cells we use the data from [97]: $\chi = 10^3 Pa$, $\xi = 5\times10^{16} Pa{\cdot}m^{-2}{\cdot}s$, $\eta = 5\times10^4 Pa{\cdot}s$, $v_+ = 2$ and $v_- = 1.7$. We obtain for the velocity $(\chi/\sqrt{\xi\eta})V^* = 0.37\times10^{-7} m\cdot s^{-1}$ and for the length $\sqrt{\eta}\xi L^*_\infty = 0.3\times10^{-7} m$ which is realistic [145]. In the case of pure pushing $\epsilon = -1$, we can use the area scale $S = 10^{-12} m^2$ to obtain for the stall force $\chi S Q^* = 1 nN$ which also falls into the range of accepted values [30, 146, 160, 197]. Similar estimates show that in the case of pure pulling $\epsilon = 1$, negative motility can be expected in the interval of loadings $1 - 1.7 nN$ [30, 146, 160, 197].

4.3.2 Spatial inhomogeneity of the friction coefficient

Some additional effects due to spatial inhomogeneity of the friction coefficient can be studied if we assume that in the steadily moving cell ξ is graded from rear to front. For instance, ξ may be viewed as proportional to the density of focal contacts which are known to concentrate in the frontal part of the advancing lamellipodium (see [26, 191] for nematode spermatozoa and [156] for keratocytes). If the friction coefficient is spatially inhomogeneous $\xi = \xi(y)$ with $y \in [-L_\infty/2, L_\infty/2]$ is the traveling wave coordinate $y = x - Vt$, the steady state problem can be written:

$$\left\{\begin{array}{c} -\eta\partial_y((1/\xi(y))\partial_y\sigma) + \sigma = 1 \\ \sigma(-L_\infty/2) = q_- \text{ and } \sigma(L_\infty/2) = q_+ \\ V = (\partial_y\sigma/\xi(y))(-L_\infty/2) + v_- \text{ and } V = (\partial_y\sigma/\xi(y))(L_\infty/2) + v_+ \end{array}\right. \tag{4.5}$$

The solution of the Sturm-Liouville problem (4.5) can be expressed in terms of two linearly independent functions $A(y)$ and $B(y)$ solving the following elementary problems [120]:

$$\left\{\begin{array}{c} A'' = \xi(y)A \\ A'(-L_\infty/2) = 1 = A'(L_\infty/2), \end{array}\right.$$

and

$$\left\{\begin{array}{c} B'' = \xi(y)B \\ B'(-L_\infty/2) = 1 \text{ and } B'(L_\infty/2) = -1. \end{array}\right.$$

By using solutions of these equations $A(y)$ and $B(y)$, we can write the force velocity relation in the following implicit form

$$\begin{cases} \Delta V = (2-Q\epsilon)\mathcal{A}(A)(L_\infty/2) + Q\mathcal{S}(A)(L_\infty/2) \\ V = V_m + ((2-Q\epsilon)/2)\mathcal{A}(B)(L_\infty/2) + \frac{Q}{2}\mathcal{S}(B)(L_\infty/2) \end{cases}$$

where $\mathcal{A}(f)(y) = (f(y)-f(-y))/2$, $\mathcal{S}(f)(y) = (f(y)+f(-y))/2$. Suppose, for instance, that $\xi(y) = 1 + \theta\xi_1(y)$, where $\theta << 1$ is a small parameter and the function $\xi_1(y)$ is odd. Then, up to higher order terms in θ we obtain:

$$\begin{cases} \mathcal{A}(A)(L_\infty/2) = \tanh(L_\infty/2) \\ \mathcal{S}(A)(L_\infty/2) = -\frac{\theta}{2\sinh(L_\infty)}\int_{-L_\infty/2}^{L_\infty/2}\sinh(2y)\xi_1(y)dy \\ \mathcal{A}(B)(L_\infty/2) = \frac{\theta}{2\sinh(L_\infty)}\int_{-L_\infty/2}^{L_\infty/2}\sinh(2y)\xi_1(y)dy \\ \mathcal{S}(B)(L_\infty/2) = -(\tanh(L_\infty/2))^{-1} \end{cases}$$

In the case $Q = 0$ the explicit force velocity relation takes the form

$$V - V_m = \frac{\theta}{2\sinh(L_\infty)}\int_{-L_\infty/2}^{L_\infty/2}\sinh(2y)\xi_1(y)dy.$$

and one can see that $V > V_m$ if the friction is stronger at the front (contraction increases velocity) and $V < V_m$ if it is stronger at the back (contraction slows down the cell). In the case of general loads, $Q > 0$, we obtain an implicit representation of the force velocity relation:

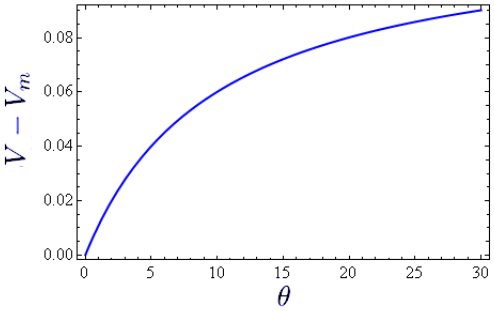

Figure 4.4: The behavior of the function $V(\theta)$ for $\xi_1(y) = \exp(10(y/L_\infty - 1/2))$

$$\begin{cases} \Delta V = (2-Q\epsilon)\tanh(\frac{L_\infty}{2}) - \frac{2Q\theta}{\sinh(L_\infty)}\int_0^{L_\infty/2}\sinh(2y)\xi_1(y)dy \\ V = V_m + \frac{\theta(2-Q\epsilon)}{\sinh(L_\infty)}\int_0^{L_\infty/2}\sinh(2y)\xi_1(y)dy - \frac{Q}{2\tanh(\frac{L_\infty}{2})} \end{cases}$$

Given that the integral $\int_0^{L_\infty/2}\sinh(2y)\xi_1(y)dy$ is positive in the case of the frictional bias at the front, we obtain in this case larger lengths and faster velocities. If, instead, the friction is stronger at the back, the cell will have smaller length and will move slower. These results are compatible with the observation that adhesion complexes predominantly position themselves at the front of the moving cell [26, 156, 191].

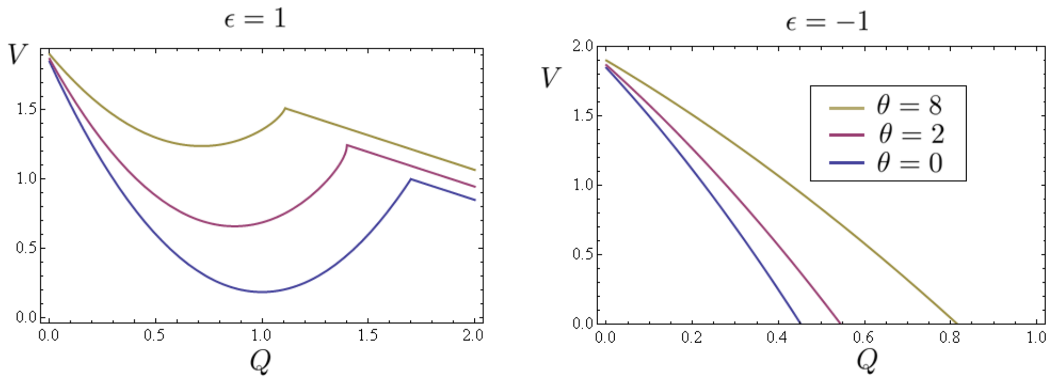

Figure 4.5: Force velocity relations with θ as a parameter.

In Fig.4.4 and Fig.4.5 we illustrate our results by using exponential bias function $\xi_1(y) = \exp(10(y/L_\infty - 1/2))$. In this setting if the front concentration of adhesive complexes is twice as high as at the rear we obtain $\theta = 2$ and if it is four times larger, we should take $\theta = 8$. From Fig.4.5 we see that even in the case of inhomogeneity level plausible for keratocyte $\theta = 8$ [156] the general shape of the force velocity curves remains qualitatively the same.

4.4 Density distribution

The assumption of infinite compressibility allows one to decouple the problem of finding density distribution from the problem of finding the stress and the velocity profiles. Then, after the 'statically determinate' mechanical problem is solved the density can be obtained by solving an auxiliary problem. Here we consider three different formulations of this problem. In the first model, which is in line with the original formulation, we assume that both polymerization and depolymerization are concentrated on the boundaries of the body and are associated with velocities v_+ and v_-, respectively. In the second model we assume that polymerization is localized in the front and is associated with v_+ while depolymerization is not localized at the back ($v_- = 0$) but is distributed and takes place everywhere in the bulk. Finally, we briefly consider the third model where both polymerization and depolymerization are localized as in the first model however the contraction stress is not constant but is a function of actin density. Then the mechanics and the mass transport become coupled and the problem can only be treated numerically. In all these cases we show that the main effects reported in the chapter remain robust.

4.4.1 Localized depolymerization

The evolution of actin density is described by the following initial value problem:

$$\begin{cases} \partial_t \rho + \partial_x(\rho v) = 0 \\ \rho(x,0) = \rho_i(x) \\ \frac{\rho(l_+(t),t)}{\rho(l_-(t),t)} = \frac{v_-}{v_+} \end{cases} \tag{4.6}$$

where the velocity distribution $v(x, l_-(t), l_+(t))$ is assumed to be known. Problem (4.6) can be solved by the method of characteristics. For instance, for a characteristic $x = \phi_{t_0}(t)$ entering the cell domain at time $t_0 > 0$ we can write

$$\begin{cases} \frac{d\phi_{t_0}(t)}{dt} = v(\phi_{t_0}(t); l_-(t), l_+(t)) \\ \phi_{t_0}(t_0) = l_+(t_0) \end{cases} \tag{4.7}$$

After the characteristics are known, the density can be recovered from the relation,

$$\rho(\phi(t),t) = \rho(\phi(t_0),t_0) \exp(-\int_{t_0}^{t} \partial_x v(\phi(u); l_-(u), l_+(u)) du).$$

In the steady state (TW) regime,

$$\begin{cases} l_-(t) = Vt \\ l_+(t) = L_\infty + Vt \\ v(x,t) = v(x - Vt) \end{cases}$$

the problem of density recovery is much simpler. Since $\rho = \rho(x - Vt)$ the mass balance equation can be integrated explicitly and we obtain,

$$\rho(x - Vt) = \frac{\dot{m}}{v(x - Vt) - V} \tag{4.8}$$

where $\dot{m}$ is the constant mass flux. Since the dimensionless total mass of the cell is equal to 1, we obtain $\dot{m} = (\int_0^{L_\infty} \frac{dy}{v(y) - V})^{-1}$. This gives us the final expression for the steady state density profile,

$$\rho(x - Vt) = \frac{1}{(v(x - Vt) - V) \int_0^{L_\infty} \frac{dy}{v(y) - V}}.$$

As we have shown, in the treadmilling dominated regime the relative flow (with respect to the mean flow) is prograde at the rear and retrograde at the front. If we superimpose it with the retrograde mean flow and subtract V we obtain a globally retrograde flow slowing down at the back of the cell where the density concentrates, see also [97]. On the contrary, the contraction dominated regime displays a prograde flow at the front and a retrograde flow at the rear. If we superimpose it again with a mean retrograde flow and subtract V we obtain that the retrograde flow is the strongest at the back of the cell but slows down at the front. This creates a tendency for the density maximum to move from the back towards the front of the cell and explains the observed mass accumulation at the center in the regime with negative mobility (see Fig.4.3).

In Fig.4.3, we presented the structure of the density profile for the case of sufficiently strong pulling in order to explain the mechanism of the switch from protrusion dominated to contraction dominated motility. In Fig.4.6 we present the profiles at zero load which are also typical for both weak pushing and pulling. The profiles of stress and velocity at $Q = 0$ have been already presented in the earlier papers [89, 97] and here we complement the picture by presenting the associated density profile as well. One can see that the density profile is in agreement with the velocity profile displaying (as can expected from our discussion above) a prograde flow at the front and a retrograde flow at the rear.

Adding a load generates a non zero mean flow which shifts the velocity profile. To illustrate the effect of this shift on the density profile we present in Fig.4.7 the inner configuration of the cell in the case of strong pushing, namely, at the stall force $Q = Q^*$.

4.4.2 Delocalized depolymerization

While the hypothesis of localized depolymerization [97] is very helpful in simplifying the motility problem, it has been argued repeatedly that depolymerization takes place everywhere in the body in a diffuse mode and has to be treated as a bulk rather than a surface phenomenon [172, 174]. To check how this changes our results, we consider the setting where $v_- = 0$ (no localized depolymerization) while the mass conservation

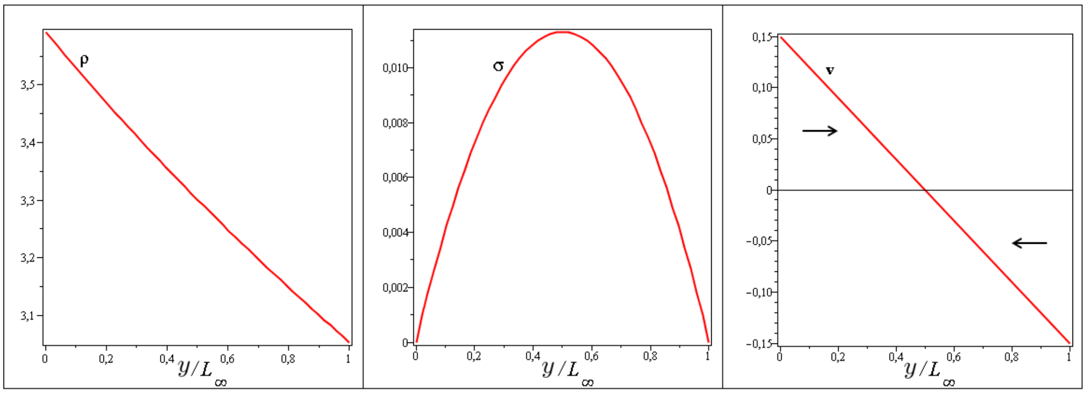

Figure 4.6: Density, stress and velocity profiles for $Q = 0$. Parameters $v_- = 1.7$ and $v_+ = 2$.

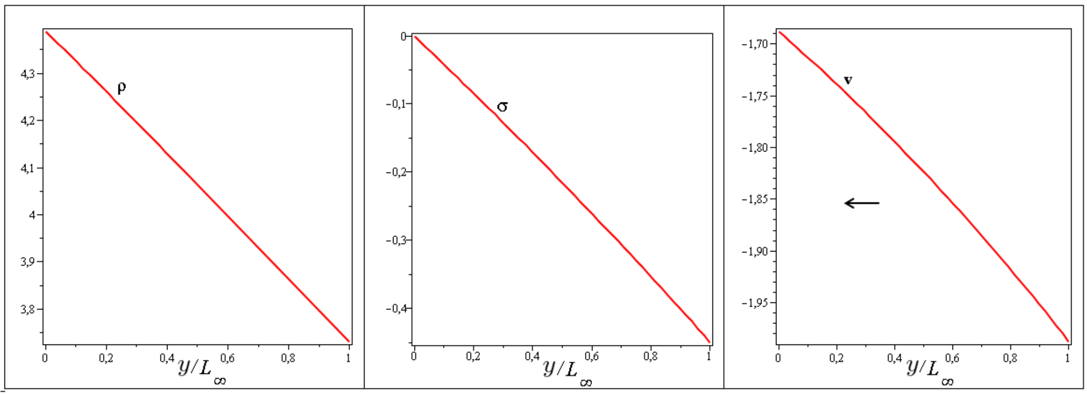

Figure 4.7: Density, stress and velocity profiles for $Q = Q^*$ and $\epsilon = -1$. Parameters $v_- = 1.7$ and $v_+ = 2$.

equation for actin has a source

$$\partial_t \rho + \partial_x(\rho v) = -\gamma\rho \tag{4.9}$$

The coefficient γ is usually estimated in the range $0.01 - 0.05s^{-1}$ [15, 102, 156].

One can see that such reformulation affects the mechanical problem only through the assumption $v_- = 0$ which gives $\Delta V = v_+$ and $V = v_+/2$. This means that such flows are associated with the line $\Delta V = 2V_m$ in Fig.4.14. Despite such narrowing of the class of boundary conditions the general formula (4.1) for the particle velocity and the general formulas for the velocities of the boundaries (4.2) remain the same. The stability condition takes the form

$$0 < v_+ < 2 - \epsilon Q$$

which means that our assumption that $v_+ \simeq 2$ in the case of pulling is not adequate any more and we must take a smaller value $v_+ \simeq 1$ which is also plausible in view of [89, 91, 102, 172]. We observe that in the presence of elasticity (mean field or not but necessarily penalizing infinite stretching, see Section 4.6) this problem disappears and all the analysis of mechanical problem made in the chapter holds.

Then the auxiliary boundary value problem for actin density will be first formulated in the dimensional form

$$\begin{cases} \partial_t \rho + \partial_x(\rho v) = -\gamma \rho \\ \rho(l_+(t), t) = \frac{\gamma M}{v_+} \end{cases}$$

The boundary condition accounts for the fact that the total mass of actin $M = \int_{l_-(t)}^{l_+(t)} \rho(x,t)dx$ is constant and all the actin depolymerized in the bulk is instantaneously repolymerized at the front. Indeed, given this boundary condition we obtain that

$$\frac{dM}{dt} = -\gamma M + \rho(l_+(t), t)v_+ = 0.$$

We can now absorb M into the scaling of ρ by setting $\hat{\rho} = \rho/\rho_0$ with $\rho_0 = M/\sqrt{\frac{\eta}{\xi}}$. The normalized problem depends on the new nondimensional parameter $\hat{\gamma} = \eta\gamma/\chi \sim 0.5 - 2.5$ and can be written as

$$\begin{cases} \partial_{\hat{t}} \hat{\rho} + \partial_{\hat{x}}(\hat{\rho}\hat{v}) = -\hat{\gamma}\hat{\rho} \\ \hat{\rho}(\hat{s}_+(\hat{t}), \hat{t}) = \frac{\hat{\gamma}}{v_+} \end{cases}$$

We can now omit the hats and write equation describing the steady TW solution

$$\partial_y(\rho(v - V)) = -\gamma \rho$$

where we recall that $y = x - Vt$. If we introduce the treadmilling mass flux $\dot{m} = -\gamma$, we may write the solution of this equation in the form

$$\rho(y) = -\frac{\dot{m}}{V - v(y)} \exp\left(\int_y^{L_\infty} \frac{\dot{m}}{V - v(u)} du\right) \tag{4.10}$$

Here the pre-exponential factor is exactly the same as in the expression for density in the case of localized depolymerization (4.8). The exponential term describes modulation due to distributed depolymerization.

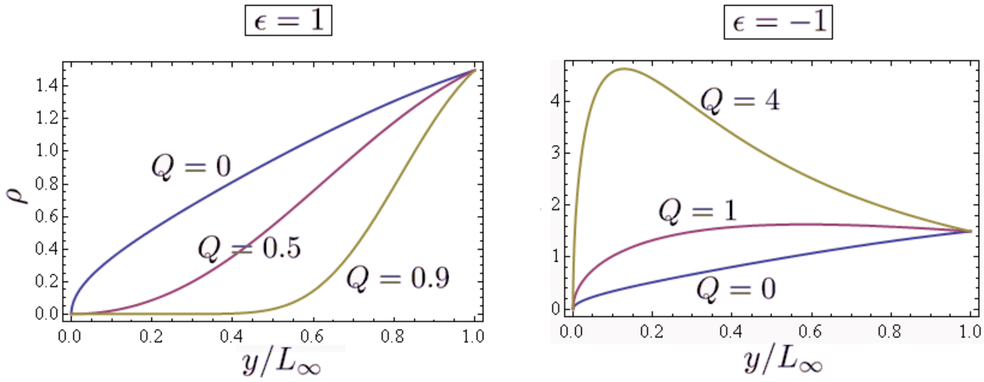

Figure 4.8: Densities in the pulling and pushing modes for $v_+ = 1$ and $\gamma = 1.5$

To see the role of this modulation we can compare the value of actin density at the front $\rho(L_\infty)$ and at the back $\rho(0)$. Since both v_+ and the mass flux $\dot{m}$ are known, we obtain

$$\rho(L_\infty) = \frac{\gamma}{v_+}.$$

To find the value at the back we need to study the asymptotics of the integral term in 4.10 which gives at small y

$$\rho(0) \sim \frac{1}{A_+} \frac{A_- - A_+}{-2A_+ \sinh(L_\infty)} y^{\frac{\gamma}{A_+} - 1},$$

where A_+ and A_- are defined in section 4.2 . From this formula we see that in the interesting case when for $\gamma > A_+$ (in our case $\gamma > 1$ ensures this inequality) that $\rho(0) = 0$. In Fig.4.8 we choose $\gamma = 1.5$ and $v_+ = 1$ and show the resulting density profiles for both pure pushing and pure pulling cases. One can see that distributed depolymerization results for the unloaded cells in an exponential decay of actin density from the front to the back which agrees with observations [91, 160, 172]. It is clear that the fine structure of the density profile in the front, which is dominated by microscopic interaction of the actin network with the membrane, is not captured by our simplified model.

From this analysis we see that the structure of the density profile can be quite different depending on the model of actin polymerization. However, in view of the fundamental decoupling between mechanics and transport in our setting, these modifications of the model do not affect the mechanical part of the problem, in particular, the force velocity relations remain unchanged. This shows the robustness of our predictions can be claimed for the whole class of models with such basic decoupling which is based on the hypotheses of infinite compressibility and density independent contraction. The former assumption will be critically tested in a special section devoted to elasticity while below we briefly address the effect of the coupling between contraction stress and actin density.

4.4.3 Density dependent contraction

It is clear that contractile pre-stress should depend on both actin and myosin densities. A rather general theory of such active gels has been developed in [96, 99, 101] where a rich variety of dynamic behaviors was discovered. However, the problem was studied in a fixed domain and therefore the force velocity relation could not be computed. Here we simplify the general setting presented in [101] by neglecting the coupling of contractility with myosin, which has been studied in detail in [25], and considering only actin filaments of the same orientation. We also assume that the dependence of active forces on actin density is not linear as in [101] but is non-monotone as proposed in [7, 8, 65, 170]. We are replacing a heuristic kernel describing microscopic interactions [96, 99, 101] by a direct solution of the mechanical problem in addition to the mass transportation problem.

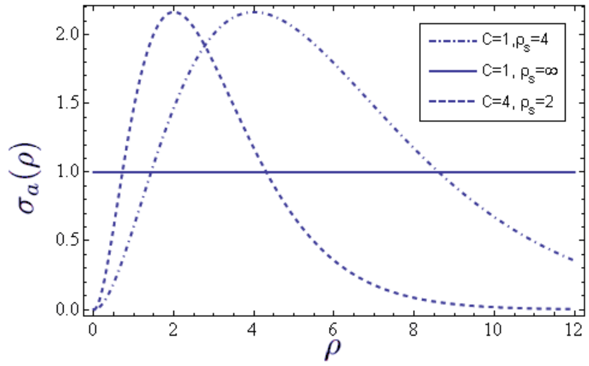

Figure 4.9: Contractile stress σ_a as a function of actin density ρ for different choices of parameters ρ_s and C taken from [65].

More specifically, we model the dependence of active stress on actin density by the following (dimensionless) relation [65]

$$\sigma_a(\rho) = C\rho^2 \exp(-2\frac{\rho}{\rho_s}).$$

Here C is a constant coefficient and ρ_s is the actin saturation density, see Fig.4.9). We then write the coupled problem in the form:

Mechanical model:

$$\left\{ \begin{array}{c} -\partial_{xx}\sigma + \sigma = \sigma_a(\rho) \\ \sigma(l_-(t),t) = q_- \text{ and } \sigma(l_+(t),t) = q_+ \end{array} \right. \tag{4.11}$$

Polymerization model:

$$\left\{ \begin{array}{l} \dot{l}_- = v_- + \partial_x\sigma(l_-(t),t) \\ \dot{l}_+ = v_+ + \partial_x\sigma(l_+(t),t) \\ l_-(0) = l_-^0 < l_+(0) = l_+^0 \end{array} \right. \tag{4.12}$$

Transportation model:

$$\left\{ \begin{array}{c} \partial_t\rho + \partial_x(\partial_x\sigma\rho) = 0 \\ \rho(l_-(t),t)v_- = \rho(l_+(t),t)v_+ \\ \rho(x,0) = \rho_i(x) \end{array} \right. \tag{4.13}$$

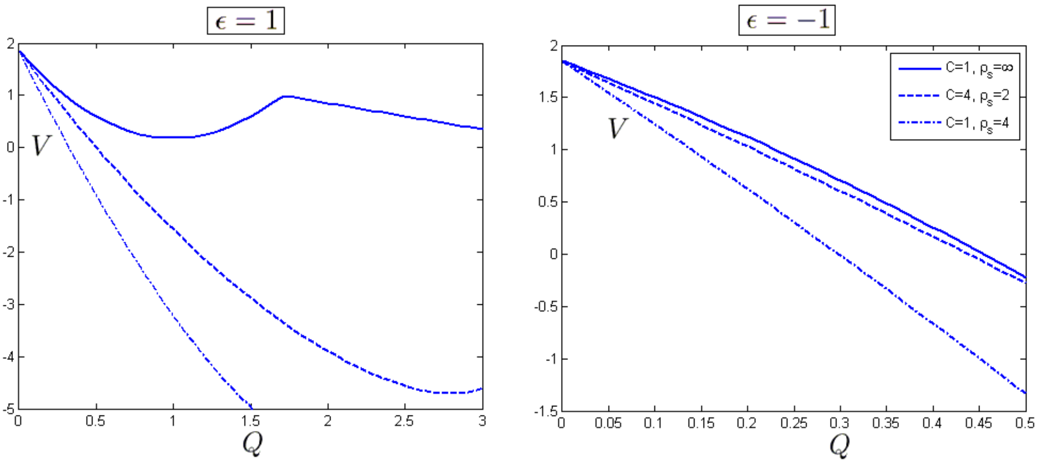

Figure 4.10: Force velocity relations for the model with actin dependant contractility. Parameters are $v_- = 1.7$, $v_+ = 2$. Initial data are $l_-^0 = 0$, $l_+^0 = 1$ and $\rho_i(x) = \frac{2}{1+v_-/v_+}\left(1 + \left(\frac{v_-}{v_+} - 1\right)x\right)$ which is the simplest choice compatible with the boundary conditions and requirement that $\int_{l_-^0}^{l_+^0} \rho = 1$.

By solving these equations numerically we can obtain the corresponding force velocity relations in both pushing and pulling regimes. This can be done in two ways. We can either assume traveling wave ansatz and solve the corresponding system of ODE by following the trivial static branch till it becomes unstable giving rise to a nontrivial dynamic TW solution. However in this case we discover the whole set of solutions including both stable and unstable. Therefore, here we follow another part and directly solve an initial value problem for the system of PDEs (4.11-4.13) and waiting for our solution to approach a stable TW attractor. Then by varying the initial data one can reach traveling waves moving with different velocities and in this way recover the full force-velocity relation. Full parametric study will be presented elsewhere and here we show only a sample of our results illustrating that the imposed coupling does not destroy the difference in convexity properties of the force velocity relations between the cases of pushing and pulling (see Fig.4.10). One can see that the conclusions of the paper are robust.

To obtain these numerical results we used the following algorithm. We first map the system (4.11-4.13) onto a fixed interval $[0,1]$ by making coordinate changes $u = \frac{x-l_-(t)}{L(t)}$ and $Y(t) = \rho L(t)$. Then, (4.11-4.13) becomes :

$$\left\{ \begin{array}{c} -\frac{1}{L^2}\partial_{uu}\sigma + \sigma = \sigma_a(\frac{Y}{L}) \\ \sigma(0,t) = q_- \text{ and } \sigma(1,t) = q_+ \end{array} \right. \tag{4.14}$$

$$\left\{ \begin{array}{c} \dot{l}_- = v_- + \frac{1}{L}\partial_u\sigma(0,t) \\ \dot{l}_+ = v_+ + \frac{1}{L}\partial_u\sigma(1,t) \\ l_-(0) = l_-^0 < l_+(0) = l_+^0 \end{array} \right. \tag{4.15}$$

$$\left\{ \begin{array}{c} \partial_t Y + \frac{1}{L}\partial_u(Y(\frac{\partial_u\sigma}{L} - \dot{l}_- - u\dot{L})) = 0 \\ Y(0,t)v_- = Y(1,t)v_+ \\ Y(y,0) = Y_i(y) \end{array} \right. \tag{4.16}$$

We then build two grids on the same interval $[0,1]$: a grid Z and its dual Z_d. By using the initial condition involving the normalized concentration profile Y_i, Eq.$(4.14)_1$ is solved and the effective drift term in Eq.$(4.16)_1$, $\partial_u\sigma/L - \left(\dot{l}_- + u\dot{L}\right)$ is computed on Z_d. We then apply an upwind finite volume scheme to Eq.$(4.16)_1$ and find the updated normalized concentration profile Y on Z which now corresponds to the next time step. Then the same procedure is repeated. The time step is chosen in an adaptive way in order to satisfy the Courant-Friedrichs-Lewy condition uniformly on Z_d.

As a note (we leave serious work in this direction to further study) we remark that when the traveling wave is no longer stable, other interesting regimes can be found. Namely, if we suppose for simplicty that,

$$\sigma_a(\rho) = \rho$$

then, the solution always tend to developp an infinite length which implies that the contractility pointwisely goes to zero and we have "dissolution" of the cell. This because again, some long time global elastic resitance (membrane, cytoskeleton) has not been considered. We incorporate this missing physical feature by adding a mean field elasticity (see Section4.6):

$$\begin{cases} -\frac{1}{L^2}\partial_{uu}\sigma + \sigma = \sigma_a(\frac{Y}{L}) \\ \sigma(0,t) = -k\frac{L-L_0}{L_0} \text{ and } \sigma(1,t) = -k\frac{L-L_0}{L_0} \end{cases}$$

then, dissolution is prevented and we find an oscillatory behavior of the fronts [4, 31, 38, 162] with an actin soliton wave (expected from [56, 96, 99, 101]) constantly treadmilling throughout the lamellipodium. See Fig.4.11.

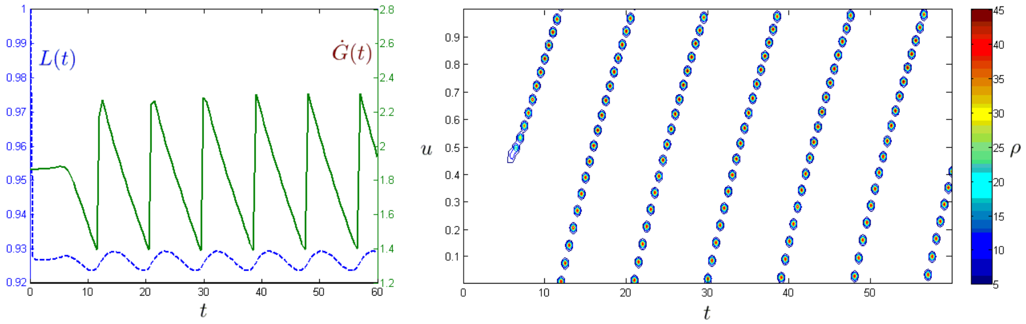

Figure 4.11: Behavior of cell length and speed and actin traveling pulse as a function of time. Parameters are $v_- = 1.7$, $v_+ = 2$, $k = 10$ and $L_0 = 1$. Initial data are $l^0_- = 0$, $l^0_+ = 1$ and $\rho_i(x) = \frac{2}{1+v_-/v_+}\left(1 + \left(\frac{v_-}{v_+} - 1\right)x\right)$ which is the simplest choice compatible with the boundary conditions and requirement that $\int_{l^0_-}^{l^0_+} \rho = 1$.

We believe the simplicity (linear dependance of contractility) of the model shall open the path to analytic understanding of the phenemenon as done in Chapter II which will lack the realistic non gaussian distribution of the membrane fluctuations but can shed considerable light on the phenomenon.

4.5 Energetics

Next we show that the divergence of the cell size at $Q \geq Q_c$ does not compromise energetics. To this end we define the work against the external forces $A = (q\dot{l})_- - (q\dot{l})_+$, the energy consumption associated with treadmilling $P_t = (vq)_- - (vq)_+$ and the power of contraction $P_c = \chi(v_+ - v_-)$. The efficiency of the energy transduction is then $\Lambda = A/(P_t + P_c)$. Notice this efficiency is different from the one defined in Sections 2.4 and 3.9 since in the presence of loads some mechanical work has to be performed to carry them. The Stokes term accounding for motility without loads could be added at the numerator. We also did not consider the maintenance heat term supposing it is negligible with repect to $P_t + P_c$. All such terms can be added easily but screen the main effect associated to loading which is studied here.

By using our steady state (TW) solution we obtain $P_t + P_c = \Delta V + QV_m - \epsilon Q\Delta V/2$ and $\Lambda = QV/(\Delta V + QV_m - \epsilon Q\Delta V/2)$. One can see that the energy consumption remains finite even in the singular regimes. A direct computation of efficiency-load relation shows that it displays a usual single maximum in the case of pushing and becomes bi-modal in the case of pulling which may carry some biological advantages (See Fig.4.12). By multiplying the force balance equation by $v(x,t)$ we obtain the energy balance equation

$$\int_{l_-(t)}^{l_+(t)} v^2 + \int_{l_-(t)}^{l_+(t)} (\partial_x v)^2 + \int_{l_-(t)}^{l_+(t)} \partial_x v = [\sigma v]_{l_-(t)}^{l_+(t)},$$

where we can identify the following contributions:

1. $D = \int_{l_-(t)}^{l_+(t)} v^2 + \int_{l_-(t)}^{l_+(t)} (\partial_x v)^2$, dissipation rate associated with surface friction and bulk viscosity.
2. $P_c = -\int_{l_-(t)}^{l_+(t)} \partial_x v > 0$, rate of energy consumption by the contractile mechanism.
3. $P_t = (qv)_- - (qv)_+ > 0$, rate of energy consumption by the treadmilling mechanism.
4. $A = (q\dot{l})_- - (q\dot{l})_+$, the power expanded against the external forces.

In these notations the energy balance can be written as $P_t + P_c = A + D$ and the mechanical efficiency can be defined as follows:

$$\Lambda = \frac{A}{P_t + P_c}$$

It is now easy to show that that $0 < |\Lambda| < 1$ and in the traveling wave limit, the efficiency can be computed explicitly

$$\Lambda = \frac{QV}{\Delta V + QV_m - \epsilon Q \Delta V/2}.$$

For the regimes presented in Fig.4.3 both, the efficiency Λ and the energy consumption rate $P_t + P_c$, are shown in Fig.4.12. One can see that in the pulling regime, the the function $\Lambda(Q)$ displays two maxima. We also observe that the divergence of the cell length does not lead to singular behavior of either the rate of energy consumption or the efficiency. If mean field elasticity (see Section 4.6) is taken into account, energy balance takes the form

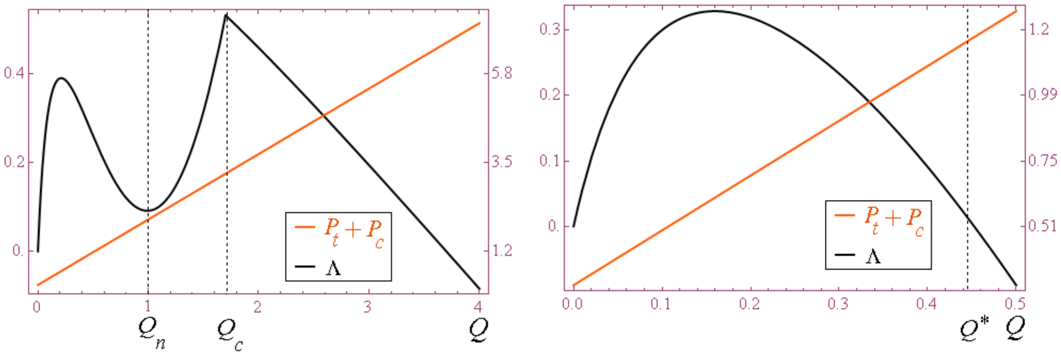

Figure 4.12: Rate of energy consumption and efficiency as functions of the load in the cases of pure pulling and pushing loading modes. The corresponding force velocity relation is shown in Fig.4.2. Driving parameters are $v_- = 1.7$ and $v_+ = 2$.

$$P_t + P_c + P_e = A + D.$$

The elasticity related contribution

$$P_e = -k\frac{L - L_0}{L_0}(\dot{L} - \Delta V)$$

remains nonzero also in TW regime where $\dot{L} = 0$

$$P_e = k\frac{L - L_0}{L_0}\Delta V$$

This contribution can be interpreted as rate of energy consumption by the treadmilling mechanism acting on the membrane. One should then redefine efficiency as,

$$\Lambda = \frac{A}{P_t + P_c + P_e}$$

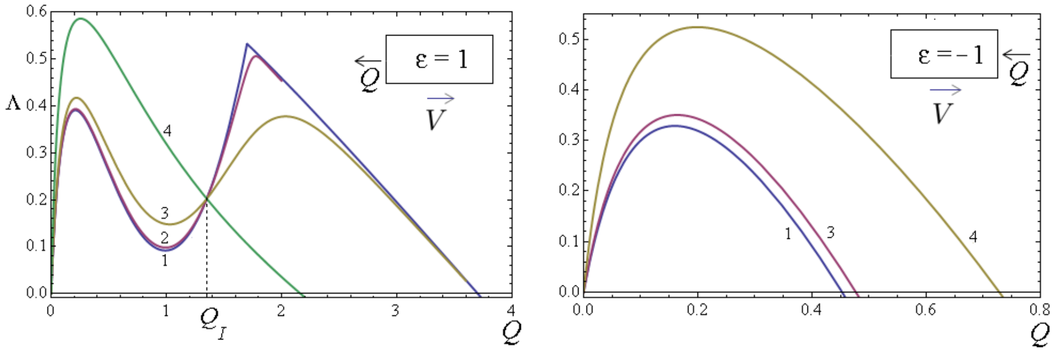

Figure 4.13: Efficiency as a function of the load in the elasticity-regularized model in pure pushing and pulling regimes with $k_{1,2,3,4} = \{0, 0.01, 0.1, 1\}$ and $L_0 = 1$. Experimental data suggest that $k = 1 - 10$ (see [14, 58]). Parameters: $v_- = 1.7$ and $v_+ = 2$. The corresponding force velocity relations are shown in Fig.4.15.

In Fig.4.13 we show that the two peak structure of the efficiency function does not disappear in the regularized model till k is sufficiently large (the treshold is given in the insert of Fig.4.15).

Despite ensuring finite energetics our model remains degenerate because it lacks a mechanism which penalizes infinite spreading of the cell at sufficiently large pulling forces. Also, one can show that the mass flux $\dot{m}$ associated with stable TW solutions may become equal to zero even for cells with finite lengths. Such behavior leads to infinite mass concentration (See Fig.4.14) for a cell dragged backwards by a pulling load ($V < 0$).

4.6 Elasticity regularization

To regularize the model we have to correct the infinite compressibility hypothesis which disregards the intermediate time stiffness of the cell. Such stiffness prevents cells from contraction-induced collapse in statics and keeps their length from diverging in the case of pulling. The implied elasticity may be associated either with the cytoskeleton or with the cell membrane and the simplest representation of this effect is through passive coupling between the leading and trailing edges [14, 58, 147, 164]. If this coupling is linear elastic, the applied loads become $q_{\pm}+k(L-L_0)/L_0$, where $k > 0$ is a dimensionless stiffness and L_0 is a prescribed dimensionless reference length: its meaning is clear from

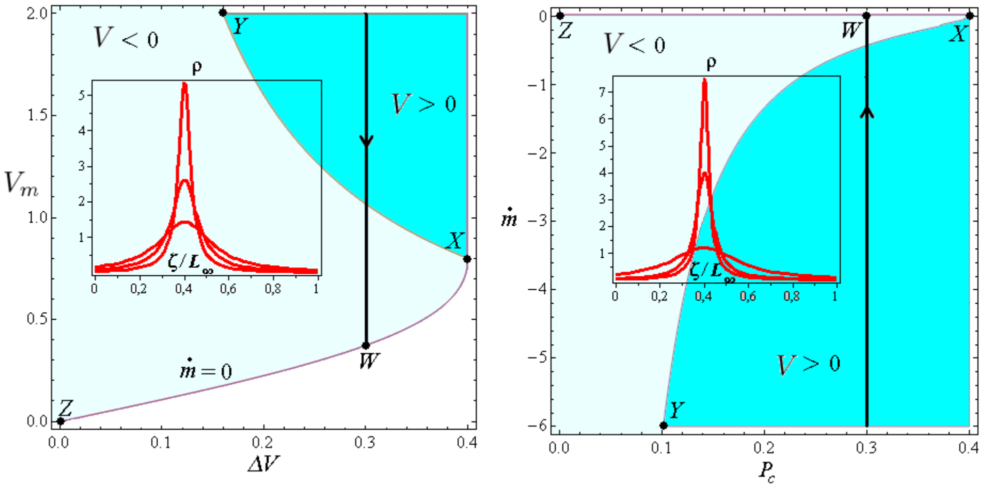

Figure 4.14: Different crawling regimes shown in the parameter spaces $(V_m, \Delta V)$ and $(\dot{m}, P_c)$. If $V > 0$ the cell moves against the load and if $V < 0$ the cell is dragged by the load. The insert shows density localization along the path indicated in the main figure by the black line and leading to singularity at point W. The loading is pure pulling with $\epsilon = 1$ and $Q = 1.6$

the fact that for $k > 1$ and $V_m = \Delta V = 0$ there exists a nontrivial static solution with $V = 0$ and $L_\infty = L_0(1 - 1/k)$ (preferred shape). In dynamics the steady state (TW) solution is now stable for all $\Delta V > 0$ and to find $L_\infty(Q)$ one needs to solve

$$\Delta V = (2 - \epsilon Q + 2k(L_\infty - L_0)/L_0)\tanh(L_\infty/2).$$

Then, the cell velocity can be found from

$$V(Q) = V_m - Q(2\tanh(L_\infty/2))^{-1}.$$

The regularized, elasticity-mediated force velocity relations are shown in Fig.4.15. We observe that all force-velocity curves cross at $Q = 0$ where $V = V^*$; the second intersection point at

$$Q_I = (2 - \Delta V/\tanh(L_0/2))/\epsilon$$

exists when $\epsilon > 0$ and $L_0 > L_\infty^*$. One can see now the length is always finite and the qualitative difference between pulling and pushing survives. For sufficently large k the negative mobility range disappears and the force-velocity relations in pushing and pulling dominated regimes become similar. The data on static configurations [14, 58,

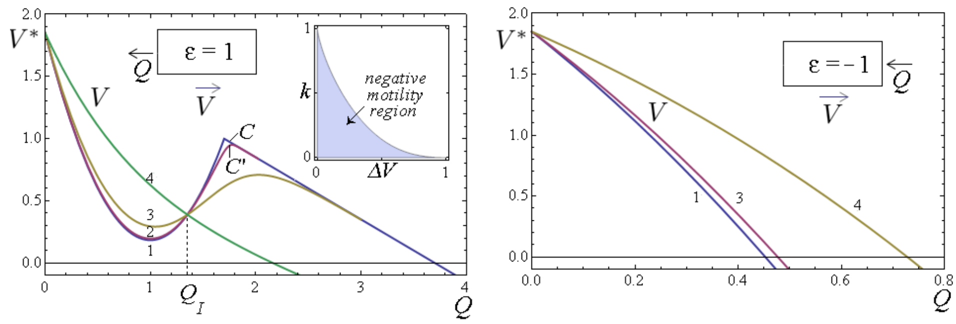

Figure 4.15: Force velocity relations in pure pushing and pulling modes with $k_{1,2,3,4} = \{0, 0.01, 0.1, 1\}$ and $L_0 = 1$. Driving parameters are $v_- = 1.7$ and $v_+ = 2$. Internal profiles corresponding to points C and C' are presented in Fig.4.3. Insert shows the domain with negative mobility in parameter space $(k, \Delta V)$.

147, 164] suggest that the dimensionless k (normalized by χ) is in the range $1 - 10$. At the same time, many models of cell dynamics are built under the assumption that the long time elasticity is negligible and $k = 0$ [34, 97, 151, 156]. Moreover, due to the presence of active cross-linkers, cells are known to be able to vary their stiffness over at least two orders of magnitude [94, 113, 165]. In view of this variability the effective stiffness may easily reach below the threshold $k = 1$ which means that negative motility regimes cannot be excluded. Instead of mean field elastic regularization we can directly incorporate distributed (Kelvin) elasticity directly into the constitutive model by assuming that

$$\sigma = \chi + \eta \partial_x v - p(\rho),$$

where the simplest pressure density relation is linear $p(\rho) = E(\rho/\rho_r - 1)$, where ρ_r is the reference density. The momentum balance equation becomes coupled with the mass conservation equation and the problem has to be solved numerically. The resulting force-velocity relation is qualitatively similar to what we have seen in the case of mean field elasticity, in particular, the negative mobility regimes persist for sufficently small E; similar results can also be obtained in the case of Maxwell elasticity: We therefore introduce two models of bulk elasticity and compare the influence of the new terms in the force balance equation on the ensuing force velocity relations. The first model, known as Kelvin (visco-)elasticity, assumes that elastic response is associated with long time behavior. The second model, known as Maxwell (visco-)elasticity, associates elasticity with fast time scales. In the version of Kelvin elasticity introduced above, the set of

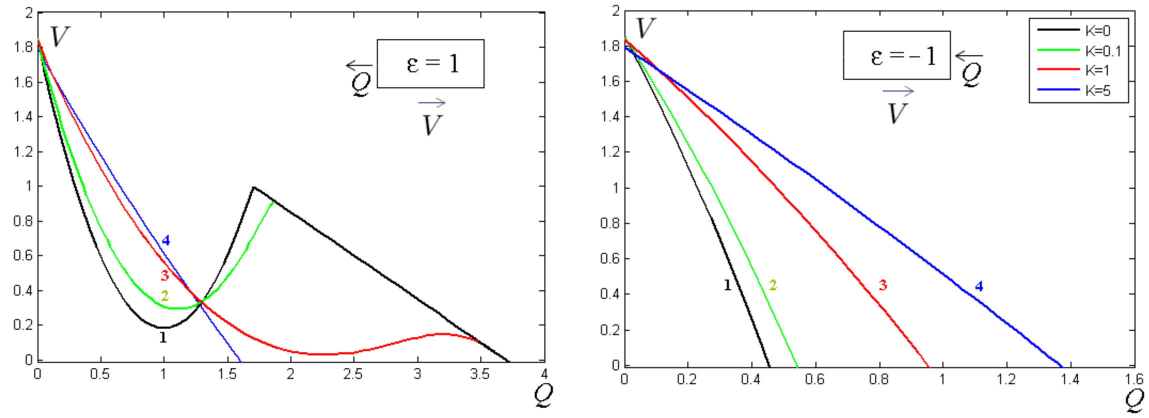

Figure 4.16: Force-velocity curves for the Kelvin model with $K_{1,2,3,4} = \{0, 0.1, 1, 5\}$. Experimental data suggest that $K = 0.1 - 10$ (see [13, 24, 37, 53, 102, 122, 138]). Other parameters are $\hat{\rho}_r = 1$, $v_- = 1.7$ and $v_+ = 2$.

non-dimensional equations can be written as:

$$\left\{ \begin{array}{c} \partial_t \rho + \partial_x(\rho \partial_x \sigma) = 0 \\ -\partial_{xx}\sigma + \sigma = 1 - K(\rho/\hat{\rho}_r - 1) \end{array} \right.$$

Here we introduced two new nondimensional parameters are $K = E/\chi$ and $\hat{\rho}_r = \rho_r/\rho_0$ where E is the zero frequency loss modulus [24, 122] and ρ_r is the reference density. The boundary value problem for the steady state (TW) solution takes the form

$$\left\{ \begin{array}{c} \rho(y) = \frac{1}{(\partial_y \sigma(y) - V)\int_0^{L_\infty} \frac{du}{\partial_y \sigma(u) - V}} \\ -\partial_{yy}\sigma + \sigma = 1 - K(\frac{\rho}{\hat{\rho}_r} - 1) \\ \sigma(0) = Q/2(\epsilon + 1) \text{ and } \sigma(L_\infty) = Q/2(\epsilon - 1) \\ V = V_m - \Delta V/2 + \partial_y \sigma(0) \text{ and } V = V_m + \Delta V/2 + \partial_y \sigma(L_\infty) \end{array} \right.$$

The force velocity relations for this model, shown in Fig.4.17, were obtained by numerical solution of this problem. We observe that introducing Kelvin elasticity eliminates density singularities shown in Fig.4.14, however the problem with the divergence of the cell length persists and can only be resolved if the linear pressure density relation is replaced by a nonlinear one.

In the case of Maxwell solid with corrotational convective derivative [34, 83, 89] the dimensional problem can be written as:

$$\begin{cases} \partial_t \rho + \partial_x(\rho v) = 0 \\ \xi v = \partial_x \sigma \\ \frac{\eta}{E}\frac{d\sigma}{dt} + \sigma = \chi + \eta \partial_x v \end{cases} \tag{4.17}$$

where E is the modulus corresponding to infinite frequency and

$$\frac{d\sigma}{dt} = \partial_t \sigma + v \partial_x \sigma = \partial_t \sigma + (\partial_x \sigma)^2.$$

The dimensionless boundary value problem for the steady (TW) solution can be written

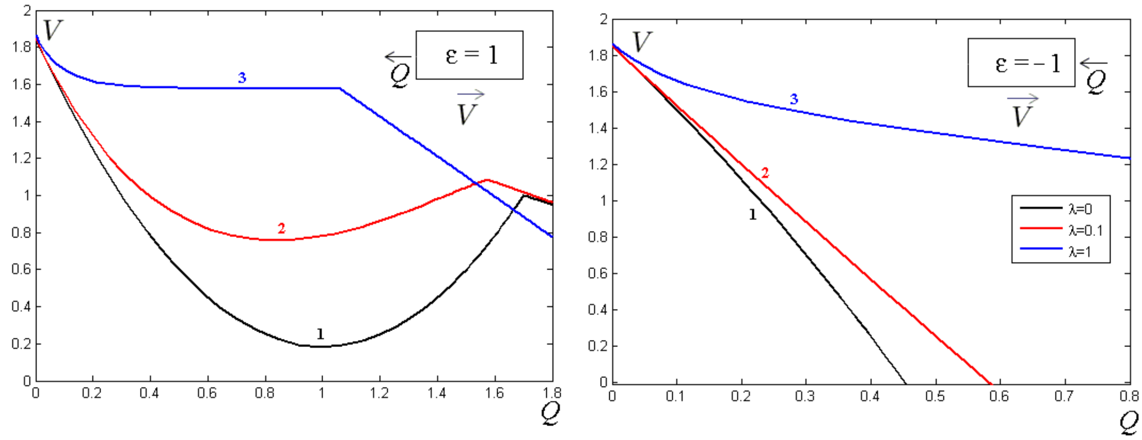

Figure 4.17: Force-velocity curves for the Maxwell model with $\lambda_{1,2,3} = \{0, 0.1, 1\}$. Experimental data suggest that $\lambda = 0.02 - 0.2$ [95, 122, 137, 156, 189] Other parameters are $\rho_0 = 1$, $v_- = 1.7$ and $v_+ = 2$.

as

$$\lambda \partial_y \sigma(\partial_y \sigma - V) - \partial_{yy}\sigma + \sigma = 1$$

where the new non dimensional parameter is $\lambda = \chi/E$. The system is equipped with the two boundary conditions:

$$\begin{cases} \sigma(0) = q_- \\ \sigma(L_\infty) = q_+ \end{cases}$$

Two remaining boundary conditions conditions

$$\begin{cases} \partial_y \sigma(0) - V = -v_- \\ \partial_y \sigma(L_\infty) - V = -v_+ \end{cases}$$

can be interpreted as equations on V and L_∞. In Fig.4.17 we show the ensuing force velocity relations (obtained numerically). One can see that the negative motility regime persists at finite λ.

Adding Maxwell elasticity however fails to regularize the problem because even at $\lambda > 0$ the cell size diverges at a finite value of the load. Morever, it does not allow for static regime. Indeed, the static problem with the corotational formulation reads in the TW formulation with no force applied reads:

$$\begin{cases} \lambda(\sigma^{'})^2 - \sigma^{''} + \sigma = 1 \\ \sigma(-L/2) = \sigma(L/2) = 0 \\ \sigma^{'}(-L/2) = -v_- \text{ and } \sigma^{'}(L/2) = -v_+ \end{cases}$$

Setting $Y = \sigma - 1$, we get,

$$\begin{cases} \lambda(Y^{'})^2 - Y^{''} + Y = 0 \\ \sigma(-L/2) = \sigma(L/2) = -1 \\ Y^{'}(-L/2) = -v_- \text{ and } Y^{'}(L/2) = -v_+ \end{cases}$$

which implies,

$$((Y^{'})^2)' - 2\lambda(Y^{'})^2 - 2Y = 0$$

Hence there exists a constant C such that,

$$(Y^{'})^2 = C\exp(2\lambda Y) - \frac{1}{2\lambda^2}(1 + 2\lambda Y)$$

from there applying Neumann BC, it is clear from $v_- > 0$ and $v_+ > 0$ that $v_- = v_+$. The phase portrait is then given by,

$$(Y^{'})^2 = F_{v_-,\lambda}(Y) = \exp(2\lambda(Y+1))\left[v_-^2 + \frac{1-2\lambda}{2\lambda^2}\right] - \frac{1+2\lambda Y}{2\lambda^2}$$

From monotony, $F_{v_-,\lambda}(Y)$ vanishes at most twice and if $v_- > 0$ the roots are necessarly strictly larger than -1 and there are no solutions. If $v_- = 0$, then the only solution $F_{v_-,\lambda}(Y)$ goes from positive to negative at -1 and the only possible solution satisfying BC is when $L = 0$ and the solution is stationary at -1. There is hence no admissible static regime. The situation changes when mean field elasticity $-k\frac{L-L_0}{L_0}$ is added and the same method shows that there is a unique trivial solution corresponding to:

$$\begin{cases} \sigma \equiv 1 \\ v_- = v_+ = 0 \\ L = L_0(1-k^{-1}) \end{cases}$$

4.7 Length regularization

In the pulling case, without elastic terms infinitely penalizing infinite length (mean field elasticity) or zero densities, the length becomes infinite at finite load. Here, we give details about the prolongation of the force velocity curve after this point in the purely viscous case, linearized Kelvin case and non linear Maxwell case.

4.7.1 Purely viscous case

The motion of the front is ruled by (4.2) In the pulling case $\epsilon > 0$ and length is increasing until the blow up load $Q_c = \frac{2-\Delta V}{\epsilon}$ where length becomes infinite. Then equation $(4.2)_2$ suggest to prolongate the force velocity curve by:

$$\forall Q \geq Q_c,\, V = V_m - \frac{Q}{2}.$$

In fact, what truely happens is that when length gets infinite the solution of,

$$\begin{gathered} -\partial_{yy}\sigma + \sigma = 1 \\ \sigma(0) = q_- \text{ and } \sigma(L_\infty) = q_+ \end{gathered}$$

is a constant equal to 1 with two independant boundary layers of finite size 1 at 0 and 1 connecting the load value and 1. The rear front is then going at velocity,

$$V^0 = v_- + \lim_{L_\infty \to \infty} \partial_y \sigma(0) = v_- + \frac{1-q_-}{1}$$

while the front front is going at velocity,

$$V^{L_\infty} = v_+ + \lim_{L_\infty \to \infty} \partial_y \sigma(L_\infty) = v_- + \frac{q_+ - 1}{1}$$

As the length is infinite, we have several choices to associate a speed to the layer. We arbitrarly take the average of both speeds which is consistent with $\dot{G}$ and therefore enables to continuously prolongate the force velocity curve even if there is a kink at point $Q = Q_c$.

4.7.2 Linearized Kelvin case

The non steady equations read,

$$\begin{cases} \partial_t \rho + \partial_x(\rho \partial_x \sigma) = 0 \\ -\partial_{xx}\sigma + \sigma = 1 - K(\frac{\rho}{\hat{\rho}_r} - 1) \end{cases}$$

Equipped with initial and boundary conditions:

$$\begin{cases} \rho(x,0) = \rho_i(x) \text{ and } l_-(0) = l_-^0,\ l_+(0) = l_+^0 \\ \sigma(l_-(t),t) = Q/2(\epsilon+1) \text{ and } \sigma(l_+(t),t) = Q/2(\epsilon-1) \\ \dot{l}_- = V_m - \Delta V/2 + \partial_x\sigma(l_-(t),t) \text{ and } \dot{l}_+ = V_m + \Delta V/2 + \partial_x\sigma(l_+(t),t) \\ \rho(l_-(t),t)\,(V_m - \Delta V/2) = \rho(l_+(t),t)\,(V_m + \Delta V/2) \end{cases}$$

It is clear that the total quantity of actin, normalized at 1 is conserved throughout time. Then, the unsteady fronts are moving according to the dynamics,

$$\begin{aligned} \dot{L} &= \Delta V + (\epsilon Q - 2(1+K))\tanh(\tfrac{L}{2}) + \tfrac{K}{\hat{\rho}_r\cosh(\frac{L}{2})}\textstyle\int_0^L \rho\cosh(\tfrac{L}{2}-u)du \\ \dot{G} &= V_m - \tfrac{Q}{2\tanh(L/2)} - \tfrac{K}{\hat{\rho}_r\sinh(\frac{L}{2})}\textstyle\int_0^L \rho\sinh(\tfrac{L}{2}-u)du. \end{aligned} \tag{4.18}$$

Then, using mean value theorem, we have from $(4.18)_1$,

$$\frac{K}{\hat{\rho}_r\cosh(\frac{L}{2})} \leq \dot{L} - \left(\Delta V + (\epsilon Q - 2(1+K))\tanh(\frac{L}{2})\right) \leq \frac{K}{\hat{\rho}_r}$$

As a consequence, if $\epsilon Q \geq 2(1+K) - \Delta V$ then $L \longrightarrow \infty$ when $t \longrightarrow 0$ and in the pulling case, it is clear that there exists a critical load Q_c such that the inequality is true and there is blow up of length. To prolongate the force velocity relation we consider $(4.18)_2$ which implies,

$$-\frac{K}{2\hat{\rho}_r} \leq \dot{G} - \left(V_m - \frac{Q}{2\tanh(\frac{L}{2})}\right) \leq \frac{K}{2\hat{\rho}_r}$$

which gives a tube where the force velocity has to be after blow up of length. Numerical computation in fact gives the same prolongation as in the purely fluid case (given for the pure pulling case here):

$$\forall Q \geq Q_c,\ V = V_m - \frac{Q}{2}$$

And only the value of the critical load Q_c depends on K.

4.7.3 Non linear Maxwell case

The unsteady equations of the model read

$$\begin{cases} \lambda\left(\partial_t\sigma + (\partial_x\sigma)^2\right) - \partial_{xx}\sigma + \sigma = 1 \\ \sigma(l_-(t),t) = q_+ \ ,\ \sigma(l_+(t),t) = q_- \text{ and } \sigma(x,0) = \sigma_0(x) \\ \dot{l}_- = v_- + \partial_x\sigma(l_-(t),t) \text{ and } \dot{l}_+ = v_+ + \partial_x\sigma(l_+(t),t) \\ l_-(0) = l_-^0 \text{ and } l_+(0) = l_+^0 \end{cases}$$

Showing the existence of a critical load where length blows up is delicate because of the quadratic non linearity. We shall admit it. The force velocity curve is then constructed numerically until the point where length becomes infinite on the travelling wave problem :

$$\lambda\partial_y\sigma(\partial_y\sigma - V) - \partial_{yy}\sigma + \sigma = 1$$

with the BC :

$$\begin{cases} \sigma(0) = q_- \\ \sigma(L_\infty) = q_+ \\ \partial_y\sigma(0) - V = -v_- \\ \partial_y\sigma(L_\infty) - V = -v_+ \end{cases}$$

As for the purely viscous case, we notice the appearance of finite size boundary layers connected by a infinite zone where stress is 1. To find the speed of the moving fronts in the infinite length limit, we suppose that inside the boundary layer, the flux of particle is almost constant, $\partial_y\sigma - V$ can be approximated by $-v_-$ at the rear boundary and $-v_+$ at the front boundary. This transforms the non linear equation in linear one on the two boundary layers where stress connects the value at boundaries with the bulk value 1,

$$V^0 = v_- + \lim_{L_\infty\to\infty} \partial_y\sigma(0)$$

while the front front is going at velocity,

$$V^{L_\infty} = v_+ + \lim_{L_\infty\to\infty} \partial_y\sigma(L_\infty)$$

We find in the pure pulling case:

$$V = V_m + \frac{1}{4}\left(-(Q-1)\left(\sqrt{(\lambda v_-)^2+4} + \lambda v_-\right) - \sqrt{(\lambda v_+)^2+4} + \lambda v_+\right)$$

which matches perfectly the critical Q_c found by numerics.

4.8 Alternative driving mode

One way to avoid density localization phenomenon illustrated in Fig.4.14 without introducing elasticity it to chose the mode of driving which automatically excludes the regimes with $\dot{m} = 0$. Thus, we may assume that instead of the kinematic fluxes, characterized by V_m and ΔV, the cell controls energetic fluxes, such as, for instance, the treadmilling rate, characterized by the total mass flux $\dot{m} < 0$, and the energetics of the contraction process, characterized by the consumed power P_c. The advantage of the parametrization $(\dot{m}, P_c)$ is that protrusion and contraction can now be controlled independently. The equivalence of the energetic and kinematic driving modes in the steady state regimes can be derived from the fact that if we choose the pair $(\dot{m}, P_c)$ as the controlling parameters, we still obtain stable traveling wave solutions given that

$$P_c < 2 - Q\epsilon \text{ and } \dot{m} < 0.$$

These traveling wave solutions can be mapped on the traveling waves solutions in the problem with kinematic driving through (v_-, v_+) if the following conditions are satisfied

$$0 < \Delta V < 2 - \epsilon Q.$$

More specifically, if we introduce the set $S_1 = \{0 < \Delta V < 2 - \epsilon Q, \dot{m} < 0\}$ in the (v_-, v_+) space and the set $S_2 = \{P_c < 2 - Q\epsilon, \dot{m} < 0\}$ in the space $(\dot{m}, P_c)$ we can compute the Jacobian of the transformation $(v_-, v_+) \to (P_c((v_-, v_+)), \dot{m}(v_-, v_+))$ between these two sets

$$det \begin{pmatrix} \frac{\partial P_c}{\partial v_-} & \frac{\partial \dot{m}}{\partial v_-} \\ \frac{\partial P_c}{\partial v_+} & \frac{\partial \dot{m}}{\partial v_+} \end{pmatrix} = \frac{\int_0^{L_\infty} \frac{dy}{(v(y)-V)^2}}{(\int_0^{L_\infty} \frac{dy}{v(y)-V})^2} \geq \frac{1}{L_\infty} > 0.$$

One can see that it is strictly positive and therefore the two descriptions of the steady state solutions are equivalent.

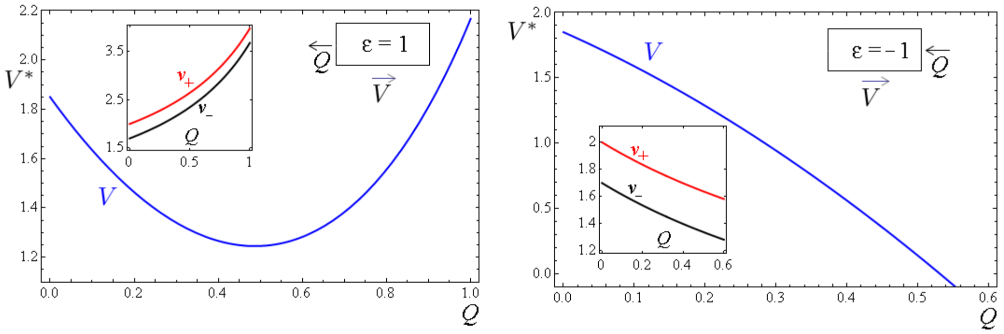

Figure 4.18: Force velocity relations in pure pushing and pulling modes with the driving through $\dot{m} = -6.1$ and $P_c = 0.3$. Inserts show the ensuing dependances of v_+ and v_- on Q.

In the elasticity-free case $k = E = 0$ the problem with $(\dot{m}, P_c)$ prescribed instead of $(V_m, \Delta V)$ exhibits stable steady state (TW) solutions when $\dot{m} < 0$ and $P_c < 2 - \epsilon Q$.

The resulting force velocity relations, illustrated in Fig.4.18, show that the regimes with negative mobility persist also in this setting. At $Q_c = (2 - P_c)/\epsilon$, the cell length L_∞ diverges but the problem can be again regularized by bringing back the mean field elastic coupling. Interestingly, by fixing the parameters P_c and $\dot{m}$ we induce a dependence of the polymerization and depolymerization rates (v_-, v_+) on Q (see Fig.4.18) which agrees with the trends suggested in [97] based on the polymerization ratchet model. Ultimately, the choice of the driving mode (fixing P_c may be replaced by the control of $P_t + P_c$, etc.) requires microscopic modeling and may depend on the type of the cell, the environment and the regime of loading.

4.9 Conclusion

In conclusion, we used the simplest model of a crawling cell to study the interplay between contraction and protrusion required to sustain and carry various cargoes. The minimal setting involving an elastic coupling between the front and the rear of the cell was proved sufficient to distinguish kinetically between pulling and pushing. We observe a shift from protrusion dominated motility to contraction dominated motility when the pulling force is sufficiently strong. The possibility of such active readjustement of the force producing machinery plays a fundamental role in the response of active media implying that if necessary 'pushers' can replace 'pullers' and visa versa. The model predicts concavity of the force velocity relation in the case of pushing and allows in the case of pulling for a convex-concave structure with an negative mobility range. While the detailed shape of the force velocity relation depends on the driving mode, its loading-sensitive convexity-concavity structure appear to be a robust feature of the model.

5

Conclusion and perspectives

In this manuscript, we have presented a detailed study of one dimensional and one component cell crawling model with moving boundaries relying on only essential biological ingredients. The passive behavior of the cytoskeleton inside the cellular membrane is viscoelastic with different fundamental types of viscoelasticity investigated. The two powering mechanisms of protrusion/retraction through polymerization/depolymerization of actin and contraction mediated by motor activity are respectively described by an influx of mass at the front which then disappears at the rear and positive prestress. The activity of cell adhesion is disregarded and linear passive friction is used to model the interaction with the substrate. The leitmotiv of this manuscript is not to present a full comprehensive model of cell crawling but to investigate fully the role of each fundamental element added. Lots of improvements can be brought to the model itself by taking into account several biophysical interactions between main effects. For example, actin density at the leading edge influences polymerization properties. It is also known that the motor activity changes the elastic properties of the cytoskeleton. More important limitations of the model are its one dimensional nature, the fact that the role of the cytosol is not taken into account and the passive nature of adhesion. Lots of these points can be gradually considered within the same framework and using what is already known about the model. Despite its caricatural nature, the model still captures observed effects and makes predictions that we hope to be experimentally tested.

In the first chapter we take a reverse engineering approach and pose the problem of finding the optimal spatial and temporal organization of different motility powering machinery ensuring either maximum velocity of crawling or maximal efficiency of energy transduction. We circumvent the problem of self-consistent transport of biological elements ensuring the required performance (actin filaments, myosin crosslinkers, integrins) and assume that the optimal spatial distribution of these elements can be created artificially. Supposing for simplicity that actin treadmilling is disabled, we first consider only the effect of arbitrary non homogeneous contraction to find, in agreement with experiments, that the distribution achieving the largest speed is when motors are concentrated at the trailing edge. Interestingly, we find that this speed can be made twice larger if adhesion proteins concentration is fully correlated with the one of motors. Such a correlation has been observed and partly understood at the micro level. Considering homogeneous adhesion again, we also investigate the optimal strategy for contraction distribution in term of mechanical efficiency to find again a concentration at the trailing edge but with a characteristic spreading length this time. Such a length can be understood at the micro level as resulting from the thermal mobility of bipolar filaments with respect to actin fibers. A perspective on this work, apart from trying to generalized the results in two dimensions, would be to include an arbitrary adhesion distribution in the energetic optimization procedure and to investigate more deeply the role of treadmilling.

In the second chapter, still ignoring actin treadmilling, we investigate the role of a simple drift diffusion model carrying motors. At the basis of the model is contraction driven uphill diffusion destabilizing symmetric configuration and causing polarization. The instability is due to the motion of cytoskeleton which is generated by active crosslinkers and simultaneously transports them. By studying traveling wave solutions we show that such internal flow can generate steady propulsion of a finite cell body. The most important conclusion is that the model exhibits motility initiation pattern similar to the ones observed in experiments. Namely, depending on the motor activity, the cell can either stay static or spontaneously start moving in a steady way. The force velocity of the steady regime fully contraction powered needs to be fully exposed but already shows hysteretic behavior that would be interesting to test experimentally.

In the third chapter, supposing roughly that contraction and adhesion are homogeneous, we focus on the treadmilling based motility which allows the cells not only to self-propel but also to exert forces on obstacles (to push) and to carry cargoes (to pull). We show that pushing dominated force-velocity relation is controlled by the protrusion mechanism while the pulling dominated force-velocity relation is controlled by the protrusion mechanism only at small values of the force which is replaced by the contraction mechanism at sufficiently large pulling forces. The proposed model reveals the possibility of a switch from protrusion dominated motility to contraction dominated motility in the case when a moving cell has to carry a cargo. Such switches are expected to be crucial for the general response of active matter to external forces with "pushers" and "pullers" interchanging roles depending on the orientation of the loading with respect to the direction of the overall motion. We tried to show the robust nature of this feature by investigating some main modeling extensions. On the way, we observed the appearance of treadmilling waves resulting in a non steady propagation of the cell when contractility increases with actin density. We hope to be able to give a full exposure of the effect in a near future.

6

Appendixes

6.1 Model for front oscillations

On top of its steady advance at constant speed, (traveling wave) there is evidence [14, 16] that the leading edge exhibits oscillatory behavior during its advance. This section aims at describing this effect as a consequence of actin filaments fracture under critical stress (or strain) and subsequent depolymerization as has been done in with a full 2D computational model in [38].

6.1.1 Minimal setting, necessity of mass regulation

Starting from the idea of [38], we consider a 1D layer ($[0, L(t)]$) actin gel contained in an elastic membrane clamped in one point (rear) and able to grow against a constant external load with a constant mass flux at it front. We emphasis, that the external loading is not necessary and can always be taken to zero if needed for understanding. The gel is endowed with the simple property that it is elastic up to a given density threshold at which it breaks and stress drops to zero. The membrane is a spring connecting the rear and the front.

The equations for such a model are :

$$\partial_x \sigma = 0 \text{ (Equilibrium of actin)}$$

with boundary condition :

$$\sigma(L(t), t) + k\frac{L(t) - L_0}{L_0} = q \leq 0$$

We also have mass conservation equation :

$$\partial_t \rho + \partial_x(\rho v) = 0$$

with the boundary conditions :

$$\begin{cases} \rho v(0,t) = 0 \text{ (impenetrable non moving frontier)} \\ \rho\left(v(L,t) - \dot{L}\right) = -\dot{m} \leq 0 \text{ (Constant mass flux of arriving matter)} \end{cases} \tag{6.1}$$

We close the system with the following behavior law :

$$\sigma = f(\rho) = K(\rho_0 - \rho)1_{[\rho \leq \rho_{max}]}$$

We can deduce that necessarily ρ is constant different from zero in space and obeys the relation :

$$f(\rho) = q - k\frac{L(t) - L_0}{L_0}$$

Knowing this on ρ, we can deduce the value of speed in the whole domain :

$$v(x,t) = -\frac{\dot{\rho(t)}}{\rho(t)}x$$

The last boundary condition on mass balance then provides the expected

$$\frac{d\,(\rho L)}{dt} = \dot{m}$$

which is global mass balance. Integrating this last equation gives L as a function of ρ :

$$L(t) = \frac{M_0 + \dot{m}t}{\rho(t)}$$

Where M_0 is the initial mass. We finally get :

$$f(\rho(t)) = q + k - \frac{k}{L_0}\frac{M_0 + \dot{m}t}{\rho(t)}$$

Let us first suppose that $q + k > 0$, then the above equation can be solve graphically and the solution is such that L is first increasing with time until the material is not broken, then at time T such that :

$$K(\rho_0 - \rho_{max}) = q + k - \frac{k}{L_0}\frac{M_0 + \dot{m}T}{\rho_{max}}$$

The actin network fractures and as a result length stays constant :

$$L_{eq} = \frac{L_0(q+k)}{k}$$

Density has been increasing in two different ways after and before time T, slowly first and then faster.

If we suppose that $q+k<0$, then there are not always solution, and particularly, at large times there are no solutions. Indeed after the fracture, the two curves have no intersection at all which is meaningful as the mechanical "capacity" of both actin and the membrane has been overcome by the load and the material has reached completed damage which implies that other models shall be used.

As a conclusion, if we want to plot the force velocity curve ($lim_{t\to\infty}\dot{L}$ as a function of q) of such a model, it is the null function. In particular we also see, we do not have any oscillation in this system because as mass is constantly increasing, there is no way out of the broken state.

6.1.2 Mass regulated system

Keeping the problem of the previous section, we add a new ingredient. When the system brakes, actin filaments are broken into pieces. This mechanical phenomena will release energy which enables simultaneous depolymerisation of the actin filaments. We introduce the depolymerization function,

$$\gamma_f(\rho) = \gamma 1_{\rho \leq \rho_{max}}$$

Where γ is a positive constant we now write mass balance in the following way :

$$\partial_t \rho + \partial_x(\rho v) = -\gamma_f(\rho)\rho$$

Implying that depolymerization phenomenon is an elementary reaction. The system can then be written :

$$\left\{ \begin{array}{l} f(\rho) = q - k\frac{L(t)-L_0}{L_0} \\ \dot{\rho} + \rho\partial_x v = -\gamma_f(\rho)\rho \end{array} \right. \tag{6.2}$$

The velocity film remains linear in space and integrating these equations in space and defining the total mass $M = \rho L$ on the system we have :

$$\left\{ \begin{array}{l} \dot{M} = \dot{m} - \gamma_f(\rho)M \\ f(\rho) = q + k - \frac{k}{L_0}\frac{M}{\rho} \end{array} \right. \tag{6.3}$$

If we suppose again that $q+k>0$, the behaviour of such a system is oscillatory under a condition that we are going to derive. We refer to Fig.6.1 for the following reasoning.

Let us suppose the system starts from an unbroken configuration S. As γ_f is off, we have that $\dot{M} = \dot{m}$, so the hyperbolic curve $q + k - \frac{k}{L_0}\frac{M}{\rho}$ is moving to the right. The solution lies on segment $[AB]$ until point B where it suddenly (shock) jumps in C, But then γ_f is on and mass starts decreasing exponentially. The solution is then lying on segment $[CD]$ until it reaches D where it suddenly jumps in A and starts the loop again.

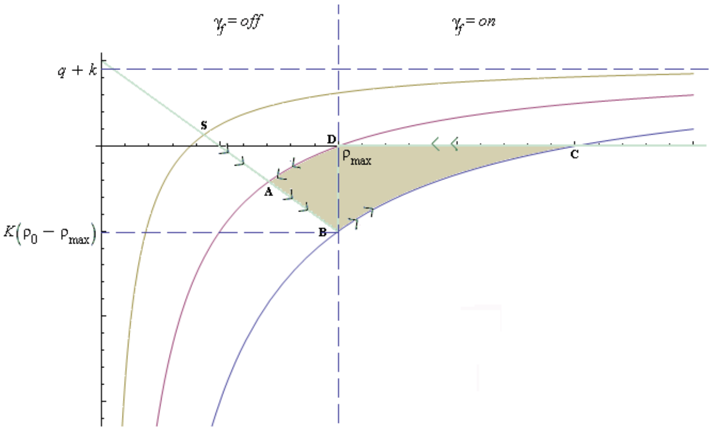

Figure 6.1: Hysteresis loop of the mass regulated system

There are a priori two conditions for the above scenario to actually take place. Let us denote M_{max} the value of mass at point B. This value has to be greater than the asymptotic value $\frac{\dot{m}}{\gamma}$ otherwise mass will not start decreasing at C but stabilize at the value $\frac{\dot{m}}{\gamma}$ in a broken state. In the same way the value of ρ for mass being equal to $\frac{\dot{m}}{\gamma}$ must be smaller then rho_{max} or there will be no jump from D to A but stabilization of the mass at $\frac{\dot{m}}{\gamma}$. Explicitly, the two conditions are :

$$\begin{cases} M_{max} = (q + k - K(\rho_0 - \rho_{max}))\,\frac{L_0\rho_{max}}{k} \geq \frac{\dot{m}}{\gamma} \\ \frac{k\dot{m}}{\gamma(q+k)L_0} \leq \rho_{max} \end{cases} \tag{6.4}$$

But the second condition is less restrictive then the first one.

The mechanical structure of these oscillations (See Fig.6.2) is the following : From A to B, Mass is added in the system which first implies, as no regulatory process (depolymerization) is on, that density increases. These actions implies an increase of length. Then at point B, actin brakes down and cannot hold stress any more. As a result there is brutal increase of density to point C. Then between C and D mass is being regulated by depolymerization which makes both mass and density decay implying

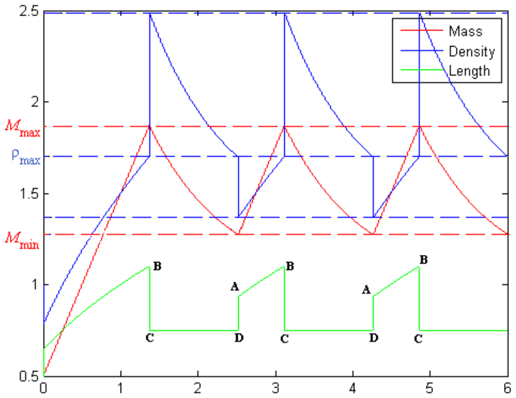

Figure 6.2: Mass, density and length oscillatory behavior for $\gamma = 1$, $q = -1$, $\rho_{max} = 1.5$, $\rho_0 = 1$, $K = 1$, $\dot{m} = 1$, $L_0 = 1$

constant length ($L = \frac{L_0(k+q)}{k}$) until density is such that stress can again be sustainned at point A.

To numerically compute oscillation, we need to add some viscosity in the model. This can be made in two different ways : Maxwell or Kelvin. In the first case a stress is added in the behaviour law which is proportional to stress rate. The system thus becomes :

$$\left\{ \begin{array}{c} \dot{M} = \dot{m} - \gamma_f(\rho)M \\ \sigma = q + k - \frac{k}{L_0}\frac{M}{\rho} \\ \lambda\dot{\sigma} + \sigma = f(\rho) \end{array} \right. \tag{6.5}$$

The small parameter $\lambda = \frac{\eta}{E}$ is then sent to zero (through η) and it can be proved the non viscous solution is then recovered. In the Kelvin way, viscous is proportional to gradient of velocity, which is known :

$$\sigma_{viscous} = \eta\partial_x v = \eta\left(\frac{\dot{\rho}}{\rho} - \gamma_f(\rho)\right)$$

The system thus becomes,

$$\left\{ \begin{array}{c} \dot{M} = \dot{m} - \gamma_f(\rho)M \\ \sigma = q + k - \frac{k}{L_0}\frac{M}{\rho} \\ \sigma = f(\rho) + \eta\left(\frac{\dot{\rho}}{\rho} - \gamma_f(\rho)\right) \end{array} \right. \tag{6.6}$$

In both cases, we get a system of two ODEs with a limit cycle (stability can be checked) which converge to the same relaxation oscillator that have been described when $\eta \to 0$.

We have seen so far that fracture with subsequent depolymerization may explain why a front is oscillating. The membrane elasticity is needed to sustain stress even if actin is broken. In this prospect, it can also be view as some passive elements which are not affected by fracture.

The problem of such a model, is that we have not been able to get a moving front so far but just an oscillating one. The force velocity relation is therefore still a flat line. We have made several attempts make a model which would account for this also.

6.1.3 Attempts to get net motion of the front

6.1.4 $L_0(M)$

One reason why we cannot get unbounded length is because the stress $k\frac{L-L_0}{L_0}$ becomes infinite when $L \to \infty$. To try to prevent this we make the hypothesis that the resting length of the passive elements is increasing as a part of the polymerized flux is going in the passive structure. We describe this fact by prescribing the function $L_0(M)$. We only make the hypothesis that this function is increasing. The system becomes :

$$\left\{ \begin{array}{c} \dot{M} = \dot{m} - \gamma_f(\rho)M \\ f(\rho) = q + k - \frac{k}{L_0(M)}\frac{M}{\rho} \end{array} \right. \tag{6.7}$$

If we want to keep the oscillatory behavior of the system, the function L_0 cannot be arbitrary but as to satisfy the inequality :

$$L_0(M) \geq \frac{dL_0(M)}{dM}M$$

In other words the function $\frac{M}{L_0(M)}$ has to be increasing. If it is not the case, as L_0 is increasing, after a certain threshold $\frac{M}{L_0(M)}$ is decreasing and converge to a given positive limit which implies that ρ converges to a given limit. Let us suppose for simplicity that the limit of $\frac{M}{L_0(M)}$ is 0. Then the limit of ρ at large times ρ_{eq} is given by :

$$f(\rho_{eq}) = q + k$$

This relation implies the following force velocity relationship :

$$\dot{L} = \frac{\dot{m}}{\rho_{eq}(q)}$$

This is growth without oscillations. If we consider the other hypothesis that $\frac{M}{L_0(M)}$ is increasing, we get oscillations with the same structure as in the previous section.

6.1.5 More realistic passive elements

The way we have introduced the passive elements not subjected to fracture through L_0 is questionable. We have tried an other possibility which is more literal. We suppose that there are two components in the gel, one unbreakable and one breakable. At each time we consider that a fraction α of the flux goes to the unbreakable matter and the rest goes to the breakable component. We keep the same notations as in the previous sections and denote the density of the new component by ρ_u (and its total mass by $M_u = \int_0^L \rho_u(x,t)dx$)
The system reads

$$\begin{cases} \partial_t \rho + \partial_x(\rho v) = -\gamma_f(\rho)\rho \\ \partial_t \rho_u + \partial_x(\rho_u v_u) = 0 \\ \partial_x \sigma = 0 \\ \sigma = f(\rho) + g(\rho_u) \end{cases} \tag{6.8}$$

where v_u is the speed of the unbreakable matter and g is the following function :

$$g(\rho_u) = E(\hat{\rho} - \rho_u)$$

The boundary conditions are :

$$\begin{cases} \rho v(0,t) = 0 \\ \rho_u v_u(0,t) = 0 \\ \rho_u \left(v_u(L,t) - \dot{L} \right) = -\alpha \dot{m} \\ \rho \left(v(L,t) - \dot{L} \right) = -(1-\alpha)\dot{m} \\ \sigma(L,t) = q \end{cases} \tag{6.9}$$

We then make the supposition that either ρ or ρ_u is independent of space. Following the same path as in previous sections we then get that :

$$\begin{cases} \dot{M} = (1-\alpha)\dot{m} - \gamma_f(\rho)M \\ q - E\hat{\rho} + E\frac{\alpha \dot{m} t + M_u^0}{M}\rho = f(\rho) \end{cases} \tag{6.10}$$

Where M_u^0 denotes the initial mass of unbreakable component. In this setting oscillations that have the same structure as in the previous section are also possible. See Fig. 6.3 The conditions so that oscillations appears are the following :

$$\frac{\alpha}{1-\alpha} < \frac{E\hat{\rho} - q}{\rho_{max}} \text{ and } \frac{(1-\alpha)\dot{m}}{\gamma} < \rho_{max}$$

But the problem is that, if length is indeed growing during these oscillations, both the "periods" and the "amplitude" of the growth and retraction are increasing in time (see

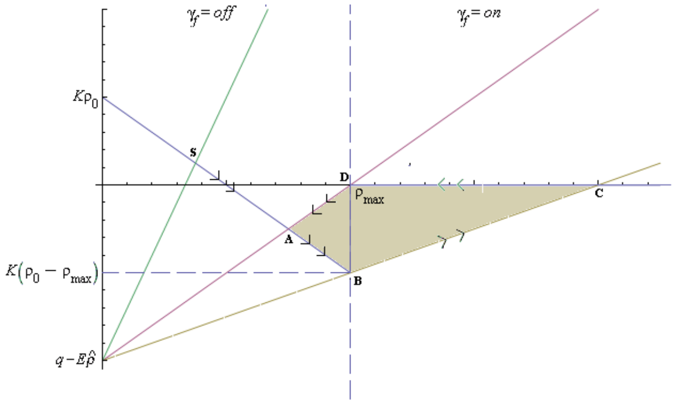

Figure 6.3: Hysteresis loop of with one elastic breakable and elastic unbreakable component

Fig.6.4). Here again to perform numerical simulations some very small viscosity was added.

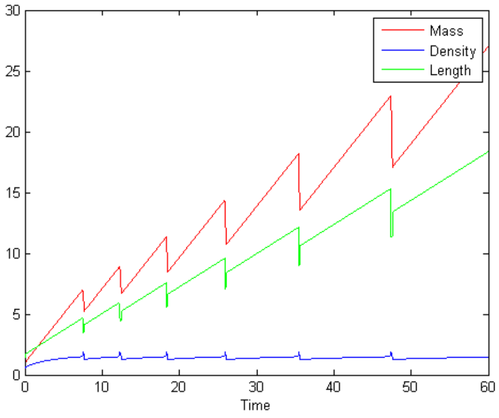

Figure 6.4: Mass, density and length oscillatory behavior for $\gamma = 1.5$, $q = 0$, $\rho_{max} = 1.5$, $\hat{\rho} = 1$, $\rho_0 = 1$, $K = 1$, $E = 2$, $\dot{m} = 1$, $\alpha = 0.2$

Mass is oscillating between the values :

$$\left[\frac{E(\alpha\dot{m}t + M_u^0)\rho_{max}}{E\hat{\rho} - q}, \frac{E(\alpha\dot{m}t + M_u^0)\rho_{max}}{K(\rho_0 - \rho_{max}) + E\hat{\rho} - q}\right]$$

While ρ is oscillating between the values :

$$\left[\frac{\rho_{max}(K+E\hat{\rho}-q)}{K\rho_{max+E\hat{\rho}-q}}, \frac{E\hat{\rho}-q}{K(\rho_0-\rho_{max})+E\hat{\rho}-q}\right]$$

Added to this growth of steps, one can also compute a growth of the periods of the steps. This increasingly large oscillations is an undesirable effect. To diminish it we have tried to postulate (as done in [38]) that α is a stochastic jump process that jumps at given uniform times T_i

$$T_i = iT, \, \forall i \in \mathbb{N}$$

where T is the polymerization "clock" [130] of the cell. At each clock step, we suppose that α follows a uniform law on $[0,1]$. We got interesting result with this approach but from the beginning the model is still biased by the fact that oscillations are more and more large when time increases. So there is not steady state distribution for length. The deviation from the mean value has a tail that increases with time. In fact, a deep problem is sitting in the mass balance equation :

$$\dot{M} = (1-\alpha)\dot{m} - \gamma_f(\rho)M$$

Let us imagine that ρ is periodic, which is what we want because the idea of the model is that ρ oscillates between a the "broken value" and the "unbroken value". Then it is impossible to get an unbounded M. Indeed, the solution of this ODE is :

$$M(t) = A\exp(-\int_0^t \gamma_f(\rho(u))du) + (1-\alpha)m\int_0^t \exp(-\int_u^t \gamma_f(\rho(s))ds)du$$

As $f(\rho) \geq 0$, the first term is clearly bounded. If we now suppose that ρ is periodic and takes its unbroken value ρ_{un} during T_{un} and its broken value ρ_{br} during T_{br}, then the second term can be dominated by :

$$\frac{(T_{un}+T_{br})(1-\alpha)\dot{m}}{\gamma\rho_b}$$

This explains why, when in the previous case, the only way to get net asymptotic growth is to have a non periodic ρ

6.1.6 More precise mass balance

In an attempt to get more elaborate mass balance, we propose an other two components model that contains elastic breakable polymerized actin and elastic unpolymerized actin. Supposing that the reaction of polymerization and depolymerization is the same, we have that :

$$\begin{cases} \partial_t \rho_p + \partial_x(\rho_p v_p) = -\gamma_f(\rho_p)\rho_p + k\rho_u \\ \partial_t \rho_u + \partial_x(\rho_u v_u) = \gamma_f(\rho_p)\rho_p - k\rho_u \\ \partial_x \sigma = 0 \\ \sigma = f(\rho_p) + g(\rho_u) \end{cases} \tag{6.11}$$

Where ρ_p denotes the density of polymerized actin and ρ_u the density of unpolymerized actin. The monomers are then turned into polymers at a rate k.
The boundary conditions are :

$$\begin{cases} \rho_p v_p(0,t) = 0 \\ \rho_u v_u(0,t) = 0 \\ \rho_u \left(v_u(L,t) - \dot{L} \right) = -\dot{m} \\ \rho_p \left(v_p(L,t) - \dot{L} \right) = 0 \\ \sigma(L,t) = q \end{cases} \tag{6.12}$$

The incoming mass flux is bringing only monomers in. We make again the hypothesis that one density at least is independent of space and do the usual integration procedure to get :

$$\begin{cases} \dot{M_p} = -(k + \gamma_f(\rho_p))M_p + k\dot{m}t + kM_0 \\ f(\rho_p) + g\left(\frac{\dot{m}t + M_0 - M_p}{M_p} \rho_p \right) = q \end{cases} \tag{6.13}$$

Where M_0 is the total initial mass. Note that when $\dot{m} = 0$, the above system reduces to :

$$\begin{cases} \dot{M_p} = -(k + \gamma_f(\rho_p))M_p + kM_0 \\ f(\rho_p) + g\left(\frac{M_0 - M_p}{M_p} \rho_p \right) = q \end{cases} \tag{6.14}$$

Which is fully similar to the system of the previous section with a membrane and a mass flux. We therefore have static oscillations in this setting and we can wonder if the mass flux added in this way can trigger drifted oscillations. The answer is sadly because mass is still oscillating and the period of the steps is still increasing. Mass varies between the two quantities (See Fig.6.5) :

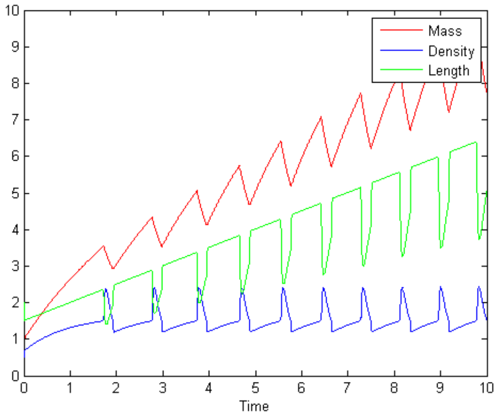

Figure 6.5: Mass, density and length oscillatory behavior for $\gamma = 1.5$, $q = 0$, $\rho_{max} = 1.5$, $\hat{\rho} = 1$, $\rho_0 = 1$, $K = 1$, $E = 1$, $\dot{m} = 1$, $k = 1$

$$\left[\frac{\dot{m}}{1+\alpha}t + \frac{M_0}{1+\alpha}, \frac{\dot{m}}{1+\beta}t + \frac{M_0}{1+\beta}\right]$$

with,

$$\alpha = \frac{K(\rho_0 - \rho_{max}) + E\hat{\rho} - q}{E} \text{ and } \beta = \frac{E\hat{\rho} - q}{E}$$

The conclusion of this computation is that it may be compulsory to add some spatial correlation in the distribution even very simple.

6.2 A remark on the distributions of integrins and myosins

We discuss here some physical models associated to the disctributions c_1 and c_2. We refer to notations of Chapter I.

6.2.1 Dynamics of c_1 (integrins)

The real dynamic of adhesion sites [23] is very complex. A very widely used assumption in the context of cell motility [56, 74, 89, 102, 156, 163] that assumes that the lifetime of focal contacts is very small with respect to the observation time with a microscopic justification often referred to given in [173] is to assume that ϕ_1 is the identity. There is evidence (both experimental [25, 63, 64, 126, 161] and theoretical [53, 118]) that this describes the behavior accurately only if the retrograde flow is small enough and that the real behavior of adhesion strength is biphasic with respect to speed (corresponding to a nonlinear ϕ_1 which linearly increases for small arguments and then decreases linearly after some given threshold). Added to this, α_1 is not constant in real cases but graded from trailing to leading edge [26, 191]. In [15] a reaction-drift-diffusion with a source term physical model ruling c_1 was proposed (See (eq.6 of S.I.) for justification and precise meaning of parameters):

$$\left\{\begin{array}{c} \tau^{-1}\partial_t c_1 = \alpha^{-2}D_A\partial_{yy}c_1 - \tau^{-1}\partial_y(\vartheta(v-V)c_1) + S_A - \gamma c_1 \\ \alpha^{-2}D_A\partial_y c_1(-L/2) - \tau^{-1}\vartheta(v-V)c_1(-L/2) = \alpha^{-2}D_A\partial_y c_1(L/2) - \tau^{-1}\vartheta(v-V)c_1(L/2) = 0 \end{array}\right.$$

Where v is the speed of the retrograde flow. As a consequence,

$$\tau^{-1}\frac{d\int_{-L/2}^{L/2} c_1}{dt} = LS_A - \gamma\int_{-L/2}^{L/2} c_1$$

Thus, after a (non dimensional)relaxation time of order $(\tau\gamma)^{-1}$,

$$\int_{-L/2}^{L/2} c_1 \simeq \frac{LS_A}{\gamma}$$

Hence,

$$\int_{-L/2}^{L/2} \alpha_1 = \mu L$$

where, $\mu = \frac{S_A}{\gamma c_1^0}$ is a given non dimensional constant and L is an unknown of the problem. As we have supposed that ϕ_1 is the identity, we may just renormalize α_1 and ξ with μ:

$$\left\{\begin{array}{c} \alpha_1 := \frac{\alpha_1}{\mu} \\ \xi := \mu\xi \end{array}\right.$$

and set that

$$\int_{-L/2}^{L/2} \alpha_1 = L$$

This normalization is in agreement with the usual assumption as if α_1 is supposed to be homogeneous,

$$\alpha_1 \equiv 1$$

6.2.2 Dynamics of c_2 (myosins)

For this physical process, it is also clear that in general ϕ_2 is not a linear function [25, 65, 158] but can be approximated by identity for small enough concentrations. According to [15, 25, 187] the bound myosin distribution c_2 is ruled by a drift diffusion equation with zero flux boundary conditions implying that the total amount of bound myosin ($\int_{-L/2}^{L/2} c_2$) leading to active contractile stress is conserved.

$$\left\{ \begin{array}{c} \tau^{-1}\partial_t c_2 = \alpha^{-2} D_M \partial_{yy} c_2 - \tau^{-1}\partial_y((v-V)c_2) \\ \alpha^{-2} D_M \partial_y c_2(-L/2) - \tau^{-1}(v-V)c_2(-L/2) = \alpha^{-2} D_M \partial_y c_2(L/2) - \tau^{-1}(v-V)c_2(L/2) = 0 \end{array} \right.$$

A more complete description with the reaction terms added in [187] (eq.5 of S.T.)

$$\left\{ \begin{array}{c} \tau^{-1}\partial_t c_2 = \alpha^{-2} D_M \partial_{yy} c_2 - \tau^{-1}\partial_y((v-V)c_2) + K_{on} c_3 - K_{off} c_2 \\ c_3 = \frac{1}{L}(\alpha^{-1} M_T - \int_{-L/2}^{L/2} c_2) \\ D_M \partial_y c_2(-L/2) - (v-V)c_2(-L/2) = D_M \partial_y c_2(L/2) - (v-V)c_2(L/2) = 0 \end{array} \right.$$

Where c_3 is the concentration of free myosin that is assumed to diffuse very fast and hence is constant and M_T the total amount of bound and free myosin. Here, the total amount of bound myosin from the beginning is not constant but after a relaxation time (non dimensional) of $(\tau(K_{on} + K_{off}))^{-1}$, this amount is very close to $\frac{K_{on} M_T}{\alpha(K_{on}+K_{off})}$. As a consequence,

$$\int_{-L/2}^{L/2} \alpha_2 = M$$

where,

$$M = \frac{K_{on} M_T}{c_2^0 \alpha (K_{on} + K_{off})}$$

As we have supposed that ϕ_2 is the identity, we may again just renormalize α_2 and χ with M

$$\left\{ \begin{array}{l} \alpha_2 := \frac{\alpha_2}{M} \\ \chi := M\chi \end{array} \right.$$

and set that,

$$\int_{-L/2}^{L/2} \alpha_2 = 1$$

A consequence of this model is that if we suppose α_2 is homogeneous as in [89, 97] and references therein then,

$$\alpha_2 = \frac{1}{L}$$

which depends on length while [89, 97] assumes that

$$\alpha_2 = 1$$

thus having in mind a source term producing bound myosin by unit length (like in the previous case for integrins). This source term would correspond to the fact that c_3 is supposed to always be in excess and hence be constant. This also corresponds to two different rheological models. $\alpha_2 = 1$ keeps the contractile stress constant regardless of the volume and assumes that myosin is crosslinking actin fibers in parallel $\alpha_2 = \frac{1}{L}$ would rather correspond to myosin crosslinking actin fibers in series. In a muscle, it is clear that both structures are there with a given number of cross bridges in parallel forming an half sarcomer that goes in serie with many others. The structure of contractility in eukaryotic cells is less transparent. At this stage, we do not know what is the real answer. It is a fundamental problem to known how ATP is consumed, is it a given quantity for each cell or a twice 'bigger' cell has twice more ATP ?

6.3 Imposing the sign constraint $g \geq 0$ in the minimization problem (2.21)

The constraint can be rewritten with the dirac mass δ:

$$\forall u_0 \in [0,1], \int_0^1 \delta(u-u_0) g(u) du \geq 0$$

Fixing, u_0 we may start again the optimization procedure except that g is now written,

$$g(u) = \lambda_0 \psi_0(u) + \lambda_1 \psi_1(u) + \lambda_2 \psi_2(u) + \lambda_3 \psi_3(u, u_0)$$

where,

$$\psi_3(u, u_0) = \delta(u-u_0) + 2L^2 \sum_{k=1}^{\infty} \frac{\sin(k\pi u_0)\sin(k\pi u)}{k^2\pi^2}$$

Which can be computed using Fourier series,

$$\psi_3(u, u_0) = \delta(u-u_0) + L^2 \left[u(1-u_0) 1_{[u \leq u_0]} + u_0(1-u) 1_{[u > u_0]} \right]$$

Then additionally, to the equality constraints giving the Lagrange multipliers, we write the Karush-Kuhn-Tucker [47] conditions corresponding to the inequality constraint:

$$\begin{cases} g(u_0) \geq 0 \\ \lambda_3 \leq 0 \\ \lambda_3 g(u_0) = 0 \end{cases}$$

The total system then depends of u_0 and has to hold for all u_0. We did not manage to get an analytic result this way. Still, the method is operative numerically by taking a grid of u_0 and is an alternative to the large scale direct implementation optimization presented in Numerical method. Let us consider a (large) integer N and a set of $\{u_i\}_{3\leq i\leq N}$ where the constraint of positivity is applied. Then the solution $\bar{g}$ can be written,

$$\bar{g}(u) = g(u) + \sum_{i=3}^{N} \lambda_i \psi_3(u, u_i)$$

while we denote the counterpart of Γ is

$$\bar{\Gamma}(u) = \Gamma(u) + \sum_{i=3}^{N} \lambda_i \delta(u - u_i)$$

we have the new system,

$$\begin{cases} 1 = \lambda_0 A_0 + \lambda_2 A_2 + \sum_{i=3}^{N} \lambda_i \psi_0(u_i) \\ 2V \sinh(L/2) = \lambda_1 S_1 + \sum_{i=3}^{N} \lambda_i \psi_1(u_i) \\ 2f_L \sinh(L/2) = \lambda_0 C_0 + \lambda_2 C_2 + \sum_{i=3}^{N} \lambda_i \psi_2(u_i) \\ \forall i \geq 3,\ \bar{g}(u_i) \geq 0,\ \lambda_i \leq 0 \text{ and } \lambda_i \bar{g}(u_i) = 0 \end{cases}$$

It is a little surprise to find again functions ψ_0, ψ_1 and ψ_2 but it is fully consistent with the fact the distribution $\delta(u - u_0)$ generates the so called fundamental solution. Hence the property:

$$g(u) = \int_0^1 \psi_3(v, u)\Gamma(v)dv$$

holds very generally as a solution of equation (2.23) with an arbitrary righthandside Γ. And the efficiency can be computed with the integral:

$$\int_0^1 \bar{g}\bar{\Gamma} = \int_0^1 g\Gamma + \sum_{i=3}^{N} \lambda_i \int_0^1 \psi_3(u, u_i)\Gamma(u)du = \int_0^1 g\Gamma + \sum_{i=3}^{N} \lambda_i g(u_i)$$

where we have used the Kuhn-Tucker conditions. Then, using the relation defining the Lagrange multipliers we have the unchanged relation:

$$\int_0^1 \bar{g}\bar{\Gamma} = \lambda_0 + 2\sinh(L/2)(V\lambda_1 + f_L\lambda_2)$$

And the efficiency again reads as in the case without the positivity constraint:

$$\Lambda = \frac{L^2V^2}{\lambda_0 + 2\sinh(L/2)(V\lambda_1 + f_L\lambda_2) - 2Lf_L^2\tanh(L/2) + L\epsilon}$$

6.4 Justification of the 1D model from the perspective of a 2D model

Below we present arguments in support of our 1D model. We did not include this material into the paper because the modeling of cell motility in 1D framework is rather common (see, for instance, [52, 97, 124, 156]) and the detailed justification is usually omitted. In case the reviewers find it appropriate we can include some of this material into our Supplementary Information.

To justify the reduced model we start with a 3D problem describing the flow of an active gel [89] with a tensorial active prestress. We neglect orientational degrees of freedom assuming that the activity is 'frozen'.

We proceed in two steps. First we justify reduction from 3D to 2D by using the fact that "..the lamellipod is only a few tenths of a micron thick but is tens of microns long and wide" [97, 156]: we average the flow over the thickness and in this way eliminate one of the dimensions. Then we use the Graded Radial Extension assumption [15, 104, 156] to further simplify the problem and extract a 1D (toy) model from the more adequate 2D model. Since the goal of this work is to uncover some very basic effects by means of analytical study, we necessarily have to sacrifice some details that can be easily brought back if the goal is to perform comprehensive numerical simulations.

Our schematic view of the lamellipodial geometry is shown in Fig.6.6. We know that L_1 and L_2 exceed h by at least two orders of magnitude [97, 156]. When the keratocyte cell is moving rapidly, L_1 is several times smaller than L_2 [15, 52, 57, 90].

Inside the moving domain Ω_t we have to solve the following (simplified) system of equations [89]:

$$\begin{cases} div(\sigma) = 0 \\ \sigma = \frac{\eta}{2}\left(\nabla v + \nabla v^T\right) + \chi \end{cases}$$

where σ is the stress tensor , v is the velocity vector and χ is the constant active prestress tensor. The mass balance equation fully uncouples under the assumption that both polymerization and depolymerization localize on the boundaries [15, 104, 156]. Then if ρ is the mass density we can write

$$\partial_t \rho + div(\rho v) = 0.$$

Consider first the side view (x, z plane) and assume that $L_2 \gg L_1 \gg h$. The force balance in the x, z can then be written as:

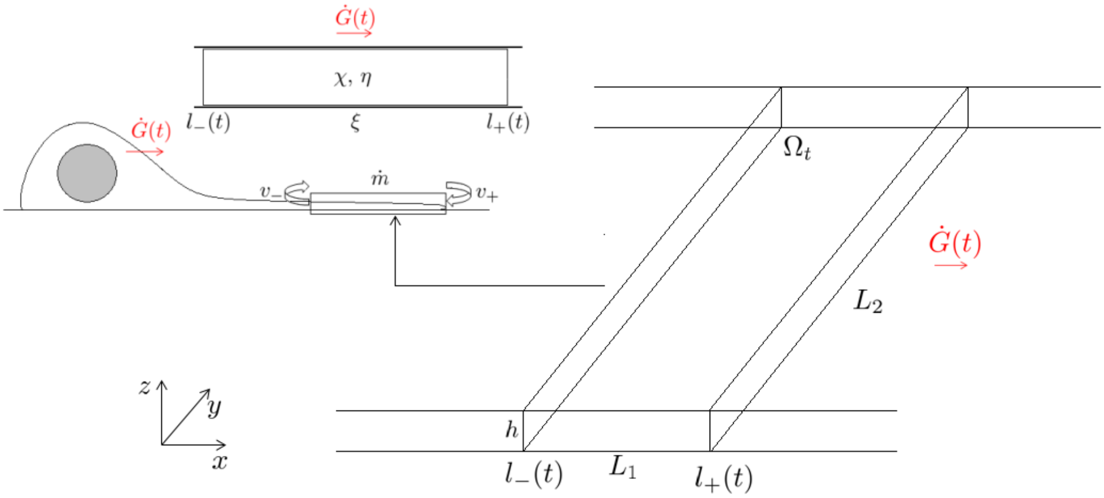

Figure 6.6: Schematic representation of the 3D geometry of the lamellipode.

$$\begin{cases} \partial_{xx}v_x + \frac{1}{2}\partial_z(\partial_z v_x + \partial_x v_z) = 0 \\ \partial_{zz}v_z + \frac{1}{2}\partial_x(\partial_z v_x + \partial_x v_z) = 0 \end{cases}$$

To avoid the study of the surface topography which is almost flat inside the lamellipode, we assume that the flow takes place between two horizontal surfaces. Then, the lubrication approximation suggests, introducing the averaged horizontal velocity:

$$\langle v_x \rangle (x) = \frac{1}{h}\int_0^h v_x(x,z)dz$$

By integration and application of BC on the top,

$$\begin{cases} v_z = 0 \\ \sigma_{xz} = \frac{-\xi}{2}v_x, \end{cases}$$

and bottom,

$$\begin{cases} v_z = 0 \\ \sigma_{xz} = \frac{\xi}{2}v_x, \end{cases}$$

and then using the fact that h is small (with respect to $\sqrt{\eta/\xi}$) along with the assumption that $\chi_{xz} = 0$, we obtain the 1D equation:

$$\eta \partial_{xx}\langle v_x \rangle = (\xi/2)\frac{v_x(0) + v_x(h)}{h} \simeq \xi \langle v_x \rangle$$

The other average velocity

$$\langle v_z \rangle (x) = \frac{1}{h}\int_0^h v_z(x,z)dz = 0$$

by the symmetry of the problem. Hence, up to the first order in h, we can replace the two dimensional problem as a one dimensional problem:

$$\begin{cases} \eta\partial_{xx}\langle v_x\rangle = \xi\langle v_x\rangle \\ \eta\partial_x v_x(l_-) = q_- - \chi_{xx} \\ \eta\partial_x v_x(l_+) = q_+ - \chi_{xx} \end{cases}$$

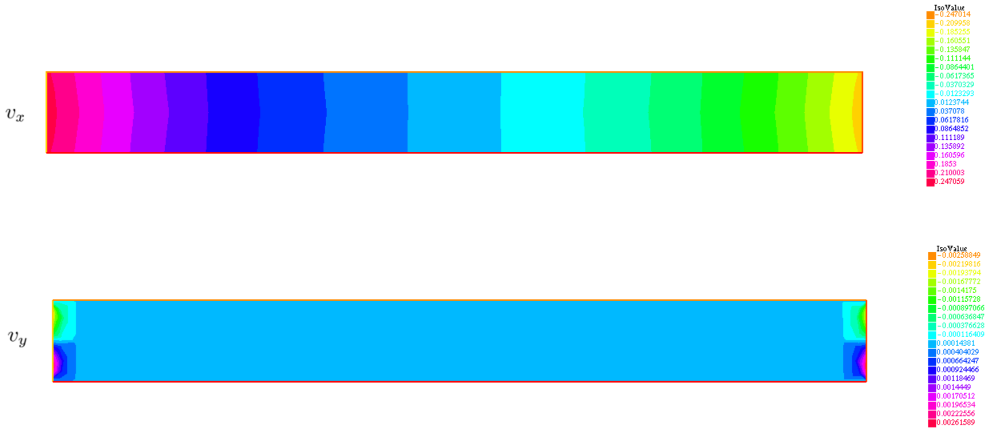

Figure 6.7: Numerical simulation of the problem for $\chi_{xz} = \chi_{zz} = 0$ and $L = 10h$

Such a reduced description misses the boundary layers which we illustrate through the finite element simulations of the full 2D problem in Fig.6.7. One can see that the flow is practically one-dimensional outside narrow zones near the front and the rear of the lamellipode. Some potentially non-trivial effects due to the boundary layers at rear and front can be absorbed into augmented boundary conditions (not studied in this paper).

Next we consider in more detail the remaining 2D problem (by assuming that L_2 is now finite). We assume that the problem has been already averaged over the thickness (h is small). The geometry of the 2D cell body is shown in Fig.6.8 where we also specify the boundary conditions on the moving surfaces. Balance of mass fully uncouples from this problem provided the Graded Radial Extension approximation [15, 104, 156] is used to describe the mass flux brought by polymerization/depolymerization of actin (see kinematic boundary conditions shown in Fig.6.8). Such modeling assumptions have been used in [15, 156] where one can find relevant data on fish keratocytes.

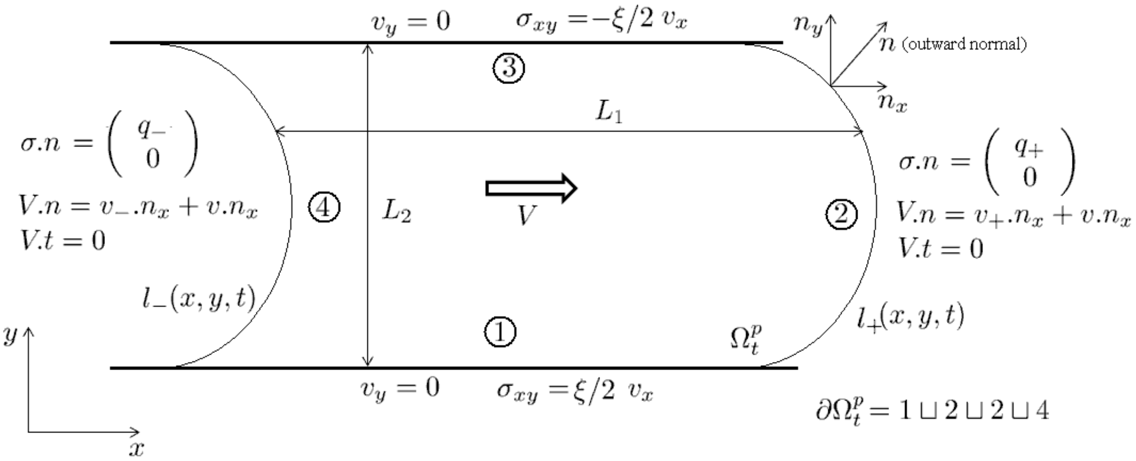

Figure 6.8: Description of the 2D problem in x, y coordinates.

The 2D bulk equations can be written as:

$$\begin{cases} div(\sigma) = \xi v \\ \sigma = \frac{\eta}{2}\left(\nabla v + \nabla v^T\right) + \chi \end{cases}$$

where the bulk term ξv is due to the lubrication type averaging over thickness. Suppose that $L_2 >> L_1$ and that the domain remains rectangular at all times. In this way we avoid solving the free boundary problem (we replace the front and the back of the cell by specified flat surfaces). Then the bulk equations can be written as

$$\begin{cases} \partial_{xx} v_x + \frac{1}{2}\partial_y(\partial_y v_x + \partial_x v_y) = \xi v_x \\ \partial_{yy} v_y + \frac{1}{2}\partial_x(\partial_y v_x + \partial_x v_y) = \xi v_y \end{cases}$$

If we suppose that the $L_2 \gg L_1$, it becomes legitimate to look for potential solutions:

$$v_x = \partial_x \phi \text{ and } v_y = \partial_y \phi$$

Then the bulk equations read:

$$\begin{cases} \eta \partial_x(\triangle \phi) = \xi \partial_x \phi \\ \eta \partial_y(\triangle \phi) = \xi \partial_y \phi \end{cases}$$

Hence,

$$\eta \triangle \phi = \xi \phi + const$$

with boundary conditions on (2):

$$\eta\partial_{xx}\phi = q_+ - \chi_{xx} \text{ and } \partial_{xy}\phi = 0$$

and on (4):

$$\eta\partial_{xx}\phi = q_- - \chi_{xx} \text{ and } \partial_{xy}\phi = 0$$

given that we supposed $\chi_{xy} = \chi_{yy} = 0$. It is now natural to separate variables $\phi(x, y) = f(x)g(y)$ and use the fact mixed derivatives vanishes on the boundaries (2) and (4). We then find that $g(y) = const$ and that $f(x)$ solves:

$$\eta f'' = \xi f$$

Therefore we obtain that in the bulk, the velocity v_x depends on x only and solves the same equation as in the paper:

$$\eta\partial_{xx}v_x = \xi v_x$$

with boundary conditions:

$$\begin{cases} \eta\partial_x v_x(l_-) = q_- - \chi_{xx} \\ \eta\partial_x v_x(l_+) = q_+ - \chi_{xx} \end{cases}$$

At the same time we know that,

$$v_y \equiv 0$$

Finally, putting together the two projections we recover the one dimensional problem solved in the paper.

$$\eta\partial_{xx}v_x = \xi v_x$$

with boundary conditions:

$$\begin{cases} \eta\partial_x v_x(l_-) = q_- - \chi_{xx} \\ \eta\partial_x v_x(l_+) = q_+ - \chi_{xx} \end{cases}$$

In the 2D setting we have to deal with non-1D boundary conditions at the surfaces (1) and (3) generating boundary layers, (see Fig.6.9). One can see that the velocity $v_y = 0$ outisde boundary layers and that v_x varies practically in 1D. Observe that in [52, 124], where the focus is was palced on protrusion/retraction of the keratocyte, the same one dimensional assumptions have been made. Also in [156] the same 1D formulation was obtained motivated by the full 2D computations of a moving keratocyte.

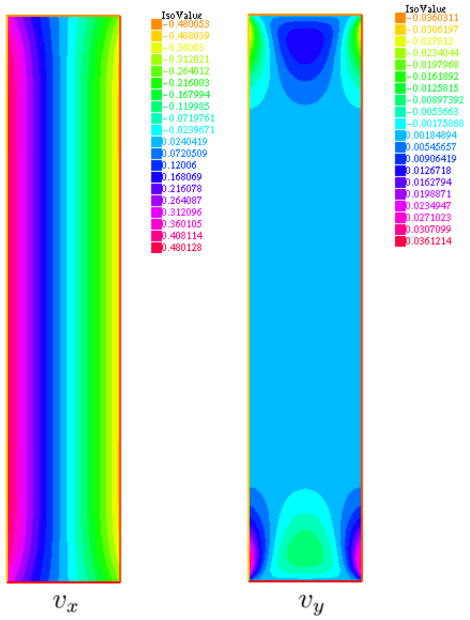

v_x v_y

Figure 6.9: Numerical simulation of the problem for $\chi_{xy} = \chi_{yy} = 0$ and $L_2 = 5L_1$

6.5 Numerical methods

6.5.1 Numerical method for the Cauchy problem

We can model velocity, stress, and density fields as well as fronts using the following (non dimensional) Keller-Segel with Stefan boundary conditions like system :

$$\left\{ \begin{array}{c} -\partial_{xx}\sigma + \sigma = F(\rho_a) + G(\rho_m) \\ \sigma(l_-(t),t) = q_- \text{ and } \sigma(l_+(t),t) = q_+ \end{array} \right. \tag{6.15}$$

$$\left\{ \begin{array}{l} \dot{l}_- = v_- + \partial_x\sigma(l_-(t),t) \\ \dot{l}_+ = v_+ + \partial_x\sigma(l_+(t),t) \\ l_-(0) = l_-^0 < l_+(0) = l_+^0 \end{array} \right. \tag{6.16}$$

$$\left\{ \begin{array}{c} \partial_t\rho_a + \partial_x(\partial_x\sigma\rho_a) = 0 \\ \rho_a(l_-(t),t)v_- = \rho_a(l_+(t),t)v_+ \text{ (treadmilling condition)} \\ \rho_a(x,0) = \rho_a^0(x) \end{array} \right. \tag{6.17}$$

$$\left\{ \begin{array}{c} \partial_t\rho_m + \partial_x(\partial_x\sigma\rho_m - D\partial_x\rho_m) = 0 \\ \rho_m(l_-(t),t)v_- + D\partial_x\rho_m(l_-(t),t) = \rho_m(l_+(t),t)v_+ + D\partial_x\rho_m(l_+(t),t) = 0 \\ \rho_m(x,0) = \rho_m^0(x) \end{array} \right. \tag{6.18}$$

1. $l_-(t)$ and $l_+(t)$ are unknowns functions of time which stand for the rear and front of the cell.
$$l_-, l_+ : \left| \begin{array}{ccc} \mathbb{R}^+ & \longrightarrow & \mathbb{R} \\ t & \longmapsto & l_-, l_+(t) \end{array} \right.$$
We suppose that $l_- < l_+$ for all times (we in fact need to derive conditions so that this assumption holds true) and we denote by Ω the set between the two curves l_- and l_+.

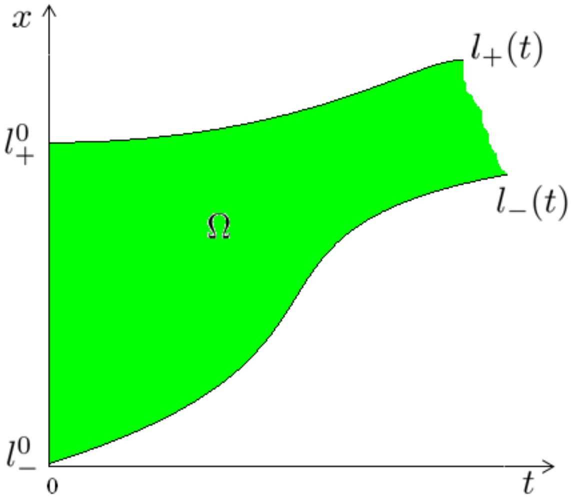

Figure 6.10: The set Ω

2. In the parametrized interval $[l_-(t), l_+(t)]$ functions $\rho_a(x,t)$,$\rho_m(x,t)$ and $\sigma(x,t)$ denote respectively actin density, bounded myosin density and stress inside the cell in the referential of the lab. All functions σ, ρ_a, ρ_m are functions of space and time :
$$v, \sigma, \rho : \left| \begin{array}{ccc} \Omega & \longrightarrow & \mathbb{R} \\ (x,t) & \longmapsto & v, \sigma, \rho(x,t) \end{array} \right.$$
3. Functions F and G are denoted "elastic" and "antielastic"
$$F, G : \left| \begin{array}{ccc} \mathbb{R}^+ & \longrightarrow & \mathbb{R} \\ \rho & \longmapsto & F, G(\rho) \end{array} \right.$$
F models the passive elastic response of the cell. We shall investigate several behaviour laws (perfect gases, Hook's law, etc..).In this prospect F may change

sign passing the normalized "prefered" actin density. It may also be important for mathematical analysis to suppose that F is convex (Some estimations on the tube of solutions can be made with this hypothesis).
G models contractile effect of myosin bundles crosslinking actin. In this prospect, G has to be negative.

We have already investigated several parts of this system in our work, providing well poseness properties in some cases. We do not aim at showing such properties but we present in this general setting the numerical procedure we designed to find a solution.

We first make a change of variable to pose a problem on the segment $[0, 1]$:

$$\left\{ \begin{array}{c} y = \frac{x - l_-(t)}{l_+(t) - l_-(t)} \\ s = t \end{array} \right.$$

The jacobian of this change of variable is strictly positive provided $L(t) = l_+(t) - l_-(t) > 0$ is positive, which is the only case we are interested in. We also make the change of unknown functions :

$$Y_a = L\rho_a \text{ and } Y_m = L\rho_m$$

Equations (6.15-6.18) become:

$$\left\{ \begin{array}{c} -\frac{1}{L^2}\partial_{yy}\sigma + \sigma = F(\frac{Y_a}{L}) + G(\frac{Y_m}{L}) \\ \sigma(0, s) = q_- \text{ and } \sigma(1, s) = q_+ \end{array} \right. \tag{6.19}$$

$$\left\{ \begin{array}{c} \dot{l}_- = v_- + \frac{1}{L}\partial_y\sigma(0, s) \\ \dot{l}_+ = v_+ + \frac{1}{L}\partial_y\sigma(1, s) \\ l_-(0) = l_-^0 < l_+(0) = l_+^0 \end{array} \right. \tag{6.20}$$

$$\left\{ \begin{array}{c} \partial_s Y_a + \partial_y(Y_a \frac{\frac{\partial_y\sigma}{L} - \dot{s}_- - y\dot{L}}{L}) = 0 \\ \rho_a(0, s)v_- = \rho_a(1, s)v_+ \\ Y_a(y, 0) = Y_a^0(y) \end{array} \right. \tag{6.21}$$

$$\left\{ \begin{array}{c} \partial_s Y_m + \partial_y(Y_m \frac{\frac{\partial_y\sigma}{L} - \dot{r} - y\dot{L}}{L} - \frac{D}{L^2}\partial_y Y_m) = 0 \\ Y_m(0, s)v_- + \frac{D}{L}\partial_y Y_m(0, s) = Y_m(1, s)v_+ + \frac{D}{L}\partial_y Y_m(1, s) = 0 \\ Y_m(y, 0) = Y_m^0(y) \end{array} \right. \tag{6.22}$$

Let us now suppose that the equivalent drift $\frac{\frac{\partial_y\sigma}{L} - \dot{l}_- - y\dot{L}}{L}$ and the equivalent diffusion $\frac{D}{L}$ are known from the solution of (6.19). Then equations (6.21) and (6.22) are well posed. For equation (6.22) we must indeed impose two boundary conditions and for equation (6.21), we know that the fluxes at both ends are negative and equal from the treadmilling condition. So as classical we only impose one boundary condition on the characteristic as compulsory for this type of problem.

We use this simple fact to design a numerical scheme that solve this type of problem :

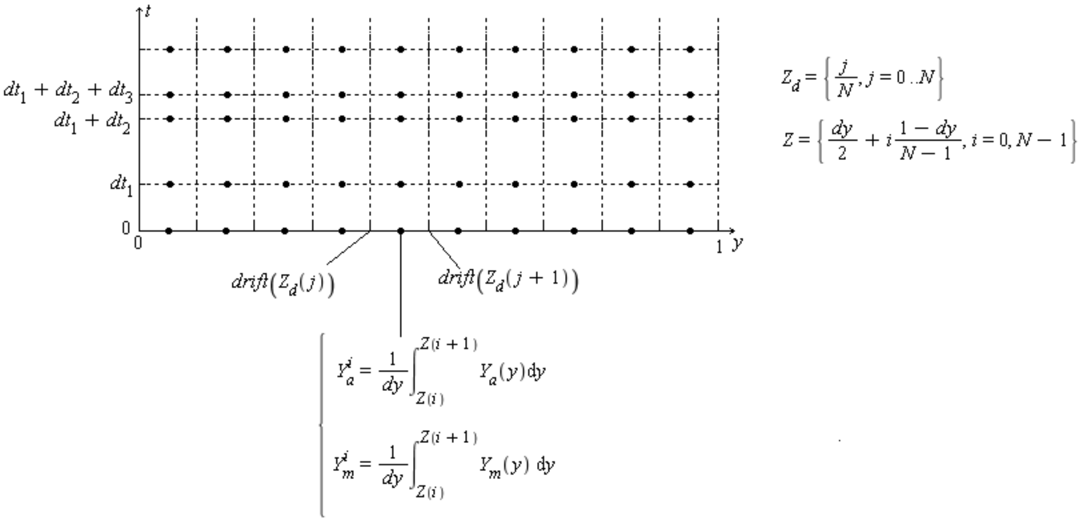

Figure 6.11: Grid used to numerically solve system(6.19-6.21-6.22)

1. We built two grids of same spacing on $[0, 1]$ (see Fig.6.11) The grid Z and its dual Z_d
2. Using the initial conditions from (6.21) and (6.22) we solve (6.19) on the dual grid Z_d using a classical finite differences procedure of order two in space. From there we compute the field $\frac{1}{L}\partial_y\sigma(y, 0)$
3. Choosing a time step (we shall see further how), using (6.20) we compute $\dot{l}_-(0)$ and $\dot{l}_+(0)$ and hence $l_-(dt)$ and $l_+(dt)$ with Euler scheme. We then know on the dual grid Z_d, the equivalent drift and diffusion.

4. We apply an upwind finite volume scheme (conservative and consistent) to compute on Z the density distribution $Y_a(y, dt)$ and $Y_m(y, dt)$. Two classical "tricks" to prevent gibbs oscillations in presence of a stationary shock and to compute accurately the right diffusion when there is one (in 6.22) are implemented.
5. We start over the procedure to compute the next time step

The stability of such a scheme is given by Courant-Friedreich-Lewy conditions in equations (6.21) and (6.22) (Using the maximum of the drift at each time step so that no Riemann problem interfere with an other). Therefore, the timestep is adaptive and ensures stability. This scheme is very robust to discontinuities and is conservative. Therefore the essential properties :

$$\forall s > 0,$$

$$\int_0^1 Y_a(y, s)dy = \int_0^1 Y_a^0(y)dy$$

and,

$$\int_0^1 Y_m(y, s)dy = \int_0^1 Y_m^0(y)dy$$

are conserved for the numerical solution.

From a mathematical point of view, lots of things need to be proved starting from existence and uniqueness of a weak solution of the original problem (Maybe an "entropy condition" needs to be added in some cases) to the convergence of this scheme to the solution. We left this to future work.

6.5.2 Efficiency Optimization

In a attempt to make conjectures we designed the following elementary finite element procedure to find the maximum of efficiency. We approximate the function g by a staircase function with n elements :

$$g(y) = \sum_{i=1}^{n} a_i 1_{[\frac{i-1}{n}, \frac{i}{n}]}(y)$$

Thus, the discretized problem is maximization problem on a finite set of values $(a = \{ai\}, L) \in \mathbb{R}_+^{n+1}$ of functional

$$\Lambda_n(a,L) = \frac{L}{4\sinh(L/2)^2}\frac{(a.S(L))^2}{na.a/L-(a.C(L))^2/\sinh(L)-aa^T:F(L)+n^2\epsilon}$$

with constrains,

$$\begin{cases} 1.a = nM \\ a \geq 0 \\ a.C(L) = 2nf_L\sinh(L/2) \end{cases}$$

where $\forall i,j \in [1,n]$,

$$\begin{cases} S_i = \sinh(\frac{L}{2}\frac{n-2i+1}{n}) \\ C_i = \cosh(\frac{L}{2}\frac{n-2i+1}{n}) \\ F_{i,j} = \Psi(\frac{2i-1}{n},\frac{2j-1}{n}) \end{cases}$$

We then use classical discrete optimization package from Matlab.

References

[1] M Abercrombie. Croonian Lecture, 1978 - Crawling movement of metazoan cells. *Proceedings of the Royal Society OF London series B-Biological Sciences*, 207(1167):129–&, 1980. 2, 12, 113

[2] Aphrodite Ahmadi, M. C. Marchetti, and T. B. Liverpool. Hydrodynamics of isotropic and liquid crystalline active polymer solutions. *Phys. Rev. E*, 74:061913, 2006. 56

[3] Bruce Alberts, Alexander Johnson, Julian Lewis, Martin Raff, Keith Roberts, and Peter Walter. *Molecular biology of the cell*. Garland Science Taylor & Francis Group, 4 edition, 2002. 4, 10, 55

[4] J. Allard and A. Mogilner. Traveling waves in actin dynamics and cell motility. *Current Opinion in Cell Biology*, 2012. 131

[5] F. Alouges, A. DeSimone, and L. Heltai. Numerical strategies for stroke optimization of axisymmetric microswimmers. *Mathematical Models and Methods in Applied Sciences*, 21(02):361–387, 2011. 40

[6] F. Alouges, A. DeSimone, and A. Lefebvre. Optimal strokes for axisymmetric microswimmers. *The European Physical Journal E: Soft Matter and Biological Physics*, 28:279–284, 2009. 40

[7] Wolfgang Alt and Micah Dembo. Cytoplasm dynamics and cell motion: two-phase flow models. *Mathematical Biosciences*, 156(1Ũ2):207 – 228, 1999. 18, 128

[8] Wolfgang Alt and Robert T. Tranquillo. Basic morphogenetic system modeling shape changes of migrating cells: How to explain fluctuating lamellipodial dynamics. *Journal of Biological Systems*, 03(04):905–916, 1995. 128

[9] Steven J. Altschuler, Sigurd B. Angenent, Yanqin Wang, and Lani F. Wu. On the spontaneous emergence of cell polarity. *Nature*, 454(7206):886–889, 2008. 56

[10] Julia C. Arciero, Qi Mi, Maria F. Branca, David J. Hackam, and David Swigon. Continuum Model of Collective Cell Migration in Wound Healing and Colony Expansion. *Biophysical Journal*, 100(3):535–543, 2011. 4

[11] E Atilgan, D Wirtz, and SX Sun. Morphology of the lamellipodium and organization of actin filaments at the leading edge of crawling cells. *Biophysical Journal*, 89(5):3589–3602, 2005. 7

[12] E Atilgan, D Wirtz, and SX Sun. Mechanics and dynamics of actin-driven thin membrane protrusions. *Biophysical Journal*, 90(1):65–76, 2006. 7

[13] S. Banerjee and M. C. Marchetti. Substrate rigidity deforms and polarizes active gels. *EPL (Europhysics Letters)*, 96(2):28003, 2011. 3, 12, 14, 137

[14] Erin L. Barnhart, Greg M. Allen, Frank Julicher, and Julie A. Theriot. Bipedal Locomotion in Crawling Cells. *Biophysical Journal*, 98(6):933–942, 2010. 3, 4, 18, 25, 56, 57, 114, 134, 135, 149

[15] Erin L. Barnhart, Kun-Chun Lee, Kinneret Keren, Alex Mogilner, and Julie A. Theriot. An adhesion-dependent switch between mechanisms that determine motile cell shape. *PLoS Biol*, 9(5):e1001059, 05 2011. 10, 12, 19, 56, 125, 160, 161, 164, 166

[16] Carlsson AE Bayly PV, Taber LA. Damped and persistent oscillations in a simple model of cell crawling. *Journal of The Royal Society Interface*, pages 1742–5662, 2011. 18, 149

[17] GI Bell. Models for specific adhesion of cells to cells. *Science*, 200(4342):618–627, 1978. 11

[18] PB Bell. Cell behavior - A tribute to Abercrombie,Michael - Bellairs,R, Curtis,A, Dunn,G. *American Scientist*, 72(1):88–89, 1984. 2, 12

[19] R Bellairs. Michael Abercrombie (1912-1979). *International Journal of Developmental Biology*, 44(1, Sp. Iss. SI):23–28, 2000. 2, 12

[20] Henri Berestycki. *Equations de reaction-diffusion et dynamiques de populations biologiques*. UPMC, 2008. 24, 26

[21] Bernardin, D. *Introduction a la rheologie des fluides : approche macroscopique*. Ecole de printemps, G.D.R. Materiaux vitreux, 2003 3

[22] A Bernheim-Groswasser, J Prost, and C Sykes. Mechanism of actin-based motility: A dynamic state diagram. *Biophysical Journal*, 89(2):1411–1419, 2005. 16

[23] AD Bershadsky, NQ Balaban, and B Geiger. Adhesion-dependent cell mechanosensitivity. *Annual Review of Cell and Developmental Biology*, 19:677–695, 2003. 12, 159

[24] David Boal. *Mechanics of the Cell*. Cambridge University Press, 2002. 3, 25, 57, 137

[25] Justin S. Bois, Frank Jülicher, and Stephan W. Grill. Pattern formation in active fluids. *Phys. Rev. Lett.*, 106:028103, 2011. 9, 10, 12, 18, 56, 57, 65, 67, 68, 70, 84, 86, 128, 159, 161

[26] D Bottino, A Mogilner, T Roberts, M Stewart, and G Oster. How nematode sperm crawl. *Journal of Cell Science*, 115(2):367–384, 2002. 12, 18, 120, 122, 160

[27] Dennis Bray. *Cell Movements: From Molecules to Motility*. Garland Science, 2 edition, 2000. 1, 4, 8, 55

[28] Haim Brezis. *Analyse Fonctionelle*. 1983. 42

[29] Jan Brugués and Jaume Casademunt. Self-organization and cooperativity of weakly coupled molecular motors under unequal loading. *Phys. Rev. Lett.*, 102(11):118104, 2009. 120

[30] Claudia Brunner, Allen Ehrlicher, Bernd Kohlstrunk, Detlef Knebel, Josef Käs, and Michael Goegler. Cell migration through small gaps. *European Biophysics Journal*, 35:713–719, 2006. 114, 117, 120

[31] D.T. Burnette, S. Manley, P. Sengupta, R. Sougrat, M.W. Davidson, B. Kachar, and J. Lippincott-Schwartz. A role for actin arcs in the leading-edge advance of migrating cells. *Nature cell biology*, 13(4):371–382, 2011. 131

[32] E. Caglioti, P. L. Lions, C. Marchioro, and M. Pulvirenti. A special class of stationary flows for two-dimensional euler equations: A statistical mechanics description. *Communications in Mathematical Physics*, 143, 1992. 75

[33] John W Cahn. On spinodal decomposition. *Acta Metallurgica*, 9(9):795 – 801, 1961. 86

[34] A. C. Callan-Jones and F. Julicher. Hydrodynamics of active permeating gels. *New Journal of Physics*, 13, 16 2011. 3, 9, 17, 136, 137

[35] Vincent Calvez, Rhoda J. Hawkins, Nicolas Meunier, and Raphael Voituriez. Analysis of a Nonlocal Model for Spontaneous Cell Polarization. *SIAM Journal on Applied Mathematics*, 72(2):594+, 2012. 14

[36] Vincent Calvez, Nicolas Meunier, and Raphael Voituriez. A one-dimensional Keller-Segel equation with a drift issued from the boundary. *Comptes Rendus Mathematique*, 348(11Ũ12):629 – 634, 2010. 56

[37] Otger Campas, L. Mahadevan, and Jean-Francois Joanny. Actin Network Growth under Load. *Biophysical Journal*, 102(5):1049–1058, 2012. 3, 7, 16, 137

[38] Luca Cardamone, Alessandro Laio, Vincent Torre, Rajesh Shahapure, and Antonio DeSimone. Cytoskeletal actin networks in motile cells are critically self-organized systems synchronized by mechanical interactions. *Proceedings of the National Academy of Sciences of the USA*, 108(34):13978–13983, 2011. 7, 131, 149, 157

[39] A. E. Carlsson. Mechanisms of cell propulsion by active stresses. *New Journal of Physics*, 13, 2011. 16, 118

[40] Anders E. Carlsson and David Sept. Mathematical modeling of cell migration. In *Biophysical tools for biologists: Vol 1 in vitro techniques*, volume 84 of *Methods in cell biology*, pages 911+. Elsevier academic press INC, 2008. 17, 56

[41] AndersE. Carlsson and Alex Mogilner. Mathematical and physical modeling of actin dynamics in motile cells. In Marie-France Carlier, editor, *Actin-based Motility*, pages 381–412. Springer Netherlands, 2010. 7

[42] J. Carr and R. L. Pego. Metastable patterns in solutions of ut = e2 uxx - f(u). *Communications on Pure and Applied Mathematics*, 42(5):523–576, 1989. 84

[43] Bin Chen and Huajian Gao. Mechanical Principle of Enhancing Cell-Substrate Adhesion via Pre-Tension in the Cytoskeleton. *Biophysical Journal*, 98(10):2154–2162, 2010. 11, 53

[44] Bin Chen and Huajian Gao. Mechanical Principle of Enhancing Cell-Substrate Adhesion via Pre-Tension in the Cytoskeleton. *Biophysical Journal*, 98(10):2154–2162, 2010. 53

[45] C.C. Chen and C.S. Lin. On the symmetry of blowup solutions to a mean field equation. In *Annales de l'Institut Henri Poincare (C) Non Linear Analysis*, volume 18, pages 271–296. Elsevier, 2001. 75

[46] Daniel T. N. Chen, Qi Wen, Paul A. Janmey, John C. Crocker, and Arjun G. Yodh. Rheology of Soft Materials. In Langer, JS, editor, *Annual Review of Condensed Matter Physics, Vol 1*, volume 1 of *Annual Review of Condensed Matter Physics*, pages 301–322. 2010. 3

[47] P.G. Ciarlet. *Introduction a l'analyse numerique matricielle et a l'optimisation.* Masson, 1988. 162

[48] Kristopher Clark, Michiel Langeslag, Carl G. Figdor, and Frank N. van Leeuwen. Myosin ii and mechanotransduction: a balancing act. *Trends in Cell Biology*, 17(4):178 – 186, 2007. 9

[49] B Cleuren and C Van den Broeck. Brownian motion with absolute negative mobility. *Physical Review E*, 67(5, Part 2),2003. 120

[50] Gabor Csucs, Katharina Quirin, and Gaudenz Danuser. Locomotion of fish epidermal keratocytes on spatially selective adhesion patterns. *Cell Motility and the Cytoskeleton*, 64(11):856–867, 2007. 55, 57

[51] Vladimir Igorevich Arnold D. V. Anosov. *Dynamical Systems: Bifurcation theory and catastrophe theory.* Springer-Verlag, 1994. 107

[52] Adriana T. Dawes, G. Bard Ermentrout, Eric N. Cytrynbaum, and Leah Edelstein-Keshet. Actin filament branching and protrusion velocity in a simple 1D model of a motile cell. *Journal Of Theoretical Biology*, 242(2):265–279,2006. 16, 164, 168

[53] PA DiMilla, K Barbee, and DA Lauffenburger. Mathematical-model for the effects of adhesion and mechanics on cell-migration speed. *Biophysical Journal*, 60(1):15–37, 1991. 3, 12, 18, 113, 137, 159

[54] K. Doubrovinski and K. Kruse. Self-organization of treadmilling filaments. *Phys. Rev. Lett.*, 99:228104, 2007. 16

[55] K. Doubrovinski and K. Kruse. Self-organization in systems of treadmilling filaments. *European Physical Journal E*, 31(1):95–104,2010. 16, 56

[56] K. Doubrovinski and K. Kruse. Cell motility resulting from spontaneous polymerization waves. *Phys. Rev. Lett.*, 107:258103, 2011. 12, 19, 114, 115, 131, 159

[57] AD Doyle and J Lee. Cyclic changes in keratocyte speed and traction stress arise from Ca2+-dependent regulation of cell adhesiveness. *Journal of Cell Science*, 118(2):369–379, 2005. 164

[58] XinXin Du, Konstantin Doubrovinski, and Miriam Osterfield. Self-organized cell motility from motor-filament interactions. *Biophysical Journal*, 102(8):1738 – 1745, 2012. 3, 4, 56, 114, 134, 135

[59] T. Erdmann and U. S. Schwarz. Stability of adhesion clusters under constant force. *Phys. Rev. Lett.*, 92:108102, 2004. 11

[60] T Erdmann and US Schwarz. Stochastic dynamics of adhesion clusters under shared constant force and with rebinding. *Journal of Chemical Physics*, 121(18):8997–9017,2004. 11

[61] D.A. Fletcher and J.A. Theriot. An introduction to cell motility for the physical scientist. *Physical Biology*, 1(1):T1, 2004. 16

[62] Huajian Gao, Jin Qian, and Bin Chen. Probing mechanical principles of focal contacts in cell-matrix adhesion with a coupled stochastic-elastic modelling framework. *Journal of the Royal Society Interface*, 8(62):1217–1232, 2011. 11, 40, 53

[63] Margaret L. Gardel, Benedikt Sabass, Lin Ji, Gaudenz Danuser, Ulrich S. Schwarz, and Clare M. Waterman. Traction stress in focal adhesions correlates biphasically with actin retrograde flow speed. *Journal of Cell Biology*, 183(6):999–1005, 2008. 12, 18, 159

[64] Margaret L. Gardel, Ian C. Schneider, Yvonne Aratyn-Schaus, and Clare M. Waterman. Mechanical Integration of Actin and Adhesion Dynamics in Cell Migration. In Schekman, R and Goldstein, L and Lehmann, R, editor, *Annual Review of Cell and Developmental Biology, Vol 26*, volume 26 of *Annual Review of Cell and Developmental Biology*, pages 315–333. 2010. 12, 18, 159

[65] Uduak George, Angelique Stéphanou, and Anotida Madzvamuse. Mathematical modelling and numerical simulations of actin dynamics in the eukaryotic cell. *Journal of Mathematical Biology*, pages 1–47, 2012. 10.1007/s00285-012-0521-1. 128, 129, 161

[66] Fabien Gerbal, Paul Chaikin, Yitzhak Rabin, and Jacques Prost. An elastic analysis of listeria monocytogenes propulsion. *Biophysical Journal*, 79(5):2259 – 2275, 2000. 14, 16

[67] F. Gladiali, M. Grossi, H. Ohtsuka, and T. Suzuki. Morse indices of multiple blow-up solutions to the two-dimensional gel'fand problem. *arXiv preprint arXiv:1210.1373*, 2012. 75

[68] Maria E. Gracheva and Hans G. Othmer. A continuum model of motility in ameboid cells. *Bulletin of Mathematical Biology*, 66(1):167 – 193, 2004. 18

[69] WH Guo, MT Frey, NA Burnham, and YL Wang. Substrate rigidity regulates the formation and maintenance of tissues. *Biophysical Journal*, 90(6):2213–2220, 2006. 11

[70] Peter Hanggi, Fabio Marchesoni, Sergey Savel'ev, and Gerhard Schmid. Asymmetry in shape causing absolute negative mobility. *Physical Review e*, 82(4, Part 1), 2010. 120

[71] R. J. Hawkins, O. Bénichou, M. Piel, and R. Voituriez. Rebuilding cytoskeleton roads: Active-transport-induced polarization of cells. *Physical Review E*, 80(4):040903+, 2009. 14, 56, 67

[72] R. J. Hawkins, M. Piel, G. Faure-Andre, A. M. Lennon-Dumenil, J. F. Joanny, J. Prost, and R. Voituriez. Pushing off the Walls: A Mechanism of Cell Motility in Confinement. *Physical Review Letters*, 102(5), 2009. 14, 16

[73] R. J. Hawkins and R. Voituriez. Mechanisms of Cell Motion in Confined Geometries. *Mathematical Modelling of Natural Phenomena*, 5(1):84–105, 2010. 14

[74] Rhoda J. Hawkins, Renaud Poincloux, Olivier Benichou, Matthieu Piel, Philippe Chavrier, and Raphael Voituriez. Spontaneous Contractility-Mediated Cortical Flow Generates Cell Migration in Three-Dimensional Environments. *Biophysical Journal*, 101(5):1041–1045, 2011. 12, 14, 19, 56, 159

[75] Marc Herant and Micah Dembo. Form and Function in Cell Motility: From Fibroblasts to Keratocytes. *Biophysical Journal*, 98(8):1408–1417, 2010. 18, 56, 114, 115

[76] A. V. Hill. The Heat of Shortening and the Dynamic Constants of Muscle. *Proceedings of the Royal Society of London. Series B, Biological Sciences*, 126(843):136–195, 1938. 28, 104

[77] Brenton D. Hoffman and John C. Crocker. Cell Mechanics: Dissecting the Physical Responses of Cells to Force. *Annual Review of Biomedical Engineering*, 11:259–288, 2009. 113

[78] Jonathon Howard, Stephan W. Grill, and Justin S. Bois. Turing's next steps: the mechanochemical basis of morphogenesis. *Nature Reviews Molecular Cell Biology*, 12(6):392–398, 2011. 14, 56, 57, 67

[79] Longhua Hu and Garegin A. Papoian. Mechano-chemical feedbacks regulate actin mesh growth in lamellipodial protrusions. *Biophysical Journal*, 98(8):1375 – 1384, 2010. 7

[80] HE Huxley. Electron microscope studies of the organisation of the filaments in striated muscle. *Biochimica et Biophysica Acta*, 12(3):387–400, 1953. 8

[81] HE Huxley. Muscle structure and theories of contraction. *Progress in Biophysics and Molecular Biology*, 7:255–&, 1957. 8

[82] Alexandra Jilkine and Leah Edelstein-Keshet. A comparison of mathematical models for polarization of single eukaryotic cells in response to guided cues. *PLoS Comput Biol*, 7(4):e1001121, 04 2011. 56, 65

[83] J. F. Joanny, F. Julicher, K. Kruse, and J. Prost. Hydrodynamic theory for multi-component active polar gels. *New Journal of Physics*, 9,2007. 3, 9, 17, 137

[84] Jean-Francois Joanny and Jacques Prost. Constructing Tools for the Description of Cell Dynamics. In Duplantier, B and Rivasseau, V, editor, *Biological Physics: Poincare seminar 2009*, volume 60 of *Progress in Mathematical Physics*, pages 1–32. Commissariat Energie Atomique, Div Sci Matiere; Daniel Iagolnitzer Fdn; Ecole Polytechnique, 2011. 12th Poincare Seminar on Biological Physics, Inst Henri Poincare, Paris, France, 2009. 9, 17

[85] JF Joanny, F Julicher, and J Prost. Motion of an adhesive gel in a swelling gradient: A mechanism for cell locomotion. *Physical Review Letters*, 90(16), 2003. 120

[86] Karin John, Philippe Peyla, Klaus Kassner, Jacques Prost, and Chaouqi Misbah. Nonlinear study of symmetry breaking in actin gels: Implications for cellular motility. *Physical Review Letters*, 100(6), 2008. 14, 15, 56, 114

[87] Daniel D. Joseph. *Fluid Dynamics of Viscoelastic Liquids (Applied Mathematical Sciences)*. Springer, 1990. 3

[88] F Julicher, A Ajdari, and J Prost. Modeling molecular motors. *Reviews of Modern Physics*, 69(4):1269–1281, 1997. 28, 103, 104

[89] F. Julicher, K. Kruse, J. Prost, and J.-F. Joanny. Active behavior of the cytoskeleton. *Physics Reports-review Section of Physics Letters*, 449(1-3):3–28, 2007. 3, 7, 8, 9, 12, 17, 28, 57, 65, 67, 103, 124, 126, 137, 159, 161, 162, 164

[90] Kinneret Keren, Zachary Pincus, Greg M. Allen, Erin L. Barnhart, Gerard Marriott, Alex Mogilner, and Julie A. Theriot. Mechanism of shape determination in motile cells. *Nature*, 453(7194):475–U1, 2008. 56, 164

[91] Kinneret Keren, Patricia T. Yam, Anika Kinkhabwala, Alex Mogilner, and Julie A. Theriot. Intracellular fluid flow in rapidly moving cells. *Nature Cell Biology*, 11(10):1219–U137, 2009. 126, 127

[92] Jin Seob Kim and Sean X. Sun. Continuum modeling of forces in growing viscoelastic cytoskeletal networks. *Journal of Theoretical Biology*, 256(4):596–606, 2009. 7

[93] Simone Koehler, Volker Schaller, and Andreas R. Bausch. Collective Dynamics of Active Cytoskeletal Networks. *PLOS ONE*, 6(8), 2011. 2

[94] Gijsje H. Koenderink, Zvonimir Dogic, Fumihiko Nakamura, Poul M. Bendix, Frederick C. MacKintosh, John H. Hartwig, Thomas P. Stossel, and David A. Weitz. An active biopolymer network controlled by molecular motors. *Proceedings of the National Academy of Sciences of the USA*, 106(36):15192–15197, 2009. 3, 8, 16, 136

[95] TP Kole, Y Tseng, I Jiang, JL Katz, and D Wirtz. Intracellular mechanics of migrating fibroblasts. *Molecular Biology of the Cell*, 16(1):328–338, 2005. 3, 138

[96] K Kruse, S Camalet, and F Julicher. Self-propagating patterns in active filament bundles. *Physical Review Letters*, 87(13), 2001. 128, 131

[97] K. Kruse, J. F. Joanny, F. Julicher, and J. Prost. Contractility and retrograde flow in lamellipodium motion. *Physical Biology*, 3(2):130–137, 2006. 3, 7, 8, 21, 57, 114, 115, 116, 118, 119, 120, 124, 136, 144, 161, 162, 164

[98] K Kruse, JF Joanny, F Julicher, J Prost, and K Sekimoto. Generic theory of active polar gels: a paradigm for cytoskeletal dynamics. *European Physical Journal E*, 16(1):5–16, 2005. 9, 17

[99] K Kruse and F Julicher. Actively contracting bundles of polar filaments. *Physical Review Letters*, 85(8):1778–1781, 2000. 58, 61, 128, 131

[100] K. Kruse, A. Zumdieck, and F. Julicher. Continuum theory of contractile fibres. *EPL (Europhysics Letters)*, 64(5):716, 2003. 56

[101] Karsten Kruse and Frank Julicher. Self-organization and mechanical properties of active filament bundles. *Phys. Rev. E*, 67:051913, 2003. 56, 58, 61, 65, 66, 84, 128, 131

[102] Kamila Larripa and Alex Mogilner. Transport of a 1D viscoelastic actin-myosin strip of gel as a model of a crawling cell. *Physica A-Statistical Mechanics and its Applications*, 372(1):113–123, 2006. 3, 8, 12, 19, 125, 126, 137, 159

[103] Eric Lauga and Thomas R. Powers. The hydrodynamics of swimming microorganisms. *Reports on Progress in Physics*, 72(9), 2009. 23, 34

[104] J Lee, A Ishihara, JA Theriot, and K Jacobson. Principles of locomotion for simple-shaped cells. *Nature*, 362(6416):167–171, 1993. 164, 166

[105] R.J. LeVeque. *Finite volume methods for hyperbolic problems*, volume 31. Cambridge university press, 2002. 85

[106] Oliver Lieleg, Mireille M. A. E. Claessens, and Andreas R. Bausch. Structure and dynamics of cross-linked actin networks. *Soft Matter*, 6(2):218–225, 2010. 2

[107] Oliver Lieleg, Kurt M. Schmoller, Christian J. Cyron, Yuxia Luan, Wolfgang A. Wall, and Andreas R. Bausch. Structural polymorphism in heterogeneous cytoskeletal networks. *Soft Matter*, 5(9):1796–1803, 2009. 2

[108] M. J. Lighthill. On the squirming motion of nearly spherical deformable bodies through liquids at very small reynolds numbers. *Communications on Pure and Applied Mathematics*, 5(2):109–118, 1952. 28, 103

[109] Maria L. Lombardi, David A. Knecht, Micah Dembo, and Juliet Lee. Traction force microscopy in Dictyostelium reveals distinct roles for myosin II motor and actin-crosslinking activity in polarized cell movement. *Journal of Cell Science*, 120(Pt 9):1624–1634, 2007. 55, 57

[110] Alex J. Loosley and Jay X. Tang. Stick-slip motion and elastic coupling in crawling cells. *Physical Review E*, 86(3, Part 1), 10 2012. 4, 56

[111] J. Lowengrub and L. Truskinovsky. Quasi-incompressible cahn-hilliard fluids and topological transitions. *Proceedings of the Royal Society of London. Series A: Mathematical, Physical and Engineering Sciences*, 454(1978):2617–2654, 1998. 86

[112] L. Machura, M. Kostur, P. Talkner, J. Luczka, and P. Hanggi. Absolute negative mobility induced by thermal equilibrium fluctuations. *Physical Review Letters*, 98(4), 2007. 120

[113] Frederick C. MacKintosh and Christoph F. Schmidt. Active cellular materials. *Current Opinion in Cell Biology*, 22(1):29–35, 2010. 3, 136

[114] M. C. Marchetti, J.-F. Joanny, S. Ramaswamy, T. B. Liverpool, J. Prost, M. Rao, and R. Aditi Simha. Soft Active Matter. *ArXiv e-prints*, 2012. 102

[115] Y Marcy, J Prost, MF Carlier, and C Sykes. Forces generated during actin-based propulsion: A direct measurement by micromanipulation. *Proceedings of the National Academy of Sciences of the USA*, 101(16):5992–5997, 2004. 15

[116] Mirjam Mayer, Martin Depken, Justin S. Bois, Frank Julicher, and Stephan W. Grill. Anisotropies in cortical tension reveal the physical basis of polarizing cortical flows. *Nature*, 467(7315):617–U150, 2010. 56

[117] JL McGrath, NJ Eungdamrong, CI Fisher, F Peng, L Mahadevan, TJ Mitchison, and SC Kuo. The force-velocity relationship for the actin-based motility of Listeria monocytogenes. *Current Biology*, 13(4):329–332, 2003. 16

[118] Qi Mi, David Swigon, Beatrice Riviere, Selma Cetin, Yoram Vodovotz, and David J. Hackam. One-dimensional elastic continuum model of enterocyte layer migration. *Biophysical Journal*, 93(11):3745–3752, 2007. 12, 159

[119] S. Michelin and E. Lauga. Unsteady feeding and optimal strokes of model ciliates. *arXiv preprint arXiv:1210.1331*, 2012. 40

[120] S.G. Mikhlin. *Linear integral equations*. Hindustan publishing corp., 1960. 35, 45, 120

[121] TJ Mitchison and LP Cramer. Actin-based cell motility and cell locomotion. *Cell*, 84(3):371–379, 1996. 13

[122] Mohammad R. K. Mofrad. Rheology of the Cytoskeleton. *Annual Review of Fluid Mechanics*, 41:433–453, 2009. 2, 3, 137, 138

[123] A Mogilner. On the edge: modeling protrusion. *Current Opinion in Cell Biology*, 18(1):32–39, 2006. 7

[124] A Mogilner and L Edelstein-Keshet. Regulation of actin dynamics in rapidly moving cells: A quantitative analysis. *Biophysical Journal*, 83(3):1237–1258, 2002. 16, 18, 164, 168

[125] A Mogilner and G Oster. Cell motility driven by actin polymerization. *Biophysical Journal*, 71(6):3030–3045, 1996. 7, 16

[126] Alex Mogilner. Mathematics of cell motility: have we got its number? *Journal of Mathematical Biology*, 58(1-2):105–134, 2009. 10, 12, 17, 18, 113, 159

[127] Alex Mogilner, Jun Allard, and Roy Wollman. Cell polarity: Quantitative modeling as a tool in cell biology. *Science*, 336(6078):175–179, 2012. 55

[128] Yoichiro Mori, Alexandra Jilkine, and Leah Edelstein-Keshet. Wave-pinning and cell polarity from a bistable reaction-diffusion system. *Biophysical Journal*, 94(9):3684 – 3697, 2008. 14

[129] R. Dyche Mullins. Cytoskeletal Mechanisms for Breaking Cellular Symmetry. *Cold Spring Harbor Perspectives in Biology*, 2(1), 2010. 14

[130] Alex Mogilner Noa Ofer and Kinneret Keren. An actin 'disassembly clock' determines shape and speed of lamellipodial fragments. *PNAS*, 2011. 157

[131] V. Noireaux, R.M. Golsteyn, E. Friederich, J. Prost, C. Antony, D. Louvard, and C. Sykes. Growing an actin gel on spherical surfaces. *Biophysical Journal*, 78(3):1643 – 1654, 2000. 15

[132] H. Ohtsuka. A concentration phenomenon around a shrinking hole for solutions of mean field equations. *Osaka J. Math*, 39:395–407, 2002. 75

[133] JM Oliver, JR King, KJ McKinlay, PD Brown, DM Grant, CA Scotchford, and JV Wood. Thin-film theories for two-phase reactive flow models of active cell motion. *Mathematical Medicine and Biology*, 22(1):53–98, 2005. 18

[134] Fumio Oosawa and Sho Asakura. *Thermodynamics of the polymerization of protein / Fumio Oosawa and Sho Asakura*. Academic Press, London ; New York :, 1975. 4

[135] Javier G. Orlandi, Carles Blanch-Mercader, Jan Brugues, and Jaume Casademunt. Cooperativity of self-organized brownian motors pulling on soft cargoes. *Phys. Rev. E*, 82(6):061903, 2010. 120

[136] N. Osterman and A. Vilfan. Finding the ciliary beating pattern with optimal efficiency. *Proceedings of the National Academy of Sciences*, 108(38):15727–15732, 2011. 40

[137] Porntula Panorchan, Jerry S. H. Lee, Thomas P. Kole, Yiider Tseng, and Denis Wirtz. Microrheology and ROCK signaling of human endothelial cells embedded in a 3D matrix. *Biophysical Journal*, 91(9):3499–3507, 2006. 3, 138

[138] Amit Pathak, Vikram S. Deshpande, Robert M. McMeeking, and Anthony G. Evans. The simulation of stress fibre and focal adhesion development in cells on patterned substrates. *Journal of the Royal Society Interface*, 5(22):507–524, 2008. 3, 137

[139] Xiaoling Peng, Jianyong Huang, Chunyang Xiong, and Jing Fang. Cell adhesion nucleation regulated by substrate stiffness: A monte carlo study. *Journal of Biomechanics*, 45(1):116 – 122, 2012. 11

[140] B. Perthame and A.-L. Dalibard. Existence of solutions of the hyperbolic Seller-Segel model. *ArXiv Mathematics e-prints*, 2006. 90

[141] B. Perthame, C. Schmeiser, M. Tang, and N. Vauchelet. Travelling plateaus for a hyperbolic Keller-Segel system with attraction and repulsion: existence and branching instabilities. *Nonlinearity*, 24:1253–1270, 2011. 90

[142] Benoit Perthame. *Growth, reaction, movement and diffusion from biology*. UMPC, 2008. 14, 20, 56

[143] CS Peskin, GM Odell, and GF Oster. Cellular motions and thermal fluctuations - The brownian ratchet. *Biophysical Journal*, 65(1):316–324, 1993. 6, 120

REFERENCES

[144] Renaud Poincloux, Olivier Collin, Floria Lizárraga, Maryse Romao, Marcel Debray, Matthieu Piel, and Philippe Chavrier. Contractility of the cell rear drives invasion of breast tumor cells in 3D Matrigel. *Proceedings of the National Academy of Sciences*. 14, 55, 57

[145] Earnshaw William C. Pollard, Thomas D. *Cell biology*. Saunders Elsevier, 2 edition, 2004. 4, 5, 6, 7, 120

[146] Marcus Prass, Ken Jacobson, Alex Mogilner, and Manfred Radmacher. Direct measurement of the lamellipodial protrusive force in a migrating cell. *Journal of cell biology*, 174(6):767–772, 2006. 114, 117, 120

[147] Jacques Prost, Camilla Barbetta, and Jean-François Joanny. Dynamical control of the shape and size of stereocilia and microvilli. *Biophysical Journal*, 93(4):1124 – 1133, 2007. 114, 134, 136

[148] Jacques Prost, Jean-François Joanny, Peter Lenz, and Cécile Sykes. The physics of listeria propulsion. In *Cell Motility*, Biological and Medical Physics, Biomedical Engineering, pages 1–30. Springer New York, 2008. 14

[149] E. M. Purcell. Life at low Reynolds number. *American Journal of Physics*, 45(1):3–11, 1977. 34, 65

[150] SM Rafelski and JA Theriot. Crawling toward a unified model of cell motility: Spatial and temporal regulation of actin dynamics. *Annual Review of Biochemistry*, 73:209–239, 2004. 17

[151] J. Ranft, J. Prost, F. Julicher, and J. F. Joanny. Tissue dynamics with permeation. *European Physical Journal E*, 35(6), JUN 2012. 3, 136

[152] XF Ren and L Truskinovsky. Finite scale microstructures in nonlocal elasticity. *Journal of Elasticity*, 59(1-3):319–355, 2000. 65, 96

[153] Anne J. Ridley, Martin A. Schwartz, Keith Burridge, Richard A. Firtel, Mark H. Ginsberg, Gary Borisy, J. Thomas Parsons, and Alan Rick Horwitz. Cell migration: Integrating signals from front to back. *Science*, 302(5651):1704–1709, 2003. 113

[154] T. Risler. Cytoskeleton and Cell Motility. *ArXiv e-prints*, 2011. 24

[155] A Ros, R Eichhorn, J Regtmeier, TT Duong, P Reimann, and D Anselmetti. Brownian motion - Absolute negative particle mobility. *Nature*, 436(7053):928, 2005. 120

[156] Boris Rubinstein, Maxime F. Fournier, Ken Jacobson, Alexander B. Verkhovsky, and Alex Mogilner. Actin-Myosin Viscoelastic Flow in the Keratocyte Lamellipod. *Biophysical Journal*, 97(7):1853–1863,2009. 3, 10, 12, 19, 23, 56, 120, 122, 125, 136, 138, 159, 164, 166, 168

[157] David Saintillan and Michael J. Shelley. Emergence of coherent structures and large-scale flows in motile suspensions. *Journal of the Royal Society Interface*, 9(68):571–585, 2012. 55, 119

[158] G Salbreux, J F Joanny, J Prost, and P Pullarkat. Shape oscillations of non-adhering fibroblast cells. *Physical Biology*, 4(4):268, 2007. 161

[159] G. Salbreux, J. Prost, and J. F. Joanny. Hydrodynamics of cellular cortical flows and the formation of contractile rings. *Phys. Rev. Lett.*, 103:058102, 2009. 56

[160] Christian H. Schreiber, Murray Stewart, and Thomas Duke. Simulation of cell motility that reproduces the force-velocity relationship. *Proceedings of the National Academy of Sciences of the USA*, 107(20):9141–9146, 2010. 16, 114, 117, 120, 127

[161] Ulrich S. Schwarz and Margaret L. Gardel. United we stand, integrating the actin cytoskeleton and cell matrix adhesions in cellular mechanotransduction. *Journal of Cell Science*, 2012. 12, 18, 159

[162] R. Shahapure, F. Difato, A. Laio, G. Bisson, E. Ercolini, L. Amin, E. Ferrari, and V. Torre. Force generation in lamellipodia is a probabilistic process with fast growth and retraction events. *Biophysical Journal*, 98(6):979–988, 2010. 131

[163] Danying Shao, Wouter-Jan Rappel, and Herbert Levine. Computational Model for Cell Morphodynamics. *Physical Review Letters*, 105(10), 2010. 12, 19, 56, 114, 115, 159

[164] MP Sheetz, JE Sable, and HG Dobereiner. Continuous membrane-cytoskeleton adhesion requires continuous accommodation to lipid and cytoskeleton dynamics. *Annual Review of Biophysics and Biomolecular Structure*, 35:417–434, 2006. 114, 134, 136

[165] M. Sheinman, C. P. Broedersz, and F. C. MacKintosh. Actively stressed marginal networks. *ArXiv e-prints*, June 2012. 3, 136

[166] D.I. Shreiber, V.H. Barocas, and R.T. Tranquillo. Temporal variations in cell migration and traction during fibroblast-mediated gel compaction. *Biophysical Journal*, 84(6):4102–4114, 2003. 20

[167] Maria Shutova, Changsong Yang, Jury M. Vasiliev, and Tatyana Svitkina. Functions of Nonmuscle Myosin II in Assembly of the Cellular Contractile System. *PLOS One*, 7(7), 2012. 40

[168] RA Simha and S Ramaswamy. Hydrodynamic fluctuations and instabilities in ordered suspensions of self-propelled particles. *Physical Review Letters*, 89(5), 2002. 55, 56, 119

[169] TP STOSSEL. On the Crawling of Animal-Cells. *Science*, 260(5111):1086–1094, 1993. 2, 12, 113

[170] Angélique Stéphanou, Eleni Mylona, Mark Chaplain, and Philippe Tracqui. A computational model of cell migration coupling the growth of focal adhesions with oscillatory cell protrusions. *Journal of Theoretical Biology*, 253(4):701 – 716, 2008. 19, 128

[171] Daisuke Suzuki and Toyonori Munakata. Rectification efficiency of a brownian motor. *Phys. Rev. E*, 68:021906, 2003. 28, 103

[172] TM Svitkina, AB Verkhovsky, KM McQuade, and GG Borisy. Analysis of the actin-myosin II system in fish epidermal keratocytes: Mechanism of cell body translocation. *Journal of Cell Biology*, 139(2):397–415, 1997. 10, 16, 124, 126, 127

[173] K Tawada and K Sekimoto. Protein friction exerted by motor enzymes through a weak-binding interaction. *Journal of Theoretical Biology*, 150(2):193–200, 1991. 12, 159

[174] JA Theriot and TJ Mitchison. Actin microfilament dynamics in locomoting cells. *Nature*, 352(6331):126–131, 1991. 124

[175] JA Theriot, TJ Mitchison, LG Tilney, and DA Portnoy. The rate of actin-based motility of intracellular listeria-monocytogenes equals the rate of actin polymerization. *Nature*, 357(6375):257–260, 1992. 14

[176] P. Guthardt Torres, I. B. Bischofs, and U. S. Schwarz. Contractile network models for adherent cells. *Physical Review E*, 85(1, Part 1), 2012. 4, 8

[177] P. Guthardt Torres, K. Doubrovinski, and K. Kruse. Filament turnover stabilizes contractile cytoskeletal structures. *EPL*, 91(6), 2010. 58, 61

[178] A van Oudenaarden and JA Theriot. Cooperative symmetry breaking by actin filament polymerization in a model for cell motility. *Biophysical Journal*, 78(1, Part 2):1421Pos, 2000. 14

[179] Ben Vanderlei, James J. Feng, and Leah Edelstein-Keshet. A computational model of cell polarization and motility coupling mechanics and biochemistry. *Multiscale Modeling & Simulation*, 9(4):1420–1443, 2011. 14, 20

[180] AB Verkhovsky, TM Svitkina, and GG Borisy. Self-polarization and directional motility of cytoplasm. *Current Biology*, 9(1):11–20, 1999. 14, 55, 57, 65

[181] M Vicente-Manzanares, DJ Webb, and AR Horwitz. Cell migration at a glance. *Journal of Cell Science*, 118(21), 2005. 113

[182] Miguel Vicente-Manzanares, Xuefei Ma, Robert S. Adelstein, and Alan Rick Horwitz. Non-muscle myosin II takes centre stage in cell adhesion and migration. *Nature Reviews Molecular Cell Biology*, 10(11):778–790, 2009. 16, 40, 55, 57

[183] HY Wang and G Oster. The Stokes efficiency for molecular motors and its applications. *Europhysics Letters*, 57(1):134–140, 2002. 28, 103

[184] Qi Wang, Xiaofeng Yang, David Adalsteinsson, Timothy C. Elston, Ken Jacobson, Maryna Kapustina, and M. Gregory Forest. Computational and modeling strategies for cell motility. pages 257–296, 2012. 17, 18, 114, 115

[185] YX Wang, EL Botvinick, YH Zhao, MW Berns, S Usami, RY Tsien, and S Chien. Visualizing the mechanical activation of Src. *Nature*, 434(7036):1040–1045, 2005. 40

[186] Haguy Wolfenson, Yoav I. Henis, Benjamin Geiger, and Alexander D. Bershadsky. The Heel and Toe of the Cell's Foot: A Multifaceted Approach for Understanding the Structure and Dynamics of Focal Adhesions. *Cell Motility and the Cytoskeleton*, 66(11):1017–1029,2009. 40

[187] Charles W. Wolgemuth, Jelena Stajic, and Alex Mogilner. Redundant Mechanisms for Stable Cell Locomotion Revealed by Minimal Models. *Biophysical Journal*, 101(3):545–553,2011. 10, 16, 19, 114, 115, 161

[188] CW Wolgemuth. Lamellipodial contractions during crawling and spreading. *Biophysical Journal*, 89(3):1643–1649, 2005. 18, 114, 115

[189] F Wottawah, S Schinkinger, B Lincoln, R Ananthakrishnan, M Romeyke, J Guck, and J Kas. Optical rheology of biological cells. *Physical Review Letters*, 94(9), 2005. 3, 138

[190] Patricia T. Yam, Cyrus A. Wilson, Lin Ji, Benedict Hebert, Erin L. Barnhart, Natalie A. Dye, Paul W. Wiseman, Gaudenz Danuser, and Julie A. Theriot. Actin-myosin network reorganization breaks symmetry at the cell rear to spontaneously initiate polarized cell motility. *Journal Of Cell Biology*, 178(7):1207–1221,2007. 14, 15, 55, 57

[191] Mark Zajac, Brian Dacanay, William A. Mohler, and Charles W. Wolgemuth. Depolymerization-driven flow in nematode spermatozoa relates crawling speed to size and shape. *Biophysical Journal*, 94(10):3810–3823, 2008. 12, 120, 122, 160

[192] M.H. Zaman, R.D. Kamm, P. Matsudaira, and D.A. Lauffenburger. Computational model for cell migration in three-dimensional matrices. *Biophysical Journal*, 89(2):1389–1397, 2005. 20

[193] Noureddine Zebda, Oleksii Dubrovskyi, and Konstantin G. Birukov. Focal adhesion kinase regulation of mechanotransduction and its impact on endothelial cell functions. *Microvascular Research*, 83(1):71 – 81, 2012. 11

[194] WenLiang Zhang, Jin Qian, HaiMin Yao, WeiQiu Chen, and HuaJian Gao. Effects of functionally graded materials on dynamics of molecular bond clusters. *Science China Physics, Mechanics & Astronomy*, 55:980–988, 2012. 11, 53

[195] Yuan Zhong, Dong Kong, Lanhong Dai, and Baohua Ji. Frequency-dependent focal adhesion instability and cell reorientation under cyclic substrate stretching. *Cellular and Molecular Bioengineering*, 4:442–456, 2011. 11

[196] Falko Ziebert, Sumanth Swaminathan, and Igor S. Aranson. Model for self-polarization and motility of keratocyte fragments. *Journal of The Royal Society Interface*, 9(70):1084–1092, 2012. 19, 56, 114, 115

[197] Juliane Zimmermann, Claudia Brunner, Mihaela Enculescu, Michael Goegler, Allen Ehrlicher, Josef Kaes, and Martin Falcke. Actin Filament Elasticity and Retrograde Flow Shape the Force-Velocity Relation of Motile Cells. *Biophysical Journal*, 102(2):287–295, 2012. 114, 117, 120